3.5 VERTICAL VARIATION OF THE ATMOSPHERIC CHEMICAL PROCESSES

The availability of measurements of pollutant concentrations aloft has increased significantly and, with them, the scientific interest in the vertical variation of the atmospheric chemical processes. Most of the primary pollutants are emitted at ground level or very close to it; therefore, the simplest description of the system would be that all the concentrations decrease with height. Thus, all the reaction rates decrease with height in the troposphere. However, this is not always the case, with the vertical variability of the ozone concentration being an important exception.

It is widely known that in the South Coast Air Basin (SCAB) after sunrise, the ground heating generates a growing mixed layer that eliminates the stable stratification. Inside this layer the vertical mixing is efficient and the vertical concentration profiles of primary and secondary pollutants (O_3, etc.) do not exhibit any significant vertical gradients. During the evening hours, the atmosphere becomes more and more stable and the vertical pollutant dispersion becomes extremely slow. Emissions of primary pollutants remain near the ground. For example, NO is emitted near the ground where it reacts with the existing O_3, producing NO_2. This reaction, combined with the unavailability of sunlight for the triggering of O_3 producing photochemical reactions (e.g., NO_2 photolysis, etc.), results in destruction of the O_3 close to the ground. The inability of the emitted NO to diffuse upwards in the stable atmosphere protects the O_3 aloft. Therefore, the typical O_3 concentration during the early morning in the SCAB is practically zero close to the ground, while significant O_3 concentrations exist aloft. As the convective layer grows in depth the next morning, pollutants from aloft are rapidly entrained and mixed downward. By this mechanism, the upper air chemistry or its lack thereof, assists in the creation of elevated O_3 levels during the morning hours.

Existence of phenomenon discussed above lead to several additional questions concerning the production of acidic species like sulfate and nitrate. Is it possible to have trapping of the precursors of these species aloft resulting in an increased production of

acidity aloft that later fumigates to the ground? Even if the precursor concentrations decrease with height, are there additional chemical pathways aloft that are going to lead to the increased production of acidic species aloft? We shall attempt to look into these two questions by using the aircraft data collected during SCAQS, together with current knowledge of the corresponding processes.

3.5.1 Vertical Distribution of SO_2

Significant quantities of SO_2(g) are emitted in the SCAB by tall stacks at heights around 100m (including the plume rise). If the effective emission height is within the mixing layer, then the vertical dispersion of the plume is relatively rapid and the vertical distribution of the corresponding chemistry is relatively uniform. Emission of SO_2 by elevated point sources results in relatively interesting behavior when the mixing layer is below the effective emission height (stack height plus plume rise). In this case, the emitted SO_2(g), accompanied by the primary sulfate, will be trapped aloft and their corresponding ground-level concentrations will be reduced.

The episode of December 10-11, 1987, is a typical example of this phenomenon. The measured concentration of SO_2 at 335 m over Long Beach at 7:30 a.m. on December 11, is roughly a factor of 2 higher than the ground-level concentration. The vertical SO_2 profile measured by an aircraft performing a spiral over Fullerton at 4:30 p.m. on December 11 indicated an SO_2 concentration of 12 ppb at 250 m and only 2 ppb near the ground. On the contrary, measurements indicated that SO_2 had fumigated to the ground at Hawthorne at 3 p.m. and at Long Beach at 4 p.m. of the same day. An initial theoretical analysis of this episode has been presented in Section 3.4.

Despite the trapping of SO_2 aloft, the measured sulfate concentrations aloft were less than 50% of the ground-level concentrations. The occurrence of the fog episode near the ground is the major cause for this strange behavior. The imaginary scenario of the absence of fog near the ground can be examined by using the results of the 'gas-phase chemistry only' simulations described in Section 3.4.

According to the base case simulation, SO_2 is trapped aloft over Hawthorne until

1 p.m., when it fumigates to the ground. The time for fumigation depends critically on the mixing height as shown in Section 3.4. Without taking into account the sulfate production inside the fog layer, the sulfate concentrations aloft predicted by the model exceed the ground-level concentrations for most of the day, something not observed due to the fog episode.

This analysis indicates that the potential exists for the gas-phase production of sulfate aloft and its fumigation later onto the ground during days with very small mixing heights during the winter. During these conditions, photochemical activity is generally low; therefore, the absolute production rates of sulfate are also small. The fumigation of primary sulfate emitted with the SO_2 is then going to be the major process affecting ground sulfate levels. The existence of fog near the ground reverses the above process, increases the ground-level sulfate, and results in upward diffusion of sulfate.

3.5.2 In-cloud Production of Acidic Species

The process described in the previous paragraph can be reversed if the ground-level fog is replaced by clouds aloft. Clouds provide the medium–the liquid water–for the production of acidic species like sulfate. Therefore, one can hypothesize that the clouds can process primary pollutants, produce acidic species, which, after the cloud dissipation, will diffuse to the ground. Before attempting to test this hypothesis with SCAQS data, it would be useful to review our knowledge of the corresponding aqueous-phase processes and examine which species can actually be produced inside a cloud. As a basis for this analysis, we shall use the work of Pandis and Seinfeld (1989).

The dissolution of SO_2 in the cloudwater, and its oxidation to sulfate, is a dominant chemical process in clouds. There are several chemical pathways for such a transformation with the most important being the oxidation of S(IV) by $H_2O_2(aq)$. Other important pathways include reactions with O_2 (catalyzed by Fe^{3+} and Mn^{2+}) with OH and O_3. The rate of these aqueous-phase reactions can easily be more than one order of magnitude faster than the gas-phase SO_2 oxidation. The comparison of the in-cloud sulfate production rate aloft, with the corresponding gas-phase production

rate at ground level, is further complicated by the difference in SO_2(g) concentrations in these heights. Even if SO_2 is oxidized much faster inside the cloud, the SO_2 concentration in urban areas like Los Angeles is usually much higher near the ground, resulting in roughly similar sulfate production rates.

No important aqueous-phase reaction pathways seem to exist for the production of NO_3^- inside clouds; therefore, clouds cannot enhance the ambient nitrate concentration levels.

The presence of a cloud has been shown to enhance the production of formic acid. Formaldehyde dissolves in cloudwater where it reacts with dissolved OH(aq) to produce HCOOH which can be transferred back to the gas phase.

In conclusion, our current knowledge indicates that the potential exists, at least theoretically, for the production of sulfate aloft in a cloud and its subsequent transfer close to the ground.

3.5.3 Vertical Distribution of Sulfate

The sulfate concentrations measured aloft during the August and December SCAQS intensive days have been compared with corresponding ground-level concentrations. For all of these measurements the sulfate concentrations at the ground exceed the sulfate concentrations aloft (Figure 3.5.1). A strong correlation exists, as one would expect, between the ground and upper air sulfate concentrations. The concentrations of sulfate during the December episode were closer to the ground concentrations for two reasons: (1) the measurements were taken at a much smaller height (only 350 m), and (2) the mixing heights were much lower and a significant part of SO_2 and sulfate emissions were trapped aloft.

This comparison is based on only two episodes and it cannot be conclusive, but it suggests a strong tendency of sulfate to diffuse upwards and not the opposite. Another factor that should be considered is that during the above SCAQS intensive days there were only sparse isolated clouds. Therefore, the previous comparison indicates that during these specified periods, the upper air heterogeneous production of sulfate,

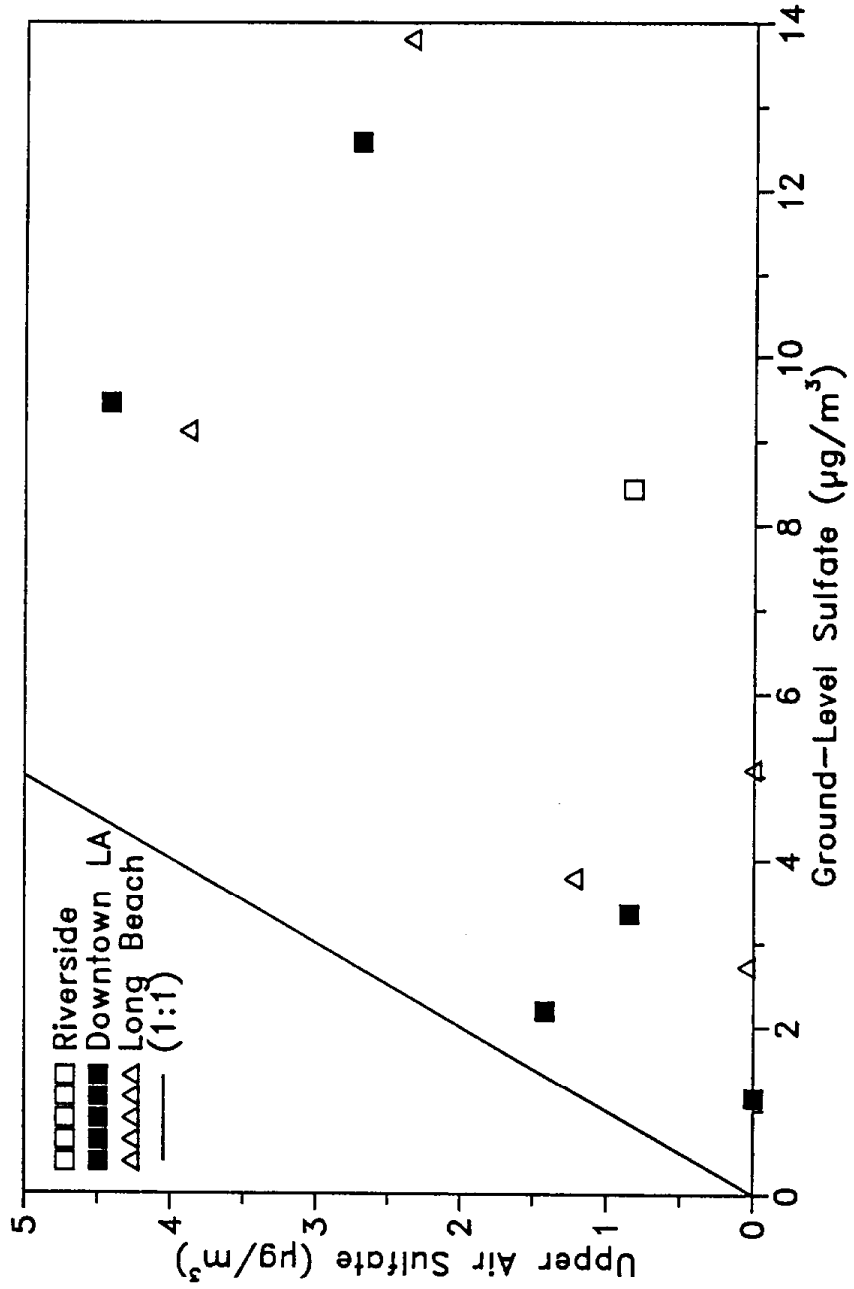

FIGURE 3.5.1. Comparison between the aerosol sulfate concentrations measured at the ground with the corresponding concentrations measured aloft during the August and December SCAQS intensive days.

if it existed at all, did not influence appreciably the ground sulfate levels. Further examination of the above described processes under more appropriate meteorological conditions (e.g., periods of cloudiness) could provide additional insights.

4. SOURCE APPORTIONMENT OF ACIDIC SPECIES IN THE SOUTHERN CALIFORNIA AIR BASIN

4.1 OBJECTIVES

The objectives of this section are to investigate the sources, transportation, and fate of acidic atmospheric components in the SoCAB. To examine the source/receptor relationships in the basin, a number of summary statistics and several multivariate statistical methods1—classical factor analysis, Target Transformation Factor Analysis (TTFA), stepwise multiple regression, and potential source contribution function analysis (PSCF)--have been applied to parts or all of the acidic species and trace element concentration data for particle samples collected at the Burbank, Claremont, and Rubidoux sites. These sites are shown in Figure 4.1.1 along with a contour plot of the surrounding terrain. The data analysis methods have been applied to these data to provide an improved understanding of the nature and behavior of the acidic species observed in the SoCAB during the SCAQS field exercises.

4.2 DESCRIPTION OF DATA AND DATA QUALITY ANALYSES

The study concentrated on two data sets generated from the airborne particle and related samples collected at the Burbank, Claremont, and Rubidoux sites during the intensive study days of the SCAQS study in 1987. The first data set includes surface and upper wind data and the concentrations of 15 acidic chemical species, one trace element, and two mass components that were collected with SCAQS samplers and analyzed using either ion chromotography, atomic absorption, colorimetry, or gravimetry. These species include gaseous SO_2, $SO_4^=$ (PM-2.5, PM-10), gaseous HNO_3 and NH_3, NO_3^- (=gaseous NO_3^- + PM-2.5 NO_3^-), NO_3^- (PM-10, PM-2.5 L3 and PM-2.5 L9), NO_3^- (Total), NH_4^+ (PM-10, PM-2.5 L5 and PM-2.5 L9), Cl (PM-10 and PM-2.5), PM-10 Na, and Mass (PM-2.5, PM-10). A paper titled "Multi-Component Size-Classifying Aerosol and Gas Samplers for Ambient Air Monitoring," is included in Appendix C of this report. For definitions of L9, L3, and L5 see the details concerning the SCAQS samplers.

FIGURE 4.1.1. Map of the South Coast Air Quality Study region.

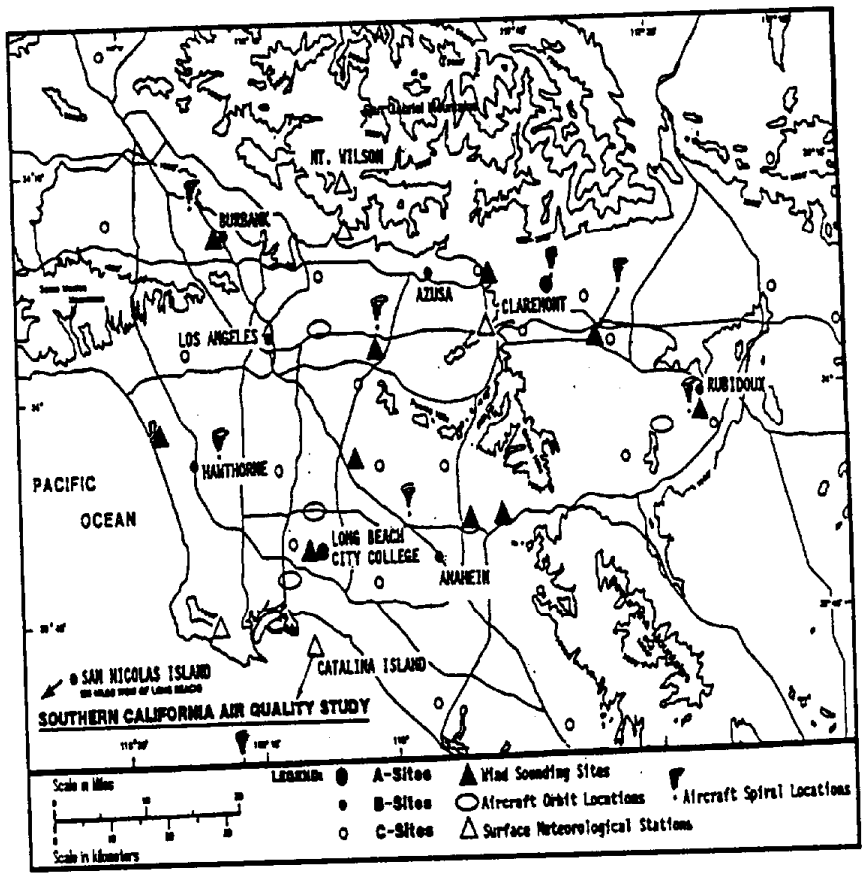

The first data set contains 85 samples each for the Burbank and Rubidoux sites that were collected on the 17 intensive study days during the summer and fall of 1987, and 55 samples for the Claremont site that were collected during the 11 intensive study days in the summer of 1987. The second set of data was obtained from Professor R.C. Henry of the University of Southern California. This set of data contains concentrations of 31 trace elements (PM-2.5) collected with a SCAQS sampler, on the 11 intensive study days in the summer of 1987, using XRF analysis. Unfortunately, the concentrations of a number of species in most of the samples are below detection limits. Only those species with less than 1/3 of the measurements below detection limits were used in the subsequent analyses. Data quality analysis was then applied to these data, with minor data quality problems discovered. The PM-2.5 trace element values seem reasonable for most species except for PM-2.5 sulfur collected at Claremont. In this particular case, the XRF values for PM-2.5-S appear to have serious discrepancies relative to the IC $SO_4^=$ values. The scatter plots of the concentrations of sulfur calculated from the IC $SO_4^=$ values against the concentrations of XRF S in PM-2.5 samples are shown in Figures 4.2.1-4.2.3. It can be seen that either XRF overestimates sulfur or IC underestimates sulfate since the elemental sulfur should have been completely oxidized into sulfate in the SoCAB environment. For the scatter plots of Rubidoux and Burbank, there are good correlations between the S values, but a measurement bias by one or another method. However, for the scatter plot of Claremont, there is a poor correlation indicating a substantial error has been introduced in the IC, the XRF, or both analyses. It is not possible to determine which analysis method is correct; thus, both values have been used in the subsequent statistical analysis. Other species also show substantial deviations between the IC and XRF concentrations. The scatter plots of the IC values against the XRF values for chlorine show biases for one or the other analytical method (Figures 4.2.4 and 4.2.5).

After calculating the summary statistics and performing the PSCF analyses of the species, the concentration data of all the species chosen for other analyses were corrected for missing values and below detection limit values. For the IC samples, the below detection limit data were replaced with the detection limit. Then missing values were replaced with the mean concentrations of the respective species. For the XRF samples, the below detection limit concentration measurements were replaced with the

FIGURE 4.2.1. Comparison of the S concentrations in PM2.5 samples collected at Burbank calculated from the IC $SO_4^=$ values with the XRF S determinations.

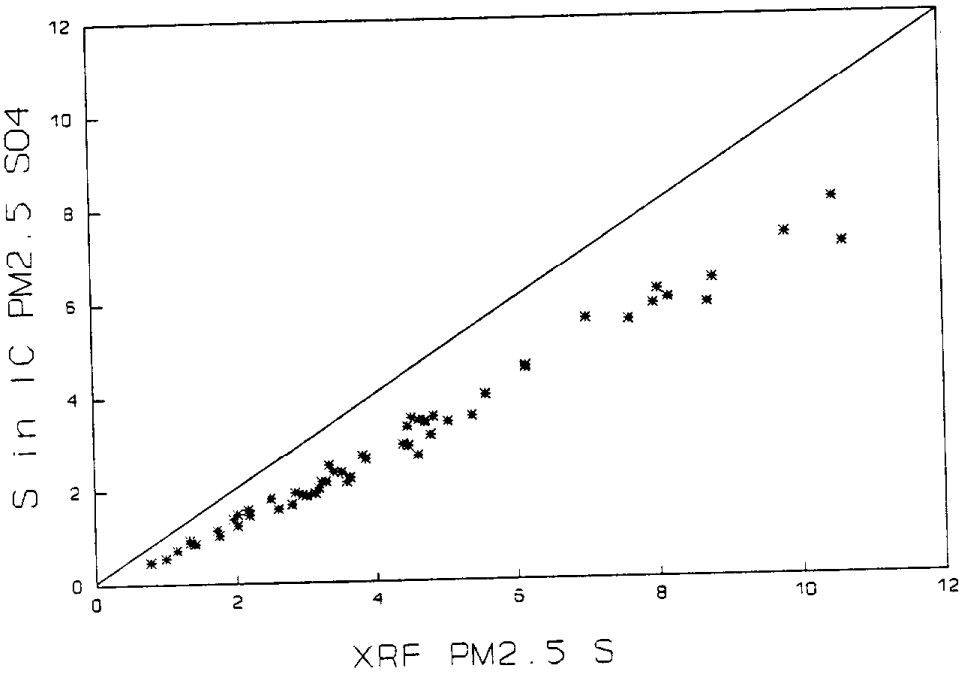

FIGURE 4.2.2. Comparison of the S concentrations in PM2.5 samples collected at Claremont calculated from the IC $SO_4^=$ values with the XRF S determinations.

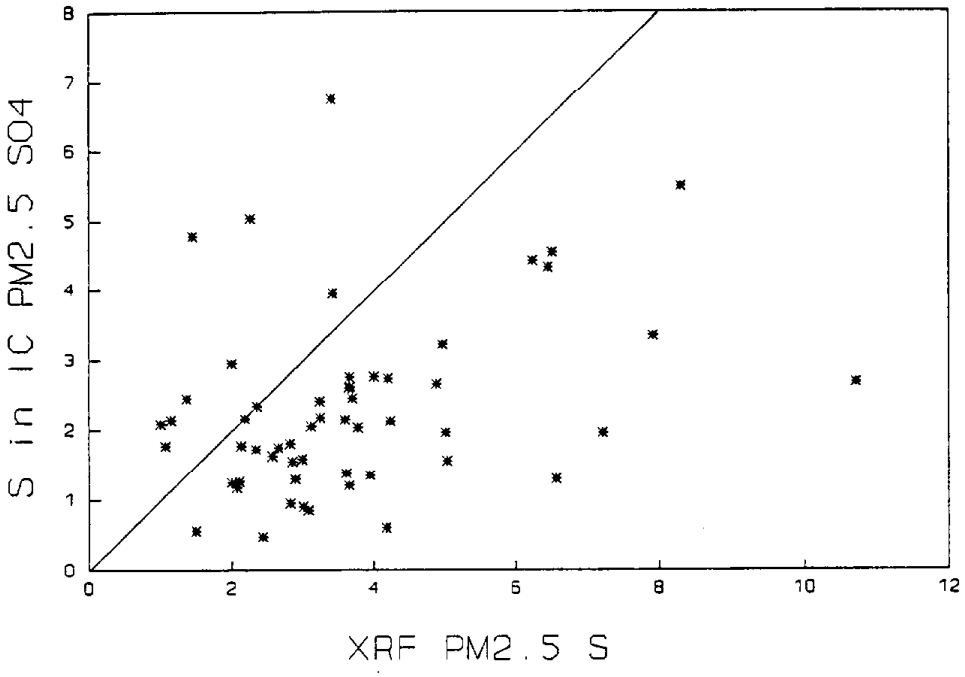

FIGURE 4.2.3. Comparison of the S concentrations in PM2.5 samples collected at Rubidoux calculated from the IC $SO_4^=$ values with the XRF S determinations.

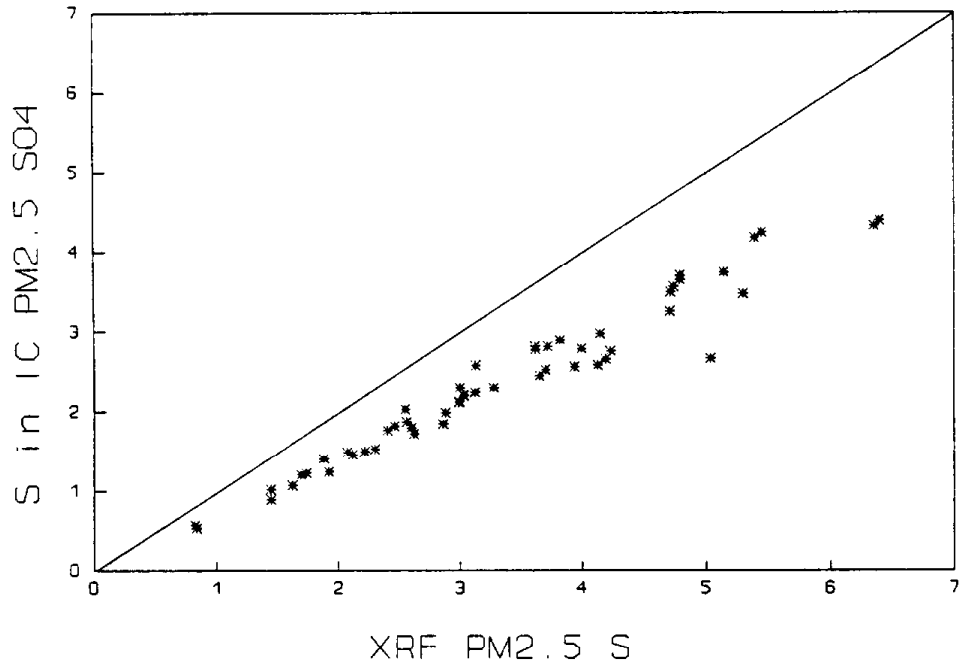

FIGURE 4.2.4. Comparison of the chlorine concentrations measured in Burbank PM2.5 samples using IC and XRF.

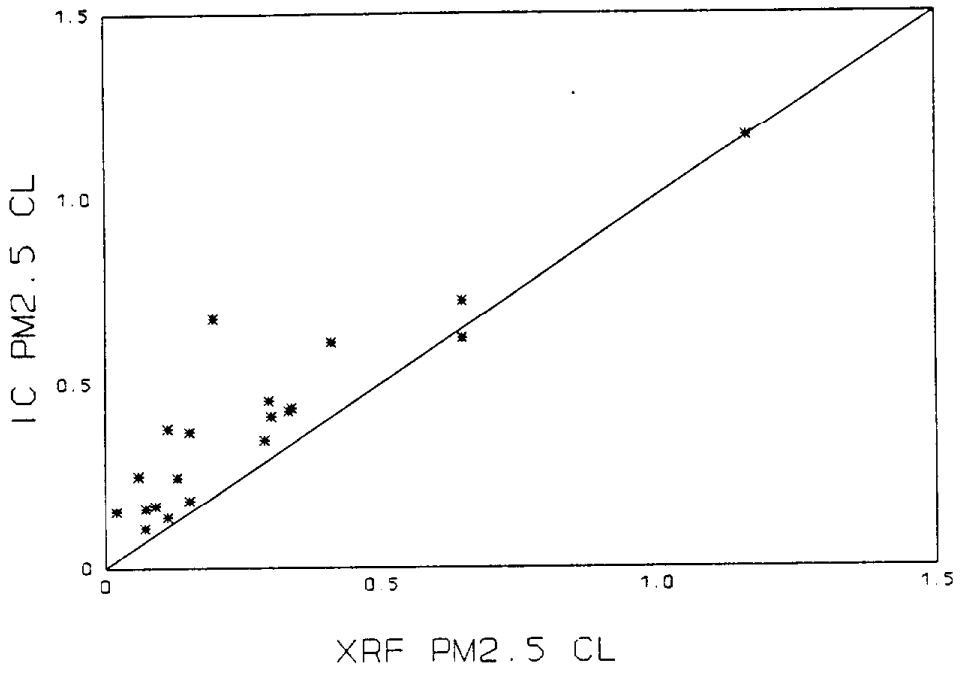

FIGURE 4.2.5. Comparison of the chlorine concentrations measured in Claremont PM2.5 samples using IC and XRF.

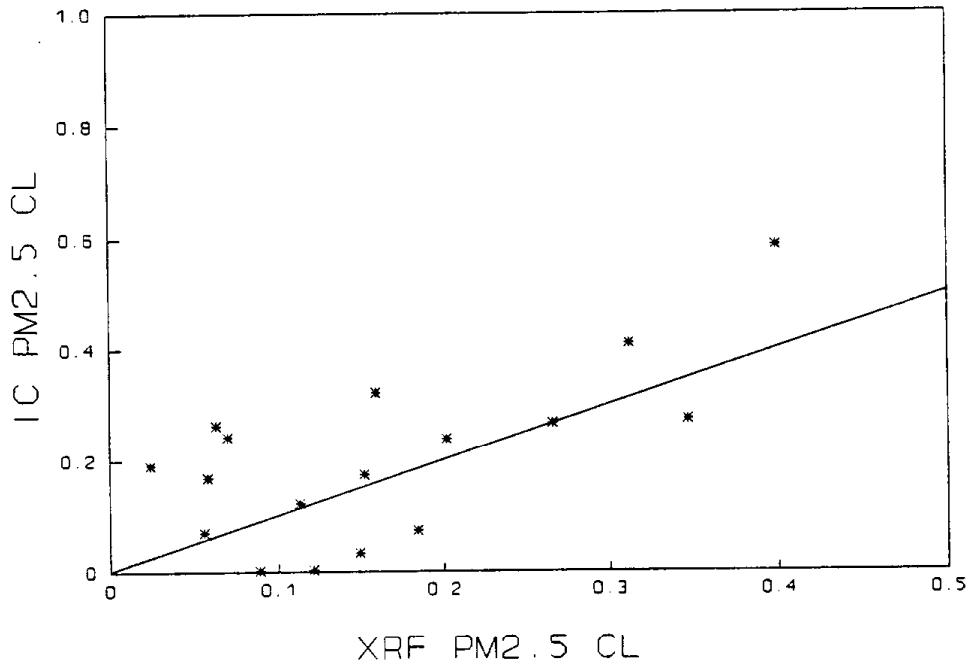

values obtained by multiplying the detection limit by a uniformly distributed random number (0 < Random Number < 1). The missing values were also replaced by the mean concentrations of the species. The corrected data were then used for subsequent multivariate analyses.

4.3 DATA ANALYSES

4.3.1 Summary Statistics

Eighteen summary statistics were calculated for each of the 15 chemical species measured at the three sampling sites (Table 4.3.1- Table 4.3.3). These indices include the mean, median, mode, geometric mean, and the variance with measures of the range. All of the statistics indicate that these species have positively-skewed distributions except PM-2.5- NO_3^- L9 (Claremont) and gaseous NO_3^- (Rubidoux). These indices are useful for understanding the distribution of each chemistry variable, and provide an indication of the critical concentration values to be used in the potential source contribution function analysis.

4.3.2 Factor Analyses

In studies of the environment, many variables are measured to characterize the system. However, not all of the measured species vary independently of one another. Thus, it is essential to have mathematical techniques that permit the study of the simultaneous variation of multiple variables. One such analysis is based on examining the relationships between pairs of variables. This correlation analysis, however, does not provide a clear view of the multiple interactions in the data. Thus, various forms of eigenvector analyses are used to convert the correlation data into multivariate information. Factor analysis is the name given to one of the variety of forms of eigenvector analysis. It was originally developed and used in psychology to provide mathematical models of psychological theories of human ability and behavior (Harman, 1976). However, eigenvector analysis has found wide application throughout the physical and life sciences. Unfortunately, a great deal of confusion exists in the

TABLE 4.3.1. Summary statistics for SCAQS --- Burbank sampling site, California, 1987.

Summary Statistic	CLPM10	CLPM25	NH4L5	NH4L9	NH4PM10	NO3GAS	NO3L3	NO3L9	NO3PM10	NO3TOT	HNO3	NH3	SO2	SO4PM10	SO4PM25
Sample Size	85	85	85	85	85	85	85	85	85	85	85	85	85	85	85
Average	0.729	0.215	8.15	4.94	6.59	33.09	18.24	11.03	16.24	29.01	15.21	3.64	4.23	8.77	7.20
Median	0.269	0.058	7.40	3.75	4.74	22.16	12.53	4.99	11.61	23.24	7.57	3.07	3.55	7.40	5.79
Mode	0.017	-0.095	7.40	0.00	4.74	0.00	0.00	4.88	11.61	0.00	0.00	0.00	0.00	7.40	5.79
Geometric Mean			6.09				4.96	10.26						6.13	4.94
Variance	1.150	0.189	29.07	18.45	63.97	906.00	332.03	213.81	278.63	499.05	284.13	9.28	7.56	44.43	32.17
Standard Deviation	1.073	0.435	5.39	4.30	8.00	30.10	18.22	14.62	16.69	22.34	16.86	3.05	2.75	6.67	5.67
Standard Error	0.116	0.047	0.59	0.47	0.87	3.27	1.98	1.59	1.81	2.42	1.83	0.33	0.30	0.72	0.62
Minimum	-0.111	-0.143	0.35	0.00	-0.08	0.00	-1.94	0.11	0.63	-1.09	0.00	-0.34	0.00	0.59	0.56
Maximum	6.264	2.223	27.71	19.10	63.52	152.58	102.38	73.02	87.87	83.82	69.70	12.90	15.60	27.55	24.18
Range	6.375	2.366	27.36	19.10	63.60	152.58	104.32	72.91	87.24	84.91	72.16	13.24	15.60	26.96	23.62
Lower Quartile	0.053	-0.082	4.17	1.66	2.27	9.85	6.12	1.99	6.09	10.39	1.54	1.46	2.64	3.64	2.83
Upper Quartile	1.167	0.370	11.32	6.84	8.83	50.68	26.27	9.97	18.00	44.89	23.75	5.58	5.08	11.95	10.22
Interquartile Range	1.114	0.452	7.15	5.18	6.57	40.83	20.15	7.98	11.90	34.50	22.21	4.12	2.44	8.31	7.39
Skewness	2.608	2.195	0.90	1.33	4.62	1.31	1.96	2.23	2.17	0.68	1.06	1.07	1.51	0.98	1.07
Standardized Skewness	9.817	8.261	3.38	5.01	17.39	4.93	7.36	8.38	8.15	2.55	3.99	4.02	5.69	3.70	4.01
Kurtosis	8.880	5.839	1.13	1.70	30.42	1.96	5.07	4.98	5.08	-0.45	0.34	0.93	3.34	0.34	0.59
Standardized Kurtosis	16.712	10.989	2.12	3.19	57.25	3.69	9.54	9.37	9.56	-0.84	0.64	1.74	6.29	0.65	1.10

TABLE 4.3.2. Summary statistics for SCAQS --- Claremont sampling site, California, 1987.

Summary Statistic	CLPM10	CLPM25	NH4L5	NH4L9	NH4PM10	NO3GAS	NO3L3	NO3L9	NO3PM10	NO3TOT	HNO3	NH3	SO2	SO4PM10	SO4PM25
Sample Size	55	55	55	55	55	55	55	55	55	55	55	55	55	55	55
Average	0.340	0.047	6.74	3.82	3.19	25.42	11.97	4.99	10.30	27.21	13.92	2.09	3.61	8.35	6.97
Median	0.217	0.002	6.07	3.28	2.66	18.70	11.31	3.68	9.70	22.37	6.21	1.24	2.59	7.82	6.25
Mode	-0.033	-0.066	6.07	3.28	0.00	0.00	11.31	4.73	9.70	22.37	0.00	0.00	2.59	7.82	6.25
Geometric Mean				3.10			8.46	3.21	8.42	21.53			2.88	7.31	6.02
Variance	0.216	0.022	19.41	5.17	7.68	370.66	56.16	19.07	37.30	307.60	237.63	15.49	6.15	19.53	15.22
Standard Deviation	0.464	0.149	4.41	2.27	2.77	19.25	7.49	4.37	6.11	17.54	15.42	3.94	2.48	4.42	3.90
Standard Error	0.063	0.020	0.59	0.31	0.37	2.60	1.01	0.59	0.82	2.37	2.08	0.53	0.33	0.60	0.53
Minimum	-0.091	-0.105	0.00	0.47	-0.06	0.00	0.01	0.12	1.30	3.11	-0.05	-0.30	0.52	2.26	1.42
Maximum	2.359	0.586	26.49	10.50	9.66	68.87	31.44	18.94	27.49	64.96	52.71	28.05	10.91	22.66	20.20
Range	2.450	0.691	26.49	10.03	9.72	68.87	31.44	18.82	26.18	61.85	52.76	28.34	10.39	20.40	18.78
Lower Quartile	0.004	-0.066	4.09	2.30	0.92	10.81	6.68	1.65	5.67	13.19	2.16	0.53	1.78	4.90	4.12
Upper Quartile	0.511	0.122	8.40	5.06	4.99	39.70	15.87	7.05	14.31	35.30	24.51	2.09	4.92	9.55	8.22
Interquartile Range	0.507	0.188	4.31	2.76	4.08	28.89	9.19	5.40	8.64	22.11	22.35	1.57	3.14	4.65	4.10
Skewness	2.220	1.423	1.76	0.76	0.67	0.84	0.74	1.27	0.84	0.76	1.08	5.67	1.25	1.19	1.32
Standardized Skewness	6.720	4.308	5.33	2.30	2.03	2.55	2.25	3.85	2.55	2.30	3.28	17.16	3.77	3.59	3.99
Kurtosis	6.492	2.093	6.37	0.16	-0.49	-0.40	0.10	1.28	0.34	-0.50	-0.17	36.39	1.14	1.45	1.87
Standardized Kurtosis	9.828	3.168	9.65	0.24	-0.74	-0.60	0.15	1.93	0.51	-0.76	-0.25	55.09	1.72	2.20	2.83

TABLE 4.3.3. Summary statistics for SCAQS --- Rubidoux sampling site, California, 1987.

Summary Statistic	CLPM10	CLPM25	NH4L5	NH4L9	NH4PM10	NO3GAS	NO3L3	NO3L9	NO3PM10	NO3TOT	HNO3	NH3	SO2	SO4PM10	SO4PM25
Sample size	85	85	85	85	85	85	85	85	85	85	85	85	85	85	85
Average	0.782	0.450	25.30	7.96	7.49	29.16	26.82	23.20	28.05	31.79	2.38	20.85	3.22	6.69	5.49
Median	0.615	0.299	22.22	6.78	6.09	26.11	24.95	18.73	23.86	29.94	1.39	18.59	2.57	6.56	5.29
Mode	0.000	-0.053	22.22	0.00	0.00	27.72	24.95	0.00	0.00	29.94	1.39	18.59	0.00	0.00	0.00
Geometric Mean										23.34		13.87			
Variance	0.535	0.323	486.44	47.94	48.41	492.83	478.03	536.10	553.26	449.84	14.07	248.52	4.92	18.59	13.00
Standard Deviation	0.731	0.569	22.06	6.92	6.96	22.20	21.86	23.15	23.52	21.21	3.75	15.76	2.22	4.31	3.61
Standard Error	0.079	0.062	2.39	0.75	0.76	2.41	2.37	2.51	2.55	2.30	0.41	1.71	0.24	0.47	0.39
Minimum	-0.093	-0.107	-0.09	-0.09	-0.10	0.00	-0.84	-0.26	-0.13	0.29	0.00	0.03	0.00	0.00	0.00
Maximum	3.346	2.260	113.31	44.39	40.41	126.83	129.99	165.07	146.40	117.38	14.18	91.80	10.98	15.87	14.24
Range	3.439	2.367	113.40	44.48	40.51	126.83	130.83	165.33	146.53	117.09	19.56	91.78	10.98	15.87	14.24
Lower Quartile	0.142	0.006	6.88	3.41	2.90	12.61	10.47	7.55	13.37	16.07	0.54	8.26	1.77	3.05	2.33
Upper Quartile	1.207	0.580	37.77	10.99	10.52	39.39	35.77	31.16	39.07	43.24	3.63	28.63	4.49	9.86	7.97
Interquartile Range	1.065	0.574	30.90	7.58	7.63	26.78	25.30	23.60	25.69	27.17	3.08	20.37	2.72	6.81	5.64
Skewness	0.948	1.541	1.59	2.01	1.75	1.37	1.59	3.10	1.88	1.12	0.90	1.54	1.36	0.31	0.44
Standardized Skewness	3.567	5.801	5.97	7.55	6.59	5.15	5.98	11.68	7.06	4.20	3.37	5.81	5.11	1.15	1.65
Kurtosis	0.621	2.079	4.00	8.11	5.26	3.45	4.89	16.14	6.67	2.22	1.05	4.06	2.20	-0.82	-0.59
Standardized Kurtosis	1.169	3.913	7.53	15.26	9.90	6.49	9.21	30.38	12.56	4.17	1.97	7.64	4.13	0.00	0.00

literature in regard to the terminology of eigenvector analysis. Various changes in the way the method is applied has resulted in it being called factor analysis, principal components analysis, principal components factor analysis, empirical orthogonal function analysis, Karhunen-Loeve transform, etc., depending on the way the data are scaled before analysis or how the resulting vectors are treated after the eigenvector analysis is completed.

All of the eigenvector methods have the same basic objective: the compression of data into fewer dimensions and the identification of the structure of interrelationships that exist between the variables measured or the samples being studied. In many chemical studies, the measured properties of the system can be considered to be the linear sum of the terms representing the fundamental effects in that system times appropriate weighing factors.

In this study, factor analysis is used to examine the interrelationships between the measured ambient concentrations. These analyses identify species that co-vary because they have been emitted by the same source. However, meteorology and geography can combine to also cause materials emitted by different sources to co-vary in the resulting data set.

4.3.3 Principal Component Analysis

Principal component analysis (PCA) has been described by Roscoe et al. (1982). A varimax rotation was used. For this study, we first performed an eigenvector analysis. A subset of the resulting vectors are transformed using an optimum model for each of the PM-2.5 data sets characterizing the particle samples collected at each of the three sites. These models are useful in recognizing possible sources and identification of potential errors in the data sets. PCA analysis is capable of analyzing both particle and gaseous chemical species. The results are summarized in Tables 4.3.4-4.3.6. In these tables, only the loadings with values greater than 0.5 are given. These values are large enough to be significant for data sets of this size.

TABLE 4.3.4. Factor loadings for varimax rotated 5-factor model for PM2.5 aerosols at Burbank.

Variable/Factor	1	2	3	4	5	Communality
Gaseous NH_3	-0.540	.	.	.	.	0.343*
PM2.5-NH_4^+ L5	0.845	.	.	.	.	0.931
PM2.5-NH_4^+ L9	0.900	.	.	.	.	0.847
Gaseous NO_3^-	.	.	.	0.765	.	0.928
PM2.5-NO_3^- L3	0.801	.	.	.	.	0.797
PM2.5-NO_3^- L9	0.720	.	.	.	.	0.813
Gaseous HNO_3	.	.	.	0.896	.	0.950
Gaseous SO_2	.	.	.	.	0.687	0.606
PM2.5-$SO_4^=$	0.822	.	.	0.491	.	0.924
PM2.5-Ba	.	.	0.544	.	.	0.605
PM2.5-Ca	.	0.874	.	.	.	0.893
PM2.5-Fe	.	0.920	.	.	.	0.920
PM2.5-K	.	0.568	0.590	.	.	0.678
PM2.5-Mg	.	0.518	0.838	.	.	0.984
PM2.5-Na	.	.	0.937	.	.	0.909
PM2.5-P	.	0.545	.	.	0.687	0.782
PM2.5-S	0.809	.	.	0.513	.	0.926
PM2.5-Si	.	0.922	.	.	.	0.950
PM2.5-Ti	.	0.806	.	.	.	0.803
PM2.5-Zn	.	.	.	.	.	0.271*
% Variance Explained	38.3	28.3	10.4	7.6	5.8	
Eigenvalue	6.72	4.96	1.83	1.34	1.01	

*Variables for which the five factor model failed to adequately reproduce the system variance.

TABLE 4.3.5. Factor loadings for varimax rotated 6-factor model for PM2.5 aerosols at Claremont.

Variable/Factor	1	2	3	4	5	6	Communality
Gaseous NH_3	.	.	.	.	0.817	.	0.765
PM2.5-NH_4^+ L5	.	.	.	.	0.754	.	0.832
PM2.5-NH_4^+ L9	.	0.944	.		.	.	0.919
Gaseous NO_3^-	.	.	0.822	.	.	.	0.889
PM2.5-NO_3^- L3	.	0.804	.	.	.	.	0.824
PM2.5-NO_3^- L9	.	0.804	.	.	.	.	0.871
Gaseous HNO_3	.	.	0.930	.	.	.	0.927
Gaseous SO_2	.	.	0.548	.	.	.	0.416*
PM2.5-$SO_4^=$	.	0.712	0.580	.	.	.	0.867
PM2.5-Al	0.929	.	.	.	.	.	0.916
PM2.5-Ba	0.497	.	.	.	.	.	0.549
PM2.5-Ca	0.895	.	.	.	.	.	0.845
PM2.5-Cu	.	.	.	0.935	.	.	0.907
PM2.5-Fe	0.963	.	.	.	.	.	0.950
PM2.5-K	0.937	.	.	.	.	.	0.920
PM2.5-Mg	0.877	.	.	.	.	.	0.830
PM2.5-Na	.	.	.	.	.	0.815	0.759
PM2.5-P	0.672	.	.	.	.	.	0.649
PM2.5-S	.	.	.	.	.	.	0.393*
PM2.5-Si	0.955	.	.	.	.	.	0.952
PM2.5-Ti	0.858	.	.	.	.	.	0.824
PM2.5-Zn	.	.	.	0.920	.	.	0.886
% Variance Explained	37.4	19.4	13.7	9.4	7.1	4.2	
Eigenvalue	7.25	3.77	2.65	1.82	1.38	0.81	

*Variables for which the model does not account well for the variance.

TABLE 4.3.6. Factor loadings for varimax rotated 5-factor model for PM2.5 aerosols at Rubidoux.

Variable/Factor	1	2	3	4	5	Communality
Gaseous NH_3	.	.	.	.	0.833	0.750
PM2.5-NH_4^+ L5	.	0.679	.	.	-0.514	0.797
PM2.5-NH_4^+ L9	.	0.955	.	.	.	0.940
Gaseous NO_3^-	.	0.886	.	.	.	0.981
PM2.5-NO_3^- L3	.	0.913	.	.	.	0.963
PM2.5-NO_3^- L9	.	0.942	.	.	.	0.948
Gaseous HNO_3	.	.	0.852	.	.	0.842
Gaseous SO_2	.	.	.	-0.494	.	0.392*
PM2.5-$SO_4^=$	.	0.876	.	.	.	0.798
PM2.5-Al	0.968	.	.	.	.	0.976
PM2.5-Ca	0.842	.	.	.	.	0.763
PM2.5-Cl	.	.	-0.524	0.523	.	0.583
PM2.5-Fe	0.972	.	.	.	.	0.978
PM2.5-K	0.928	.	.	.	.	0.968
PM2.5-Mg	0.927	.	.	.	.	0.974
PM2.5-Na	.	.	.	0.680	.	0.624
PM2.5-P	0.799	.	.	.	.	0.883
PM2.5-S	.	0.838	.	.	.	0.832
PM2.5-Si	0.989	.	.	.	.	0.990
PM2.5-Ti	0.941	.	.	.	.	0.949
PM2.5-Zn	.	.	.	.	.	0.237*
% Variance Explained	46.3	25.2	9.8	6.2	3.6	
Eigenvalue	8.72	4.75	1.85	1.17	0.68	

*Species whose variances were not adequately explained by the 5-factor model.

A 5-factor model seems to be optimum to describe potential sources contributing to the PM-2.5 samples collected at the Burbank site (Table 4.3.4). Factor 1 appears to be associated with NH_4NO_3 and $(NH_4)_2SO_4$ in both particulate and gaseous phases. The negative loading on NH_3 indicates that there is no excess gaseous NH_3 so that it is inversely correlated with particulate NH_4^+. Factor 2 represents inputs of crustal elements. Marine salts appear in the 3rd factor. Factor 4 seems to be related to gaseous NO_3^- species and nitric acid, accompanied by a small amount of $SO_4^=$. Factor 5 is a source of gaseous SO_2. The comparable factor loading of P (0.687) may arise from a correlation in P values with S because of the poor separation of the small K X-ray peak of P from the larger S peak in the XRF spectrum. Resolution of chemical species data into the 5 factors for this site appears to be reasonably good. The acidic species are separated from trace elements. This result suggests that these acidic species are secondary photochemical products that are not directly correlated with emissions from primary sources.

The source-receptor relationship for the PM-2.5 aerosols at the Claremont site is best described by a 6-factor model (Table 4.3.5). Factor 1 is associated with crustal elements. Factor 2 has moderate PM-2.5 $SO_4^=$, and high PM-2.5 NO_3^- and PM-2.5 NH_4^+ loadings. It is clear that this factor is associated with most of the NH_4NO_3 and part of the $(NH_4)SO_4$ observed at this site. The loadings for both PM- 2.5 NO_3^- and PM-2.5 NH_4^+ are higher than those for PM-2.5 $SO_4^=$, indicating a stronger correlation between PM-2.5 NH_4^+ and PM- 2.5 NO_3^-. Factor 3 is related to mostly gaseous nitrate species and nitric acid. Factor 4 suggests the presence of either a smelter or an incinerator because of the high Zn value. Factor 4 is probably an artifact. The samples had some brass filings from the plumbing. High Cu and Zn should not be trusted. The positive correlation of gaseous NH_3 and PM-2.5 NH_4^+ L5 loadings on Factor 5 may be the result of reactions within the sampler. The partial pressure of NH_3 is low because it is efficiently collected within the denuder; therefore, some of the NH_4^+ L5 dissociates into NH_3 in the SCAQS sampler. If this occurs, then the measured value of NH_3 will be related to the NH_4^+ L5 value. Factor 6 represents marine particles.

A 5-factor model is optimum to account for the source-receptor relationship for the PM-2.5 aerosols at the Rubidoux site (Table 4.3.6). Factor 1 represents a crustal elements source due to wind erosion. Factor 2 has high loadings on NH_4^+, $SO_4^=$, and

NO_3^-, with loadings higher for NH_4^+ and NO_3^- than that for $SO_4^=$, indicating a strong association between NH_4^+ and NO_3^-. The 3rd factor is obviously a marine aerosol factor with a strong anticorrelation with HNO_3. It indicates that HNO_3 might have displaced Cl. HNO_3 covaried mostly with NO_3^- species at the previous two sites rather than Cl. Factor 4 is associated with unreacted marine salts. The minor loading of SO_2 could be ignored since this species is not adequately explained by this model.

In sharp contrast to the other two sites, gaseous NH_3 and PM-2.5 NH_4^+ L5 are negatively correlated on the 5th factor. This result indicates substantial excess NH_3 at Rubidoux. The NH_3 is high enough that it can titrate the airborne acidity. Thus, when there is more HNO_3, more of the NH_3 is converted into NH_4^+ L5 and less is left in the gas phase. There is then an inverse relationship between the NH_3 and the NH_4^+ values.

4.3.4 Stepwise Multiple Regression

Another approach to the study of the origins of acidity in the SoCAB is multiple regression analysis. If the variation in particulate $SO_4^=$ and NO_3^- can be related to other measured species that were emitted by the sources of their gaseous precursors, it may be possible to identify these sources. Thus, stepwise multiple regression analysis was applied to nitrate and sulfate as the dependent variables against the independent trace elements. Thus, a model of the form

$$y_j = \beta_0 + \sum_{i=1}^{i} \beta_i x_{ij}$$

where y_j is one of the measured $SO_4^=$ or NO_3^- species, x_{ij} are the concentrations of those I species that are significantly related to the $SO_4^=$ or NO_3^- values, and β_i are the regression coefficients. The results are presented in Tables 4.3.7-4.3.15. In general, the multiple regressions explain less than half of the variance of the various species. These results reinforce the principal components results in that generally there were no strong relationships between the trace elements that might indicate primary particle

TABLE 4.3.7. Multiple regression model fitting results for PM2.5-NO_3^-L3 collected at Burbank.

Independent Variable	Coefficient	Std. error	T-value	Sig.level	R^2(Adj.)
CONSTANT	-0.833	1.981	-0.420	0.676	0.5835
PM2.5-Si	-43.351	14.706	-2.948	0.005	
PM2.5-S	1.631	0.273	5.967	0.000	
PM2.5-Ti	212.396	75.639	2.808	0.007	
PM2.5-Fe	42.446	17.093	2.483	0.017	
PM2.5-Zn	24.878	7.727	3.220	0.002	

TABLE 4.3.8. Multiple regression model fitting results for PM2.5-NO_3^-L9 collected at Burbank.

Independent Variable	Coefficient	Std. error	T-value	Sig.level	R^2(Adj.)
CONSTANT	4.213	1.883	2.238	0.030	0.3422
PM2.5-Na	6.058	5.231	1.158	0.253	
PM2.5-Mg	-125.387	55.330	-2.266	0.028	
PM2.5-Si	-39.661	11.720	-3.384	0.002	
PM2.5-P	-288.496	67.637	-4.265	0.000	
PM2.5-K	59.991	22.531	2.663	0.011	
PM2.5-Ca	59.478	17.803	3.341	0.002	
PM2.5-Ti	122.126	59.286	2.060	0.045	
PM2.5-Fe	17.241	13.001	1.326	0.192	
PM2.5-Zn	9.237	5.704	1.620	0.112	

TABLE 4.3.9. Multiple regression model fitting results for PM2.5-$SO_4^=$ collected at Burbank site.

Independent Variable	Coefficient	Std. error	T-value	Sig.level	R^2(Adj.)
CONSTANT	7.885	2.152	3.664	0.001	0.2932
PM2.5-Na	7.054	2.903	2.430	0.019	
PM2.5-Si	-23.789	14.704	-1.618	0.112	
PM2.5-P	-125.230	86.739	-1.444	0.155	
PM2.5-Ca	42.424	24.571	1.727	0.091	
PM2.5-Fe	23.199	18.353	1.264	0.212	
PM2.5-Ba	-230.199	52.261	-4.405	0.000	

TABLE 4.3.10. Multiple regression model fitting results for PM2.5-NO_3^- L3 collected at Claremont.

Independent Variable	Coefficient	Std. error	T-value	Sig.level	R^2(Adj.)
CONSTANT	10.493	2.477	4.236	0.000	0.2408
PM2.5-Al	-65.362	22.799	-2.867	0.006	
PM2.5-Si	37.132	11.709	3.171	0.003	
PM2.5-Cu	-14.649	6.991	-2.096	0.041	
PM2.5-Zn	14.567	9.933	1.466	0.149	

TABLE 4.3.11. Multiple regression model fitting results for PM2.5-NO_3^- L9 collected at Claremont.

Independent Variable	Coefficient	Std. error	T-value	Sig.level	R^2(Adj.)
CONSTANT	4.777	1.249	3.825	0.000	0.3069
PM2.5-Al	-12.921	5.250	-2.461	0.017	
PM2.5-P	-81.427	59.826	-1.361	0.180	
PM2.5-Ca	12.695	6.482	1.958	0.056	
PM2.5-Fe	14.267	5.909	2.415	0.020	
PM2.5-Ba	-165.593	76.171	-2.174	0.035	

TABLE 4.3.12. Multiple regression model fitting results for PM2.5-$SO_4^=$ L3 collected at Claremont.

Independent Variable	Coefficient	Std. error	T-value	Sig.level	R^2(Adj.)
CONSTANT	6.009	1.273	4.720	0.000	0.0653
PM2.5-P	57.096	53.738	1.063	0.293	
PM2.5-Ti	102.405	54.175	1.890	0.064	
PM2.5-Fe	-9.030	3.732	-2.420	0.019	

TABLE 4.3.13. Multiple regression model fitting results for PM2.5-NO_3^- L3 collected at Rubidoux.

Independent Variable	Coefficient	Std. error	T-value	Sig.level	R^2(Adj.)
CONSTANT	-0.818	3.490	-0.234	0.816	0.790
PM2.5-Na	-14.802	9.886	-1.497	0.141	
PM2.5-Mg	206.520	84.644	2.440	0.019	
PM2.5-Al	46.933	35.732	1.314	0.196	
PM2.5-Si	-69.920	22.724	-3.077	0.004	
PM2.5-Ti	242.555	217.914	1.113	0.272	
PM2.5-Fe	30.398	27.435	1.108	0.274	
PM2.5-Zn	16.298	16.031	1.017	0.315	
PM2.5-S	7.631	0.953	8.007	0.000	
PM2.5-Cl	-19.683	6.895	-2.854	0.006	

TABLE 4.3.14. Multiple regression model fitting results for PM2.5-NO_3^- L9 collected at Rubidoux.

Independent Variable	Coefficient	Std. error	T-value	Sig.level	R^2(Adj.)
CONSTANT	2.305	3.556	0.648	0.520	0.666
PM2.5-Na	-7.522	6.765	-1.112	0.272	
PM2.5-Si	-43.350	11.267	-3.847	0.000	
PM2.5-Ca	4.584	3.054	1.501	0.140	
PM2.5-Ti	263.606	224.560	1.174	0.246	
PM2.5-Fe	44.952	27.049	1.662	0.103	
PM2.5-Zn	26.171	14.886	1.758	0.085	
PM2.5-S	5.511	0.946	5.823	0.000	
PM2.5-Cl	-8.503	5.813	-1.463	0.150	

TABLE 4.3.15. Multiple regression model fitting results for PM2.5-$SO_4^=$ collected at Rubidoux.

Independent Variable	Coefficient	Std. error	T-value	Sig.level	R^2(Adj.)
CONSTANT	4.340	0.816	5.317	0.000	0.4248
PM2.5-Mg	-37.795	16.224	-2.330	0.024	
PM2.5-Al	-14.041	9.764	-1.438	0.157	
PM2.5-Si	7.649	6.262	1.221	0.228	
PM2.5-P	169.307	35.566	4.760	0.000	
PM2.5-Ti	116.949	55.210	2.118	0.040	
PM2.5-Fe	-10.871	7.015	-1.550	0.128	
PM2.5-Cl	3.079	1.729	1.780	0.082	

emission sources and the concentrations of the secondary acidic species. There are mixed results for NO_3^- with some positive and some negative values for the crustal elements. It is expected that gaseous HNO_3 will diffuse to the surface of alkaline crustal element particles. Many of the correlation coefficients may be the result of this process. At Burbank, the negative value with Si may indicate the presence of neutral quartz particles while Ti might be aliasing more alkaline surface particles. At Burbank, the sulfate species are positively correlated to Na.

These results indicate that the atmospheric transport of the gaseous precursors and their conversion into particulate phase acidic species tends to decouple them from the variations seen in any primary particles that might have been coemitted with the SO_2 or NO_x. Some of the results for Burbank and Claremont show possible association with the elements that characterize marine aerosols (Na, Mg) and may indicate either marine sulfate as a major part of the sulfate observed at Burbank or they may have a role in the gas-to-particle conversion for these acidic species. However, at Rubidoux, there is an anticorrelation of NO_3^- with Na suggesting that the relationship there may be more related to meteorology than heterogeneous phase chemistry. Although there has been such a role suggested for marine aerosols (Sievering et al., 1991; Luria and Sievering, 1991), the role of marine particles in contributing to the oxidative chemistry of SO_2 and NO_x, is quite uncertain at this time.

4.3.5 Target Transformation Factor Analysis

Target Transformation Factor Analysis (TTFA) is an alternative factor analysis technique that can apportion the aerosol mass to source contributions. The mathematic basis of this approach has been described in detail by Hopke (1989). A target transformation rotation is first applied to the data matrix to obtain a set of basis vectors that each represents a potential source. Source vectors are then rescaled using scaling factors that are determined by multiple regression of total mass against the unscaled factor loading for each sample period. The scaled vectors are comparable to actual source composition vectors. Since only the total particulate masses are available, TTFA modeling was restricted to the study of the particulate chemical species. TTFA is able to: (1) determine the number of independent sources

that contribute to the system, (2) determine the components of the elemental source profiles, and (3) calculate the contribution of each source to each sample. The TTFA has been employed for the PM-2.5 particulate aerosols collected at the three selective sites. The TTFA analyses were performed using the program FANTASIA (Hopke et al., 1983; Hopke and Dharmavaram, 1986). The results are presented in Tables 4.3.16-4.3.27.

A 5-factor model is derived to account for the source apportionment of samples collected at the Burbank site (Table 4.3.16). Although the analysis resolves five "sources," it is quite difficult to associate them with physically real emission sources. The relationships with the elemental concentrations that provide the most direct indications of source type identities are difficult to interpret. For example, in Table 4.3.16, Sources 2, 3, and 4 have reasonably high values for Na; therefore, they may represent marine aerosols. However, Source 3 also includes the crustal elements which might be soil and road dust. In the case of Sources 3 and 4, there are strong associations with L3 and L9 NO_3^- that are difficult to interpret. It appears that the high concentrations of the ionic species dominate the elemental values and do not clearly sort out into patterns that can be associated with real source emissions. Thus, in each case, the results will be discussed in terms of these source categories without the direct association of them with actual physical source types.

Source 1 contributes significant amounts of PM-2.5 NH_4^+ L9, NO_3^- L3, and NO_3^- L9. Source 2 mainly contributes PM-2.5 $SO_4^=$, NH_4^+ L5, and NO_3^- L3. This source also involves marine aerosols. Source 3 involves a large amount of PM-2.5 NO_3^- L3, accompanied by crustal materials and seasalt. Source 4 includes both fine particulate NO_3^- and seasalt. Source 5 mainly accounts for PM-2.5 NH_4^+ L5 and NO_3^- L3, plus a small amount of NO_3^- L9. The contributions of the sources to the individual elements are presented in Table 4.3.17. The mass contributions of each source to each sample are given in Table 4.3.18 and the average contributions for each of the days for which samples are available are given in Table 4.3.19.

A 4-factor model was the best model that could be developed to describe the source contributions for the samples collected at the Claremont site (Table 4.3.20). Source 1 contributes mainly PM-2.5 $SO_4^=$, NH_4^+ L9, and a significant amount of $SO_4^=$ and NO_3^- L3. Source 3 contributes significant amounts of NO_3^- L9 and NH_4^+ L9. The

TABLE 4.3.16. Source profile (μg of components / μg of particle) for PM2.5 aerosols collected at Burbank.

Species	Source 1	Source 2	Source 3	Source 4	Source 5
NH_4^+ L5	0.000	0.272	0.000	0.092	0.425
NH_4^+ L9	0.429	0.013	0.000	0.040	0.014
NO_3^- L3	0.245	0.163	0.802	0.455	0.295
NO_3^- L9	0.234	0.057	0.074	0.372	0.153
$SO_4^=$	0.061	0.463	0.038	0.000	0.045
Ba	0.002	0.000	0.001	0.001	0.001
Ca	0.000	0.001	0.008	0.002	0.012
Fe	0.007	0.001	0.012	0.003	0.018
K	0.008	0.002	0.004	0.003	0.004
Mg	0.003	0.002	0.005	0.002	0.001
Na	0.000	0.023	0.030	0.024	0.000
P	0.001	0.000	0.000	0.000	0.002
Si	0.008	0.000	0.017	0.001	0.019
Ti	0.000	0.000	0.002	0.000	0.001
Zn	0.001	0.003	0.006	0.003	0.009

TABLE 4.3.17. Source apportionment ($\mu g/m^3$) for samples collected at Burbank.

Species	Source 1	Source 2	Source 3	Source 4	Source 5	Avg Pred Contrib	Avg Obs	Avg % Contrib
Error								
NH_4^+ L5	.421E-06	.476E+01	.267E-05	.205E+00	.188E+01	.685E+01	.714E+01	40.3
NH_4^+ L9	.388E+01	.227E+00	.668E-04	.899E-01	.638E-01	.427E+01	.439E+01	7.5
NO_3^- L3	.221E+01	.286E+01	.305E+01	.101E+01	.130E+01	.104E+02	.130E+02	66.5
NO_3^- L9	.212E+01	.998E+00	.281E+00	.827E+00	.675E+00	.490E+01	.502E+01	56.3
$SO_4^=$	.554E+00	.812E+01	.146E+00	.138E-03	.200E+00	.902E+01	.906E+01	2.5
Ba	.137E-01	.970E-08	.359E-02	.248E-02	.306E-02	.228E-01	.158E-01	380.2
Ca	.423E-02	.236E-01	.297E-01	.474E-02	.533E-01	.116E+00	.120E+00	144.1
Fe	.647E-01	.218E-01	.462E-01	.582E-02	.791E-01	.218E+00	.215E+00	21.6
K	.748E-01	.266E-01	.172E-01	.605E-02	.198E-01	.144E+00	.122E+00	42.3
Mg	.266E-01	.287E-01	.190E-01	.532E-02	.346E-02	.831E-01	.706E-01	64.1
Na	.235E-05	.402E+00	.113E+00	.542E-01	.152E-03	.570E+00	.449E+00	122.7
P	.839E-02	.987E-03	.189E-02	.144E-04	.101E-01	.214E-01	.199E-01	66.6
Si	.765E-01	.693E-05	.640E-01	.166E-02	.838E-01	.226E+00	.233E+00	64.6
Ti	.107E-02	.408E-02	.838E-02	.740E-03	.498E-02	.192E-01	.220E-01	381.8
Zn	.607E-02	.507E-01	.238E-01	.733E-02	.384E-01	.126E+00	.124E+00	109.6

AVERAGE ERROR ROWS AND COLS = 104.7%

TABLE 4.3.18. Source contribution for samples collected at Burbank.

Start Time (Julian day)	End Time (Julian day)	Source 1 ($\mu g/m^3$)	Source 2 ($\mu g/m^3$)	Source 3 ($\mu g/m^3$)	Source 4 ($\mu g/m^3$)	Source 5 ($\mu g/m^3$)	Total Mass Predicted	Total Mass Measured
169.000	169.209	0.251	6.326	14.389	5.150	0.000	26.116	23.556
169.208	169.371	0.697	8.428	22.021	1.794	8.179	41.119	43.123
169.375	169.536	1.082	19.567	31.559	0.000	0.000	52.208	49.654
169.542	169.704	0.547	19.868	21.669	0.000	0.000	42.084	36.057
169.708	170.002	0.500	13.467	9.964	4.406	0.000	28.337	28.478
174.000	174.209	1.516	55.398	0.322	0.000	5.269	62.505	43.433
174.208	174.370	1.603	56.389	5.776	2.655	8.090	74.512	75.029
174.375	174.539	1.481	67.039	9.558	0.000	2.221	80.299	86.599
174.542	174.704	1.691	73.916	4.808	0.000	2.436	82.851	82.716
174.708	175.001	1.152	30.464	0.976	9.631	6.402	48.625	46.441
175.000	175.209	1.452	41.038	0.000	24.469	4.629	71.588	63.867
175.208	175.367	1.897	48.856	0.000	25.029	9.823	85.605	79.718
175.375	175.540	1.373	52.397	10.761	0.668	6.778	71.976	84.039
175.542	175.705	1.330	54.632	6.588	0.000	2.224	64.774	60.714
175.708	176.000	0.874	22.654	0.000	15.169	2.122	40.819	42.116
193.000	193.206	0.222	8.396	0.000	2.749	0.640	12.008	16.731
193.208	193.372	0.272	10.465	0.000	10.467	5.904	27.108	31.884
193.375	193.537	0.316	16.944	6.040	0.000	5.025	28.325	31.797
193.542	193.705	0.270	11.909	8.975	0.000	8.814	29.968	28.465
193.708	193.998	0.272	8.831	2.955	3.804	0.000	15.863	13.880
194.000	194.206	0.401	12.940	0.000	5.955	0.593	19.888	19.206
194.208	194.371	0.866	24.124	0.000	11.990	5.718	42.698	39.714
194.375	194.539	0.973	40.840	4.378	0.000	6.177	52.368	55.952
194.542	194.704	0.726	29.537	5.723	0.000	5.904	41.890	36.546
194.708	194.999	0.584	16.658	0.000	5.030	2.586	24.858	27.449
195.000	195.207	1.031	31.338	0.000	7.822	3.536	43.727	40.655
195.208	195.371	1.086	31.196	0.000	11.565	7.055	50.903	52.281
195.375	195.538	1.301	49.175	1.037	0.000	7.942	59.455	65.155
195.542	195.705	0.803	28.321	10.649	0.000	9.825	49.598	48.037
195.708	195.996	1.122	31.647	0.000	14.972	3.711	51.452	49.649
238.000	238.207	0.826	19.905	0.000	11.576	0.000	32.307	32.478
238.208	238.372	0.626	19.232	7.944	2.241	4.509	34.552	49.614
238.375	238.534	0.870	19.582	9.206	13.321	4.985	47.964	52.027
238.542	238.705	0.500	16.333	13.880	0.000	1.287	32.000	33.671
238.708	239.000	0.656	18.037	1.326	2.427	3.424	25.869	28.986
239.000	239.206	0.588	17.323	0.000	5.484	5.788	29.182	30.954
239.208	239.374	0.888	17.408	0.533	10.993	8.120	37.944	49.809
239.375	239.552	0.789	22.191	14.063	3.352	8.399	48.794	58.907
239.542	239.705	0.929	30.374	14.060	0.000	5.112	50.475	47.575
239.708	239.998	0.827	16.833	0.000	13.378	0.000	31.038	34.437
240.000	240.207	1.082	18.349	0.000	17.137	0.000	36.568	39.508
240.208	240.372	1.671	30.060	0.000	24.341	5.441	61.513	58.785
240.375	240.538	0.689	53.323	8.814	9.290	7.767	79.883	82.571
240.542	240.706	0.928	66.472	2.941	0.000	0.000	70.341	69.514
240.708	241.000	0.781	36.660	0.000	8.104	2.556	48.100	48.477
244.000	244.211	1.042	0.790	3.790	0.000	11.007	16.629	20.992
244.208	244.371	0.262	0.000	13.362	0.000	20.590	34.214	30.935
244.375	244.539	0.322	2.989	14.986	0.000	19.092	37.388	26.915
244.542	244.705	0.366	6.765	12.785	0.000	6.452	26.368	26.631
244.708	244.997	0.336	10.535	8.739	0.000	4.986	24.595	24.306
245.000	245.205	0.494	14.406	2.090	4.743	5.321	27.053	27.804
245.208	245.372	0.514	13.937	7.235	6.662	8.514	36.862	37.631
245.375	245.538	0.674	25.488	15.185	0.000	6.818	48.165	49.713
245.542	245.705	0.733	27.909	12.382	0.000	3.501	44.525	37.213
245.708	245.997	0.888	26.894	0.965	4.013	0.899	33.658	35.133
Avg mass	($\mu g/m^3$)	0.836	26.446	6.226	5.462	5.021	43.991	44.319

TABLE 4.3.19. Daily average source contribution for samples collected at Burbank.

Sampling Period (Julian day)	Source 1 ($\mu g/m^3$)	Source 2 ($\mu g/m^3$)	Source 3 ($\mu g/m^3$)	Source 4 ($\mu g/m^3$)	Source 5 ($\mu g/m^3$)	Total Mass Predicted	Total Mass Measured
169	0.615	13.531	19.920	2.270	1.636	37.973	36.174
174	1.489	56.641	4.288	2.457	4.884	69.759	66.844
175	1.385	43.915	3.470	13.067	5.115	66.953	66.091
193	0.270	11.309	3.594	3.404	4.077	22.654	24.551
194	0.710	24.820	2.020	4.595	4.196	36.340	35.773
195	1.069	34.335	2.337	6.872	6.414	51.027	51.155
238	0.695	18.618	6.471	5.913	2.841	34.538	39.355
239	0.804	20.826	5.732	6.641	5.484	39.487	44.336
240	1.030	40.973	2.351	11.774	3.153	59.281	59.771
244	0.465	4.216	10.732	0.000	12.426	27.839	25.956
245	0.661	21.727	7.571	3.083	5.011	38.053	37.499
Avg mass ($\mu g/m^3$)	0.836	26.446	6.226	5.462	5.021	43.991	44.319

TABLE 4.3.20. Source profile (µg of components / µg of particulate samples) for PM2.5 aerosols collected at Claremont.

Species	Source 1	Source 2	Source 3	Source 4
NH_4^+ L5	0.000	0.439	0.087	0.111
NH_4^+ L9	0.201	0.059	0.190	0.065
NO_3^- L3	0.104	0.172	0.000	0.596
NO_3^- L9	0.000	0.000	0.522	0.000
$SO_4^=$	0.576	0.200	0.131	0.180
Al	0.004	0.010	0.005	0.005
Ba	0.002	0.001	0.000	0.000
Ca	0.008	0.010	0.011	0.001
Cu	0.019	0.010	0.003	0.010
Fe	0.009	0.019	0.009	0.006
K	0.007	0.008	0.005	0.002
Mg	0.003	0.004	0.003	0.002
Na	0.033	0.013	0.011	0.009
P	0.002	0.002	0.000	0.001
Si	0.011	0.025	0.012	0.012
Ti	0.002	0.002	0.001	0.000
Zn	0.019	0.026	0.010	0.000

TABLE 4.3.21. Source apportionment ($\mu g/m^3$)for samples collected at Claremont.

Species	Source 1	Source 2	Source 3	Source 4	Avg Pred Contrib	Avg Obs Contrib	Avg % Error
NH_4^+ L5	.341E-04	.307E+01	.835E+00	.195E+01	.585E+01	.686E+01	653.9
NH_4^+ L9	.351E+00	.415E+00	.183E+01	.115E+01	.374E+01	.382E+01	97.3
NO_3^- L3	.181E+00	.120E+01	.597E-06	.105E+02	.119E+02	.120E+02	24.5
NO_3^- L9	.542E-03	.129E-02	.502E+01	.173E-03	.502E+01	.499E+01	82.0
$SO_4^=$	.101E+01	.140E+01	.127E+01	.316E+01	.682E+01	.697E+01	14.3
Al	.694E-02	.724E-01	.493E-01	.884E-01	.217E+00	.214E+00	108.3
Ba	.320E-02	.777E-02	.662E-05	.413E-02	.151E-01	.144E-01	159.4
Ca	.146E-01	.695E-01	.106E+00	.211E-01	.211E+00	.207E+00	55.7
Cu	.326E-01	.705E-01	.329E-01	.173E+00	.309E+00	.277E+00	4171.0
Fe	.148E-01	.136E+00	.840E-01	.108E+00	.342E+00	.339E+00	26.7
K	.125E-01	.531E-01	.527E-01	.410E-01	.159E+00	.150E+00	29.6
Mg	.602E-02	.272E-01	.313E-01	.333E-01	.979E-01	.899E-01	54.3
Na	.577E-01	.892E-01	.103E+00	.155E+00	.405E+00	.342E+00	403.0
P	.279E-02	.112E-01	.177E-02	.109E-01	.267E-01	.257E-01	32.7
Si	.198E-01	.172E+00	.114E+00	.203E+00	.510E+00	.500E+00	33.4
Ti	.304E-02	.111E-01	.728E-02	.707E-02	.285E-01	.279E-01	254.1
Zn	.331E-01	.181E+00	.969E-01	.675E-03	.311E+00	.315E+00	103.6

AVERAGE ERROR ROWS AND COLS = 370.8%

TABLE 4.3.22. Source contribution for samples collected at Claremont.

Start Time (Julian Day)	End Time (Julian Day)	Source 1 ($\mu g/m^3$)	Source 2 ($\mu g/m^3$)	Source 3 ($\mu g/m^3$)	Source 4 ($\mu g/m^3$)	Total Mass Predicted	Total Mass Measured
169.000	169.213	4.702	2.581	5.789	5.836	18.908	33.787
169.208	169.382	0.000	8.003	6.964	20.825	35.792	41.217
169.375	169.525	2.016	2.979	2.989	20.161	28.146	33.853
169.542	169.701	8.747	0.046	3.497	13.266	25.556	28.965
169.708	169.999	5.873	2.655	4.282	8.834	21.643	27.011
174.000	174.208	6.863	0.000	11.704	21.157	39.724	40.217
174.208	174.374	0.000	0.000	18.332	28.550	46.882	54.728
174.375	174.535	23.830	1.080	8.121	33.175	66.206	74.881
174.542	174.701	39.233	1.139	3.875	25.861	70.107	81.381
174.708	174.997	13.213	0.000	9.826	18.530	41.569	38.789
175.000	175.202	6.055	0.000	15.213	22.303	43.571	49.077
175.208	175.374	0.000	4.704	28.943	51.736	85.383	79.866
175.375	175.534	6.151	0.000	13.885	45.609	65.645	75.176
175.542	175.702	10.901	3.224	2.557	20.036	36.718	48.699
175.708	175.996	13.048	0.000	6.577	15.694	35.319	35.373
193.000	193.209	1.833	4.166	1.562	0.151	7.712	12.160
193.208	193.372	0.000	13.317	12.176	26.224	51.717	38.166
193.375	193.535	0.000	13.201	0.000	3.798	16.999	29.053
193.542	193.701	9.461	5.033	0.869	10.351	25.714	37.890
193.708	193.997	1.959	2.395	1.464	4.818	10.636	14.330
194.000	194.200	0.000	6.322	3.522	2.428	12.272	13.366
194.208	194.372	0.000	7.397	8.354	17.639	33.389	27.766
194.375	194.535	4.852	10.051	0.135	19.165	34.203	38.296
194.542	194.701	34.248	5.164	0.000	13.179	52.591	58.680
194.708	194.993	11.534	6.738	3.949	8.513	30.734	28.704
195.000	195.202	0.000	6.898	16.690	16.268	39.856	37.580
195.208	195.369	15.447	4.441	13.961	14.229	48.078	49.861
195.375	195.535	21.096	0.000	7.036	17.724	45.856	42.472
195.542	195.701	19.422	2.488	5.753	21.074	48.737	46.469
195.708	195.996	4.650	1.523	3.977	13.353	23.503	31.432
238.000	238.210	5.950	0.647	8.531	11.610	26.737	35.507
238.208	238.373	0.000	18.029	19.827	62.837	100.693	64.599
238.375	238.537	0.000	15.410	11.867	46.991	74.268	58.585
238.542	238.701	0.000	4.346	4.974	23.437	32.757	55.394
238.708	238.996	10.967	3.759	2.007	7.017	23.750	31.706
239.000	239.202	4.813	3.391	7.006	8.954	24.164	30.979
239.208	239.370	0.000	9.169	12.177	29.396	50.742	49.077
239.375	239.535	0.000	5.642	4.644	32.632	42.918	50.573
239.542	239.701	30.130	1.436	1.043	24.062	56.671	69.317
239.708	239.992	15.462	0.000	7.023	16.080	38.565	39.136
240.000	240.201	6.536	0.000	14.713	22.728	43.977	56.196
240.208	240.370	0.000	1.147	24.845	29.546	55.538	73.238
240.375	240.535	20.666	0.000	21.173	48.404	90.243	77.661
240.542	240.701	63.393	0.000	3.114	26.285	92.792	75.568
240.708	240.996	42.433	0.000	9.962	22.384	74.779	56.324
244.000	244.202	0.502	2.330	0.651	0.949	4.431	12.407
244.208	244.371	0.000	10.133	0.073	0.000	10.206	23.248
244.375	244.538	0.000	13.915	0.000	9.951	23.866	25.051
244.542	244.705	2.412	7.209	0.785	2.548	12.955	29.655
244.708	244.995	7.654	1.305	1.136	5.835	15.930	25.340
245.000	245.214	5.066	1.283	4.191	6.532	17.073	27.211
245.208	245.360	1.645	5.856	5.742	14.189	27.432	45.278
245.375	245.551	0.000	0.629	2.455	28.313	31.397	45.814
245.542	245.697	15.907	1.598	0.803	8.890	27.198	29.013
245.708	245.993	8.132	0.000	4.362	8.108	20.602	20.465
Avg Mass	($\mu g/m^3$)	9.215	4.050	7.184	18.876	39.324	42.847

TABLE 4.3.23. Daily average source contribution for samples collected at Claremont.

Sampling Period (Julian Day)	Source 1 ($\mu g/m^3$)	Source 2 ($\mu g/m^3$)	Source 3 ($\mu g/m^3$)	Source 4 ($\mu g/m^3$)	Total Mass Predicted	Total Mass Measured
169	4.268	3.253	4.704	13.784	26.009	32.967
174	16.628	0.444	10.371	25.455	52.897	57.999
175	7.231	1.586	13.435	31.076	53.327	57.638
193	2.650	7.622	3.214	9.068	22.555	26.320
194	10.127	7.134	3.192	12.185	32.638	33.362
195	12.123	3.070	9.484	16.530	41.206	41.563
238	3.383	8.438	9.441	30.378	51.641	49.158
239	10.081	3.927	6.379	22.225	42.612	47.816
240	26.606	0.229	14.761	29.869	71.466	67.797
244	2.114	6.978	0.529	3.857	13.477	23.140
245	6.150	1.873	3.511	13.207	24.740	33.556
Avg Mass ($\mu g/m^3$)	9.215	4.050	7.184	18.876	39.324	42.847

TABLE 4.3.24. Source profile (µg of components / µg of particulate samples) for PM2.5 aerosols collected at Rubidoux.

Species	Source 1	Source 2	Source 3
NH_4^+ L5	0.520	0.000	0.457
NH_4^+ L9	0.035	0.158	0.055
NO_3^- L3	0.000	0.352	0.297
NO_3^- L9	0.099	0.372	0.123
$SO_4^=$	0.138	0.089	0.056
Al	0.031	0.000	0.001
Ca	0.060	0.005	0.000
Cl	0.001	0.007	0.000
Fe	0.031	0.004	0.002
K	0.011	0.002	0.002
Mg	0.005	0.001	0.001
Na	0.002	0.006	0.003
P	0.001	0.000	0.000
Si	0.063	0.002	0.002
Ti	0.002	0.000	0.000
Zn	0.001	0.001	0.001

TABLE 4.3.25. Source apportionment ($\mu g/m^3$) for samples collected at Rubidoux.

Species	Source 1	Avg Pred Source 2	Avg Obs Source 3	Avg % Contrib	Contrib	Error
NH_4^+ L5	.456E+01	.201E-02	.266E+02	.312E+02	.322E+02	21.1
NH_4^+ L9	.309E+00	.508E+01	.320E+01	.859E+01	.872E+01	12.2
NO_3^- L3	.434E-03	.113E+02	.173E+02	.286E+02	.273E+02	53.3
NO_3^- L9	.868E+00	.119E+02	.718E+01	.200E+02	.214E+02	25.0
$SO_4^=$	.121E+01	.286E+01	.328E+01	.734E+01	.709E+01	25.2
Al	.269E+00	.519E-03	.474E-01	.317E+00	.333E+00	455.6
Ca	.524E+00	.152E+00	.499E-03	.676E+00	.721E+00	261.1
Cl	.528E-02	.216E+00	.205E-01	.242E+00	.200E+00	5635.9
Fe	.270E+00	.119E+00	.124E+00	.513E+00	.504E+00	428.7
K	.985E-01	.722E-01	.981E-01	.269E+00	.244E+00	910.7
Mg	.491E-01	.439E-01	.385E-01	.132E+00	.117E+00	323.9
Na	.187E-01	.211E+00	.166E+00	.396E+00	.279E+00	313.1
P	.937E-02	.128E-01	.192E-01	.413E-01	.364E-01	135.5
Si	.551E+00	.670E-01	.142E+00	.760E+00	.771E+00	16.6
Ti	.177E-01	.107E-01	.142E-01	.425E-01	.408E-01	67.5
Zn	.988E-02	.381E-01	.616E-01	.110E+00	.936E-01	282.3

AVERAGE ERROR ROWS AND COLS = 560.5%

TABLE 4.3.26. Source contribution for samples collected at Rubidoux.

Start Time (Julian Day)	End Time (Julian Day)	Source 1 ($\mu g/m^3$)	Source 2 ($\mu g/m^3$)	Source 3 ($\mu g/m^3$)	Total Mass Predicted	Total Mass Measured
169.000	169.202	5.872	22.034	0.000	27.906	27.743
169.208	169.383	0.000	41.668	9.777	51.445	66.556
169.375	169.528	4.333	39.093	7.613	51.038	58.011
169.542	169.703	8.260	40.465	0.149	48.874	34.957
169.708	170.003	4.594	24.704	2.382	31.679	32.048
174.000	174.215	0.944	50.531	14.946	66.421	65.582
174.208	174.357	19.811	72.910	5.991	98.712	94.193
174.375	174.535	4.009	94.112	37.030	135.151	136.303
174.542	174.703	5.927	25.365	31.818	63.110	67.056
174.708	175.004	0.000	46.171	15.753	61.924	65.242
175.000	175.200	4.553	53.045	15.535	73.133	71.222
175.208	175.369	11.124	76.340	12.982	100.446	66.556
175.375	175.539	5.219	68.135	41.898	115.252	127.898
175.542	175.705	7.083	8.889	17.042	33.014	45.213
175.708	176.003	3.213	9.642	31.972	44.827	47.217
193.000	193.208	3.433	14.414	27.413	45.260	48.186
193.208	193.367	16.583	28.117	6.557	51.257	61.897
193.375	193.537	5.042	12.393	34.962	52.397	55.700
193.542	193.707	4.648	9.587	33.272	47.507	57.114
193.708	194.006	4.263	9.608	14.318	28.188	29.056
194.000	194.201	2.374	0.000	36.276	38.650	29.634
194.208	194.367	7.180	14.867	15.542	37.589	39.700
194.375	194.540	4.571	37.140	31.656	73.367	75.711
194.542	194.702	4.145	29.909	31.162	65.216	69.276
194.708	195.006	1.312	12.253	36.292	49.857	49.871
195.000	195.202	0.000	32.940	26.875	59.815	55.705
195.208	195.368	4.293	50.257	36.598	91.148	83.767
195.375	195.539	1.128	41.264	59.143	101.535	98.049
195.542	195.705	1.619	15.589	48.385	65.593	67.841
195.708	196.007	0.000	2.347	34.752	37.099	39.700
238.000	238.209	3.718	45.715	16.401	65.834	67.755
238.208	238.365	22.949	59.438	16.089	98.476	102.227
238.375	238.536	14.431	65.167	27.435	107.033	111.533
238.542	238.703	12.353	26.887	24.860	64.100	79.016
238.708	239.009	6.439	10.400	39.517	56.356	56.757
239.000	239.201	9.948	26.343	37.441	73.732	74.991
239.208	239.365	44.974	55.969	2.985	103.928	103.180
239.375	239.537	19.391	16.137	93.717	129.245	119.962
239.542	239.704	10.619	18.232	63.214	92.065	99.159
239.708	240.008	2.353	42.974	39.647	84.974	86.734
240.000	240.199	0.247	44.477	52.526	97.250	94.793
240.208	240.363	8.523	61.884	47.867	118.274	112.922
240.375	240.540	0.606	36.867	10.173	47.646	128.575
240.542	240.706	6.424	7.114	39.365	52.904	54.693
240.708	241.004	2.946	16.055	45.137	64.138	61.368
244.000	244.213	0.000	40.939	5.922	46.861	66.556
244.208	244.350	48.706	5.402	0.000	54.108	45.817
244.375	244.537	14.193	0.709	0.000	14.902	11.627
244.542	244.706	12.035	0.000	0.000	12.035	11.230
244.708	245.008	19.822	24.507	28.278	72.607	76.871
245.000	245.198	10.354	8.503	16.471	35.328	36.165
245.208	245.368	33.677	21.033	6.045	60.755	67.590
245.375	245.539	17.512	11.048	22.626	51.186	53.359
245.542	245.706	14.478	3.975	18.181	36.634	40.970
245.708	246.005	5.088	0.000	26.096	31.184	29.726
Avg Mass ($\mu g/m^3$)		8.860	29.701	25.420	63.981	66.556

TABLE 4.3.27. Daily average source contribution for samples collected at Rubidoux.

Sampling Period (Julian Day)	Source 1 ($\mu g/m^3$)	Source 2 ($\mu g/m^3$)	Source 3 ($\mu g/m^3$)	Total Mass Predicted	Total Mass Measured
169	4.612	33.593	3.984	42.188	43.863
174	6.138	57.818	21.108	85.064	85.675
175	6.238	43.210	23.886	73.334	71.621
193	6.794	14.824	23.304	44.922	50.391
194	3.916	18.834	30.186	52.936	52.838
195	1.408	28.479	41.151	71.038	69.012
238	11.978	41.521	24.860	78.360	83.458
239	17.457	31.931	47.401	96.789	96.805
240	3.749	33.279	39.014	76.042	90.470
244	18.951	14.311	6.840	40.103	42.420
245	16.222	8.912	17.884	43.017	45.562
Avg Mass ($\mu g/m^3$)	8.860	29.701	25.420	63.981	66.556

last source (4) contributes mainly NO_3^- L3. Sources 2, 3, and 4 do not include significant amounts of marine aerosols. Tables 4.3.21, 4.3.22, and 4.3.23 provide the contributions to the individual elements, to each sample in the data set, and to the average mass concentration for each day, respectively.

Only a 3-factor model could be obtained to account for the source apportionment of samples collected at Rubidoux (Table 4.3.24). The first source involves large amounts of NH_4^+ L5 and $SO_4^=$. The second source contributes significant amounts of NH_4^+ L5, NO_3^- L3 and NO_3^- L9. All three sources contribute insignificant amounts of marine aerosols. Tables 4.3.25, 4.3.26, and 4.3.27 provide the contributions to the individual elements, to each sample in the data set, and to the average mass concentration for each day, respectively.

4.3.6 Potential Source Contribution Function Analysis

4.3.6.1 Introduction

To address the role of meteorology and source-receptor relationships, calculated back trajectories have been combined with the data for the 16 IC analyzed chemical species using potential source contribution function analysis (Ashbaugh et al., 1985; Malm et al., 1986; Zeng and Hopke, 1989). The Potential Source Contribution Function (PSCF) is the probability that an air mass with specified pollutant concentrations arrive at a receptor site after having passed through a specific geographical area. Air parcel backward trajectories ending at each of the three receptor sites were calculated by AeroVironment Inc., using a model developed at the California Institute of Technology (Russell et al., 1983). The model uses a terrain-following path at 100 meters above ground. The trajectories were computed for each hour for a 24-hour period. There are 24 one-hour trajectories for each of the 17 intensive study days. Each 4-, 5-, or 7-hour sample thus has 96-, 120-, or 168-segment endpoints, respectively, associated with it. The possible source region is subdivided into an i by j grid array. Let N represent the total number of trajectory segment endpoints during the study period. If n_{ij} endpoints fall into the ij-th cell, the probability of this event, A_{ij}, is given by

$$P[A_{ij}] = \frac{n}{N} ij$$

In the same ij-th cell, if there are m_{ij} endpoints that correspond to the trajectories that arrived at a receptor site with pollutant concentrations higher (or lower) than some prespecified value, then the probability of this event, B_{ij}, is

$$P[B_{ij}] = \frac{m_{ij}}{N}$$

The potential source contribution function (PSCF) is then defined as a conditional probability:

$$PSCF = \frac{P[B_{ij}]}{P[A_{ij}]} = \frac{m_{ij}}{n_{ij}}$$

Grid cells containing pollutant sources should have high conditional probabilities. Therefore, the conditional probability function, PSCF, that was calculated based on the substantial number of total endpoints during the study period, will identify those source areas that have a potential to contribute to the high concentrations of contaminants observed at the receptor site.

Since the coordinates of trajectories' data are in the UTM system, the coordinates were converted into degrees of latitude and longitude. The calculated PSCF results and trajectories were then projected onto Lambert conic projection maps. The PSCF analyses for the 16 IC analyzed chemical species collected at the Burbank, Claremont, and Rubidoux sites, plus one computed species, nonmarine $SO_4^=$, are described later. All 51 PSCF maps (17 for each of the three sites) have been prepared and will be individually discussed. In addition, it is helpful to examine the actual trajectory paths. Thus, the 17 surface wind trajectory plots (one for each day on which samples were obtained) were produced for the three sites. These plots were for June 19, 24, 25; July 13, 14, 15; August 27, 28, 29; September 2, 3; November 11, 12, 13; and December 3, 10, and 11, 1987. These trajectory plots are shown in Appendix B. In order to compare the areas identified in this analysis to known emission sources, Figures 4.3.1 and 4.3.2 show the 1982 gridded emission inventories for NO_X and SO_X, respectively. Figure 4.3.3 shows the locations of the major electric generating stations in the SoCAB region. Table 4.3.28 provides estimates for the 1974 NH_3 emissions from various source types in the basin (Russell et al., 1983).

FIGURE 4.3.1. Gridded emission inventory values for NO_x taken from SCAQMD (1984).

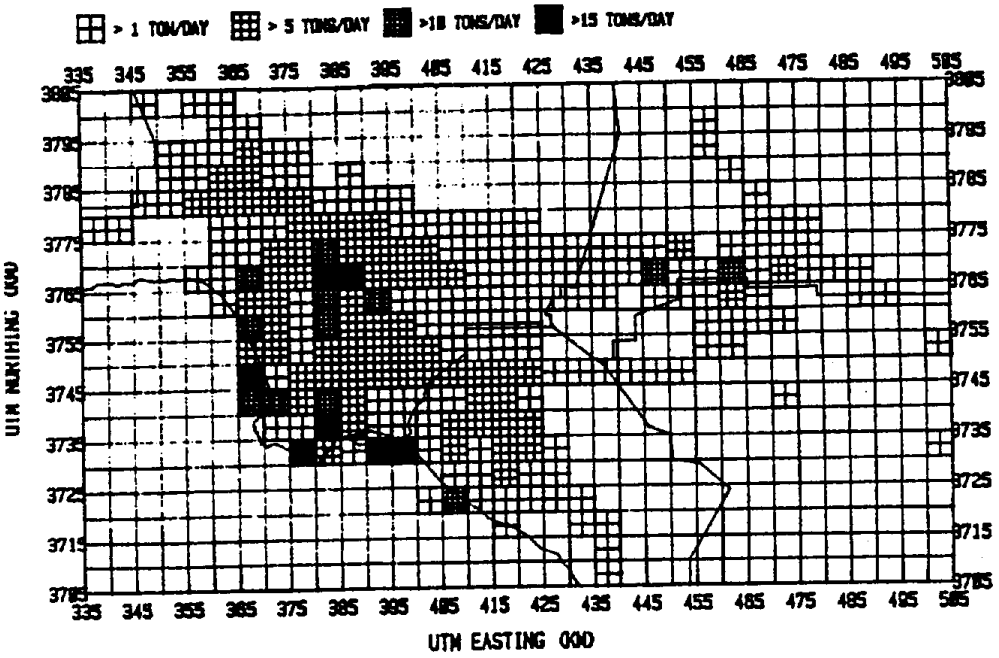

FIGURE 4.3.2. Gridded emission inventory values for SO_x taken from SCAQMD (198

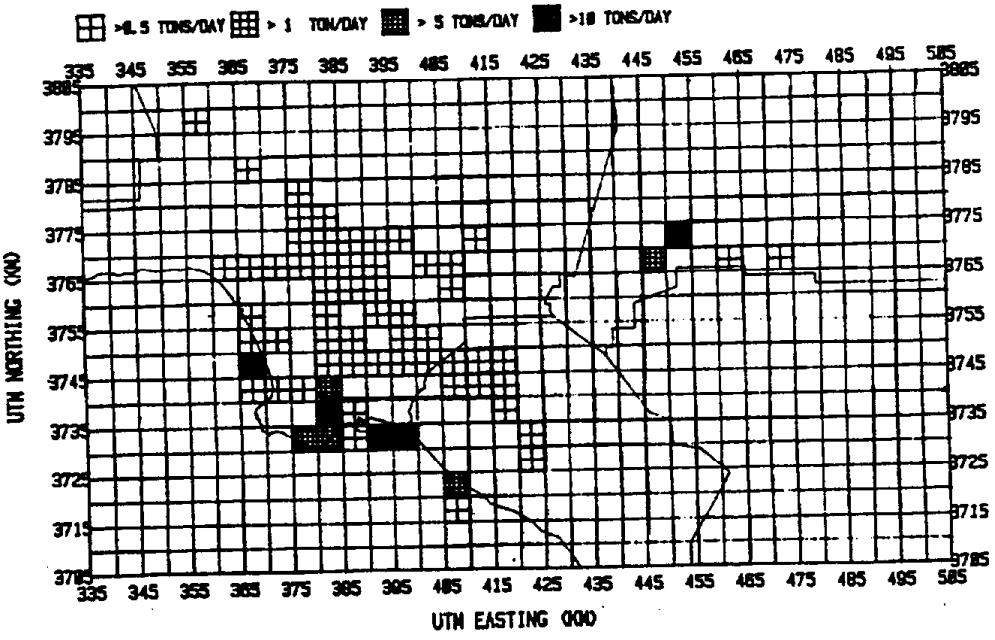

FIGURE 4.3.3. Map showing the locations of the electricity generating stations in and around the South Coast Air Basin (SCAQMD, 1984).

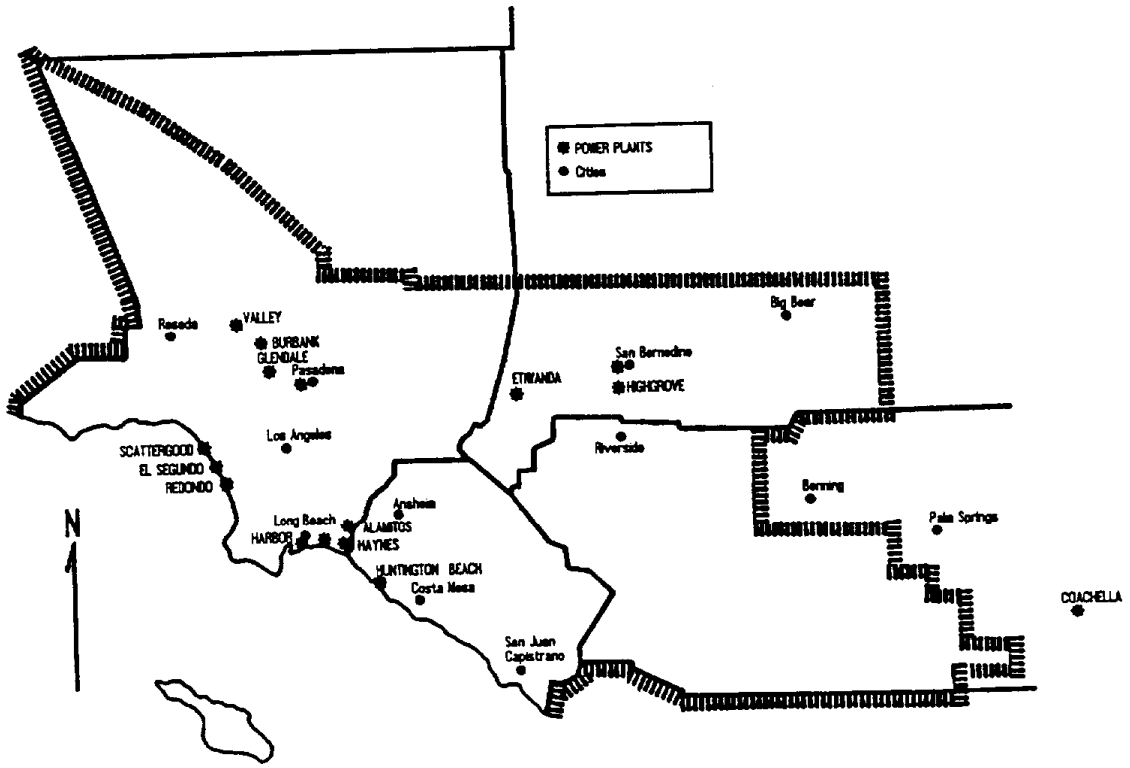

TABLE 4.3.28. Summary of ammonia emissions by source category in the South Coast Air Basin - 1974.

Source Category	Total Emissions (kg/day)
Stationary Fuel Combustion	
Electric Utility	2590.
Refinery Fuel Burning	679.
Industrial Fuel Burning	928.
Residential Commercial Fuel Burning	429.
Sub Totals	4626. (3.09%)
Mobile Source Fuel Combustion	
Automotive	4138.
Civilian Aircraft	152.
Shipping	120.
Railroad-Diesel Oil	90.
Military	120.
Off Highway Vehicles	120.
Sub Totals	4742. (3.17%)
Industrial Point Sources	3070. (1.38%)
Soil Surface	23790. (15.9%)
Fertilizer	13060. (8.72%)
Livestock	80210. (53.6%)
Domestic	21226. (14.2%)
TOTAL	149725. (100.0%)

Source: Russell *et al.*, 1983

4.3.6.2 PSCF Results

Maps were produced to identify the potential source regions of various acidic species by using the IC species data from samples collected at the three sites during SCAQS and the backward trajectories computed for each site. The PSCF values were computed using a 5 km by 5 km grid size comparable to the grid size used in the trajectory calculations. The 75th percentile values were chosen as the criterion for the variables examined in the PSCF analyses.

Because of the high criterion value and the large number of trajectory endpoints associated with each sample, the statistical precision of the PSCF values for most of the grid cells is quite high. Only in the eastern section of the area are the number of endpoints and thus, the statistical precision, relatively low. So, the resulting high potential cells should reflect the likely emission areas for the species measured at each site.

Burbank

For Burbank, most of the potential source area grid cells for Cl (Figures 4.3.4 and 4.3.5) were located in the Pacific Ocean. The locations of the potential source areas in the ocean are extremely similar for both Cl in the two size ranges. Some differences exist in the land source areas for the two Cl size fractions. Source areas were identified to the west of Burbank for Cl PM-2.5 but these areas did not contribute to Cl PM-10. The specific source of fine particle Cl in this area is unknown. However, high concentrations of Cl are commonly associated with refuse incinerators (Greenberg et al., 1978a and 1978b).

Most of the high potential source areas (PSCF > = 0.8) for Na PM-10 (Figure 4.3.6) are found in the ocean with only a few cells on land (four of them close to the Burbank site and one on the coast close to Hawthorne). The nature of the land sources for Na PM-10 are unknown. These high potential regions are discussed below in detail.

Most of the potential source areas for $SO_4^=$ (Figures 4.3.7 and 4.3.8) were located in the Pacific Ocean. There is only one inland high potential source area (PSCF > = 0.8) east of Burbank, identical to that of Na PM-10. This region contributed

FIGURE 4.3.4. Cl PM10 at Burbank.

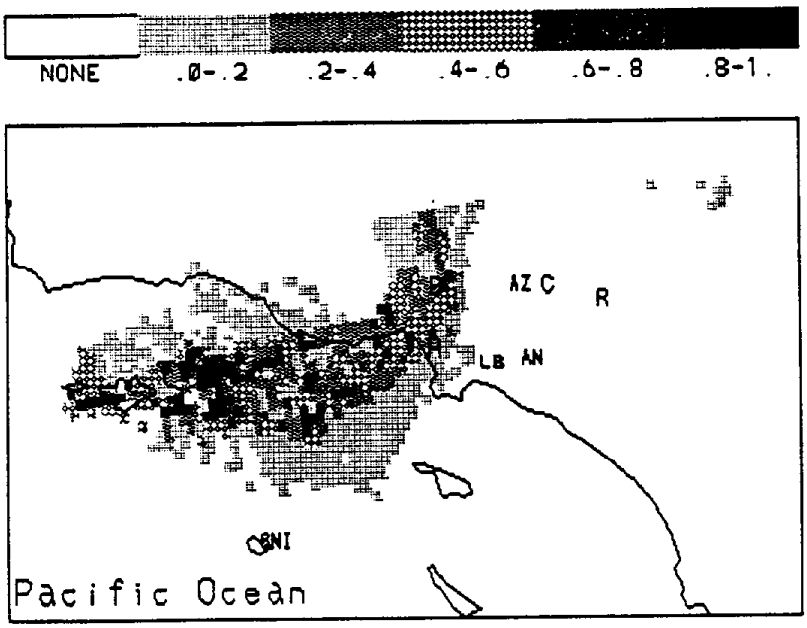

FIGURE 4.3.5. Cl PM2.5 at Burbank.

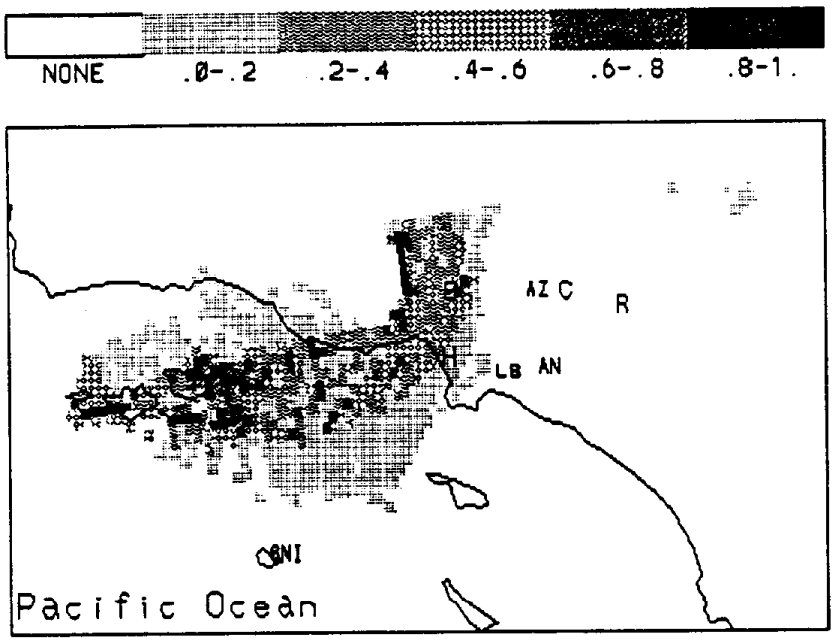

FIGURE 4.3.6. Na PM10 at Burbank

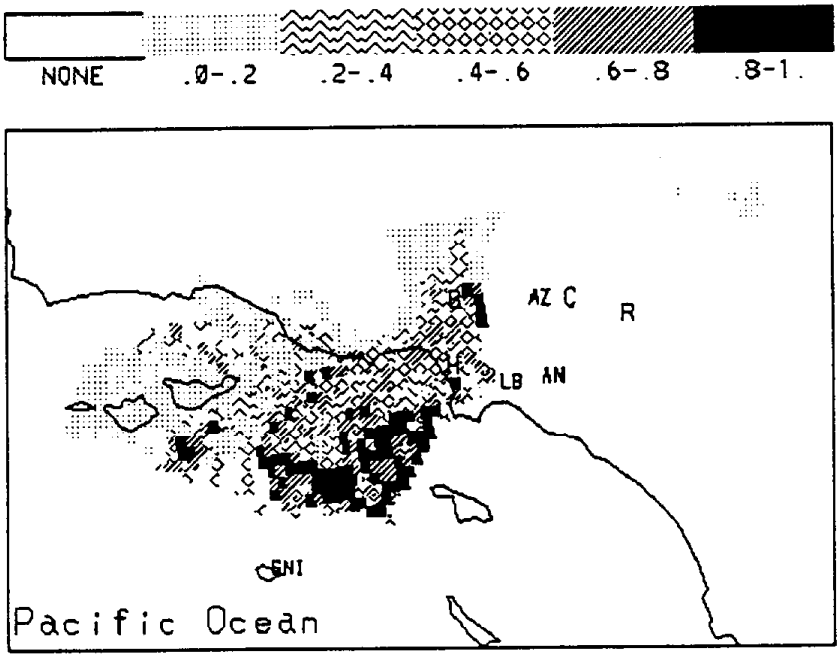

FIGURE 4.3.7. $SO_4^=$ PM10 at Burbank

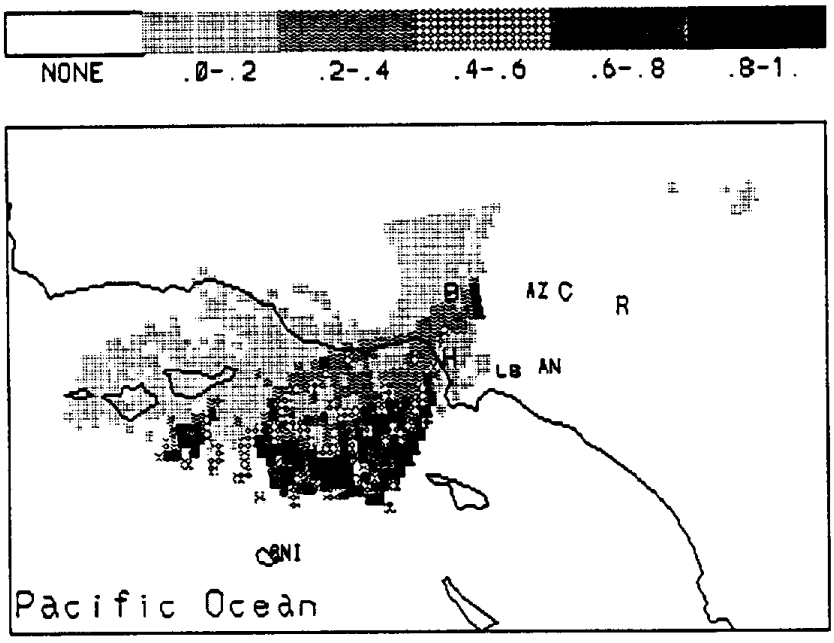

FIGURE 4.3.8. $SO_4^=$ PM2.5 at Burbank.

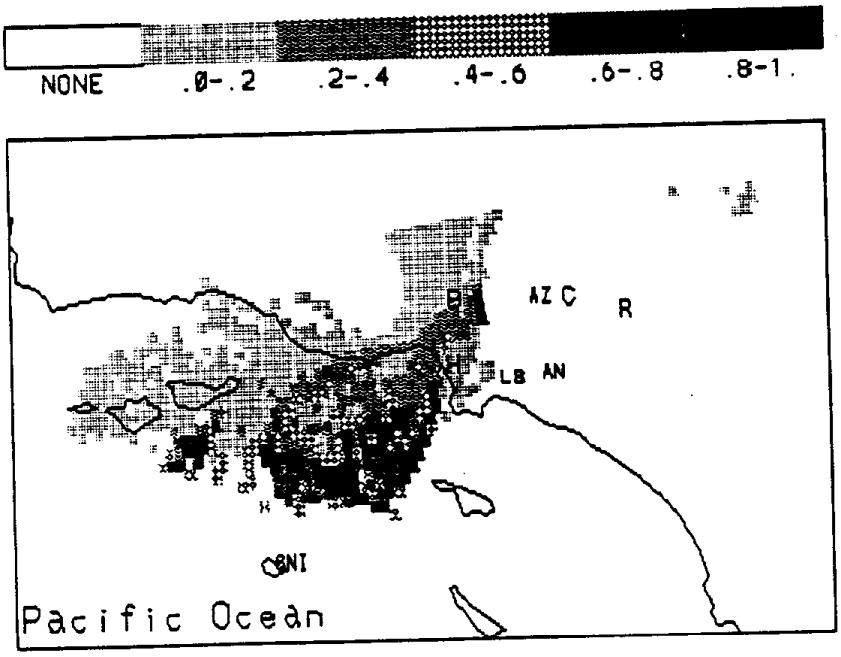

FIGURE 4.3.9. Non-marine $SO_4^=$ at Burbank.

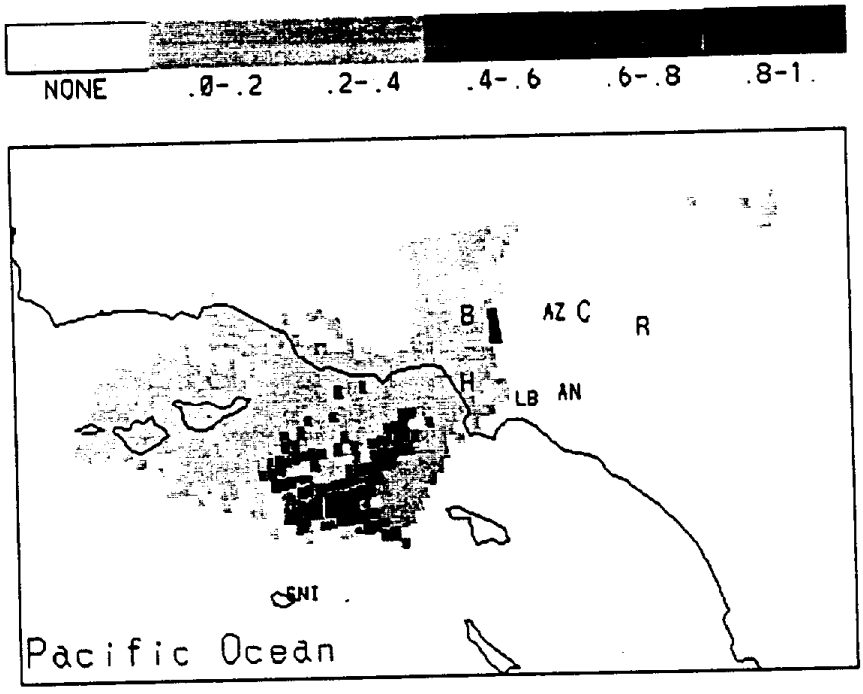

$SO_4^=$ similar to the contributions for Na PM-10. This result suggests that the $SO_4^=$ is mostly marine sulfate. The source to the east of Burbank is not readily identified.

Nonmarine sulfate ($NMSO_4$) in the PM-10 size range (Figure 4.3.9) was calculated by subtracting 0.25 times the PM-10 Na value from the $SO_4^=$ value for each sample. The $NMSO_4$ represents the anthropogenic part of the total airborne $SO_4^=$ concentration. It appears from the PSCF analysis that there is very little anthropogenic contribution to the $SO_4^=$ in the particles sampled at Burbank.

By comparing the PSCF results for Na, Cl, $SO_4^=$, and nonmarine sulfate, it appears that most of the Na and Cl in particles collected at Burbank are from marine salts. The sources of sulfate are basically sea salt sulfate and sulfate from oxidation of gaseous precursors, possibly from ships burning high sulfur oil since $SO_4^=$ appears to be spatially well correlated with Na. However, such a correlation did not appear in the principal component analysis.

The potential sources of gaseous SO_2 (Figure 4.3.10) are mostly land sources that are partitioned into three areas: one ranging to the west and northwest, another to the east side, very close to Burbank, and the third along the coast in the vicinity of the three coastal power plants. The west-side source area has also been identified in the Cl PM-2.5, NH_4^+L5, NH_3, NO_3^- L3, NO_3^- L9, NO_3^- PM-10 maps. The east-side area was identified in the HNO_3, NH_4^+L5, NH_4^+L9, NH_4^+PM-10, NO_3^- Gas, NO_3^- L3, NO_3^- L9, NO_3^- PM-10, NO_3^- TOT, $SO_4^=$ PM-10, $SO_4^=$ PM-2.5, and Na PM-10 maps. If the trajectories for this site are examined (see Appendix B), it appears that during the winter sampling campaign, the winds were primarily from the north. Because of the range of mountains around the valley, the trajectories appear to cluster toward the sides of the sampling site. Thus, these grid cells of high potential for a number of species may be an artifact of the local terrain and meteorology and really represent particles transported into the basin by the northerly winds. The third SO_2 area is west of Los Angeles, stretching along the coast. The SO_x emission source map (SCAQMD, 1984) shows several heavy SO_x emission sources (> 5 tons/day); one of them falls into the possible source region for Burbank, with identical location and one of the high potential source areas identified by the PSCF maps for SO_2. By comparing the PSCF maps and the emission source maps, it can be concluded that the emission source around UTM 3747 km N and 367 km E (>5 tons/day), identified as the coastal high potential area on PSCF map

FIGURE 4.3.10. Gaseous SO_2 at Burbank.

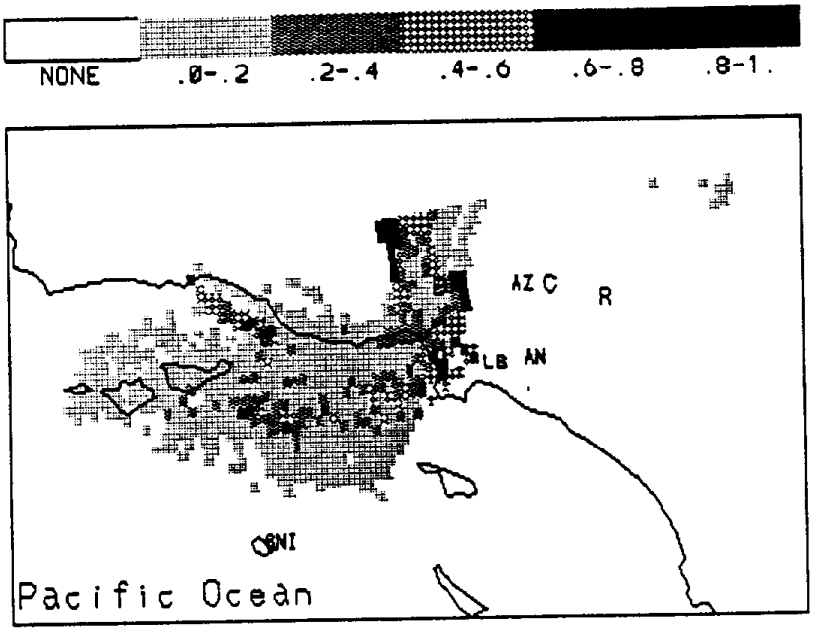

FIGURE 4.3.11. Gaseous HNO_3 at Burbank.

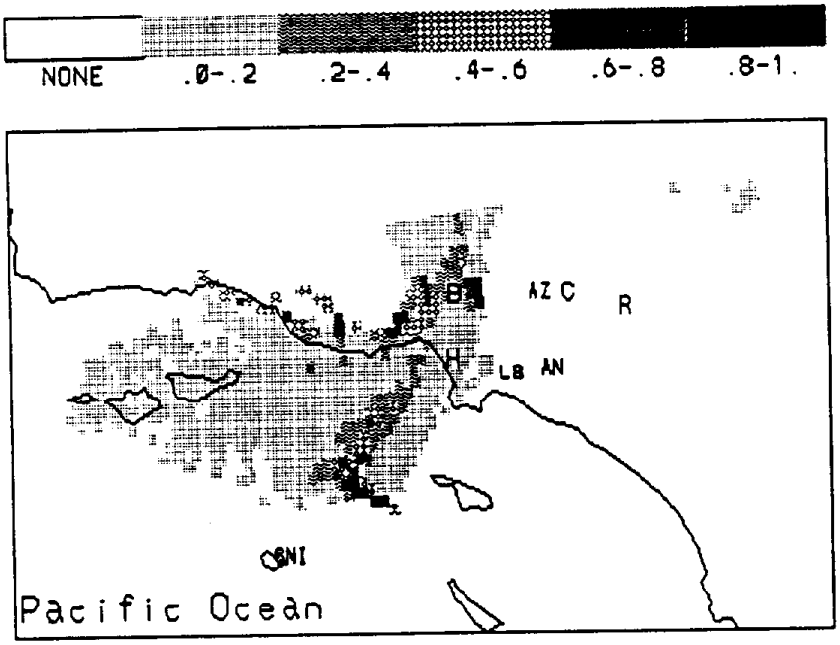

for SO_2, contains the three electric power plants (Scattergood, El Segundo, and Redondo) along the coast west of Los Angeles (Figure 4.3.3). The large area of low emission strength around downtown Los Angeles (>0.5 ton/day) is identified as an area of moderate potential (0.4<PSCF<0.6) by the PSCF maps of SO_2 and $SO_4^=$. The Valley electric power plant (>0.5 ton/day) at UTM 3787 km N and 367 km E may give rise to the identified high potential area west of Burbank in the SO_2 PSCF map. The Burbank electric power plant is east of the sampling site and may correspond to the identified high potential source east of Burbank. However, with the identification of these local areas for a number of species, it seems unlikely that these power plants are the source of the variety of identified species. The remainder of the known high emission sources make no contribution to the SO_2 concentrations at Burbank since they are not located along the paths of the air parcel trajectories leading to the Burbank site.

There are two types of major NO_x emission sources in the SoCAB, automobile traffic and electric generation sources (SCAQMD, 1984). The pattern of high potential areas in the PSCF maps of gaseous and particulate NO_3^- varies significantly from the location of major emission source areas as given by the 1982 emission map (Figure 4.3.1). The PSCF maps show basically the same pattern of a few grid cells of high potential for gaseous HNO_3 (Figure 4.3.11) and gaseous NO_3^- (Figure 4.3.12) to the east and west sides of the Burbank site. For the three particulate NO_3^- species (NO_3^- PM-2.5 L3, L9, and PM-10, Figures 4.3.13, 4.3.14, and 4.3.15) the source areas of high potential are west and east of Burbank and are quite similar and pronounced. The major potential source areas for particulate NO_3^- are close to Burbank. These results provide an indication of possible rapid gas-to-particle conversion of NO_x emitted from vehicles and electric power plants and relatively limited transport of these species to this site from more distant areas. The area east of Burbank is the major source area found for total NO_3^- (Figure 4.3.16). This result indicates that most of the particulate NO_3^- collected at Burbank may be from the Burbank power plant.

The traffic is much heavier in downtown Los Angeles than around Burbank. However, high potential grid cells are not found around Los Angeles. Thus, the emissions from the electric power plants at Valley, Burbank, and Glendale appear to provide major contributions to the NO_y collected at Burbank. The widely distributed,

FIGURE 4.3.12. Gaseous NO_3^- at Burbank.

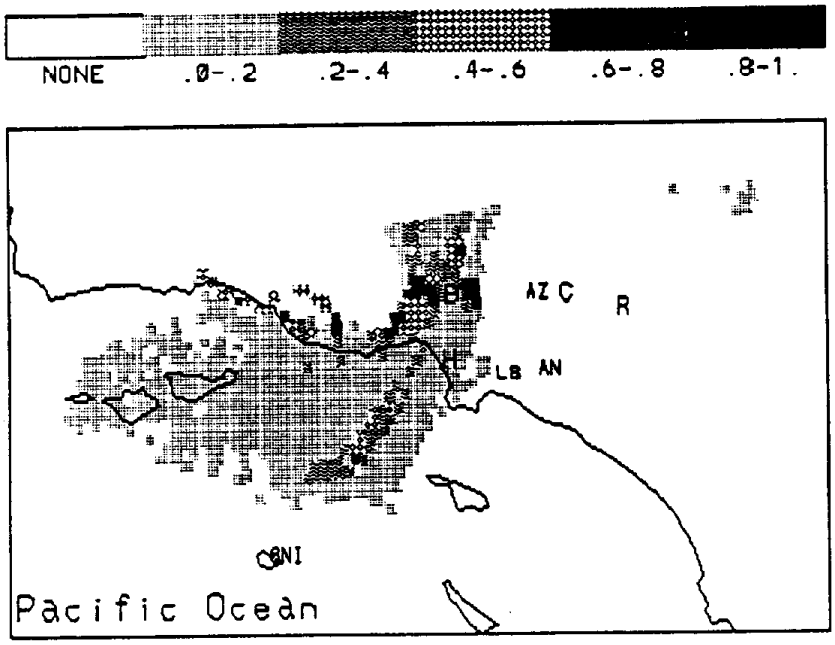

FIGURE 4.3.13. NO_3^- PM2.5 L3 at Burbank.

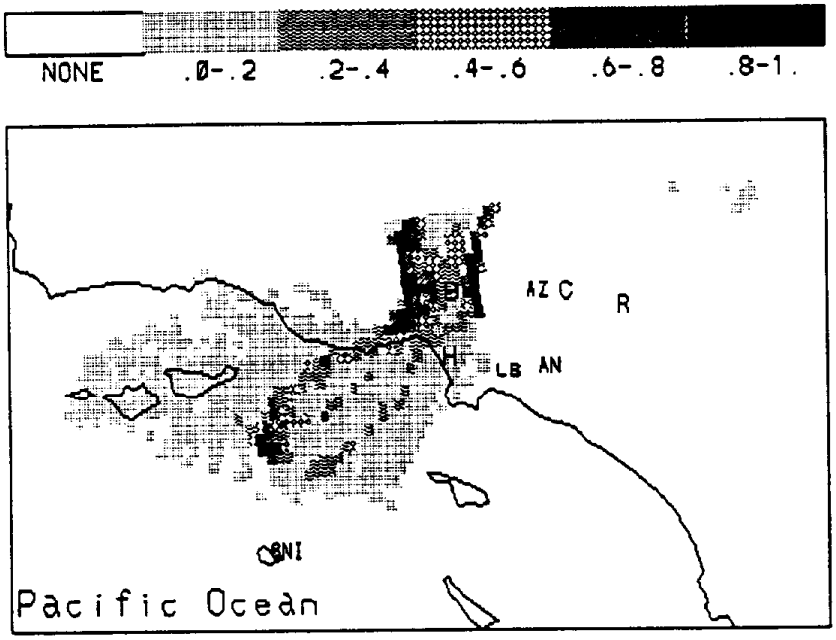

FIGURE 4.3.14. NO_3 PM2.5 L9 at Burbank.

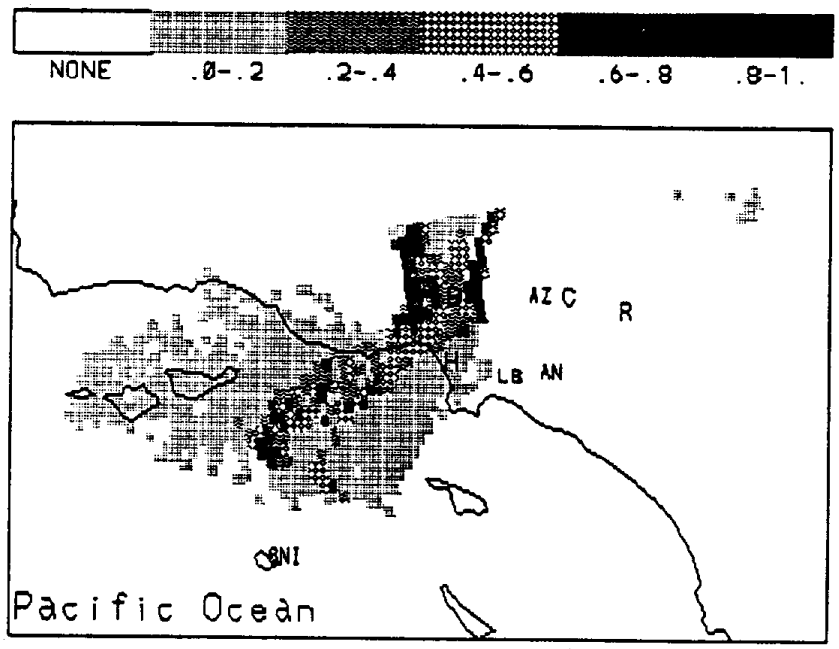

FIGURE 4.3.15. NO_3 PM10 at Burbank.

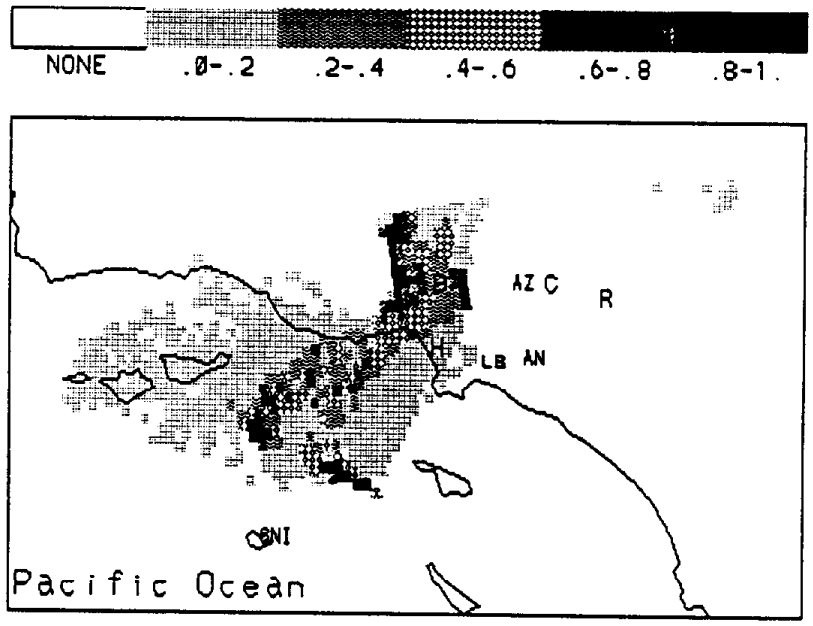

FIGURE 4.3.16. Total NO_3^- at Burbank.

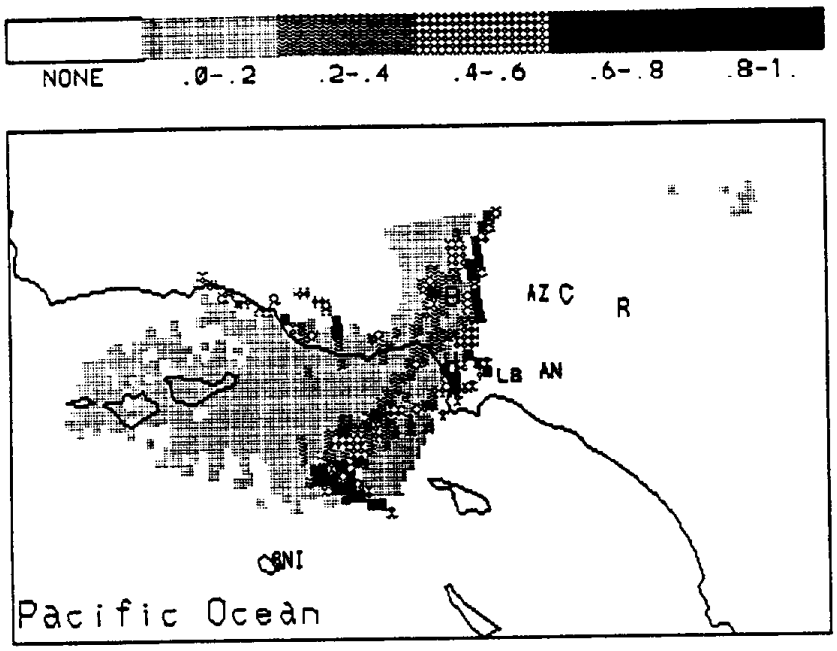

FIGURE 4.3.17. Gaseous NH_3 at Burbank.

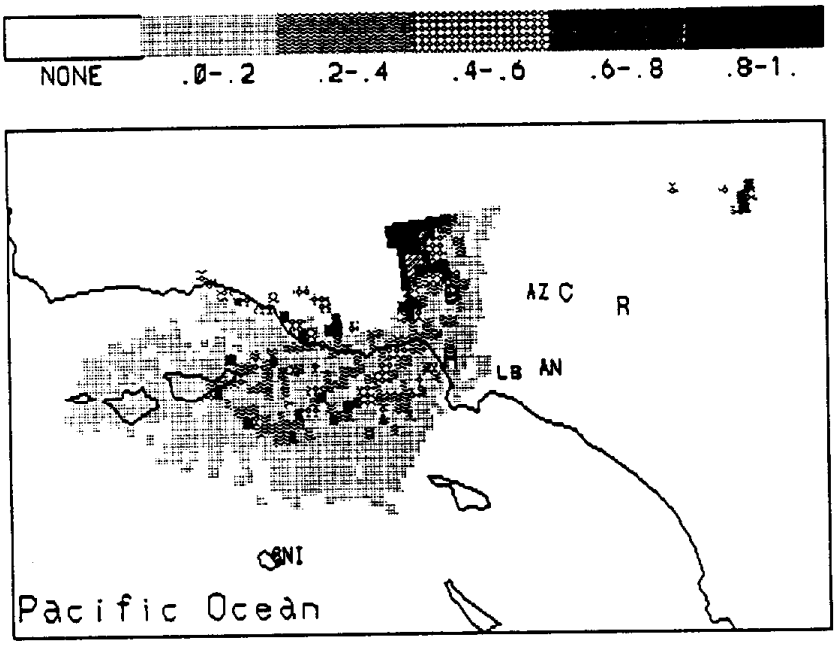

moderate potential areas around Los Angeles and Burbank identified in the PSCF maps (0.2 < PSCF < 0.6) are well correlated with the 1982 emission map (>5 ton/day). This appears to be NO_y resulting from NO_x released from motor vehicles. Two of the major emission sources indicated on the 1982 emission map--one corresponding to the electric power plants on the west coast and the other corresponding to the downtown Los Angeles area--are not identified in the PSCF maps based on the 1987 data. This result could mean that the amounts of NO_x emissions from these two sources have been greatly reduced since 1982, or that the amounts of NO_x emissions from these two sources have been greatly reduced since 1982, or that the material is lost in transit. Since the coastal power plants were identified as sulfur sources (SO_2), it appears that loss in transit is the primary reason for not observing these areas as high potential source regions for the NO_y species observed at Burbank.

Gaseous NH_3 and particulate NH_4^+ collected in the L5, L9, or PM-10 sampling trains were distributed over land and water areas. For NH_3 (Figure 4.3.17), a particularly strong source cluster is found to be at the northwest side of the Burbank sampling site. This may be a real emission source or could again be a result of the local terrain/meteorology artifact discussed earlier. Since an emissions map for NH_3 was not available, we could not look for the correspondence of this area with physical sources such as an anaerobic sewage treatment plant or a high population density area. The large high potential source area for the fine fraction NH_4^+ L5 (Figure 4.3.18) and NH_4^+ L9 (Figure 4.3.19) and the smaller NH_4^+ PM- 10 (Figure 4.3.20) area west of Burbank are portions of the high potential area of NH_3, so it is possible that they are emitted by the same source and then combine with the particulate acidic species. There is a high potential area east of Burbank that contributed to all three particulate NH_4^+ species collected at Burbank. This source area may also be an artifact region as previously discussed or may represent a real source. NH_4^+ L9 appears to originate from sources located somewhat geographically different from NH_3 or NH_4^+ L5 because the high area of NH_3 to the west of Burbank was not identified as having high potential for NH_4^+ L9.

FIGURE 4.3.18. NH_4^+ PM2.5 L5 at Burbank.

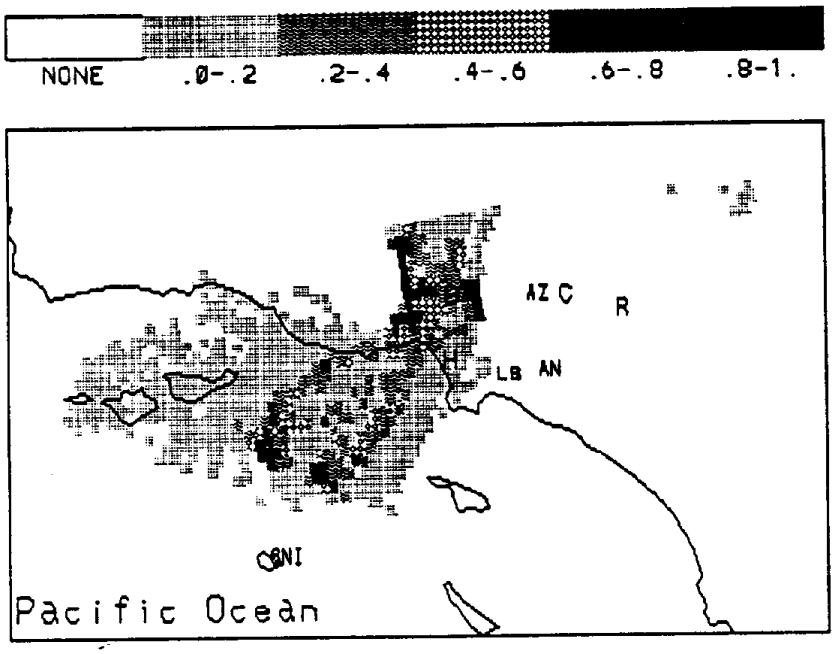

FIGURE 4.3.19. NH_4^+ PM2.5 L9 at Burbank.

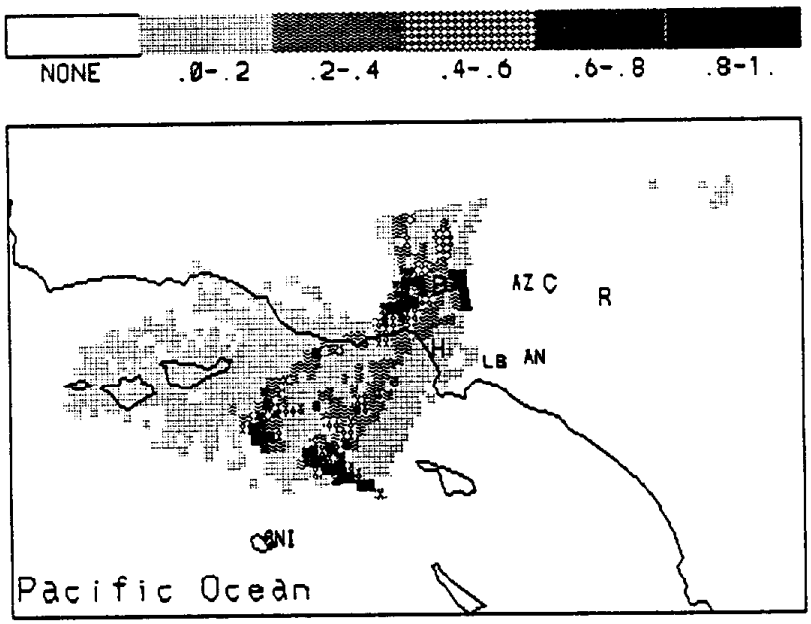

FIGURE 4.3.20. NH_4^+ PM10 at Burbank

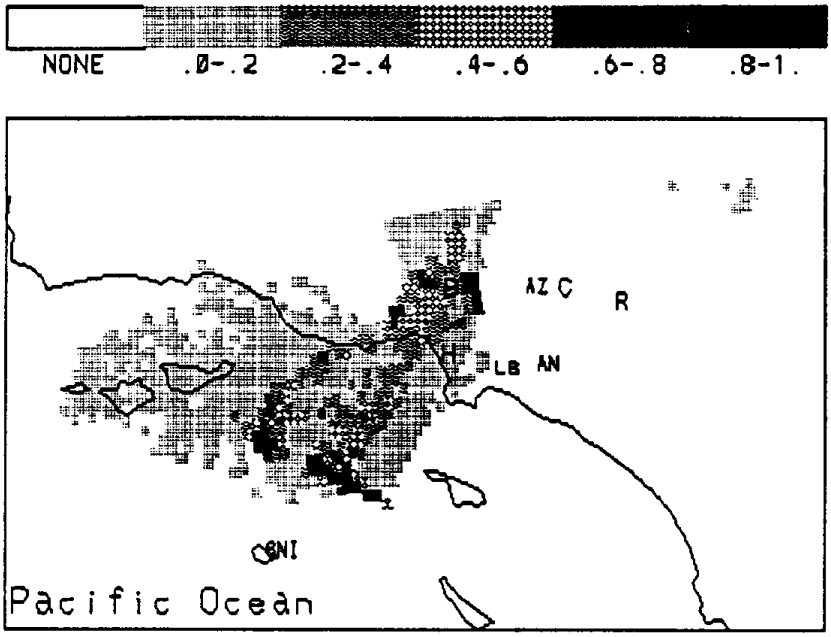

FIGURE 4.3.21. Cl PM10 at Claremont.

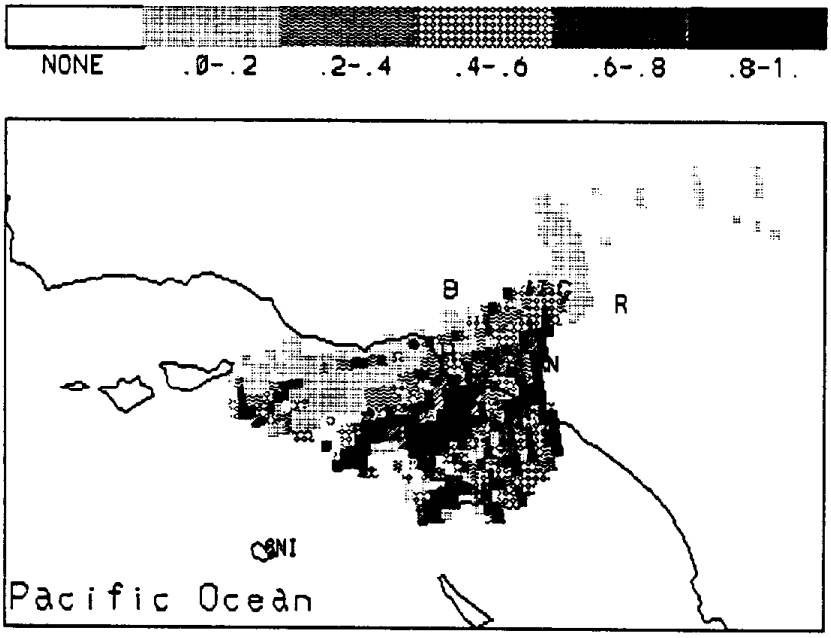

Areas in the ocean appear in both the particulate NH_4^+ and the particulate NO_3^- maps. The areas identified are in the area where off-shore ocean dumping of organic nitrogen-rich municipal sewage sludge from the metropolitan Los Angeles area has occurred (Jackson, 1982). Thus, anaerobic processes in the surficial sediments could lead to the release of NH_3 that then might have reacted with acidic particles to contribute particulate NH_4^+ and NO_3^- transported to Burbank. Because of the large number of trajectory endpoints that fall into the near shore region, it appears unlikely that this source area is an artifact.

The PSCF results for the Burbank site show that particulate NO_3^- and NH_4^+ apparently come from similar areas. However, it is unlikely to have sources of both oxidized and reduced nitrogen. Thus, what is likely to be occurring is the reaction of NH_3 with acidic NO_y so that these species strongly co-vary as shown in the PCA results. Their covariance also causes the PSCF analysis to identify regions that emit one or the other species to appear to emit both since both species increase and decrease together. In the case of the marine areas of high potential for both particulate NH_4^+ and NO_3^-, it may also be that the acidic material is transported from the land areas of the basin by off-shore winds. The acidic material then reacts with the emitted NH_3 to form particulate material that is subsequently transported back to the sampling sites by subsequent on-shore winds. Such transport has been previously reported by Russell and Cass (1984).

Claremont

High potential source areas for Cl in either the PM-10 or the PM-2.5 size range are found to spread over the ocean and along the trajectory paths on land toward the Claremont site (Figures 4.3.21 and 4.3.22). The high potential oceanic sources obviously contribute marine Cl to Claremont. Since all of the eastward trajectories to Claremont are from the ocean, all of the inland grid cells along the trajectory paths are also associated with the high marine Cl concentration and thus become potential sources for Cl collected at Claremont. Unless there is an opportunity for trajectories that do not carry marine aerosol to pass over these inland sites, they must have the same potential as the actual source area. Most of the Na source areas also lie in the ocean (Figure 4.3.23). The other single cells are all at the edges of the area covered by the trajectories and may be anomalies.

FIGURE 4.3.22. Cl PM2.5 at Claremont.

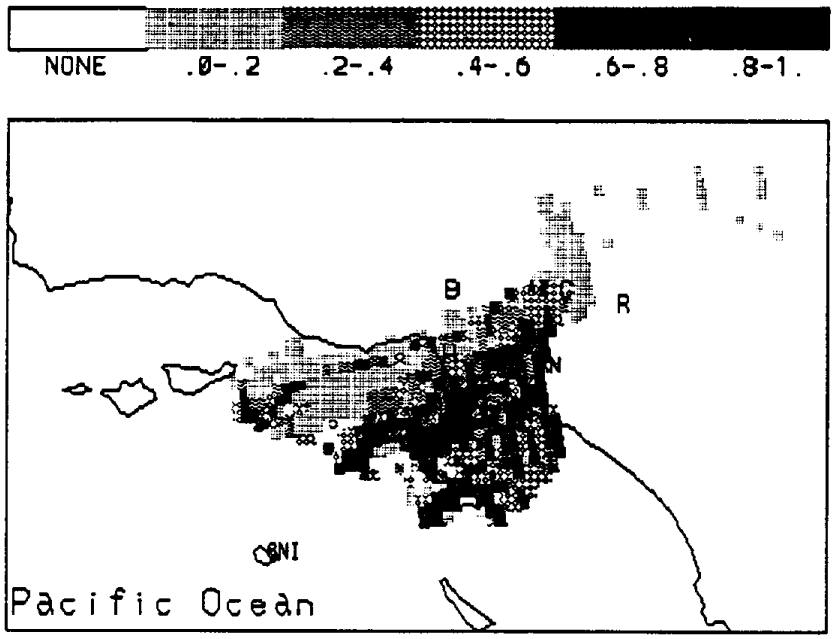

FIGURE 4.3.23. Na PM10 at Claremont.

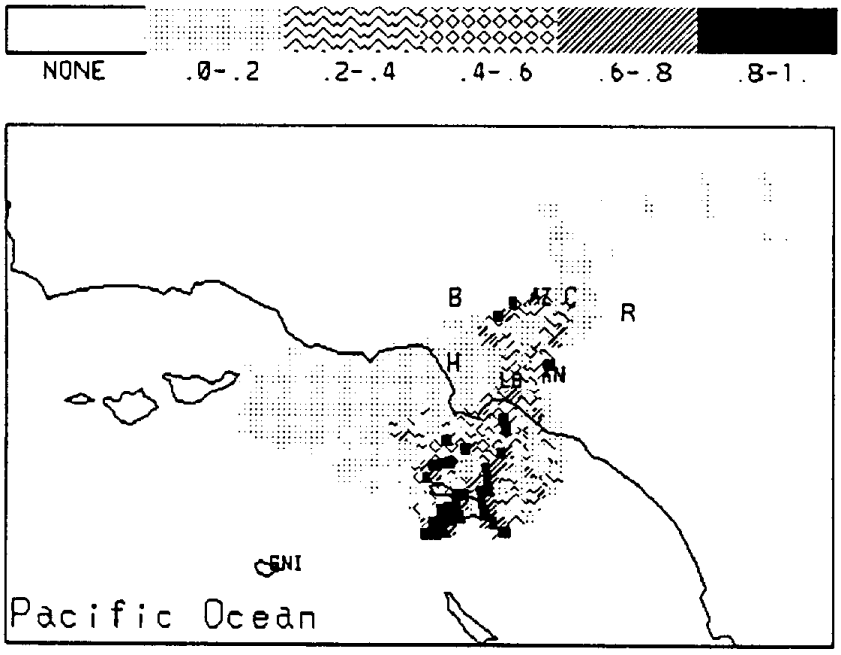

The potential source areas for PM-10 $SO_4^=$ include both ocean and land area (Figure 4.3.24). A band of high grid cells stretches from the ocean through Anaheim toward the sampling location. Another potential source area is located near the coast west of Long Beach. There appears to be no high potential areas of PM-2.5 $SO_4^=$ observed at Claremont (Figure 4.3.25) although there are somewhat enhanced values in the area of Huntington Beach and south of Long Beach along the coast where there are known SO_2 sources. The differences in PSCF patterns between PM-10 and PM-2.5 $SO_4^=$ indicate that coarse mode $SO_4^=$ potential areas are more clearly observed at Claremont than fine mode fraction sulfate. The coarse mode fraction $SO_4^=$ is likely from marine sources and the fine mode fraction sulfate comes from coastal emission sources.

A potential source area in the nonmarine $SO_4^=$ PSCF map (Figure 4.3.26) stretches from Huntington Beach on the coast to Anaheim. Based on the 1982 emission source map in Figure 4.3.3 (SCAQMD, 1984), this source could be the Huntington Beach Power Plant (>5 tons/day). The sources west and south of Long Beach are identified in the emission source map (5 tons/day - 10 tons/day and up) but are not seen in the nonmarine $SO_4^=$ PSCF map. The PM-10, PM-2.5, and nonmarine $SO_4^=$ maps suggest that sea salt in the coarse mode is a major source of the $SO_4^=$ collected at Claremont. However, the pattern of high potential grid cells on the PM-10 $SO_4^=$ PSCF map does not correlate with that of the PM-10 Na. This result suggests that the ocean is a source of some of the $SO_4^=$ that is not primary sea salt sulfate. This sulfate may be from the oxidation of dimethyl sulfide (DMS) emitted by the anaerobic digestion of waste sludge in the surficial sediments. In support of this hypothesis, there is a distinct source area for SO_2 (Figure 4.3.27) in the ocean about 50 miles offshore. Biogenic DMS could be oxidized into SO_2 in transit from the ocean to Claremont. Another source area is observed near Claremont, which may be due to the Etiwanda Electric Power Plant.

All of the PSCF values for HNO_3 were low over the entire region covered by the calculated trajectories with the exception of a single grid cell in the ocean (Figure 4.3.28). No substantial source areas were found for NO_3^- gas as well (Figure 4.3.29). For particulate NO_3^- species, there also seems to be no significant

FIGURE 4.3.24. $SO_4^=$ PM10 at Claremont.

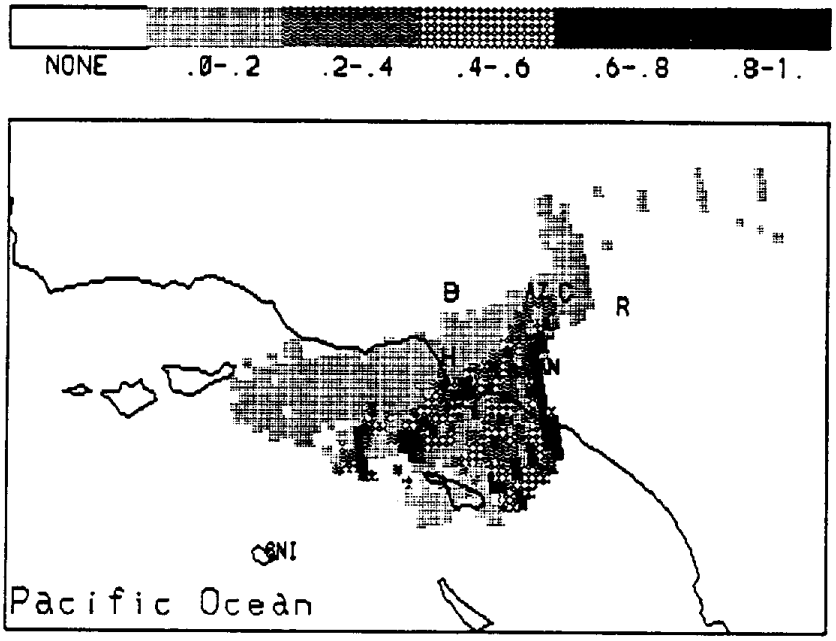

FIGURE 4.3.25. $SO_4^=$ PM2.5 at Claremont.

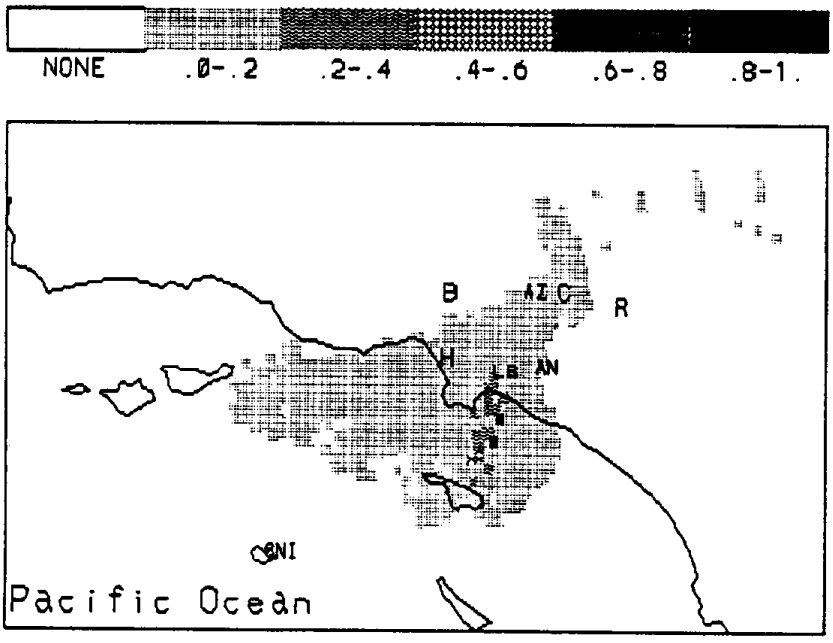

FIGURE 4.3.26. Non-marine $SO_4^=$ at Claremont.

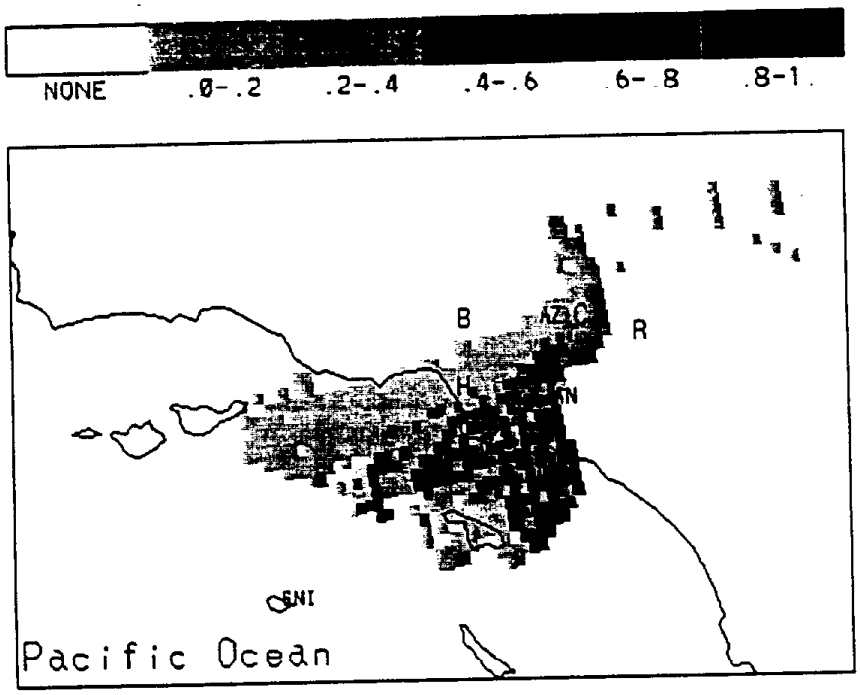

FIGURE 4.3.27. Gaseous SO_2 at Claremont.

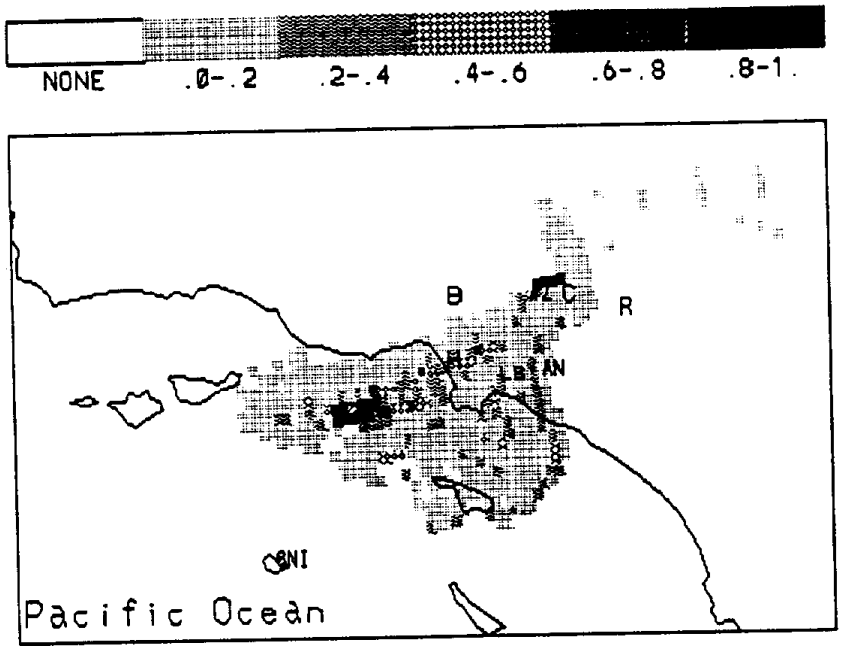

FIGURE 4.3.28. Gaseous HNO_3 at Claremont.

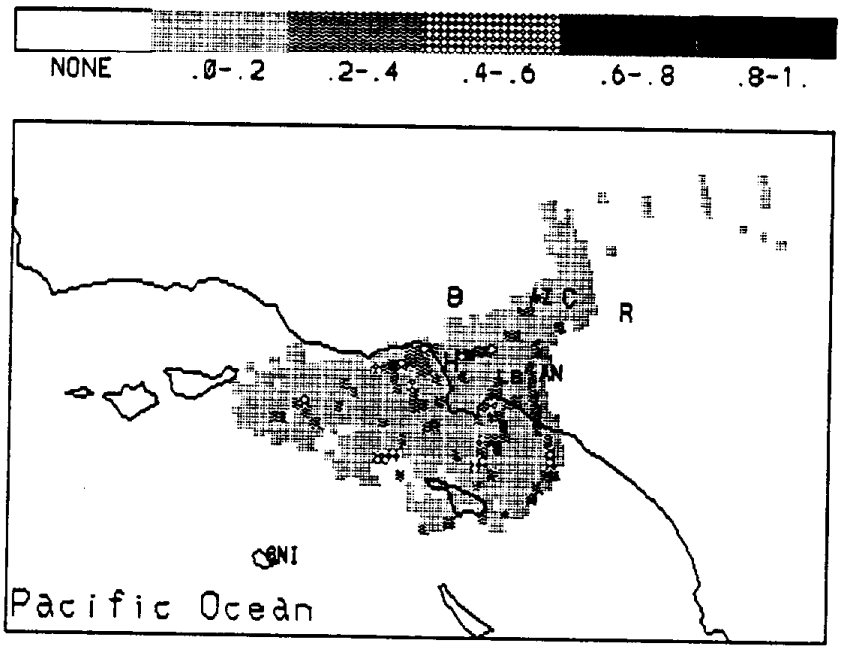

FIGURE 4.3.29. Gaseous NO_3^- at Claremont.

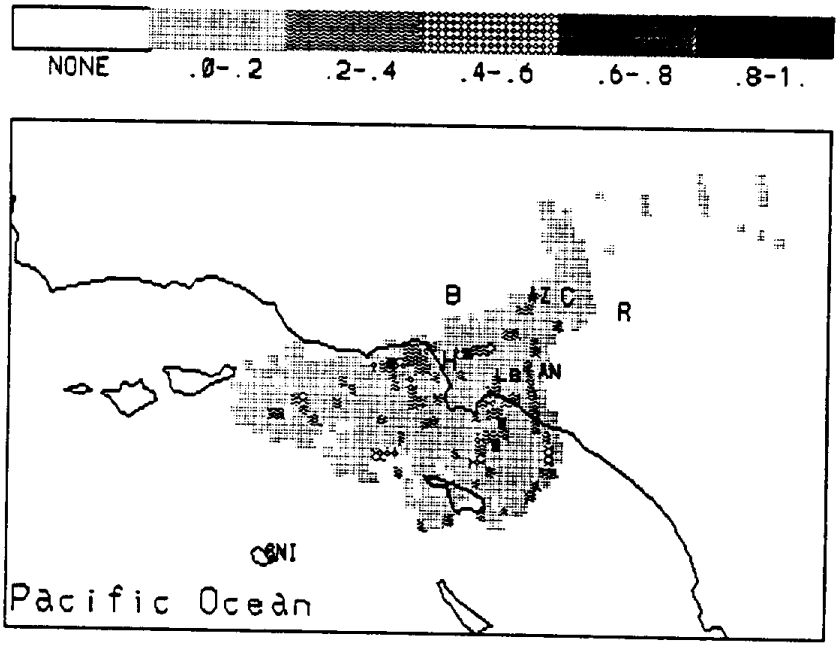

areas as the potential sources of NO_3^- L3-a volatile NO_3^- species (Figure 4.3.30). However, NO_3^- L9, the fine fraction nitrate (Figure 4.3.31), has large potential source areas that can be identified on the NO_x emission map (Figure 4.3.3) as the five electric power plants at Harbor, Long Beach, Haynes, Alamitos, and Huntington Beach. Source areas for PM-10 NO_3^- are similar to those of NO_3^- L9, but with fewer high potential grid cells (Figure 4.3.32). It appears that particulate nitrate can be associated with those power plants. The trailing of high potential cells into the ocean is likely due to the fact that all of the trajectories from that area of the ocean cross the region south of Long Beach. They then must have the same potential as the power plant area. There is also a source region near the Claremont site that corresponds to the same area as that having a high potential for SO_2. Thus, the Etiwanda Electric Power Plant may be the source of NO_x that is oxidized to the observed NO_y as well as SO_2. Also, total NO_3^- does not show high potential cells (Figure 4.3.33), presumably because of the effect of the gaseous species on the overall NO_3^- potential values.

The NH_3 PSCF map (Figure 4.3.34) identifies two land areas and one marine region. The land sources are located to the east of Claremont and in the Huntington Beach area. The source in the Claremont area may be emissions from the large feedlot near Chino (Russell et al., 1983) that are transported to Claremont by the circulating winds such as those observed on September 2, 1987. The Huntington Beach Power Plant could be a source. The marine high potential area may again be in the area of disposal of sewage sludge. The PSCF map for NH_4^+ L5 is similar to that of HNO_3 with one strong source area close to Claremont (Figure 4.3.35). NH_4^+ L5 is the volatile fine particle species that might be released by the dissociation of NH_4NO_3, and thus the covariance of NH_4^+ L5 and gaseous HNO_3 may be due, in part, to processes occurring within the sampler.

NH_4^+ L9 has a very different potential source pattern from that of NH_4^+ L5 (Figure 4.3.35). The NH_4^+ L9 PSCF map (Figure 4.3.36) has an almost identical potential pattern as that for NO_3^- L9. Most of the potential NH_4^+ L9 sources are around the coast and offshore. Therefore, the NH_4^+ L9 may result from gaseous NH_3 being transported from the marine source areas and then reacting with HNO_3 that results from the NO_x emissions from the five electric power plants on the coast. In

FIGURE 4.3.30. NO_3^- PM2.5 L3 at Claremont.

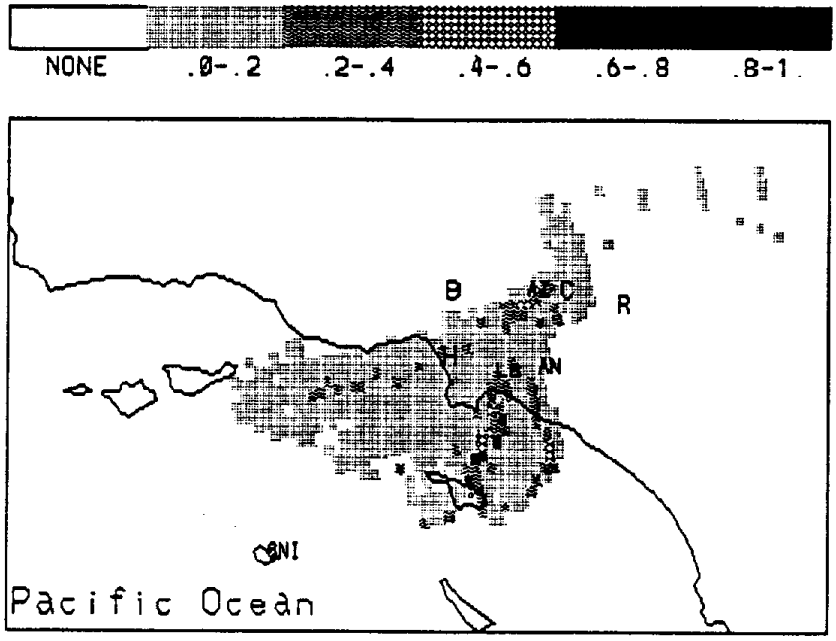

FIGURE 4.3.31. NO_3^- PM2.5 L9 at Claremont.

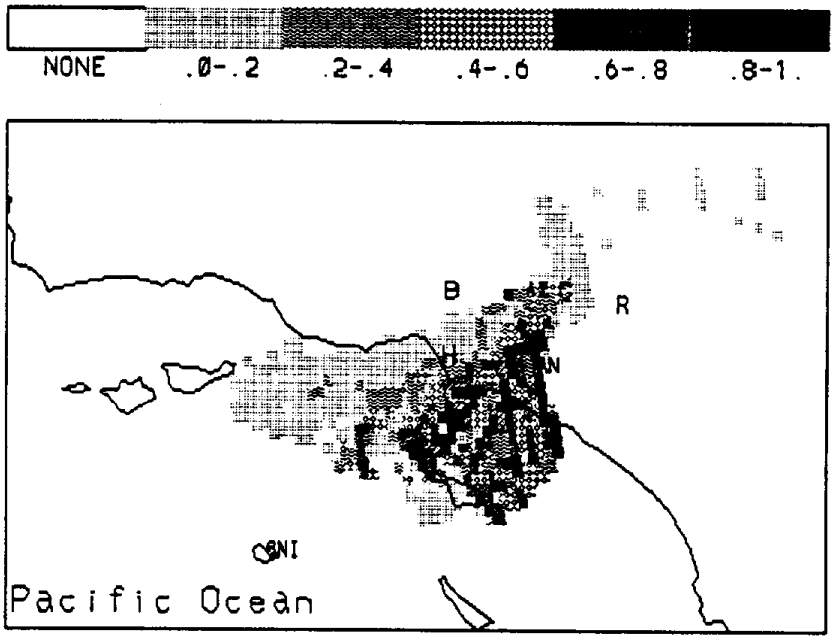

FIGURE 4.3.32. NO_3^- PM10 at Claremont.

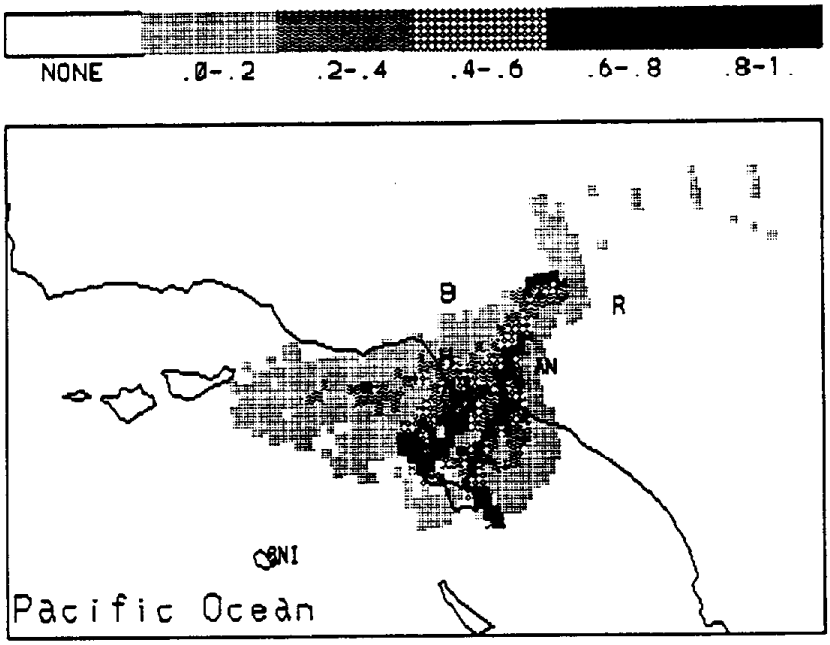

FIGURE 4.3.33. Total NO_3^- at Claremont.

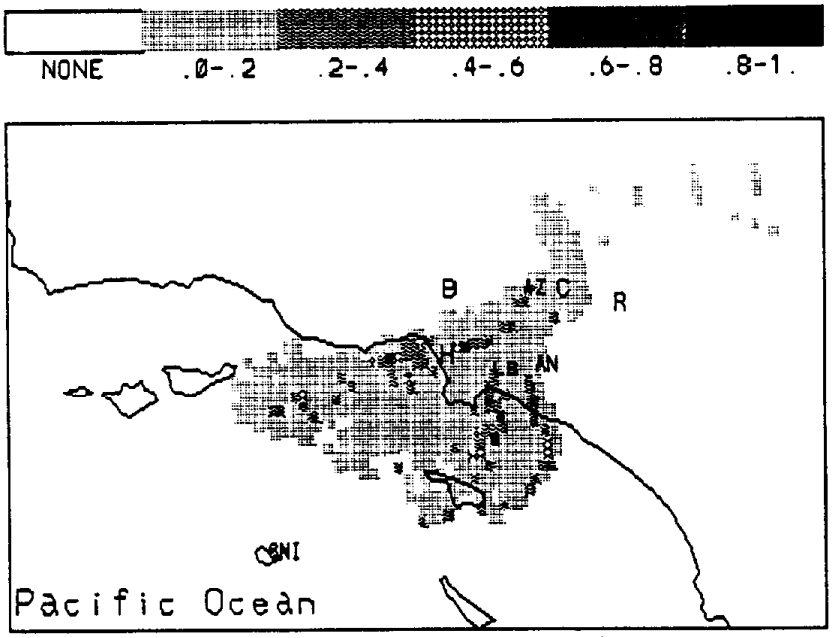

FIGURE 4.3.34. Gaseous NH_3 at Claremont.

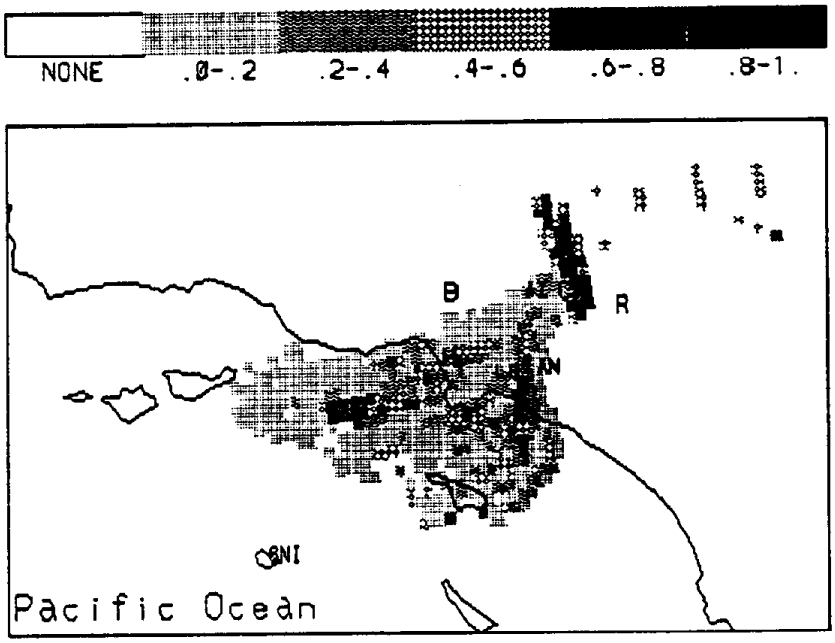

FIGURE 4.3.35. NH_4^+ PM2.5 L5 at Claremont.

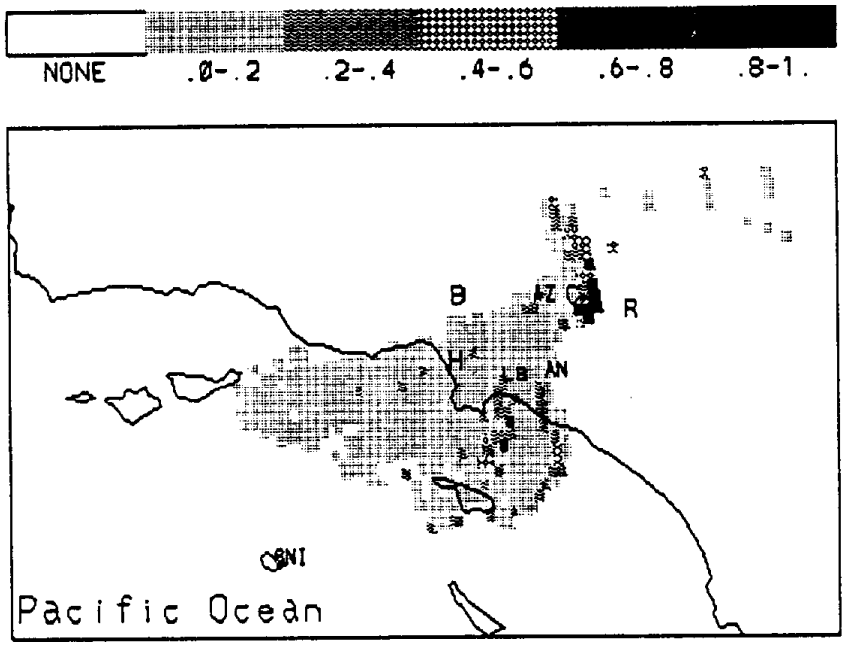

FIGURE 4.3.36. NH_4^+ PM2.5 L9 at Claremont.

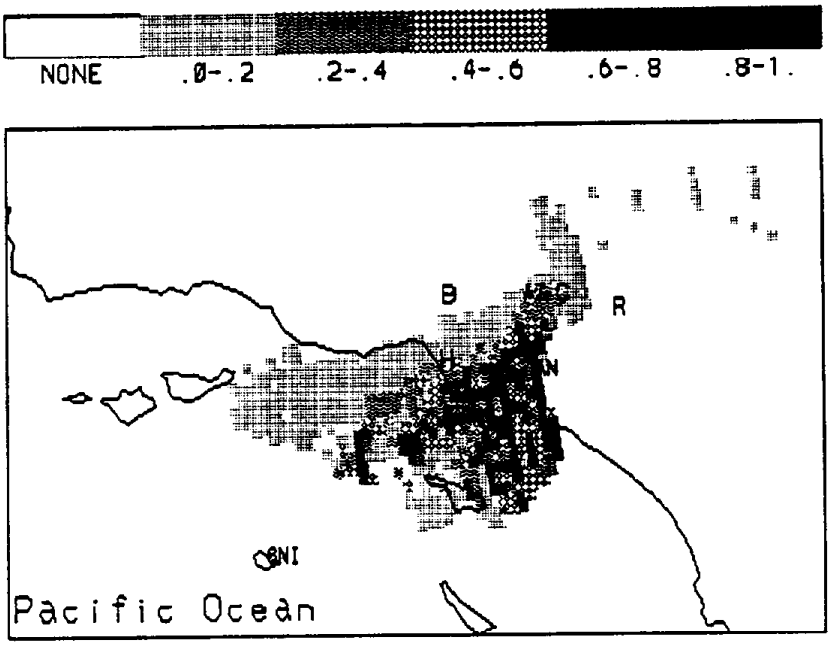

FIGURE 4.3.37. NH_4^+ PM10 at Claremont.

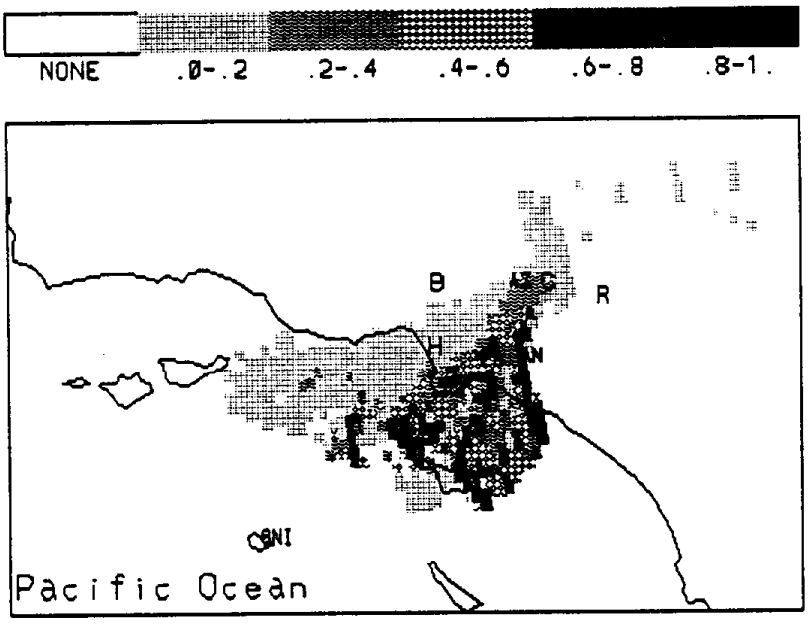

Figure 4.3.37, the NH_4^+ PM-10 map shows high potential grid cell clusters similarly to those shown in Figure 4.3.36 for NH_4^+ L9. In summary, three clusters of major land source areas and an oceanic source area contribute to most of species that control the acidity of the particles collected at Claremont. One cluster is in the area where the four electric power plants (Harbor, Long Beach, Alamitos, and Haynes) are located. The second cluster is the band stretching from the Huntington Beach Power Plant toward Claremont. The third source area is very close to Claremont and may be due to the Etiwanda Electric Power Plant.

Based on the PSCF results, sequences of source emission, atmospheric conversion, and transport may be reconstructed as follows:

1) The emissions released from the four power plants contain gaseous SO_2 and NO_x. During transport, gaseous SO_2 is oxidized into H_2SO_4 and subsequently undergoes dry deposition or reaction with gaseous NH_3 to form $(NH_4)SO_4$. Gaseous NO_x may behave analogously. Gaseous NO_x undergoes rapid gas-phase conversion into HNO_3 that can then react with NH_3 to produce particulate NH_4NO_3. By the time the air parcels arrive at Claremont, the gaseous species are no longer detected. Therefore, this cluster of sources contribute only particle NH_4^+ and NO_3^-. The secondary $SO_4^=$ from oxidation of SO_2 is well mixed with the marine $SO_4^=$, and is not clearly recognized by the PSCF analysis as from an anthropogenic source.

2) The emissions from the Huntington Beach Power Plant include gaseous SO_2 and NO_x. During transport, the gaseous species are either dry deposited or converted to particulate species. When the air parcels get to Claremont, only the particulate species are detected. The anthropogenic $SO_4^=$ can be distinguished from the marine $SO_4^=$ by the PSCF analysis of nonmarine sulfate. Therefore, this source area contributes particulate anthropogenic $SO_4^=$, NO_3^-, and NH_4^+ to the Claremont site.

3) The Etiwanda Electric Power Plant emits gaseous SO_2 and NO_x, but because of its close proximity to the sampling site, it makes only small contributions to the $SO_4^=$ and NO_3^- species.

4) The ocean source areas contribute both primary sea salt, such as NaCl and $SO_4^=$, as well as secondary $SO_4^=$ and SO_2 from the oxidation of DMS released from digestion of waste sludge.

Rubidoux

There are several high potential marine source areas for PM-10 Cl with a large cluster of grid cells in the ocean close to Santa Catalina Island (Figure 4.3.38). However, the same areas do not appear in the PM-2.5 Cl map (Figure 4.3.39). There are also scattered source grid cells to the north of Rubidoux, and to the east of Anaheim. There is a concentrated area that is very similar for both Cl size fractions. Based on the PCA model for PM-2.5 aerosols, there are two factors, the 3rd and the 4th, that involve Cl. Cl correlates with gaseous HNO_3 on the 3rd factor and with Na on the 4th factor. However, according to the PSCF map for HNO_3, the source area appears to be further south along the coast rather than in the Cl source east of Anaheim. There is a colocated high potential region for NH_4^+ in the same area as the Cl region southeast of Anaheim. The nature of this high potential area in the vicinity of Anaheim cannot be identified on the basis of the information that is currently available.

The observation that there are no significant marine source areas of fine fraction Cl is very different from the patterns observed at Burbank and Claremont in which Cl PM-2.5 has very similar maps to those of Cl PM-2.5. Almost all potential Na PM-10 source areas are found in the ocean with one spot near Rubidoux that could be a result of local soil sources (Figure 4.3.40).

Figure 4.3.41 shows that the ocean could be the sole source of $SO_4^=$ PM-10 because the high potential source grid cells in this map are either in the ocean or close to the coast. The high potential cells along the coast are too far south to be Huntington Beach Electric Power Plant and do not correspond with a SO_2 source on the 1982 emissions map. Thus, we cannot directly attribute this area to a known anthropogenic source. A similar pattern is observed for $SO_4^=$ PM-2.5 shown in Figure 4.3.42, except there are fewer high potential grid cells in this figure. The nonmarine $SO_4^=$ map (Figure 4.3.43) confirms that the high potential grid cells for PM-10 or PM-2.5 cannot be directly related to any anthropogenic source. The high potential source area on the coast in the PM-10 and PM-2.5 $SO_4^=$ maps disappears in the nonmarine $SO_4^=$ PSCF map suggesting that the sulfate observed at Rubidoux is marine sulfate.

FIGURE 4.3.38. Cl PM10 at Rubidoux.

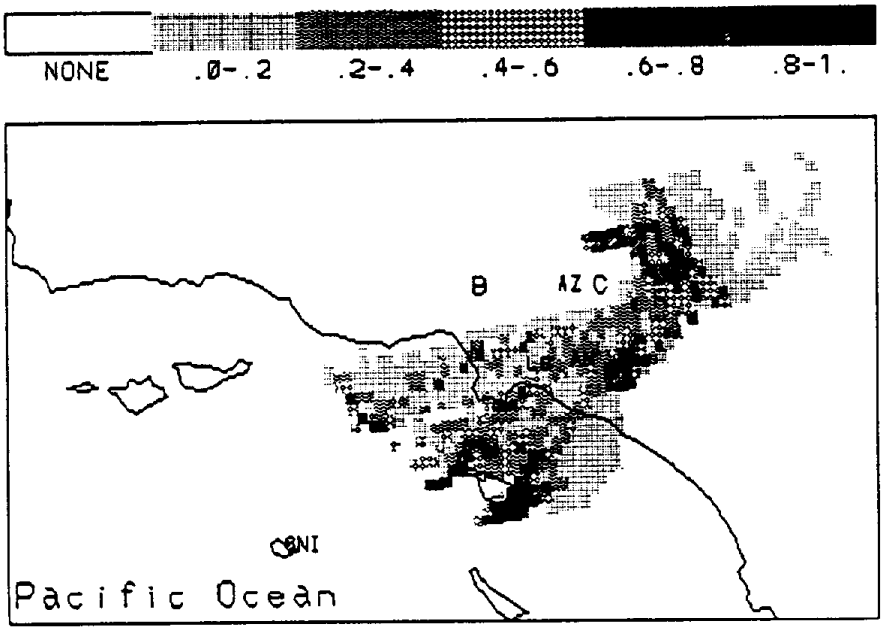

FIGURE 4.3.39. Cl PM2.5 at Rubidoux.

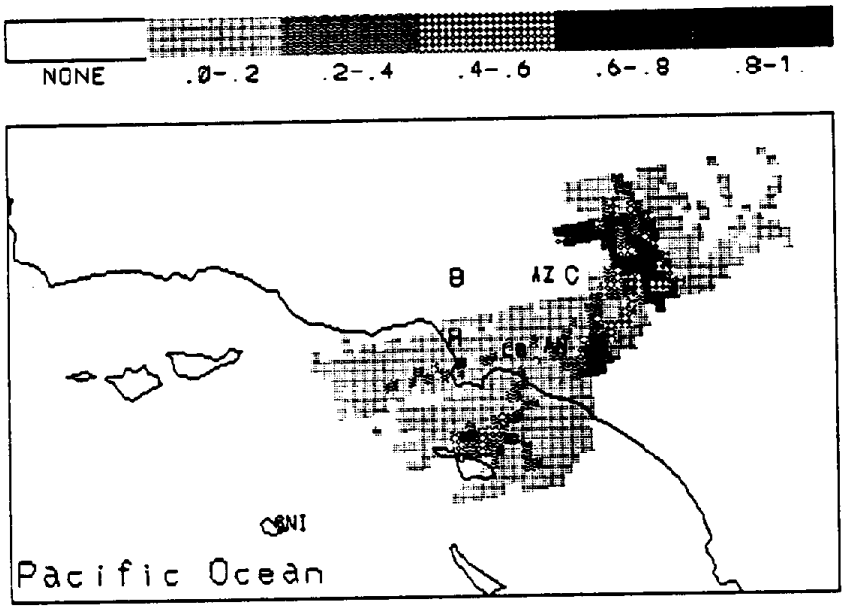

FIGURE 4.3.40. Na PM10 at Rubidoux.

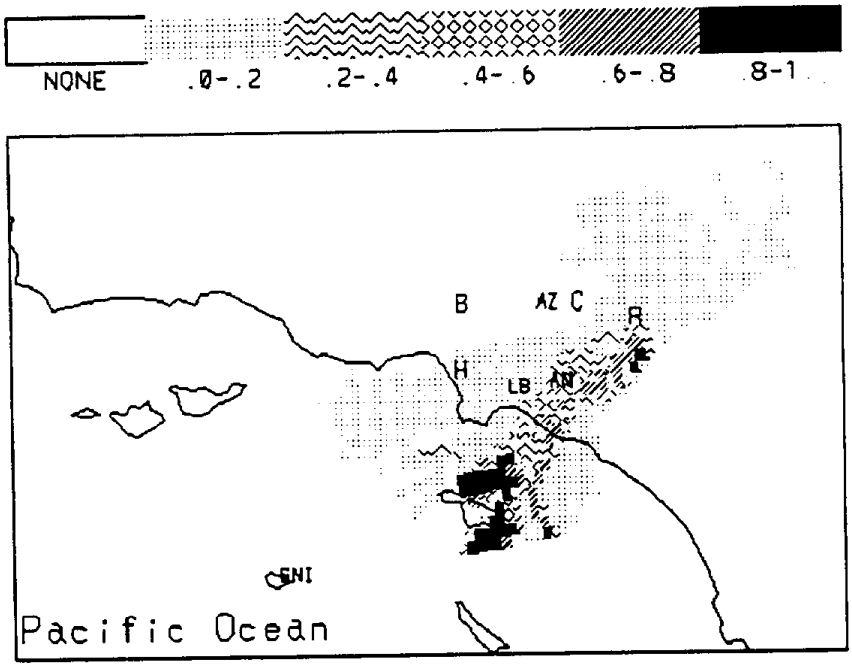

FIGURE 4.3.41. $SO_4^=$ PM10 at Rubidoux.

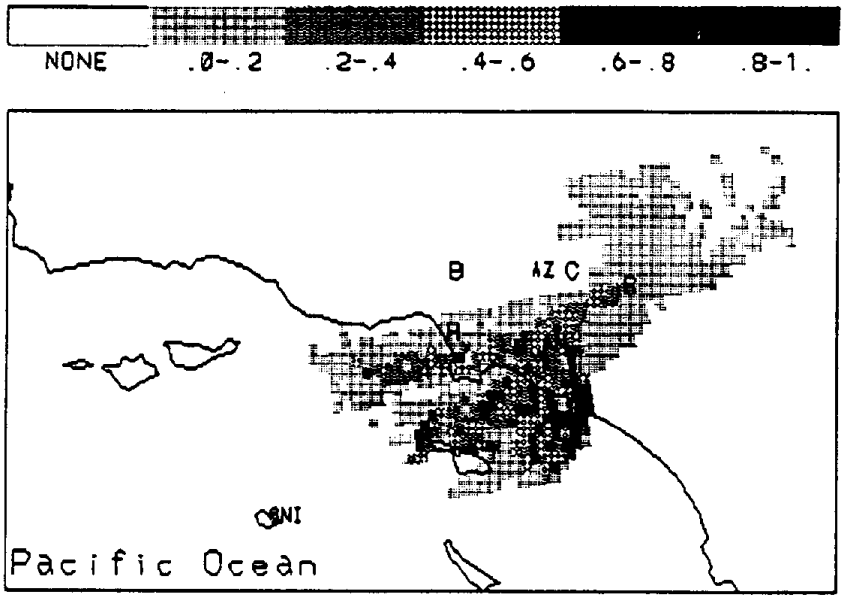

FIGURE 4.3.42. $SO_4^=$ PM2.5 at Rubidoux.

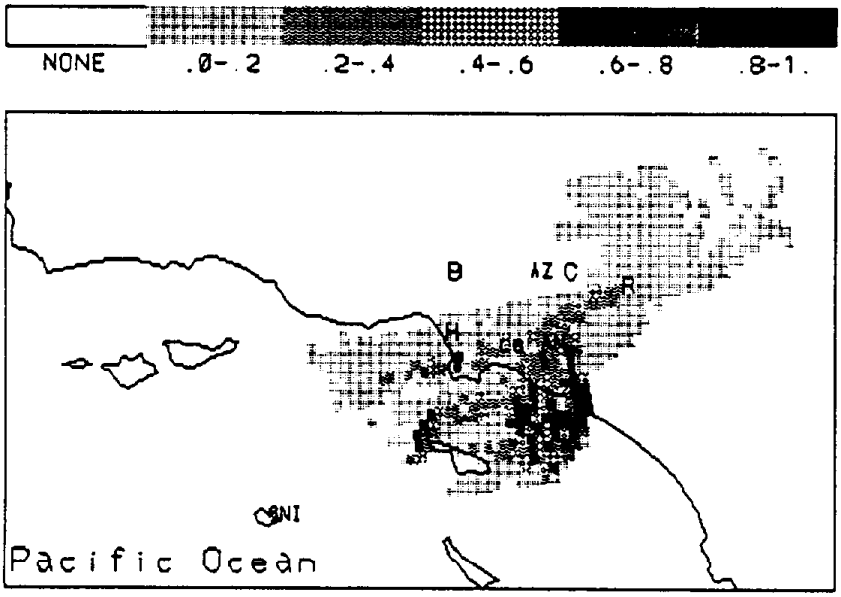

FIGURE 4.3.43. Non-marine $SO_4^=$ at Rubidoux.

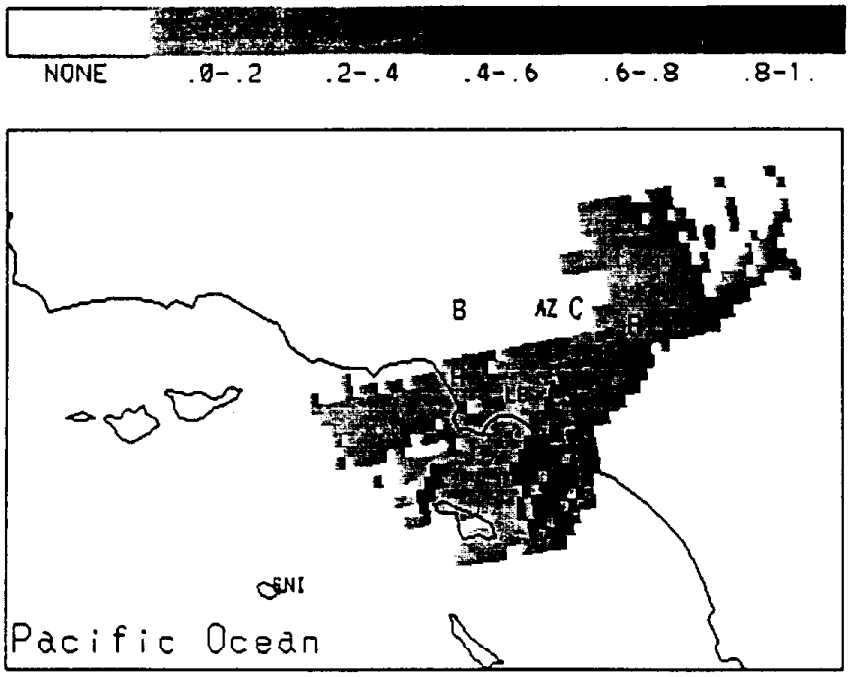

FIGURE 4.3.44. Gaseous SO_2 at Rubidoux.

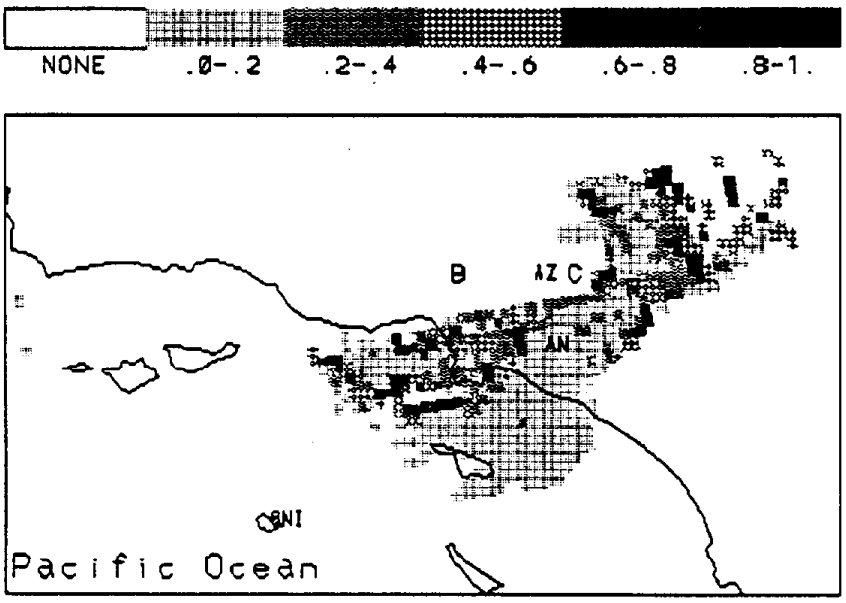

For SO_2, the high potential source cells are widely dispersed (Figure 4.3.44). There are several high potential grid cells to the north and east of the sampling site. Emission sources located in this area are the San Bernardino Electric Power Plant (>10 tons/day) and the Highgrove electric power plant (>5 tons/day). A couple of smaller emission sources (>0.5 tons/day) north and northeast of Rubidoux might also contribute gaseous SO_2. There are a number of areas of high SO_2 potential observed in the offshore area that could again represent emission of DMS from the sewage sludge in the surficial sediments. These results would suggest the need for measurements of the fluxes of reduced gas-phase species (DMS and NH_3) in these areas to confirm or refute this hypothesis.

As discussed above, there is a large cluster of HNO_3 high potential cells along the southern coastal area trailing off to the south into the ocean (Figure 4.3.45). The coastal part of this region is in the same area as seen in the particulate $SO_4^=$ although it does not appear in the nonmarine sulfate. In this case, the gaseous HNO_3 is transported much further than was observed for the other two sites. The origin of the HNO_3 is thus uncertain. Several clusters of high potential HNO_3 cells are observed in the Los Angeles area by the PSCF map for Rubidoux, whereas the maps for Burbank and Claremont do not show any high potential cells in this NO_X source area. The other potential sources correspond to anthropogenic activities such as the power plants at Redondo, El Segundo, Scattergood, and Long Beach, etc. These emissions are all brought to Rubidoux by trajectories through the channel between the Chino Hills and the Santa Ana Mountains.

The high potential areas for gaseous NO_3^-, total NO_3^-, PM-2.5 NO_3^- L3, L9, and PM- 10 NO_3^- are rather widely distributed (Figures 4.3.46-4.3.50). However, although the PSCF analysis for the NO_3^- species does not indicate strong source clusters in the entire trajectory region, there are patterns of moderate probability that follow the line of trajectories that move from the ocean past an area where there are power plants along the coast and carry the air from the coast to Rubidoux. It appears from these maps that the cluster of power plants in the Long Beach area and the Huntington Beach Electric Power Plant make noticeable contributions to the observed NO_3^- concentrations.

FIGURE 4.3.45. Gaseous HNO_3 at Rubidoux.

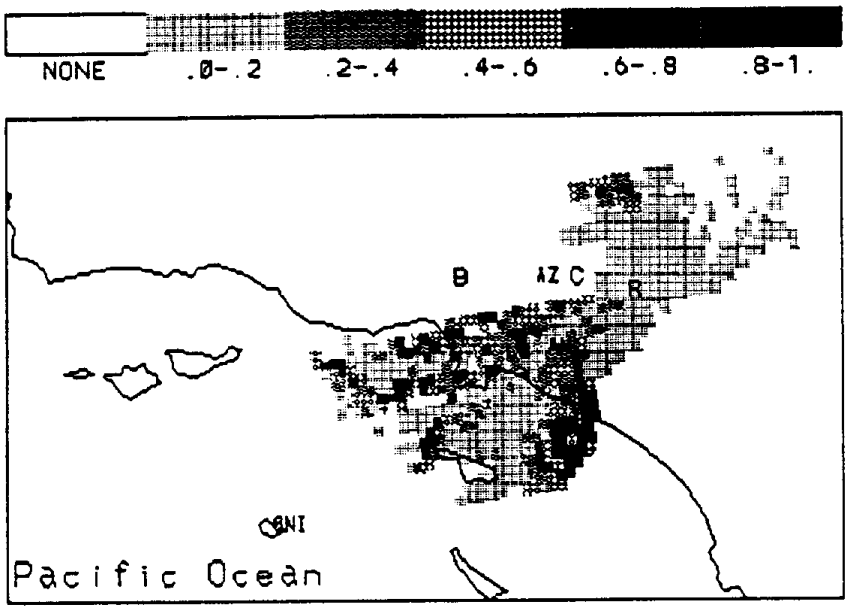

FIGURE 4.3.46. Gaseous NO_3^- at Rubidoux.

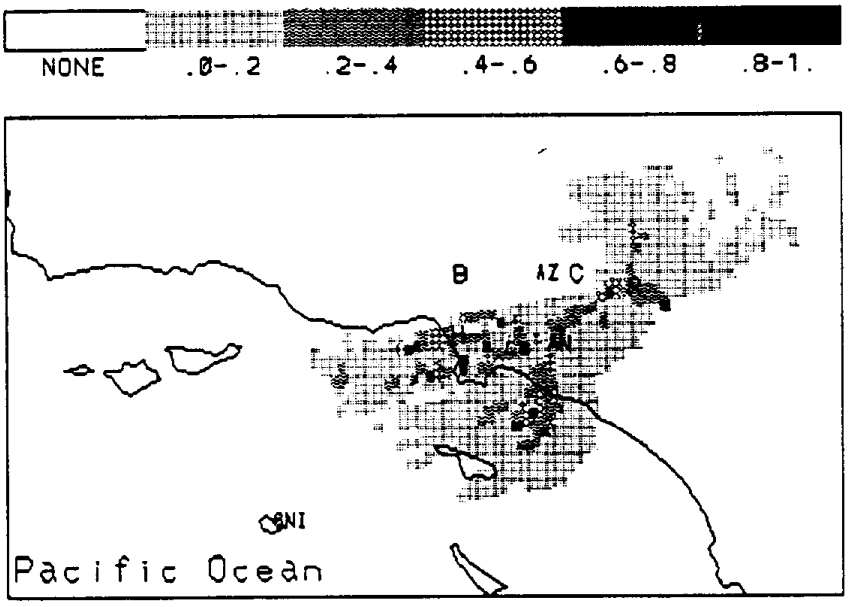

FIGURE 4.3.47. NO_3^- PM2.5 L3 at Rubidoux.

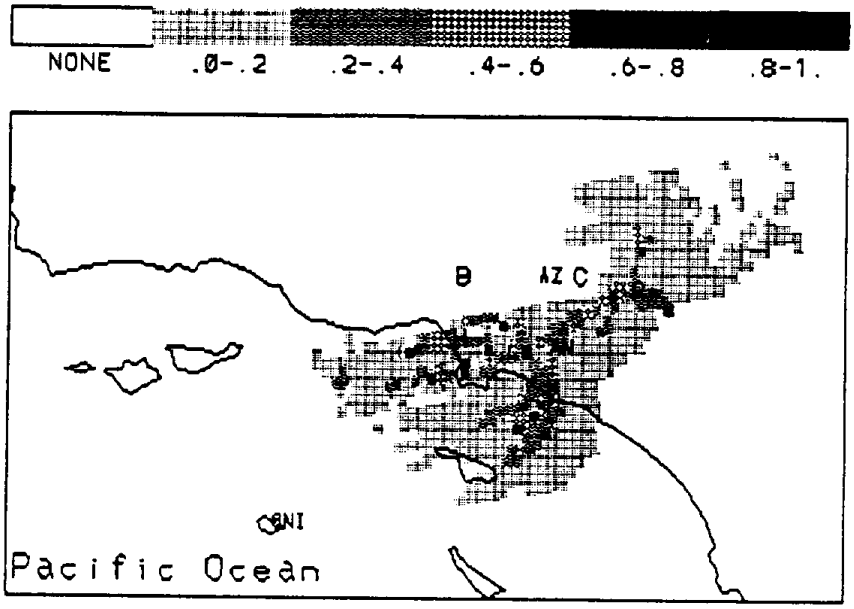

FIGURE 4.3.48. NO_3^- PM2.5 L9 at Rubidoux.

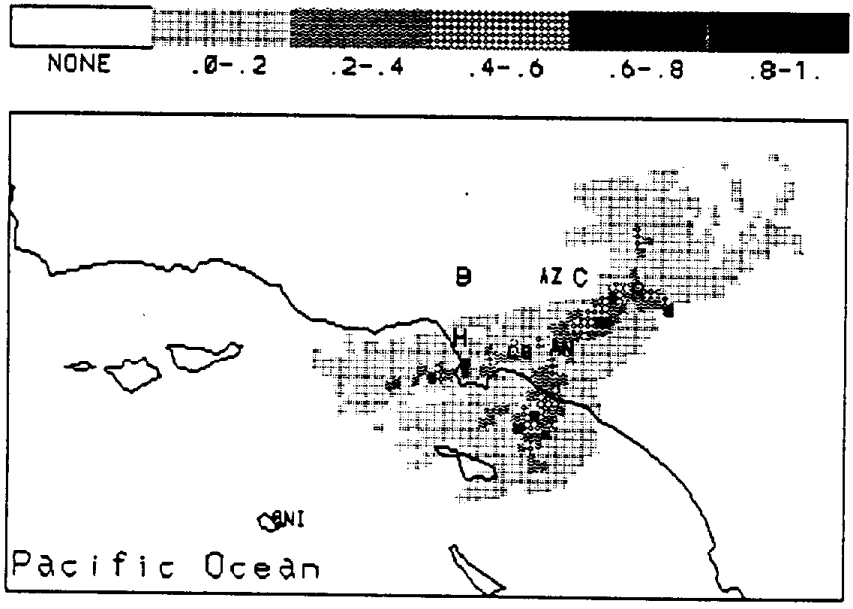

FIGURE 4.3.49. NO_3^- PM10 at Rubidoux.

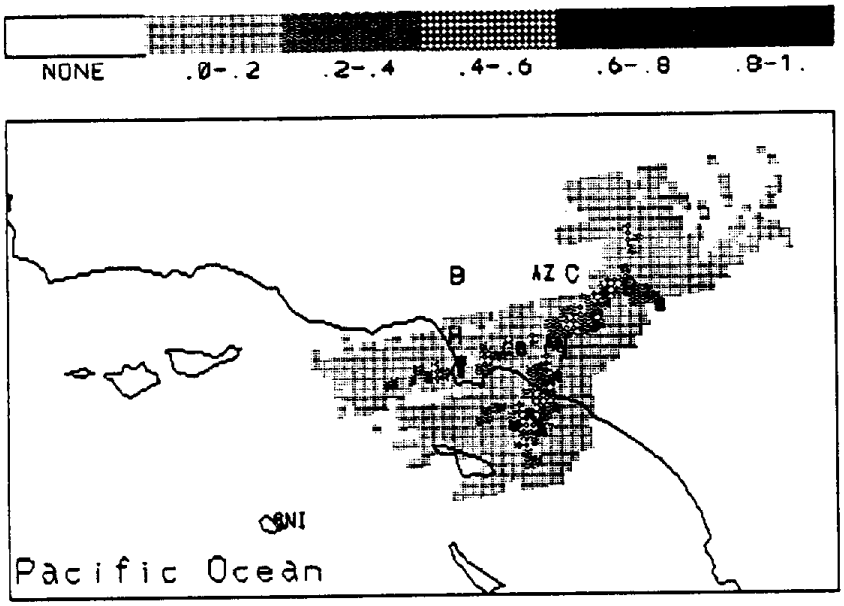

FIGURE 4.3.50. Total NO_3^- at Rubidoux.

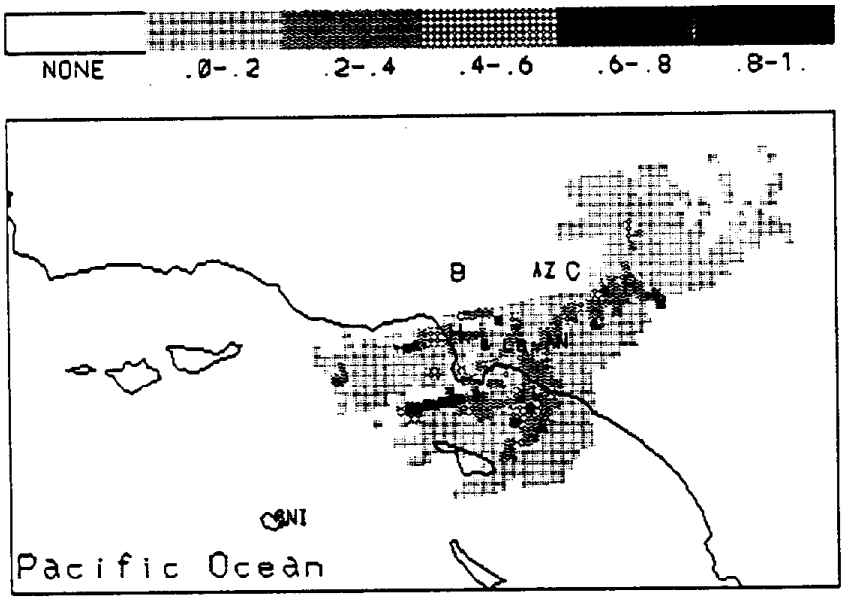

The most significant NH_3 source area observed at Rubidoux was found to be the strong spot about 20-35 miles southwest (Figure 4.3.51). This high potential area is shifted from the known large feedlot south of Chino that does not appear as a strong area in PSCF analysis. This shift could have been caused by air recirculation or by possible errors in the trajectories.

The high potential source areas of NH_4^+ L5, the volatile fine particle NH_4^+, appear to be distributed along the primary pathways toward the ocean (Figure 4.3.52) in a similar manner as the NO_3^- particulate species. Only moderate-valued cells are observed for the fine fraction NH_4^+ PM-10 sources (Figure 4.3.53). Some areas in the ocean have high potential for being the NH_4^+ PM-10 source (Figure 4.3.54). However, these areas are in different locations from those for NH_4^+ L5 or L9. The PM-10 NH_4^+ appears to primarily come along the southern pathway past Huntington Beach, but somewhat further south than the area observed for the L5 species. The single grid cell in the Chino feedlot area does appear as a high potential area for all of the particulate species. Thus, this source does affect the particulate NH_4^+ behavior but not the gaseous NH_3 map. Since a substantial excess of NH_3 is needed to inhibit the dissociation of NH_4NO_3, the observed behavior is not easily understood.

In summary, the sources that emit acidic aerosols to Rubidoux are classified as three major clusters of land sources and some marine sources. The first cluster of sources is from Los Angeles and the three power plants along the coast west and south of Los Angeles. The second source is the Huntington Beach Electric Power Plant. The third cluster is the feedlot located around Rubidoux.

FIGURE 4.3.51. Gaseous NH_3 at Rubidoux.

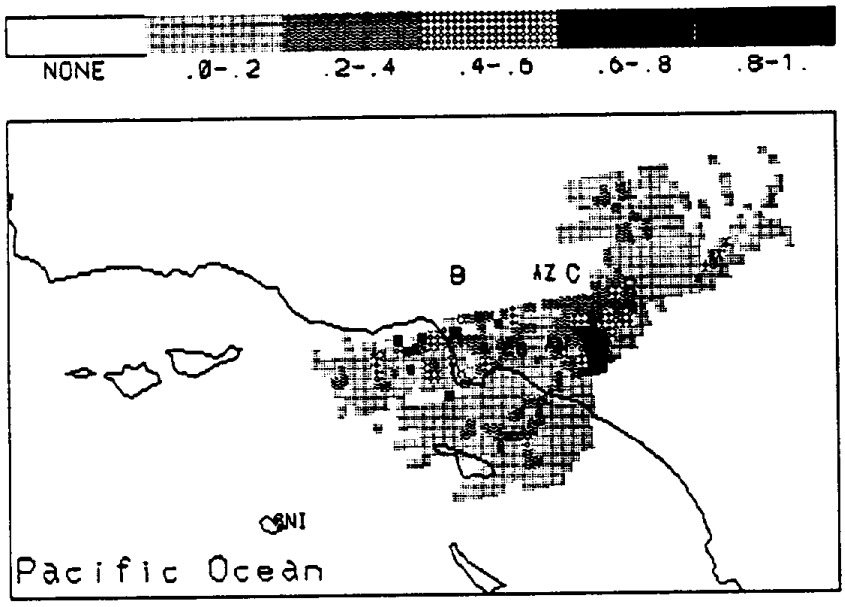

FIGURE 4.3.52. NH_4^+ PM2.5 L5 at Rubidoux.

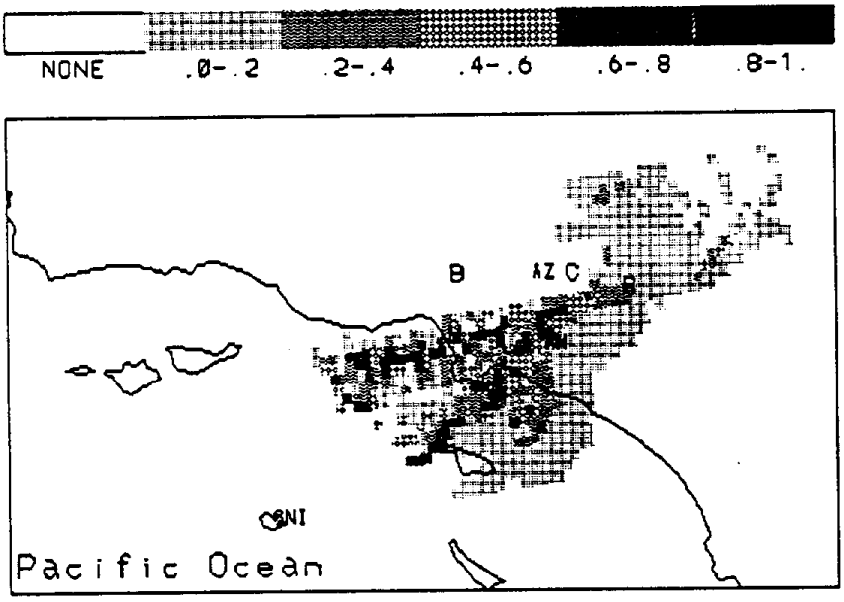

FIGURE 4.3.53. NH_4^+ PM2.5 L9 at Rubidoux.

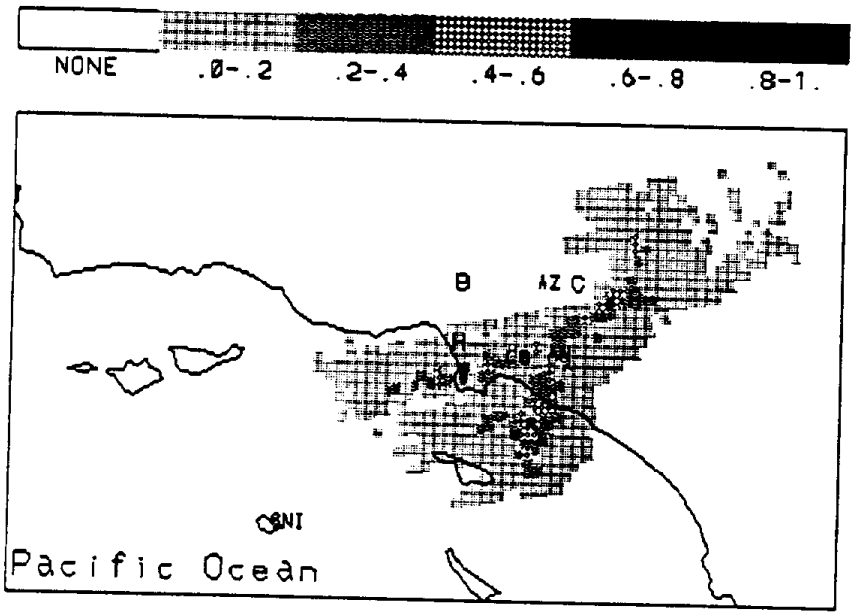

FIGURE 4.3.54. NH_4^+ PM10 at Rubidoux.

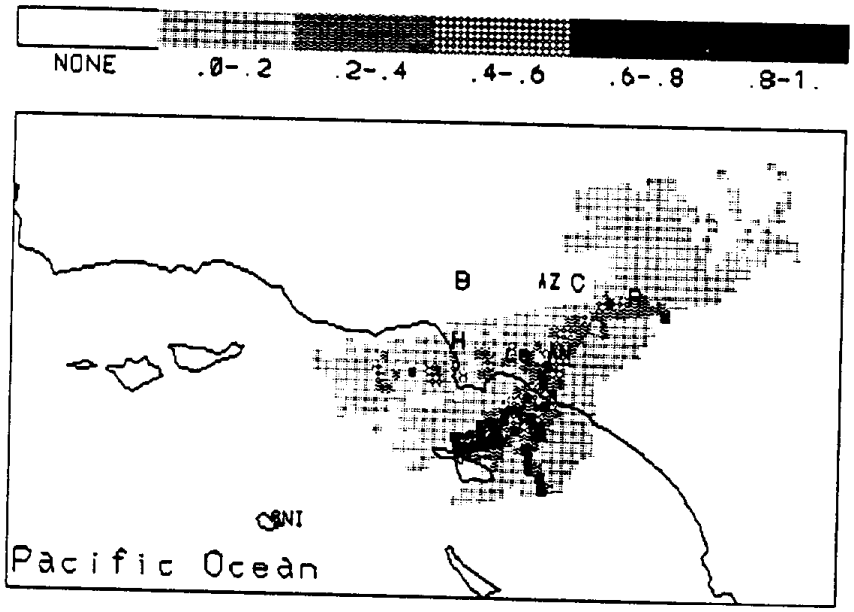

5. SUMMARY AND CONCLUSIONS

In this study, we applied various techniques to try to identify the sources of acidity in the South Coast Air Basin of California. These techniques included graphical analysis, box modeling, deterministic modeling, and receptor modeling. We used the SCAQS database, which is the most comprehensive database available to date. Some of the techniques were applied in all the episodes; i.e., both summer and winter, while others were applied only for the winter episode, which was a high aerosol episode.

The first approach we used was the graphical, which may be called a "preliminary analysis" method. We wanted to investigate whether simple graphical techniques could be used to understand the causes of complex phenomena--like increased acidity--and quantify them, if possible. In the "preliminary analysis" a good association between high SO_2 concentrations and high sulfate levels was observed at Long Beach and Hawthorne, especially for relative humidities above 50%. However the relationship is not obvious, which means that other phenomena, rather than chemistry and direct emissions, could be responsible for the observed sulfate at that site; e. g., transport from distant sources, or a combination of photochemical activity and transport.

High concentrations of sulfates and nitrates in receptor sites--like Claremont, Los Angeles and Rubidoux--were observed during the noon and afternoon hours during the June and August episodes, indicating that photochemical activity is the main source of acidic species during those episodes. Trajectory analysis also supports this conclusion. Using trajectory analysis, source and receptor relationships were also identified. The trajectory analysis showed that pollutants emitted in the coastal areas, where most of the big stationary sources are located, were transported inland. During this transport, photochemical activity in the gas phase, and reactions in the aqueous phase, most likely transformed NO_x to HNO_3 and SO_2 to H_2SO_4. The trajectory analysis, while a preliminary graphical tool, was also used as part of the more advanced deterministic modeling techniques, as well as receptor modeling methods.

In general, graphical methods can reveal qualitative information about the origin of the problem of acidity in the South Coast Air Basin, but cannot be used to extract quantitative information, unless the spatial and temporal resolution of the measurements are substantially finer than those used during SCAQS.

Graphical analysis of organic acids, similar to the one used for sulfates, was not applied, because the available measurements did not allow us to do so, and because our knowledge of the sources, emission rates, atmospheric formation and atmospheric removal is very limited. As a result, we concluded that a useful first step would be to estimate the overall emission rates of formic and acetic acids in the South Coast Air Basin of California, the in situ production of the two acids from photochemical reactions and the removal rates due to dry and wet deposition. Due to the complete lack of information regarding organic acids, we used a combination of a box modeling technique and a tracer method. Production of formic acid was seen to be dominated by in situ formation, while for acetic acid direct emissions predominate. Therefore it is suggested that air quality models need detailed treatment of the chemical reactions that produce formic acid, as well as accurate emission inventory for acetic acid. Dry deposition seems to be the major pathway for the removal of these two organic acids, accounting for about 95% of the removal rates. The maximum concentrations of formic and acetic acid during SCAQS were 19 and 17 ppb, respectively. These values indicate that these acids may play an important role in the overall acidity in Southern California, since their concentrations were found to be comparable to those of inorganic acids.

The graphical analysis of sulfates indicated that processes other than photochemical oxidation of SO_2 in the gas phase are responsible for the high sulfate concentrations during the December episode. Application of a comprehensive gas-phase trajectory model showed that the production of sulfuric acid in the gas phase can explain only 40% of the observed peak sulfate concentrations, while it can reproduce the observed sulfate levels for dry air parcels. Sensitivity analysis of the gas-aerosol model indicated that the uncertainty in the model input variables could not explain the observed excess sulfate. In addition, our trajectory analysis indicated that these high sulfate concentrations coincided with the arrival at the receptor sites of parcels that had passed through a fog layer the previous night. We speculated that heterogeneous oxidation in fog droplets may play an important role to high sulfate concentrations. As a result, we decided to develop a fog model to account for these processes, in an attempt to resolve this question.

As part of the fog model development effort, we studied the applicability of Henry's Law to measured concentrations of ionic species in fog water. Theoretical investigation indicated that extreme caution should be exercised when Henry's Law equilibrium is assumed between a bulk fogwater sample and the atmosphere from which the sample was drawn, because this assumption can lead to a significant bias in the calculations. We have shown that even if the individual fog droplets, with different chemical composition, are in equilibrium with the surrounding atmosphere, their bulk mixture is not. Furthermore, the bulk mixture is supersaturated with respect to weak acids and ammonia. If allowed, the bulk mixture can outgas these species in an effort to equilibrate with the atmosphere. The weak acids are expected to deviate from Henry's Law for bulk pH values higher than their pKa value, while ammonia is expected to deviate under all conditions of atmospheric interest. Lack of experimental measurements of the size/composition distribution of droplets precludes a direct intercomparison of the estimated and measured concentrations of weak acids and ammonia, especially in the pH range 4-7. This deviation is not expected to be as important for strong acids, like sulfuric acid, and as a result direct intercomparison between model predictions and measurements can be performed.

The model that was developed contains gas-phase chemistry, aerosol dynamics and thermodynamics, aqueous-phase chemistry, droplet microphysics, and wet removal processes. The purpose of the model development was to study the contribution of fog to acidic species formation and removal; i.e., the smog-fog-smog cycle. Both aerosol and droplet size/composition distributions are discretized in size sections and their changes are followed during the simulation. We applied the model for a number of test cases, in order to stress its capabilities, and at the same time, to study theoretically the effects of fog.

The fog increases the sulfate content of the aerosol particles considerably, due to the aqueous phase oxidation of sulfur dioxide. This increase should be expected in most urban fog episodes, where a high potential for S(IV) exists. For urban fog episodes of long duration or fogs in rural environments, where the sulfate production slows down after the first few hours due either to H_2O_2 depletion or pH decrease, deposition can dominate the chemical processes and sulfate may even decrease. The primary effect of long fog episodes is the decrease of the total concentrations (aerosol + gas-phase) of hydrochloric acid, nitric acid and ammonia, due to their transfer in the aquecus phase and the subsequent enhanced acid deposition.

The fog effects on the aerosol are not uniform over the size spectrum. The sulfate produced during the fog episodes favors the aerosol particles that have access to most of the liquid water and these are usually the large particles. In the case considered in this study the sulfate content of the dry particles larger than 0.5 mm in diameter increases by 130% while for the particles smaller than 0.5 mm it increases only by 45%. Most of the losses in mass for the other major inorganic aerosol species are concentrated in the larger particle range with losses around 50% for the >0.9 mm dry particles.

The simulation indicates that aerosol scavenging ratios of around 80% should be representative for urban radiation fogs. The aerosol scavenging ratio for sulfate should be less than this average value--70% under the conditions considered in this study--due to the preference of sulfate for the smaller particles. On the contrary, the ratio for nitrate should be higher than the average value.

Sampling and subsequent mixing of fog droplets and aerosol particles with different sizes may result in measured concentrations that are not fully representative of the fogwater chemical composition and can introduce errors in the reported values of the ionic species deposition velocities. The sampling bias will depend on the initial aerosol size/composition distribution, on the rate of temperature change and on the cutoff size of the sampling device. The use of a sampling device with a smaller cutoff size does not guarantee a better measurement in all cases.

In fog models where the liquid water depositional flux is expressed as a function of the fog liquid water content because of the difference in liquid water distributions during the growth and dissipation stages, different expressions should be used for these two stages. The difference in deposition velocities of the major ionic species during fog episodes can be explained by their different distributions over the droplet spectrum. The existence of a significant amount of sulfate in small particles before the fog starts results in a relatively small sulfate deposition velocity during the fog episode.

Application of the fog model showed that the observed sulfate levels are consistent with our current knowledge of the corresponding aqueous-phase processes, and that aqueous-phase oxidation of S(IV) by H_2O_2, O_2 (catalyzed by iron and manganese), and NO_2 can indeed produce the remaining 60% of the observed sulfate. Our calculations indicate that the quantity of liquid water associated with the aerosol, as opposed to that associated with the fog droplets, cannot provide the necessary medium for the production

of the 'excess sulfate' in the time periods involved during the December episode. Significant amounts of sulfate are predicted to be deposited during the fog lifetime. The calculated sulfate deposition rates are approximately 0.264 meq/m^2/day.

The trajectory model was also used to examine the vertical distribution of acidity and the implications with respect to fog acidity. The model predicted that there is trapping of SO_2 aloft. Despite this trapping, though, the sulfate concentrations aloft were less than 50% of the ground concentrations. The occurrence of the fog episode near the ground is the major cause of this behavior. Without taking into account the sulfate production inside the fog layer, the sulfate concentrations aloft predicted by the model exceed the ground-level concentrations for most of the day. It was also shown that the potential exists for the gas-phase production of sulfate aloft and its fumigation later onto the ground during days with small mixing heights, during the winter. The presence of clouds may enhance this phenomenon, due to in-cloud sulfate production. The presence of clouds may also enhance the production of formic acid from formaldehyde dissolved in the cloud water. No attempt was made, though, to quantify both the production of sulfate and formic acid due to the lack of the necessary data.

The fog model used in this study, in contrast to the previous methods, can be applied to quantify the effects of various sources on acid deposition in California during episodic conditions. Its main disadvantage is that it is computationally intensive and requires the knowledge of a substantial number of parameters to give accurate results. Thus, while it was used for the specific episode during SCAQS, it cannot be used on a routine basis.

An alternative methodology to deterministic modeling is that of receptor models. A number of receptor modeling techniques were applied in the South Coast Air Basin, in order to examine whether they can be used to explain the source receptor relationships of secondary acidic species, and whether their results are in agreement with those found by the other techniques. Various receptor models of different complexity were used, specifically, principal component analysis, stepwise multiple regression, target transformation factor analysis, and potential source contribution function analysis.

The first receptor modeling technique used was Principal Component Analysis. A five-factor model was able to describe the potential sources of PM-2.5 at Burbank and Rubidoux, while a six-factor model was used at Claremont. The method was able to recognize that the acidic species are secondary photochemical products, but it was unable to correlate the species to emissions from primary sources. Since the SCAQS data were collected under similar conditions; i.e., those expected to produce high concentrations of photochemical smog, the variability of the ambient measurements is less than would be expcted with a more randomized sampling scheme. The principal component analysis method relies on sample variability to separate sources. Thus, the SCAQS data are not ideally suited for separating sources by this technique.

The second statistical technique used was the stepwise Multiple Regression. The results of this method were also not satisfactory. The Multiple Regression explained only half of the variance. The result indicates that the atmospheric transport of the gaseous precursors and their conversion into particulate phase acidic species tend to decouple them from the variations seen in any primary particles, making the assignment to emission sources almost impossible.

We arrived at a similar conclusion by using the Target Transformation Factor Analysis method. As in the case of the Principal Component Analysis, the results of this factor analysis method identified up to five "sources," without being able to make an association of them with actual physical source types. One important finding of this method was that, while there is a substantial contribution of marine aerosol at Burbank, there is only minor contribution of marine aerosol at Claremont and Rubidoux.

To address the difficulties of the traditional factor analysis techniques, and to account for the role of meteorology we used a more advanced receptor modeling method, called Potential Source Contribution Function Analysis. The method combined the trajectory analysis described earlier, with a conditional probability function, to identify the location of the sources that contribute to the aerosol levels at the receptors of interest.

In contrast to the other receptor techniques, this method was able to identify possible locations of sources. A substantial fraction of the observed inorganic aerosol at Burbank and Claremont originates at the ocean and along the coastal line. This is consistent with the predictions of the deterministic model. While sea salt and sea-salt sulfate may be of natural origin, there are substantial sources of SO_2 along the coast. As

the deterministic model predicted a fraction of the emitted SO_2 reacts in the gas and the aqueous phases, thereby producing aerosol sulfate. This receptor modeling technique also predicted that the high NH_4NO_3 concentrations at Rubidoux are the result of the reaction of nitric acid generated elsewhere and transported to Rubidoux, with ammonia generated by the feedlots at Chino. This prediction is consistent with the findings of deterministic modeling (Russell et al., 1983).

In summary, we can say that simple graphical and factor analyses can give only qualitative results regarding the formation, transport and deposition of acidic compounds. Advanced receptor modeling techniques, like the Potential Source Contribution Function Analysis, are more capable to isolate the locations of the sources and to quantify their contribution to aerosol formation. Deterministic modeling is, though, the major tool with which we can study the origins of secondary organic and inorganic compounds, their transport and their deposition. The only disadvantage of deterministic models is that, because of their demand in input parameters, they can be used only for episodes during which these parameters are measured.

This study has shown that the main inorganic acids in the South Coast Air Basin are nitric and sulfuric acids. The contribution, though, of organic acidic species like formic and acetic acids should not be neglected, since our modeling effort indicated that their concentrations are comparable to those of the two inorganic species.

6. REFERENCES

Andreae, M.O., R.W. Talbot, T.W. Andreae, and R.C. Harriss (1988): Formic and acetic acid over the central Amazon region, Brasil, 1, dry season, J. Geophys. Res., 93:1616-1624.

Ashbaugh, L.L., W.C. Malm, and W.Z. Sadeh (1985): A residence time probability analysis of sulfur concentrations at Grand Canyon National Park. Atmos. Environ., 19:1263-1270.

Atkinson, R. (1990): Gas-phase tropospheric chemistry of organic compounds: A review. Atmos. Environ., 24A:1-42.

Brown, R., and W.T. Roach (1976): The physics of radiation fog, II, A numerical study. Q. J. R. Meteorol. Soc., 102:335-354.

California Air Resources Board (1981): Emissions inventory, South Coast Air Basin, Working Paper 1, 1982 AQMD Revision, Sacramento, CA, July.

Carter, W.P.L. (1990): A detailed mechanism for the gas-phase atmospheric reactions of organic compounds. Atmos. Environ., 24A:481-518.

Carter, W.P.L., and R. Atkinson (1988): Development and implementation of an up-to-date photochemical mechanism for use in airshed modeling. Summary final report to California Air Resources Board, Sacramento.

Carter, W.P.L., F.W. Lurmann, R. Atkinson, and A.C. Lloyd (1986): Development and testing of a surrogate species chemical reaction mechanism. EPA-600/3-86-031.

Cass, G.R., and F.H. Shair (1984): Sulfate accumulation in a sea breeze/land breeze circulation system. J. Geohpys. Res., 89:1429-1438.

Cass, G.R. (1979): On the relationship between sulfate air quality and visibility with examples in Los Angeles. Atmos. Environ., 13:1069-1084.

Cass, G.R. (1977): Methods for sulfate air quality management with applications to Los Angeles. Ph.D. thesis California Institute of Technology.

Chan M., and K. Durkee (1989): Southern California Air Quality Study, B-Site operations. Final Report to the California Air Resources Board. Sacramento, California.

Dagaut, P., T.J. Wallington, R. Liu, and M. Kurylo (1988): The gas-phase reactions of hydroxyl radicals with a series of carboxylic acids over the temperature range 240-440K. Int. J. Chem. Kinetics, 20:331-338.

Dollard, G.J., and M.H. Unsworth (1983): Field measurements of turbulent fluxes of wind-driven fog drops to a grass surface. Atmos. Environ., 17:775-780, 1983.

Flossmann, A.I., H.R. Pruppacher, and J.H. Topalian (1987): A theoretical study of the wet removal of atmospheric pollutants. Part II: The uptake and redistribution of $(NH_4)_2SO_4$ particles and SO_2 gas simultaneously scavenged by growing cloud drops. J. Atmos. Sci., 44:2912-2923.

Flossmann, A.I., W.D. Hall, and H.R. Pruppacher (1985): A theoretical study of the wet removal of atmospheric pollutants. Part I: The redistribution of aerosol particles captured through nucleation and impaction scavenging by growing cloud drops. J. Atmos. Sci., 42:583-606, 1985.

Forkel, R., W. Seidl, R. Dlugi, and E. Deigele (1990): A one-dimensional numerical model to simulate formation and balance of sulfate during radiation fog events. J. Geophys. Res., 95:18,501-18,515.

Forkel, R., W.-G. Panhans, R. Welch, and W. Zdunkowski (1984): A one-dimensional numerical study to simulate the influence of soil moisture, pollution and vertical exchange on the evolution of radiation fog. Beitr. Phys. Atmos., 60:340-360.

Galloway, J.N., G.E. Likens, W.C. Keene, and J.M. Miller (1982): The composition of precipitation in remote areas of the world. J. Geophys. Res., 87:8771-8786.

Goodin, W.R., G.J. McRae, and J.H. Seinfeld (1979): A comparison of interpolation methods for sparse data: Application to wind and concentration fields. J. Appl. Meteor., 18:761-771.

Greenberg, R.R., G.E. Gordon, W.H. Zoller, R.B. Jacko, D.W. Neundorf, and K.J. Yost (1978a): Composition of particles emitted from the Nicosia Municipal Incinerator. Environ. Sci. Technol., 12:1329-1332.

Greenberg, R.R., W.H. Zoller, and G.E. Gordon (1978b): Composition and size distribution of particles released in refuse incineration. Environ. Sci. Technol., 12:566-573.

Grosjean, D. (1991): Ambient levels of formaldehyde, acetaldehyde and formic acid in southern California: Results of a one-year baseline study. Environ. Sci. Technol., 25:710-715.

Grosjean, D. (1990a): Liquid chromatography analysis of chloride and nitrate with negative ultraviolet detection: Ambient levels and relative abundance of gas-phase inorganic and organic acids in Southern California. Environ. Sci. Technol., 24:77-81.

Grosjean, D. (1990b): Formic acid and acetic acid measurements during the Southern California Air Quality Study. Atmos. Environ., 24A:2699-2702.

Grosjean, D. (1990c): Atmospheric chemistry of toxic contaminants. 1. Reaction rates and atmospheric persistence. J. Air Waste Manag. Assoc., 40:1397-1402.

Grosjean, D. (1989): Organic acids in Southern California air: Ambient concentrations, mobile source emissions, in situ formation and removal processes. Environ. Sci. Technol., 23:1506-1514.

Grosjean, D. (1988): Aldehydes, carboxylic acids and inorganic nitrate during NSMCS. Atmos. Environ., 22:1637-1648.

Grosjean, D. (1983): Atmospheric reactions of pyruvic acid. Atmos. Environ., 17:2379-2382.

Grosjean, D., K. Van Cauwenberghe, J.P. Schmid, P.E. Kelley, and J.N. Pitts, Jr. (1978): Identification of C3-C10 aliphatic dicarboxylic acids in airborne particulate matter. Environ. Sci. Technol., 12:313-317.

Hanel, G. (1987): The role of aerosol properties during the condensational stage of cloud: A reinvestigation of numerics and microphysics, Beitr. Phys. Atmos., 60:321-339.

Hanst, P.L., N.W. Wong, and J. Bragin (1982): A long-path infrared study of Los Angeles smog. Atmos. Environ., 16:969-981.

Hanst, P.L., W.E. Wilson, R.K. Patterson, B. Gay, L.W.Chaney, and C.S. Burton (1975): A spectroscopic study of California smog. U.S. EPA Report EPA 650/4-75-006, Research Triangle Park, North Carolina.

Harman, H.H. (1976): Modern Factor Analysis, 3rd Ed., Rev., University of Chicago Press, Chicago.

Hegg, D.A., and T.V. Larson (1990): The effects of microphysical parametrization on model predictions of sulfate production in clouds, Tellus.

Heintzenberg J., J.A. Ogren, K.J. Noone, and L. Gardneus (1989): The size distribution of submicrometer particles within and about stratocumulus cloud droplets on Mt. Areskutan, Sweden, Atmos. Res., 24:89-101.

Hering, S.V., and D.L. Blumenthal (1989): Southern California Air Quality Study (SCAQS), Description of measurement activities. Final Report to the California Air Resources Board, Sacramento, California.

Hisham, M.W.M., and D. Grosjean (1990): Southern California Air Quality Study: Toxic Air Contaminants, Task 1. Final report to the California Air Resources Board, Agreement A832-152, DGA, Inc., Ventura, California.

Hoffmann, M.R., and J.G. Calvert (1985): Chemical transformation modules for eulerian acid deposition models, Vol. 2, The aqueous-phase chemistry. EPA/600/3-85/017, U.S. EPA, Research Triangle Park, N.C.

Hoffmann, M.R., and D.J. Jacob (1984): Kinetics and mechanisms of the catalytic oxidation of dissolved sulfur dioxide in aqueous solution: An application to nighttime fog water chemistry. SO_2, NO, and NO_2 Oxidation Mechanisms: Atmospheric Considerations, edited by J. G. Calvert. 101-172, Butterworth Publishers.

Hopke, P.K. (1989): Target transformation factor analysis as an aerosol mass apportionment method: A review and sensitivity analysis. Atmos. Environ., 22:1777-1792.

Hopke, P.K., and S. Dharmavaram (1986): Recent improvements to FANTASIA, a Target Transformation Factor Analysis Program. Comput. & Chem., 10:163-164.

Hopke, P.K., D.J. Alpert, and B.A. Roscoe (1983): FANTASIA - A Program for Target Transformation Factor Analysis to Apportion Sources in Environmental Samples. Comput. & Chem., 7:149-155.

Huebert, B.J., and C.H. Robert (1985): The dry deposition of nitric acid to grass. J. Geophys Res., 90:2085-2090.

Jackson, G.A. (1982): Sludge disposal in Southern California Basins. Environ. Sci. Technol., 16:746-757.

Jacob, D.J., and S.C. Wofsy (1988): Photochemistry of biogenic emissions over the Amazon forest. J. Geophys. Res., 93:1477-1486.

Jacob, D.J., F.H. Shair, J.M. Waldman, J.W. Munger, and M.R. Hoffmann (1987): Transport and oxidation of SO_2 in a stagnant foggy valley. Atmos. Environ., 21:1305-1314.

Jacob, D.J., J.W. Munger, J.M. Waldman, and M.R. Hoffman (1986): The H_2SO_4-HNO_3-NH_3 system at high humidities and in fogs 1. Spatial and temporal patterns in the San Joaquin Valley of California, J. Geophys. Res., 91:1073-1088.

Jacob, D.J., J.M. Waldman, M. Haghi, M.R. Hoffmann, and R.C. Flagan (1985): Instrument to collect fogwater for chemical analysis. Rev. Sci. Inst., 56:1291-1293.

Jacob, D.J., J.M. Waldman, J.W. Munger, and M.R. Hoffmann (1984): A field investigation of physical and chemical mechanisms affecting pollutant concentrations in fog droplets. Tellus, 36B:272-285.

Jacob, D.J., R.-F.T. Wang, and R.C. Flagan (1984): Fogwater collector design and characterization. Environ. Sci. Technol., 18:827-833.

Jensen, J.B., and R.J. Charlson (1984): On the efficiency of nucleation scavenging. Tellus, 36B:367-375.

Kawamura K., L.L. Ng, and I.R. Kaplan (1985): Determination of organic acids (C1=C10) in the atmosphere, motor exhaust and engine oil. Environ. Sci. Technol., 19:1082-1086.

Keene, W.C., J.N. Galloway, and J.D. Holden, Jr. (1983): Measurement of weak organic acidity in precipitation from remote areas of the world. J. Geophys. Res., 88:5122-5130.

Kelly, T.J., S.E. Schwartz, and P.H. Daum (1989): Detectability of acid producing reactions in natural clouds. Atmos. Environ., 23:569-583.

Kelly, T.J., P.H. Daum, and S.E. Schwartz (1985): Measurements of peroxides in cloudwater and rain. J. Geophys. Res., 90:7861-7871.

Liljestrand, H.M. (1985): Average rainwater pH, concepts of atmospheric acidity, and buffering in open systems. Atmos. Environ., 19:487-499.

Luria, M., and H. Sievering (1991): Heterogeneous and Homogeneous Oxidation of SO_2 in the remote marine atmosphere. Atmos. Environ., 25:1489-1496.

Malm, W.C., C.E. Johnson, and J.F. Bresch (1986): Application of Principal Component Analysis for Purposes of Identifying Source-Receptor Relationships. In Receptor Methods for Source Apportionment, T.G. Pace, Ed., Air Pollution Control Association, Pittsburgh, PA, pp. 127-148.

Martell, A.E, and R.M. Smith (1977): Critical Stability Constants Vol. 3: Other Organic Ligands. Plenum Press, New York.

Martin, L.R. (1984): Kinetic studies of sulfite oxidation in aqueous solution. SO_2, NO and NO_2 Oxidation Mechanisms: Atmospheric Considerations. Edited by J. G. Calvert, pp. 63-100, Butterworth, Stoneham, Massachusetts.

Martin, L.R., and Hill M.W. (1987): The iron catalyzed oxidation of sulfur: Reconciliation of the literature rates. Atmos. Environ., 21:1487-1490.

McRae, G.J., W.R. Goodin, and J.H. Seinfeld (1982): Development of a second generation mathematical model for urban air pollution, I, Model formulation. Atmos. Environ., 16:679-696.

Munger, J.W., J. Collett Jr, B. Daube Jr., and M.R. Hoffmann (1990): Fogwater chemistry at Riverside, California. Atmos. Environ., 24B:185-205.

Munger, J.W., J. Collett Jr., B. Daube Jr., and M.R. Hoffmann (1989): Chemical composition of coastal stratus clouds: Dependence on droplet size and distance from the coast. Atmos. Environ., 23:2305-2320.

Munger, J.W., J. Collett, Jr., B.C. Dauke, Jr., and M.R. Hoffmann (1989): Carboxylic acids and carbonyl compounds in southern California clouds and fogs. Tellus, 41B:230-242.

Munger, J.W., C. Tiller, and M.R. Hoffmann (1986): Identification of hydroxymethanesulfonate in fog water. Science, 231:247-249.

Munger, J.W., D.J. Jacob, and M.R. Hoffmann (1984): The occurrence of bisulfite-aldehyde addition products in fog- and cloudwater. J. Atmos. Chem., 1:335-350.

Munger, J.W., D.J. Jacob, J.M. Waldman, and M.R. Hoffmann (1983): Fogwater chemistry in an urban atmosphere. J. Geophys. Res., 88:5109-5121.

Noone, K.J., R.J. Charlson, D.S. Covert, J.A. Ogren, and J. Heintzenberg (1988): Cloud droplets: solute concentration is size dependent. J. Geophys. Res., 93:9477-9482.

Ogren, J.A., J. Heintzenberg, A. Zuber, K.J. Noone, and R.J. Charlson (1989): Measurements of the size-dependence of solute concentrations in cloud droplets. Tellus, 41B:24-31.

Pandis, S.N., J.H. Seinfeld, and C. Pilinis (1990): The smog-fog-smog cycle and acid deposition. J. Geophys. Res., 95:18,489-18,500.

Pandis, S.N., J.H. Seinfeld, and C. Pilinis (1990a): Chemical composition differences in fog and cloud droplets of different sizes. Atmos. Environ., 24A:1957-1969.

Pandis, S.N., and J.H. Seinfeld (1989a): Sensitivity analysis of a chemical mechanism for aqueous-phase atmospheric chemistry. J. Geophys. Res., 94:1105-1126.

Pandis, S.N., and J.H. Seinfeld (1989b): Mathematical modeling of acid deposition due to radiation fog. J. Geophys. Res., 94:12,911-12,923.

Pierson, W.R., and W.W. Brachaczek (1990): Dew chemistry and acid deposition in Glendora, California, during the 1986 carbonaceous species methods comparison study. Aerosol Sci. Technol., 12:8-27.

Pilinis, C. (1989): Numerical simulation of visibility degradation due to particulate matter: Model development and evaluation. J. Geophys. Res., 9937-9946.

Pilinis, C., and J.H. Seinfeld (1988): Development and evaluation of an Eulerian photochemical gas-aerosol model. Atmos. Environ., 22:1985-2001.

Pilinis, C., and J.H. Seinfeld (1987): Continued development of a general equilibrium model for inorganic multicomponent aerosols. Atmos. Environ., 21:2453-2466.

Pilinis, C., J.H. Seinfeld, and C. Seigneur (1987): Mathematical modeling of the dynamics of multicomponent atmospheric aerosols. Atmos. Environ., 21:943-955.

Pruppacher, H.R., and J.D. Klett (1980): Microphysics of clouds and precipitation. Reidel Pub. Co., The Netherlands.

Purdue, E.M., and K.C. Beck (1988): Chemical consequences of mixing atmospheric droplets of varied pH. J. Geophys. Res., 93:691-698.

Richards, L.W., J.A. Anderson, D.L. Blumenthal, J.A. McDonald, G.L. Kok, and A.L. Lazrus (1983): Hydrogen peroxide and sulfur(IV) in Los Angeles cloud water. Atmos. Environ., 17:911-914.

Roscoe, B.A., P.K. Hopke, S.L. Dattner, and J.M. Jenks (1982): The use of principal components factor analysis to interpret particulate compositional data sets. J. Air Pollut. Control Assoc., 32:637-642.

Russell, A.G., and G.R. Cass (1986): Verification of a mathematical model for aerosol nitrate and nitric acid formation and its use for control measure evaluation. Atmos. Environ., 20:2011-2026.

Russell, A.G., and G.R. Cass (1984): Acquisition of regional air quality model validation data for nitrate, sulfate, ammonium ion and their precursors. Atmos. Environ., 18:1815-1827.

Russell, A.G., G.J. McRae, and G.R. Cass (1983): Mathematical modeling of the formation and transport of ammonium nitrate aerosol. *Atmos. Environ.*, 17:949-964.

Schwartz, S.E. (1989): Acid deposition: Unraveling a regional phenomenon. Science, 243:753-762.

Schwartz, S E. (1986): Mass transport considerations pertinent to aqueous phase reactions of gases in liquid water clouds. In Chemistry of Multiphase Atmospheric Systems, edited by W. Jaeschke, pp. 415-471, Springer, New York.

Seinfeld, J H. (1986): Atmospheric chemistry and physics of air pollution. John Wiley, New York.

Shikiya, D., C. Liu, E. Nelson, and R. Rapaport (1987): The magnitude of ambient air toxics impact from existing sources in the South Coast Air Basin. Revision Working Paper No. 3, Planning Division, South Coast Air Quality Management District, El Monte, California

Sievering, H., J. Boatman, J. Galloway, W. Keene, Y. Kim, M. Luria, and J. Ray (1991): Heterogeneous sulfur conversion in sea-salt aerosol particles: The role of aerosol water content and size distribution. Atmos. Environ., 25A:1479-1487.

Smith, R.M., and A.E. Martell (1976): Critical stability constants, Vol. 4: Inorganic complexes. Plenum Press, New York.

South Coast Air Quality Management District (1984): Acid deposition in the South Coast Air Basin: An assessment. South Coast Air Quality Management District, El Monte, California.

Su, F., J.G. Calvert, and J.H. Shaw (1979): An FTIR spectroscopic study of the ozone-ethene reaction mechanism in O_2-rich mixtures. J. Phys. Chem., 83:3185-3190.

Talbot, R.W., K.M. Beecher, R.C. Harris, and W.R. Cofer III (1988): Atmospheric geochemistry of formic and acetic acids at a midlatitude temperate site. J. Geophys. Res., 93:1638-1652.

Ten Brink, H.M., S.E. Schwartz, and P.H. Daum (1987): Efficient scavenging of aerosol sulfate by liquid water clouds. Atmos. Environ., 21, 9:2035-2052.

Tuazon, E.C., A.M. Winer, and J.N. Pitts, Jr. (1981): Trace pollutant concentrations in a multiday smog episode in the California South Coast Air Basin by long pathlength Fourier transform infrared spectroscopy. Environ. Sci. Technol., 15:1232-1237.

Tuazon, E.C., R. A. Graham, A.M. Winer, R.R. Easton, J.N. Pitts, Jr., and P.L. Hanst (1978): A kilometer pathlength Fourier-transform infrared system for the study of trace pollutants in ambient and synthetic atmospheres. Atmos. Environ., 12:865-875.

Veyret, B., J.C. Rayez, and R. Lesclaux (1982): Mechanism of the photooxidation of formaldehyde studied by flash photolysis of CH2O-O2-NO mixtures.

Waldman, J.M. (1986): Depositional aspects of fogs and clouds, Ph.D. thesis, California Institute of Technology, Pasadena, California.

Waldman, J M. (1986): Depositional aspects of pollutant behavior in fog. Ph.D. thesis, California Institute of Technology, Pasadena, California.

Wall, S.M., W. John, and J.L. Ondo (1988): Measurement of aerosol size distributions for nitrate and major ionic species. Atmos. Environ., 22:1649-1656.

Warren, D.R., and J.H. Seinfeld (1985): Simulation of aerosol size-distribution evolution in systems with simultaneous nucleation, condensation and coagulation. Aerosol Sci. Technol., 4:31-43.

Wilkins, E.T. (1954): Air pollution aspects of the London fog of December 1952. J. R. Meteorol. Soc., 80:267-278.

Winiwarter, W., H. Puxbaum, S. Fuzzi, M.C. Facchini, G. Orsi, N. Beltz, K. Enderle, and W. Jaeschke (1988): Organic acid gas and liquid measurements in Po Valley fall-winter conditions in the presence of fog. Tellus, 40B:348-357.

Zeng, Y., and P.K. Hopke (1989): A study of the sources of acid precipitation in Ontario, Canada. Atmos. Environ., 23:1499-1509.

Appendix A.1

TRAJECTORIES STARTING AT LONG BEACH FROM AUGUST 27, 1987, 0000 PST-AUGUST 28, 1987, 2300 PST

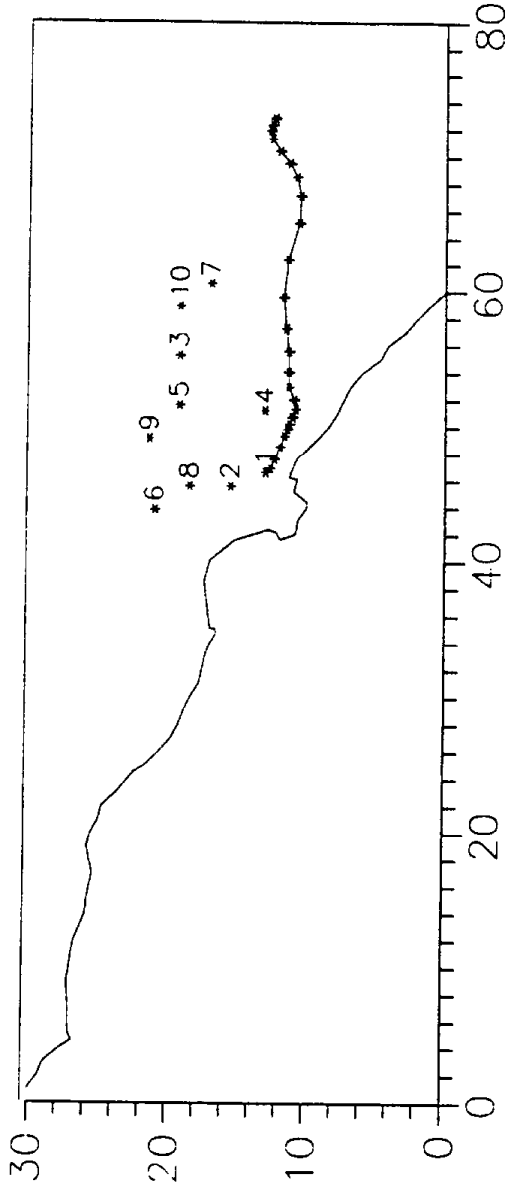

FIGURE 2.2.1. Trajectory starting at Long Beach on August 27, 1987, 0000 PST.

FIGURE 2.2.2. Trajectory starting at Long Beach on August 27, 1987, 0100 PST.

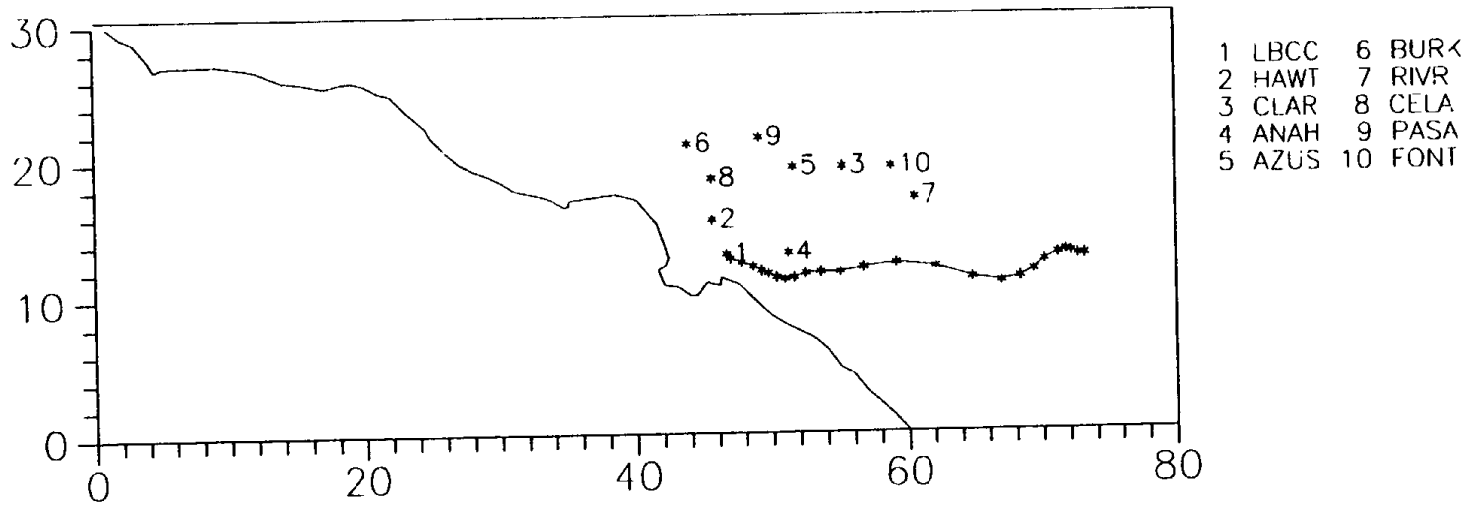

FIGURE 2.2.3. Trajectory starting at Long Beach on August 27, 1987, 0200 PST.

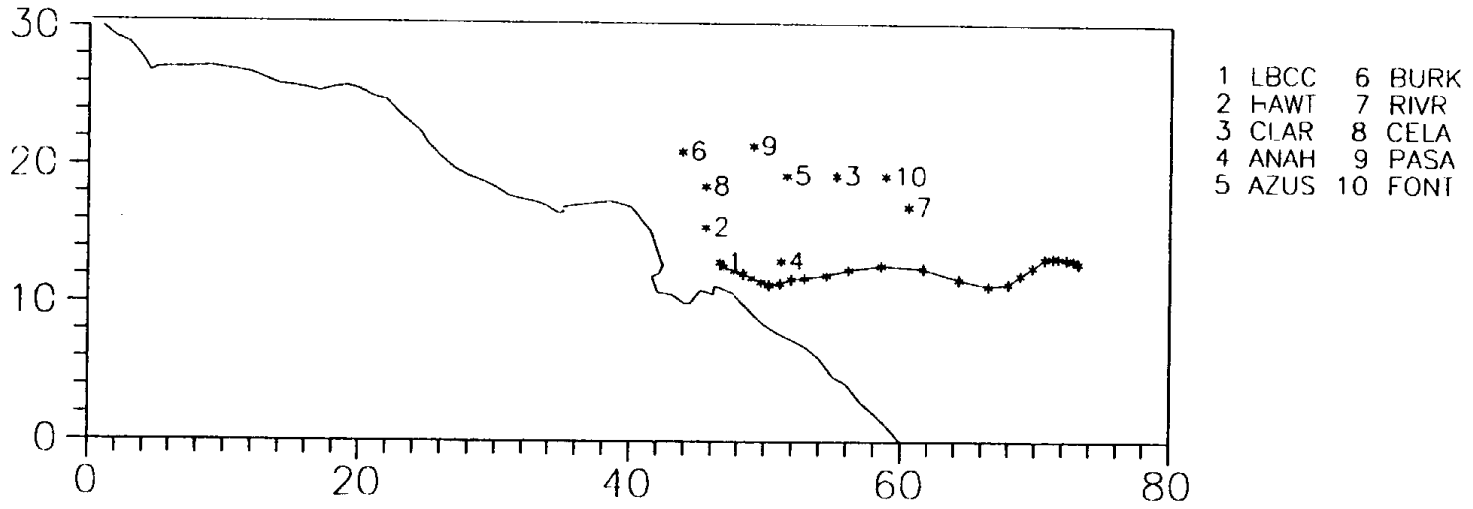

FIGURE 2.2.4. Trajectory starting at Long Beach on August 27, 1987, 0300 PST.

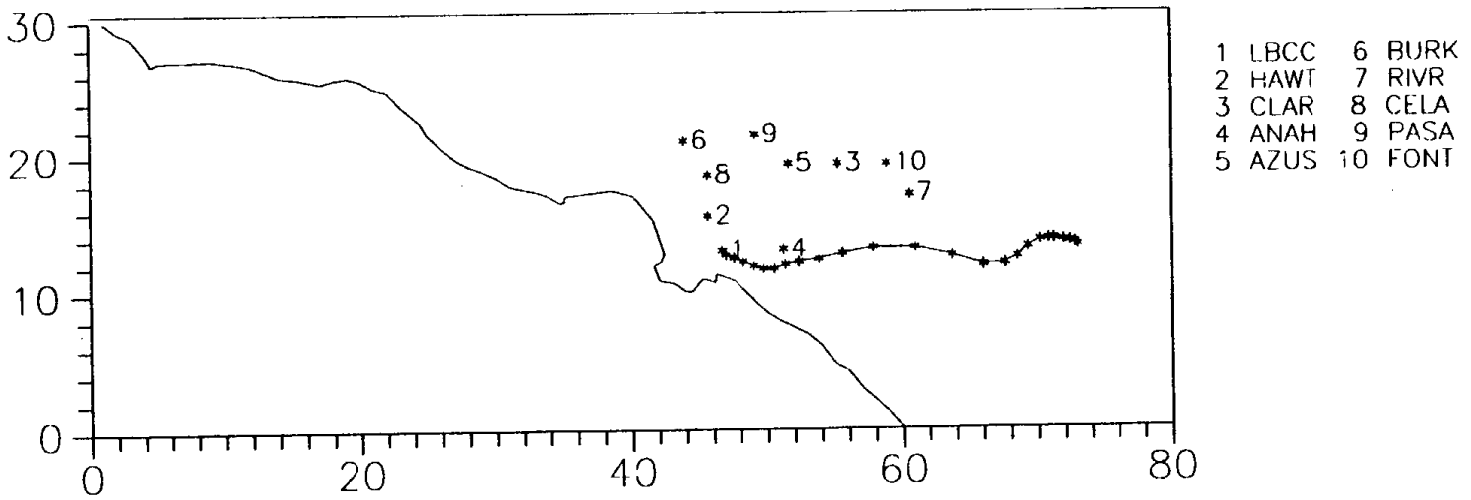

FIGURE 2.2.5. Trajectory starting at Long Beach on August 27, 1987, 0400 PST.

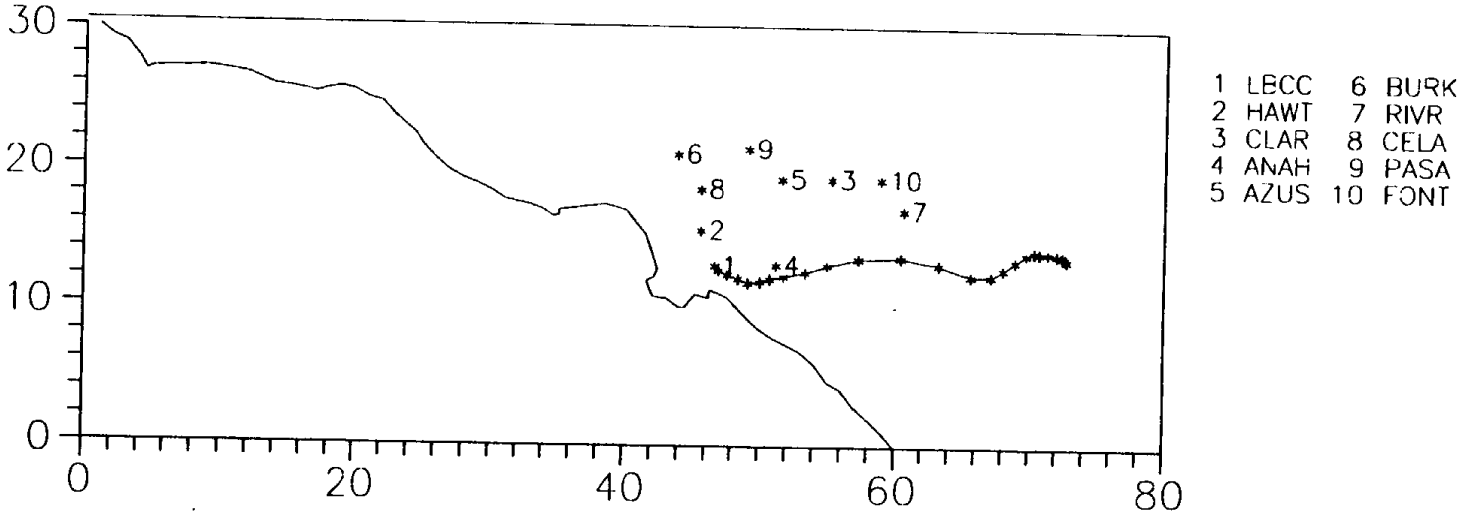

FIGURE 2.2.6. Trajectory starting at Long Beach on August 27, 1987, 0500 PST.

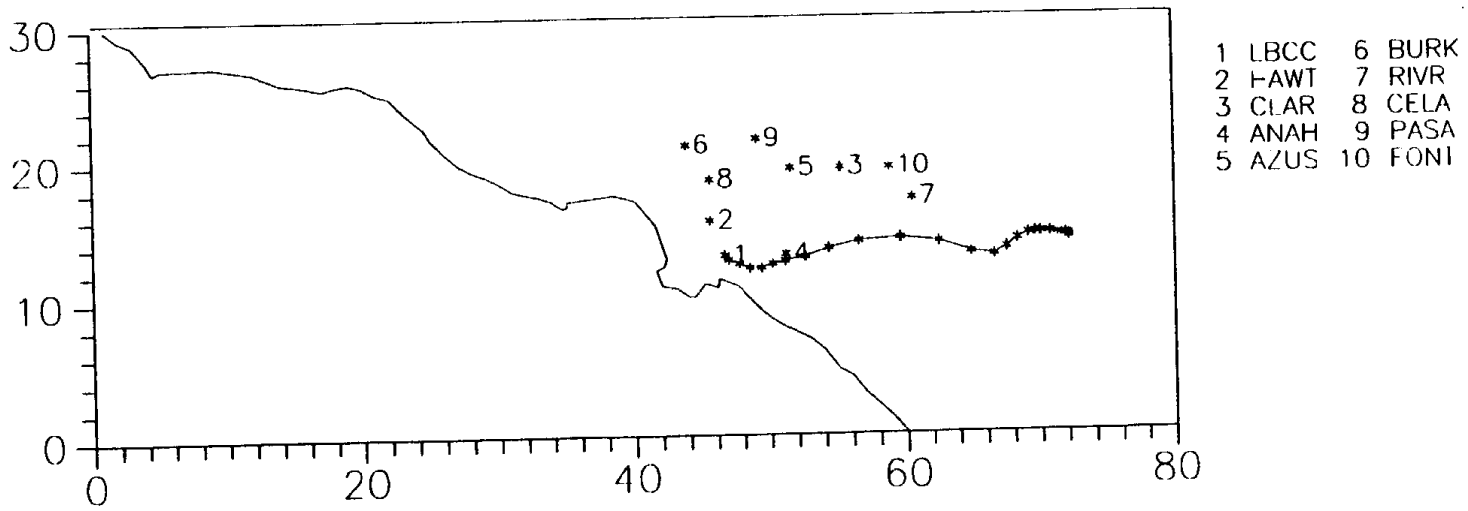

FIGURE 2.2.7. Trajectory starting at Long Beach on August 27, 1987, 0600 PST.

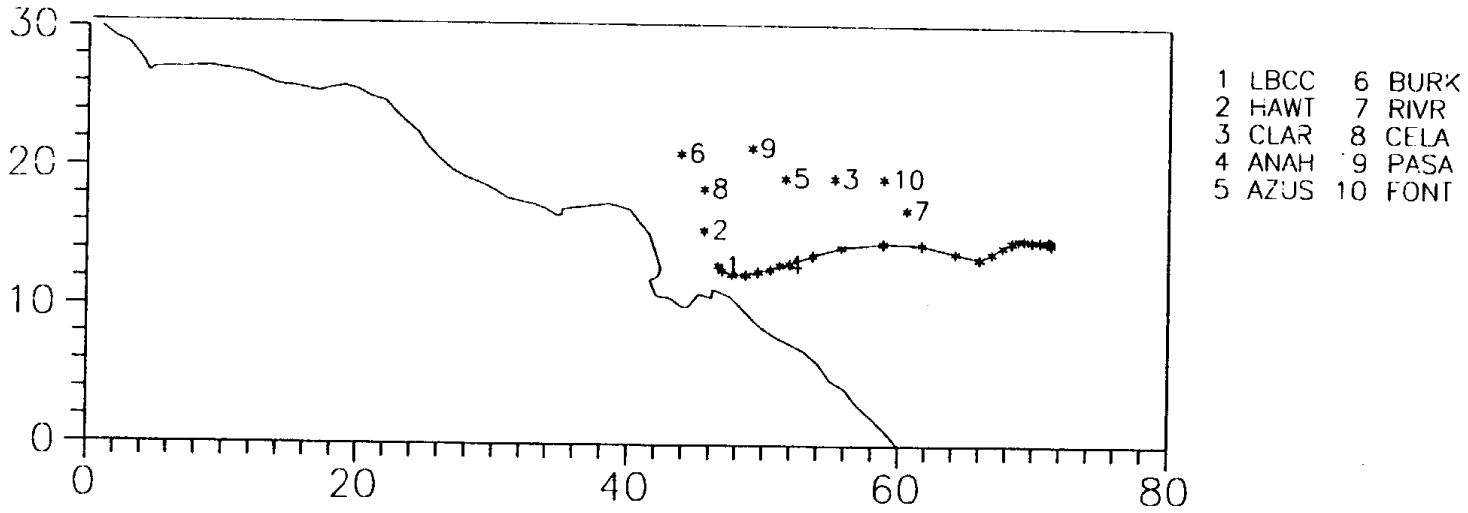

FIGURE 2.2.8. Trajectory starting at Long Beach on August 27, 1987, 0700 PST.

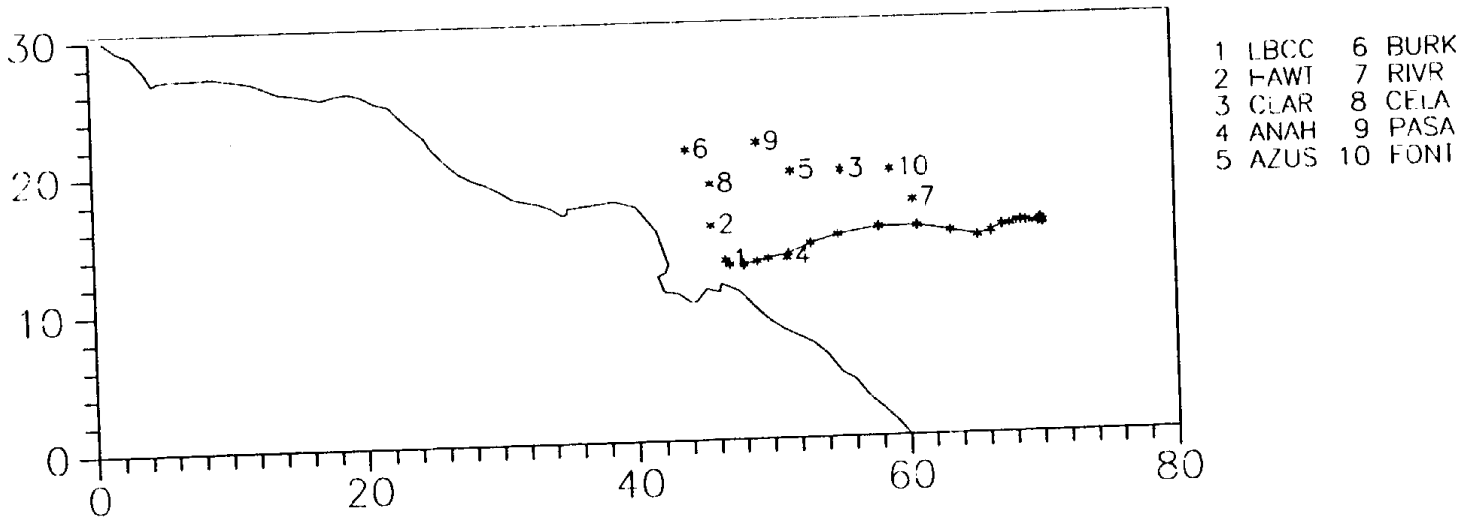

FIGURE 2.2.9. Trajectory starting at Long Beach on August 27, 1987, 0800 PST.

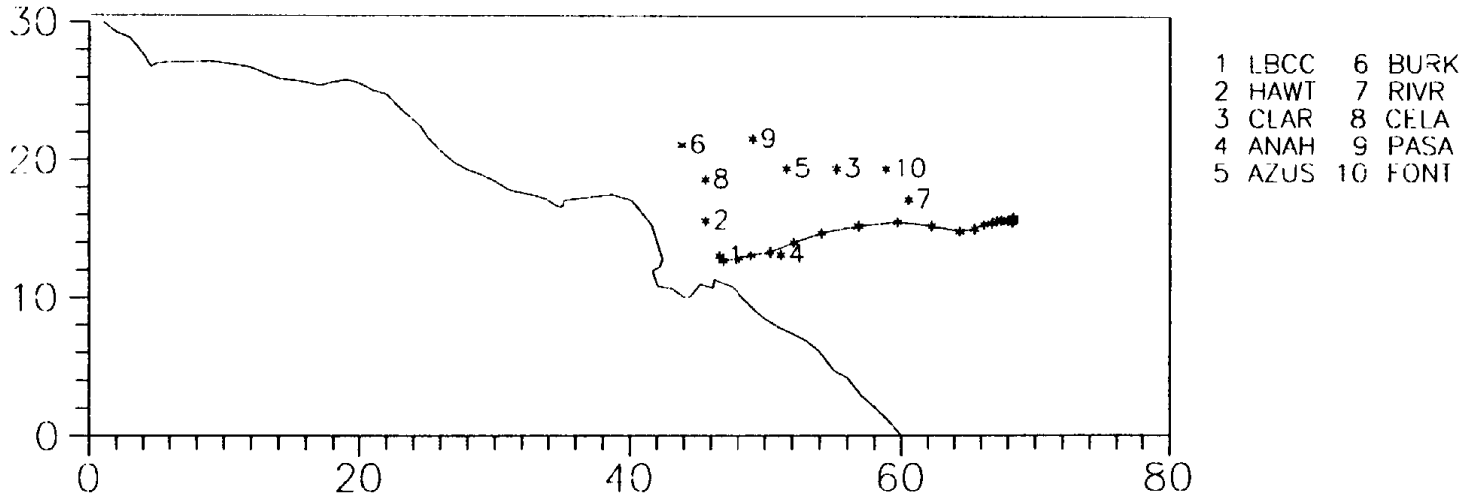

FIGURE 2.2.10. Trajectory starting at Long Beach on August 27, 1987, 0900 PST.

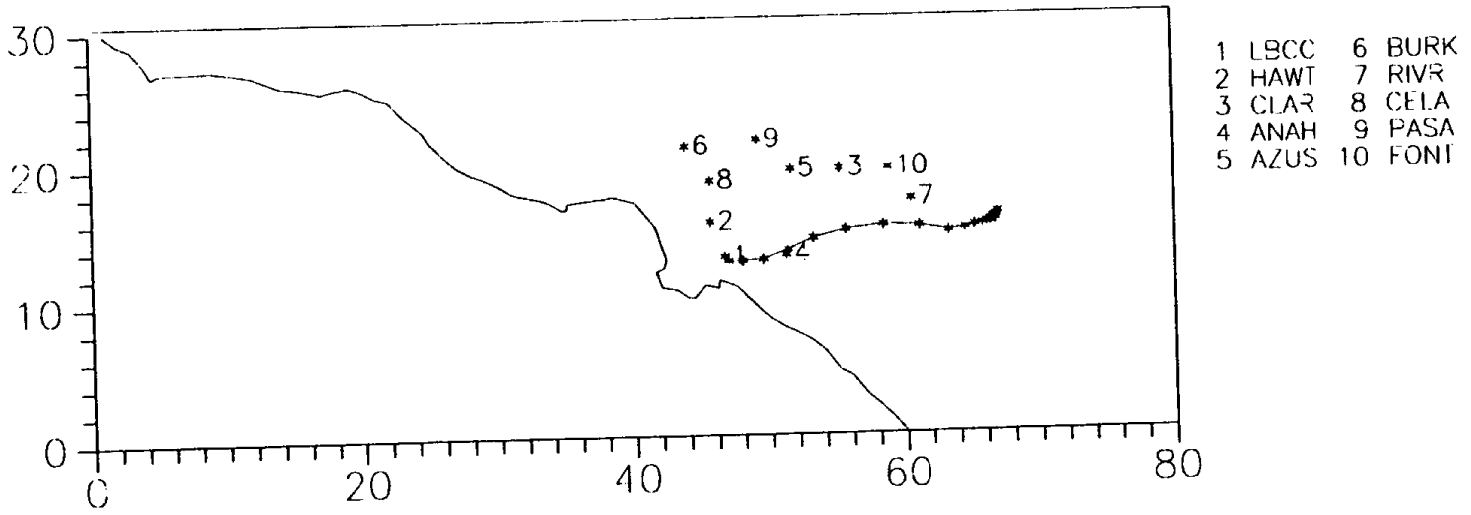

FIGURE 2.2.11. Trajectory starting at Long Beach on August 27, 1987, 1000 PST.

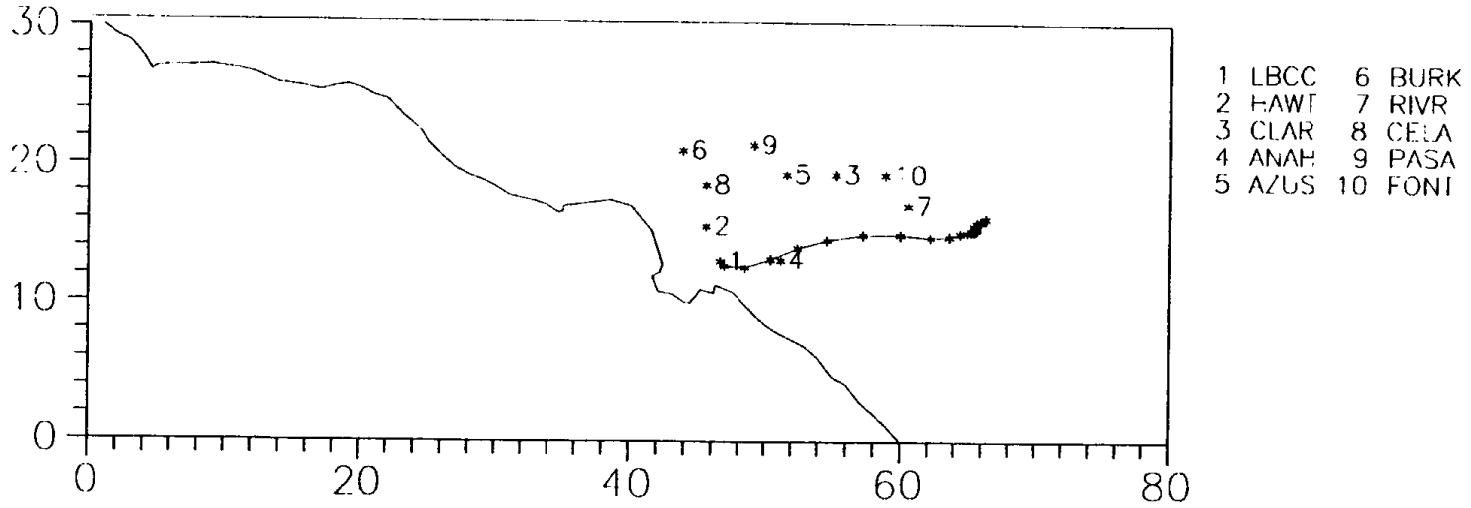

FIGURE 2.2.12. Trajectory starting at Long Beach on August 27, 1987, 1100 PST.

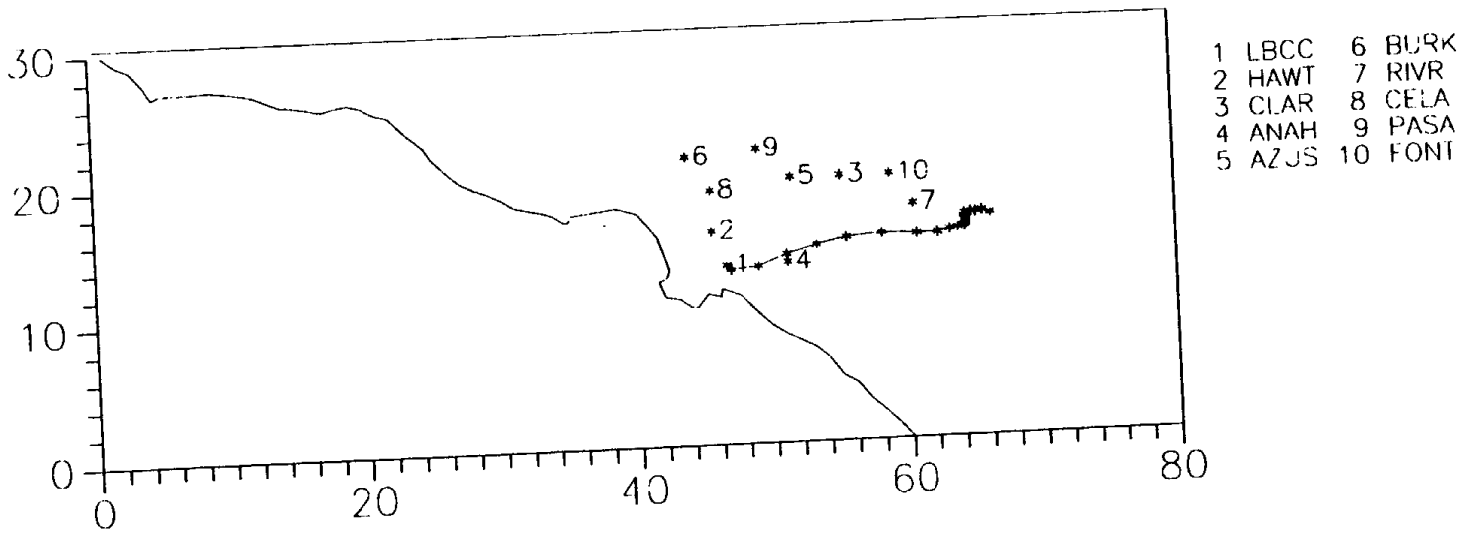

FIGURE 2.2.13. Trajectory starting at Long Beach on August 27, 1987, 1200 PST.

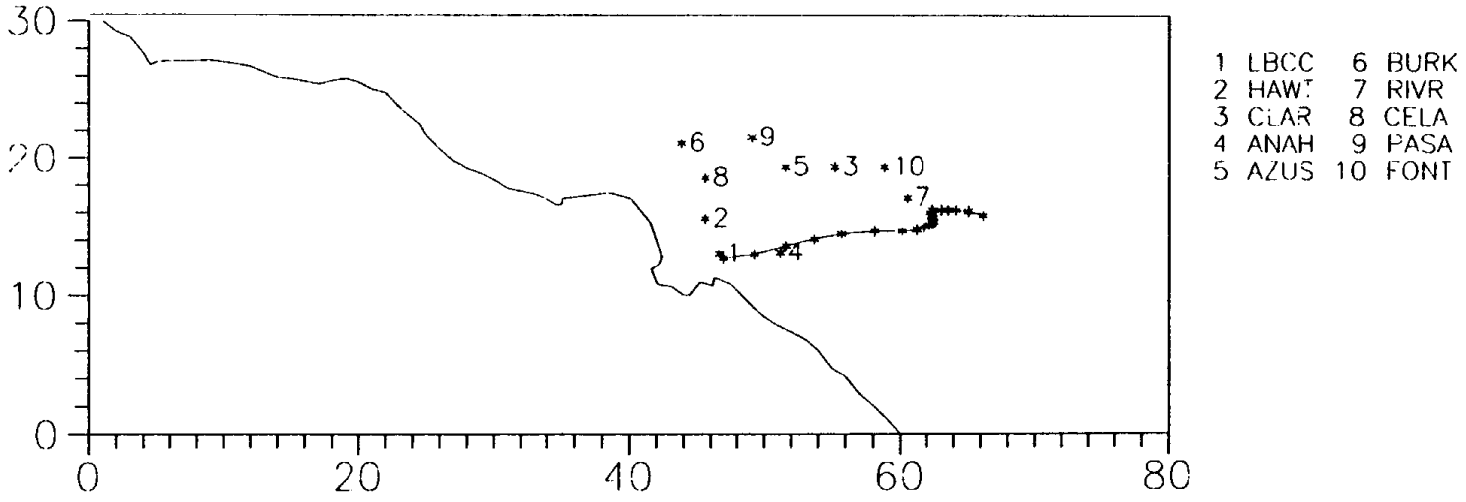

FIGURE 2.2.14. Trajectory starting at Long Beach on August 27, 1987, 1300 PST.

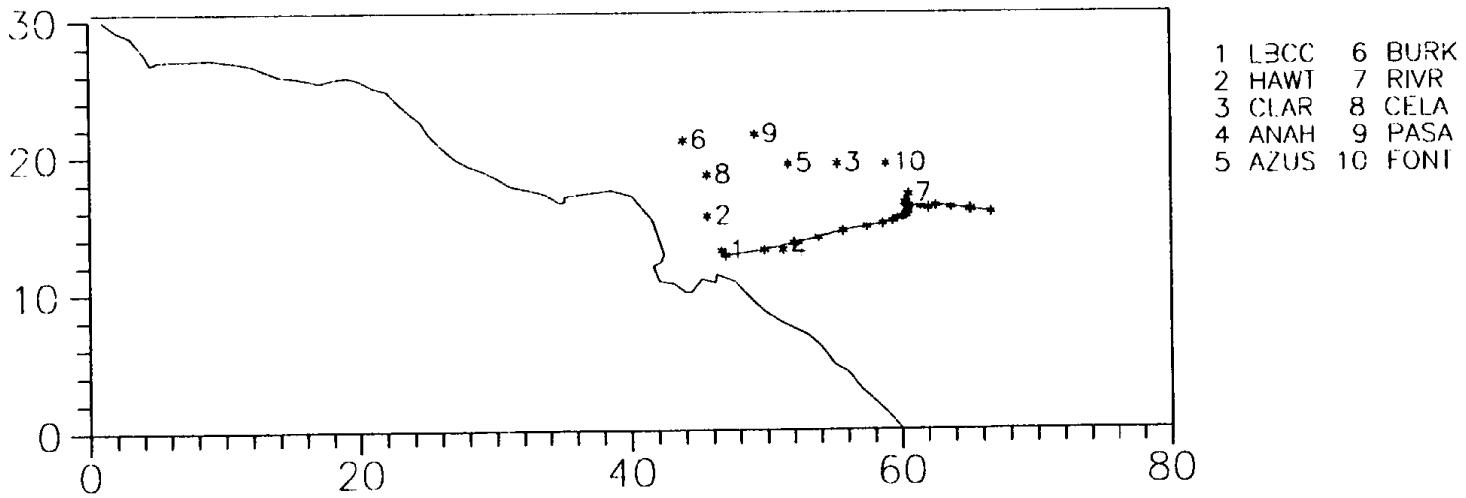

FIGURE 2.2.15. Trajectory starting at Long Beach on August 27, 1987, 1400 PST.

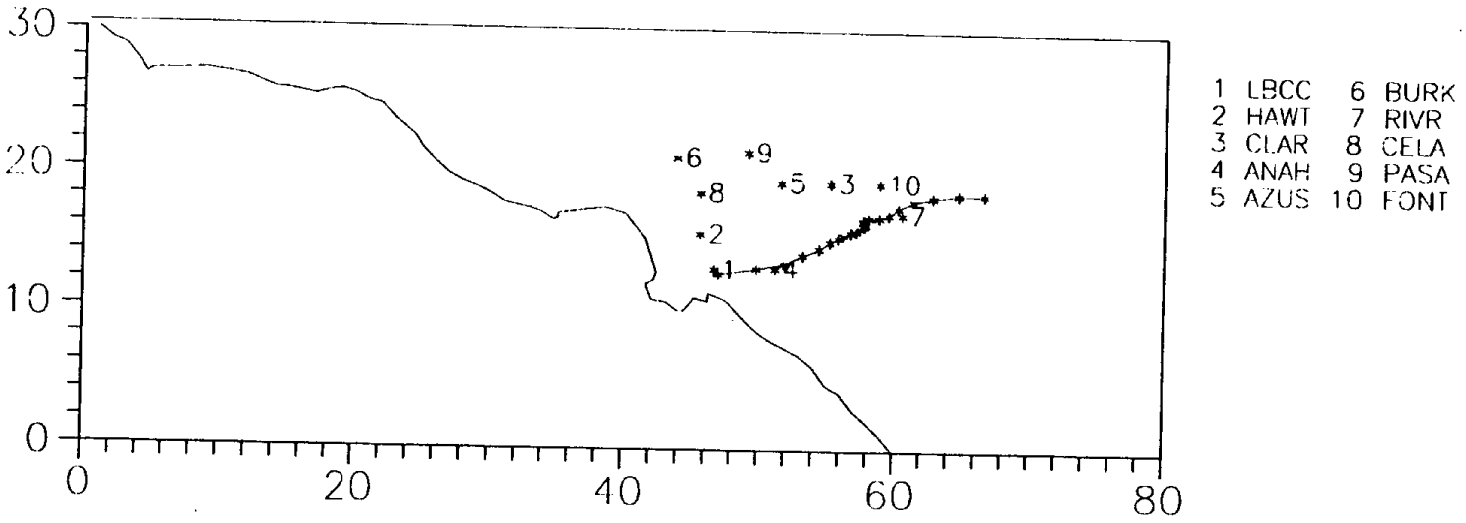

FIGURE 2.2.16. Trajectory starting at Long Beach on August 27, 1987, 1500 PST.

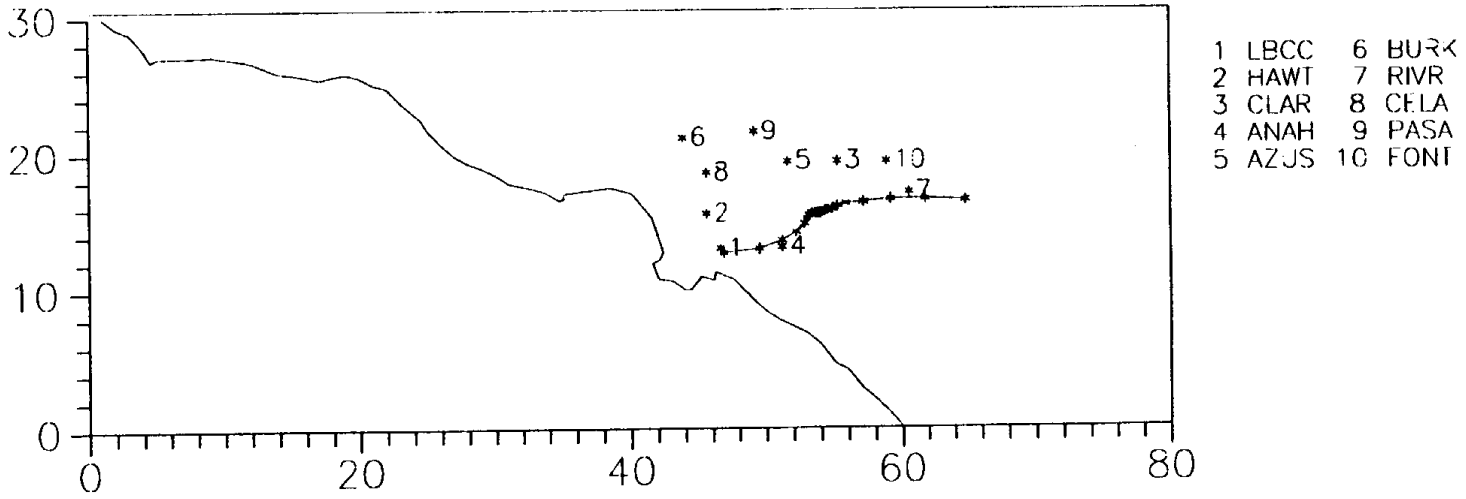

FIGURE 2.2.17. Trajectory starting at Long Beach on August 27, 1987, 1600 PST.

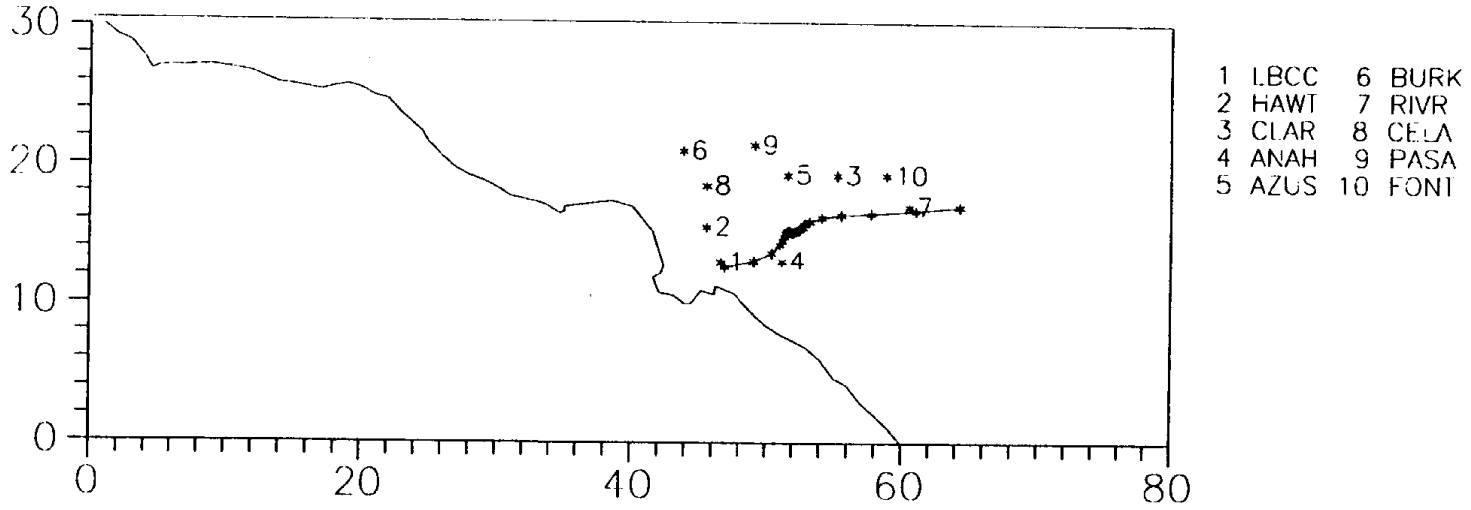

FIGURE 2.2.18. Trajectory starting at Long Beach on August 27, 1987, 1700 PST.

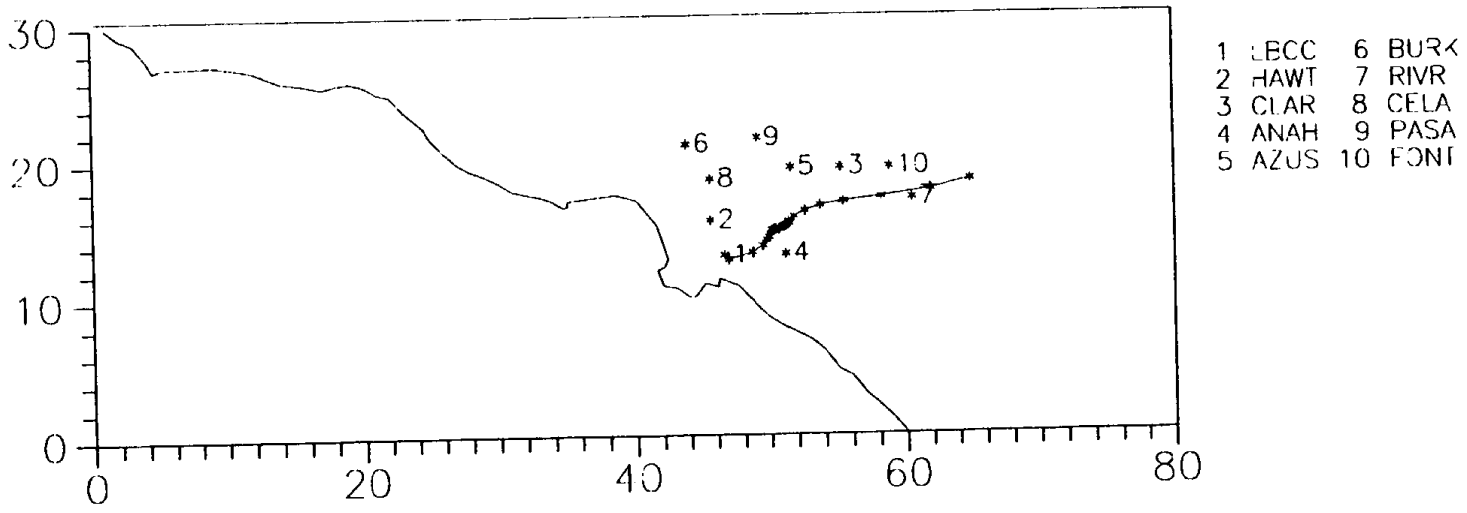

FIGURE 2.2.19. Trajectory starting at Long Beach on August 27, 1987, 1800 PST.

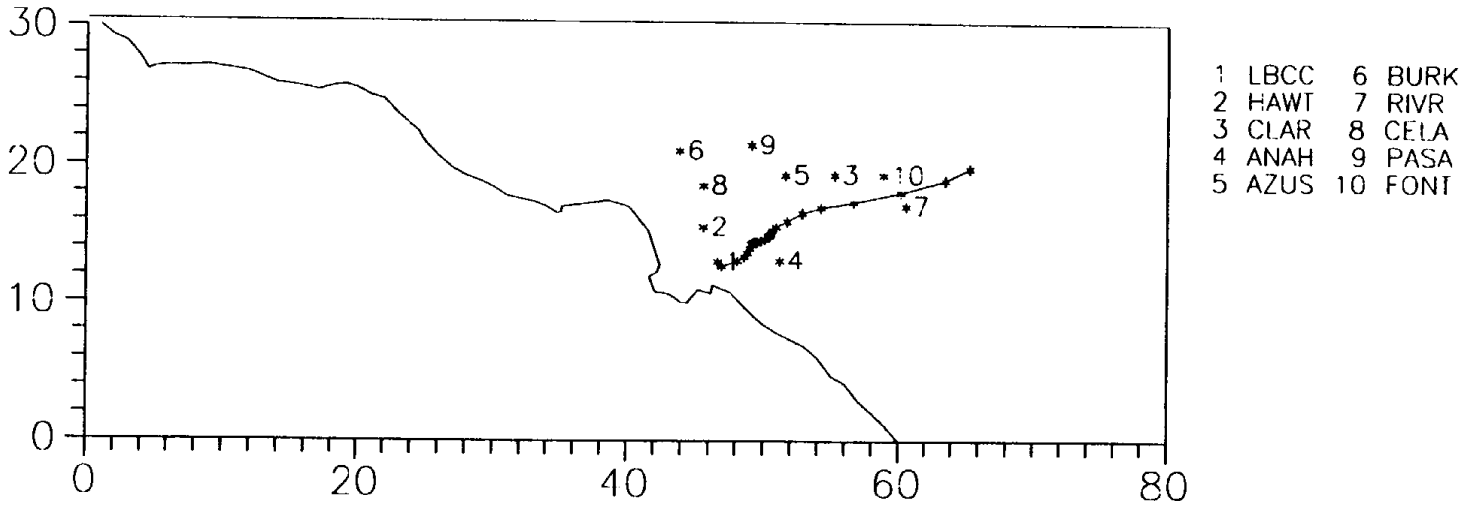

FIGURE 2.2.20. Trajectory starting at Long Beach on August 27, 1987, 1900 PST.

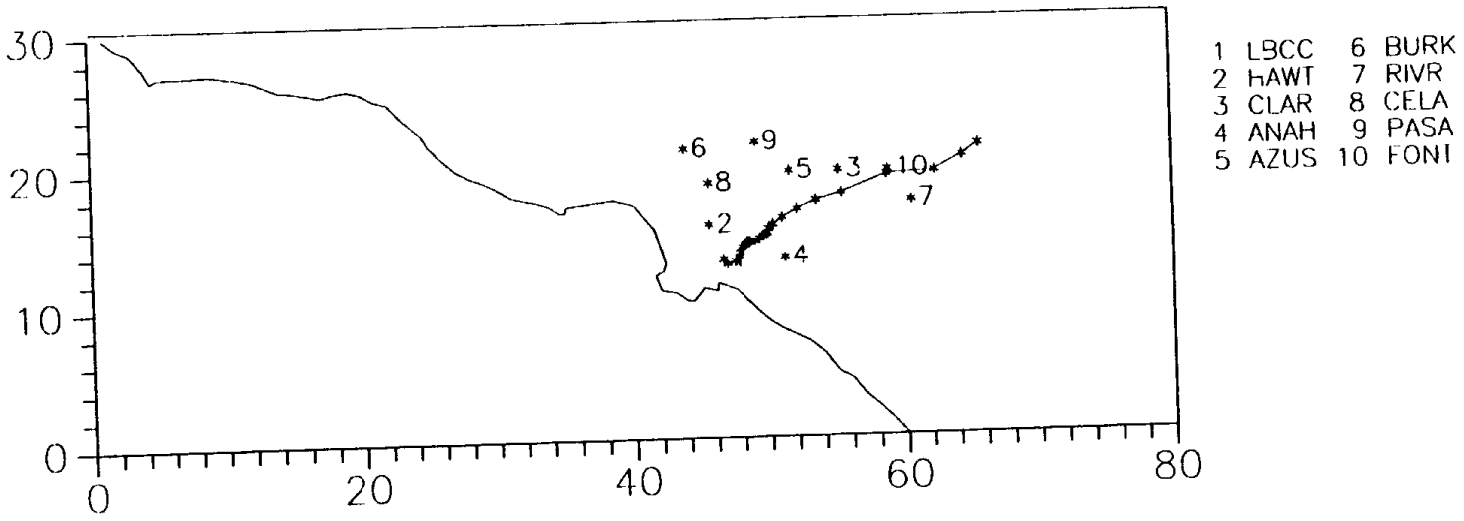

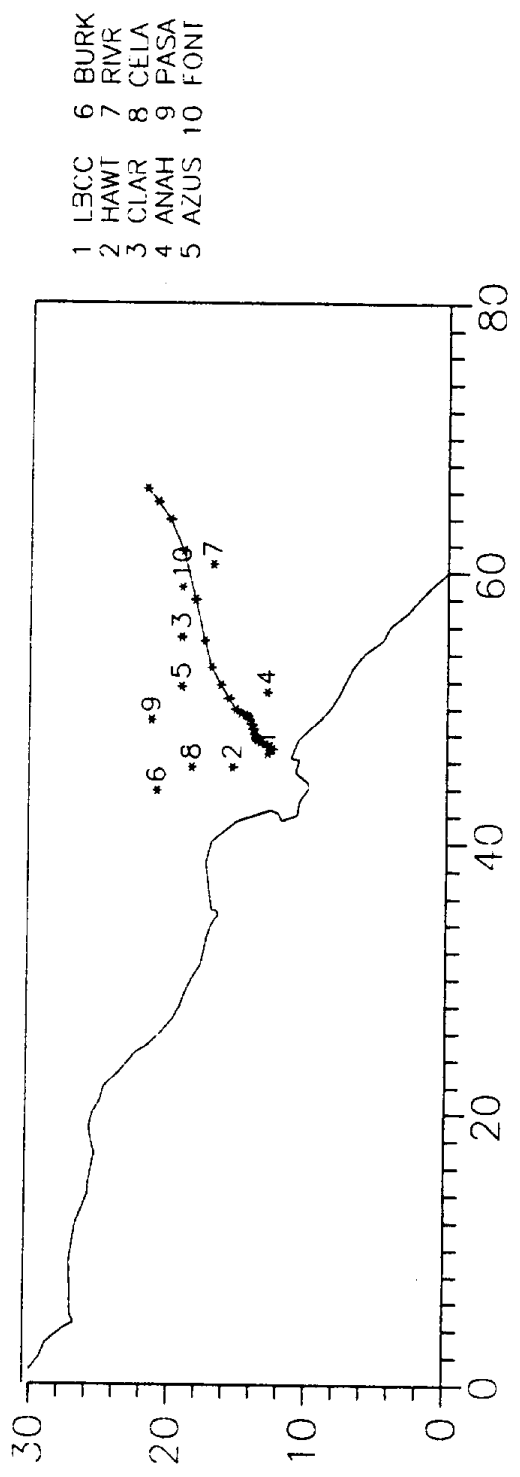

FIGURE 2.2.21. Trajectory starting at Long Beach on August 27, 1987, 2000 PST.

FIGURE 2.2.22. Trajectory starting at Long Beach on August 27, 1987, 2100 PST.

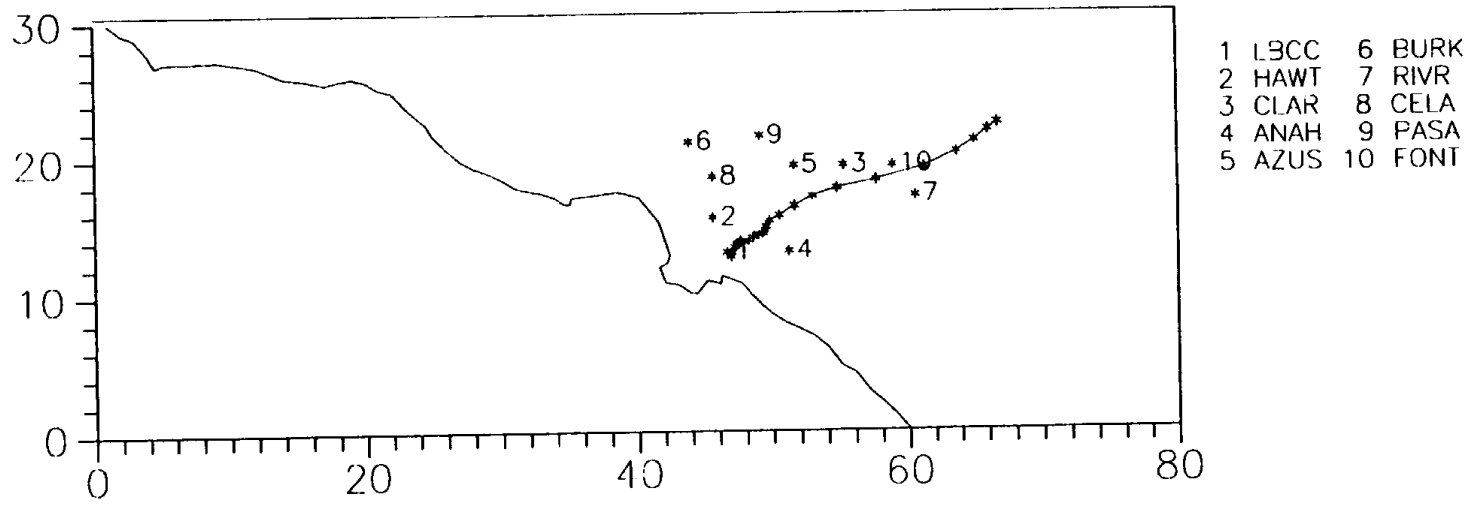

FIGURE 2.2.23. Trajectory starting at Long Beach on August 27, 1987, 2200 PST.

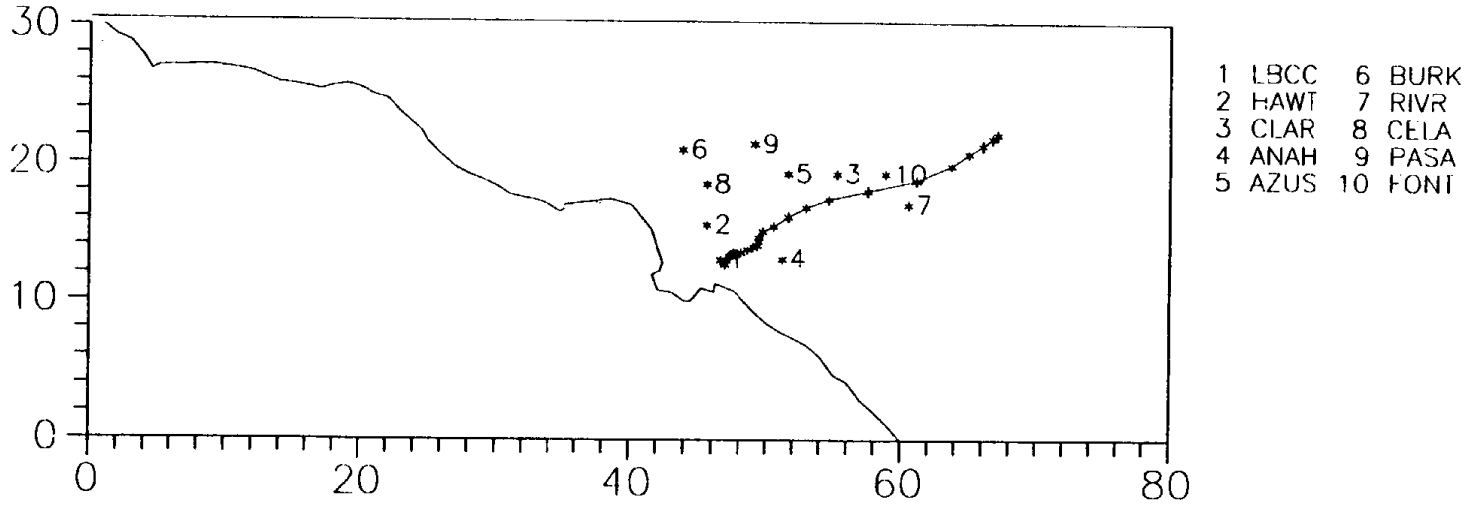

FIGURE 2.2.24. Trajectory starting at Long Beach on August 27, 1987, 2300 PST.

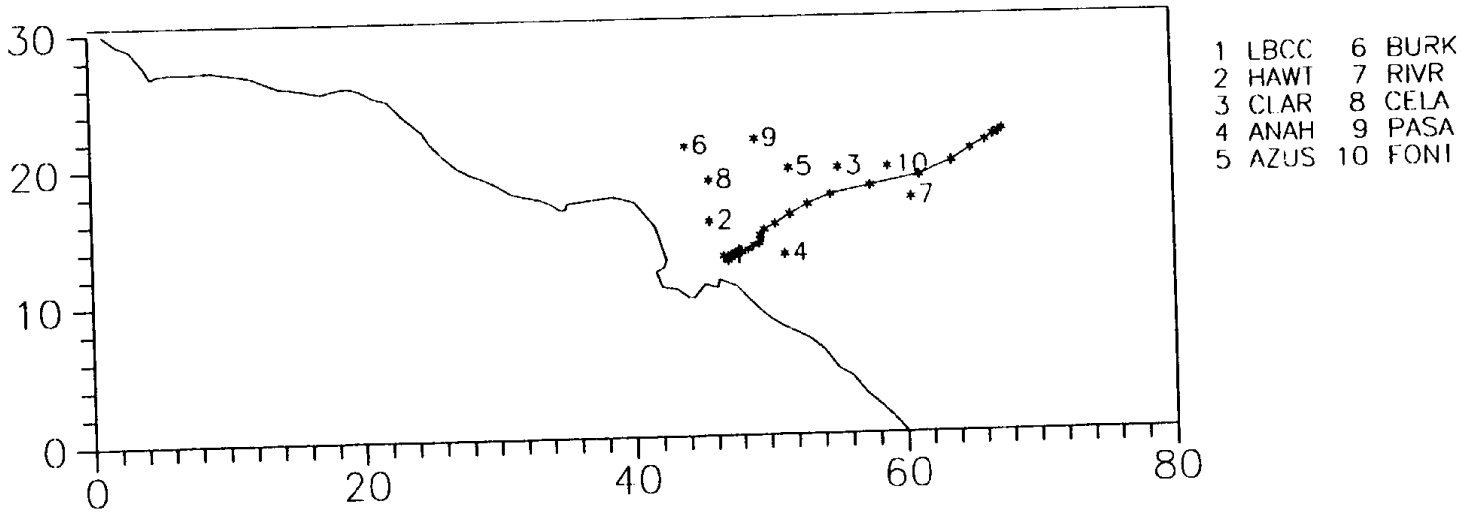

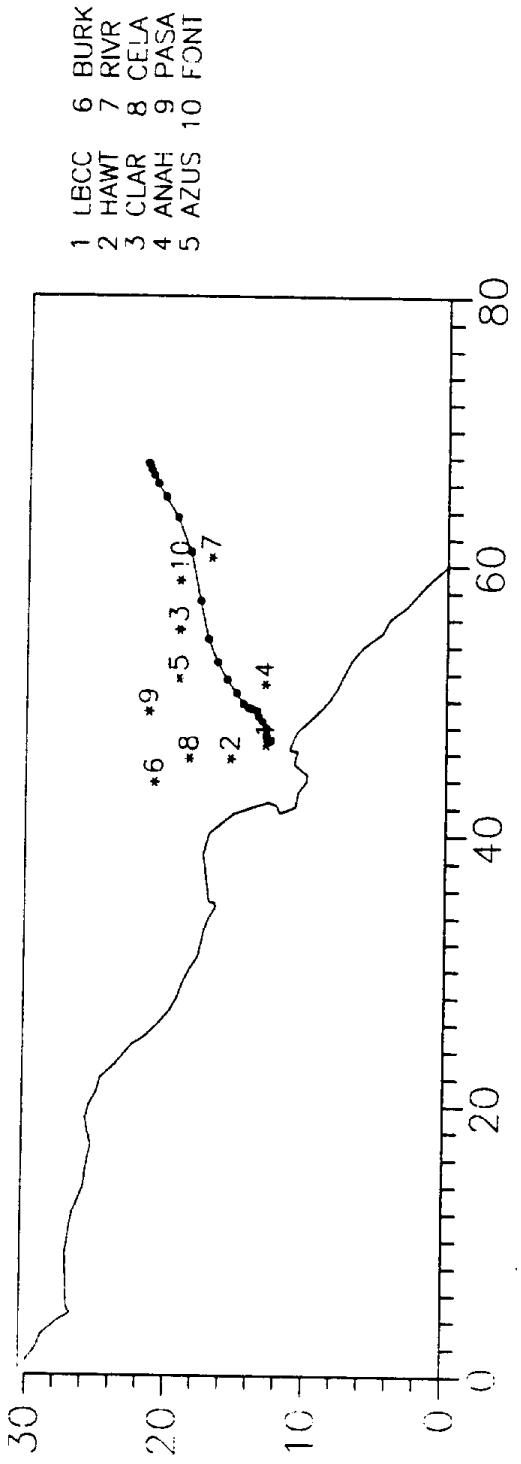

FIGURE 2.2.25. Trajectory starting at Long Beach on August 28, 1987, 0000 PST.

FIGURE 2.2.26. Trajectory starting at Long Beach on August 28, 1987, 0100 PST.

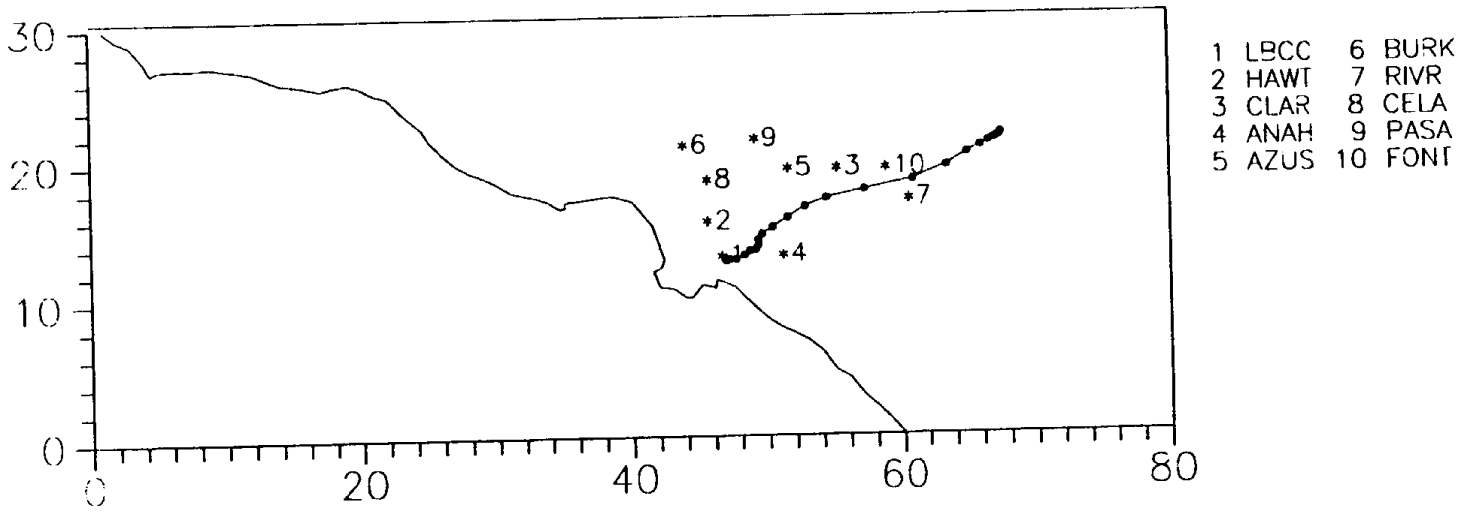

FIGURE 2.2.27. Trajectory starting at Long Beach on August 28, 1987, 0200 PST.

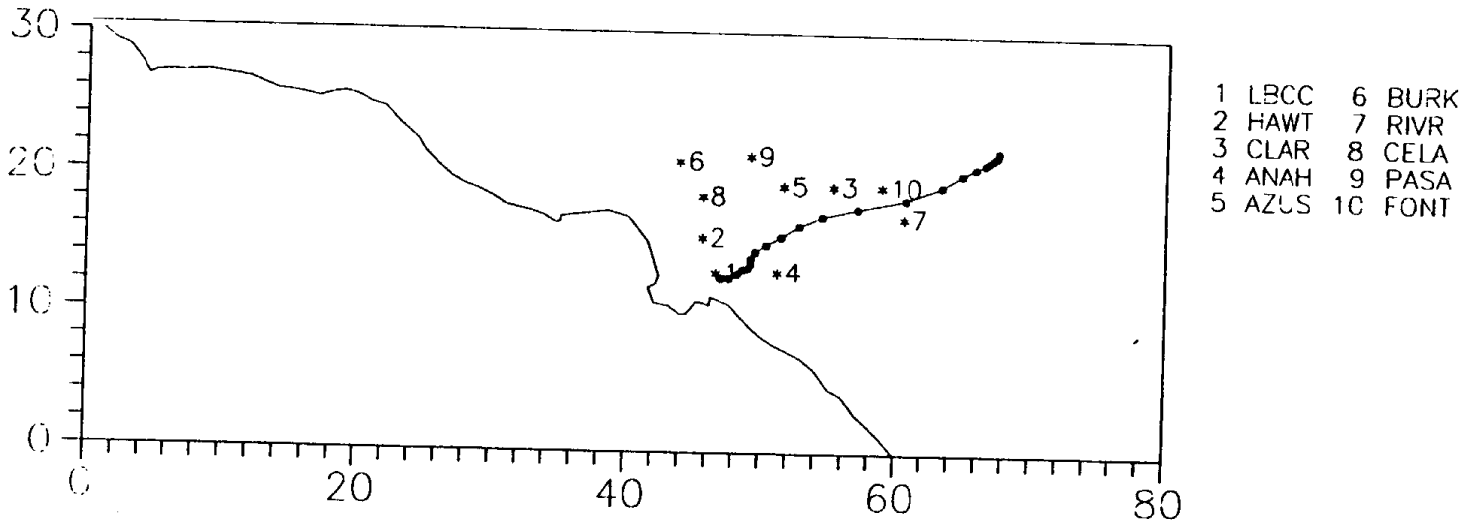

FIGURE 2.2.28. Trajectory starting at Long Beach on August 28, 1987, 0300 PST.

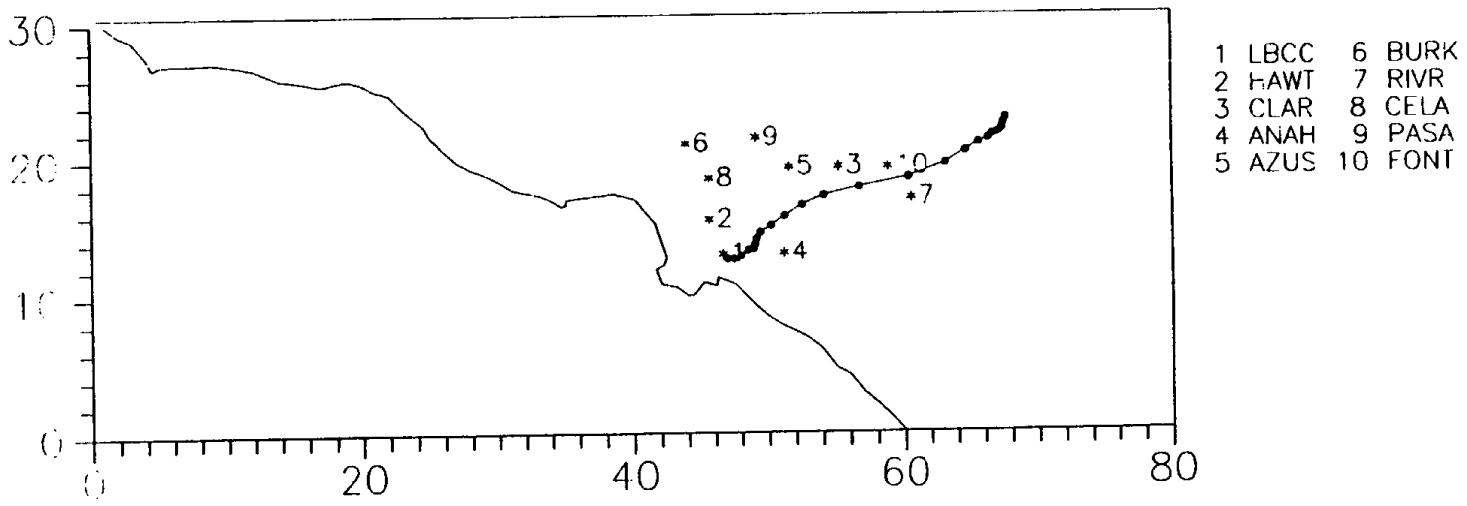

FIGURE 2.2.29. Trajectory starting at Long Beach on August 28, 1987, 0400 PST.

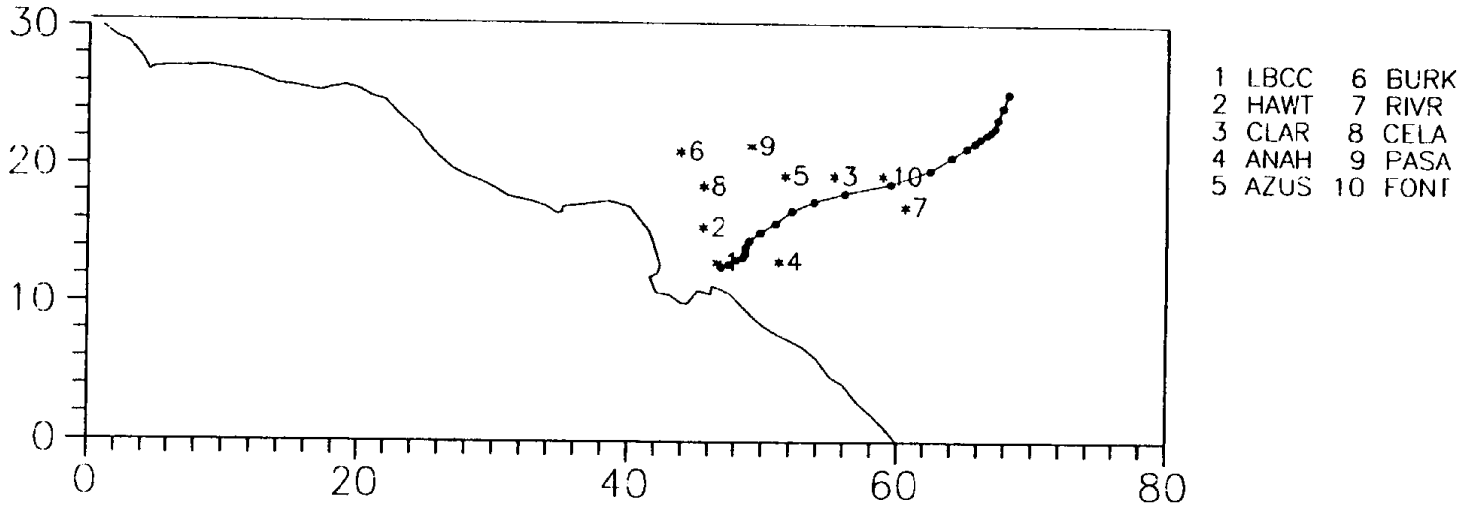

FIGURE 2.2.30. Trajectory starting at Long Beach on August 28, 1987, 0500 PST.

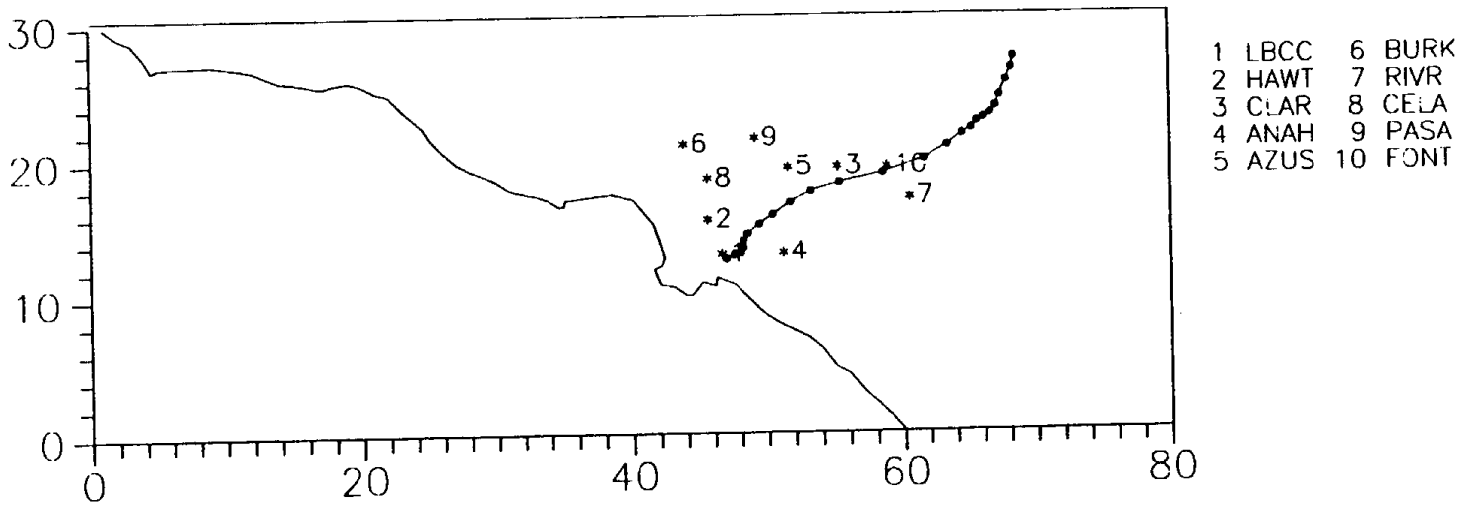

FIGURE 2.2.31. Trajectory starting at Long Beach on August 28, 1987, 0600 PST.

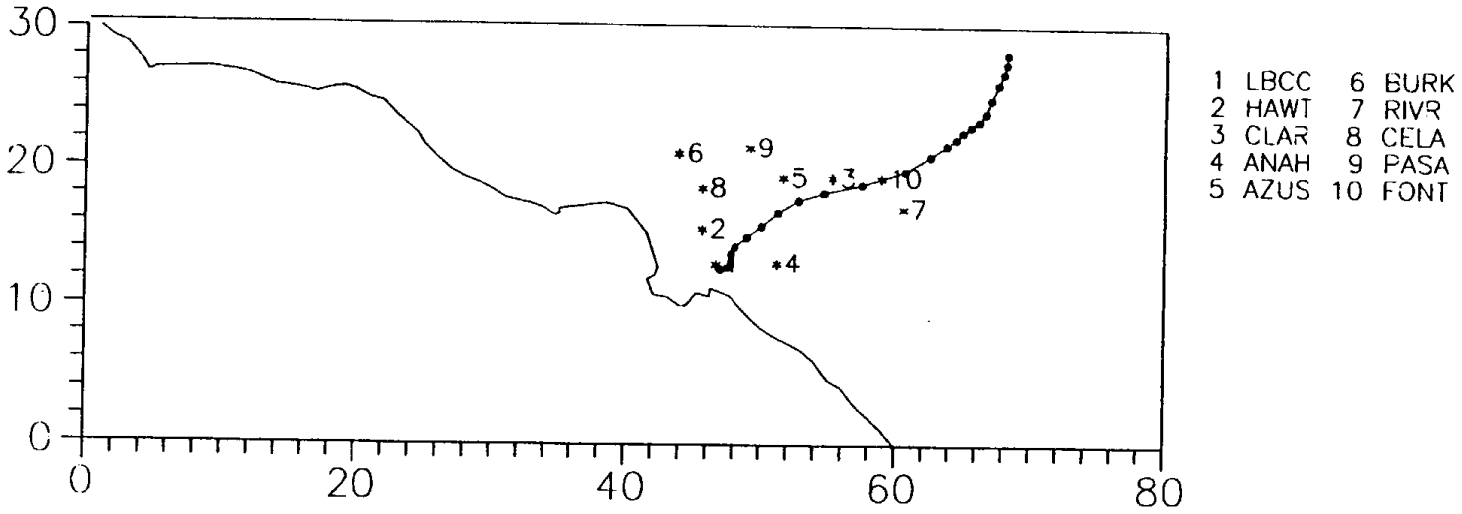

FIGURE 2.2.32. Trajectory starting at Long Beach on August 28, 1987, 0700 PST.

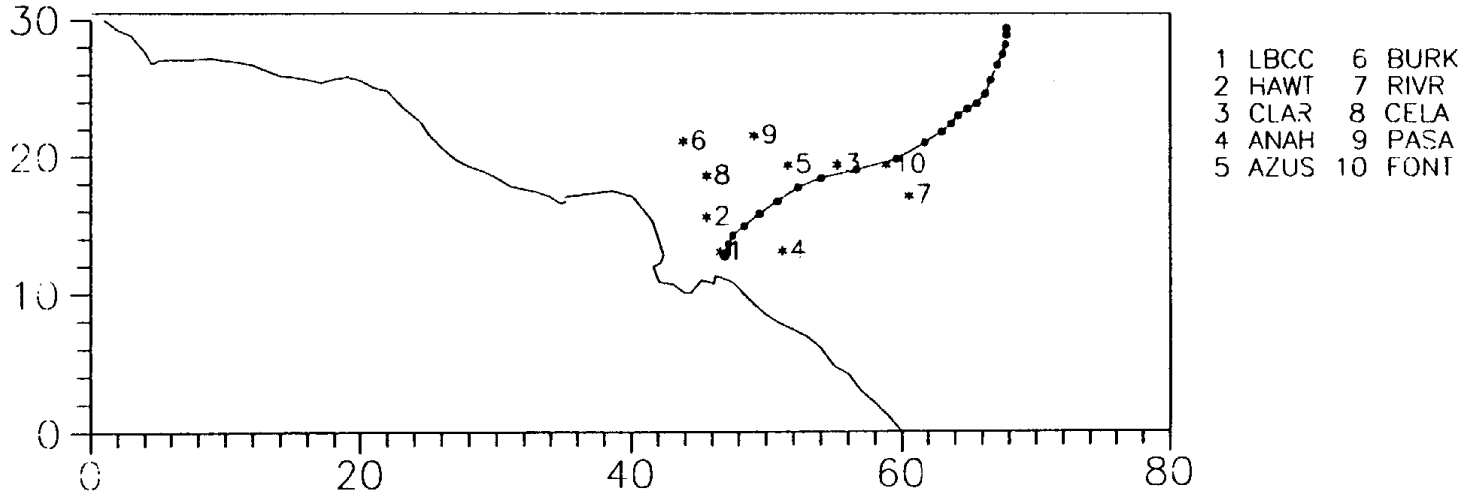

FIGURE 2.2.33. Trajectory starting at Long Beach on August 28, 1987, 0800 PST.

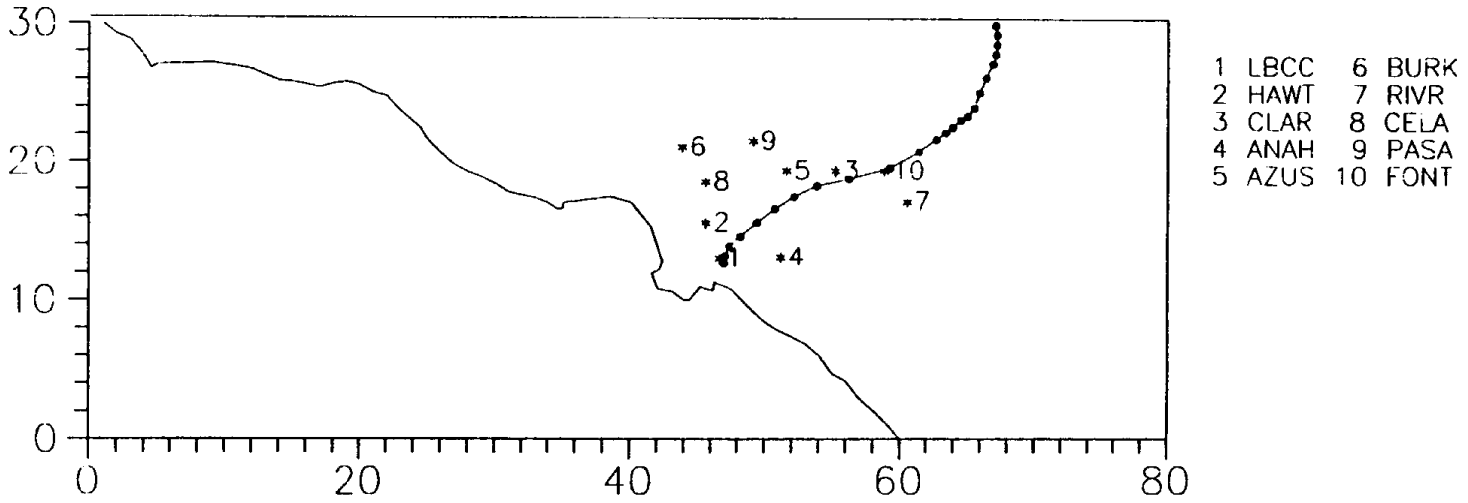

FIGURE 2.2.34. Trajectory starting at Long Beach on August 28, 1987, 0900 PST.

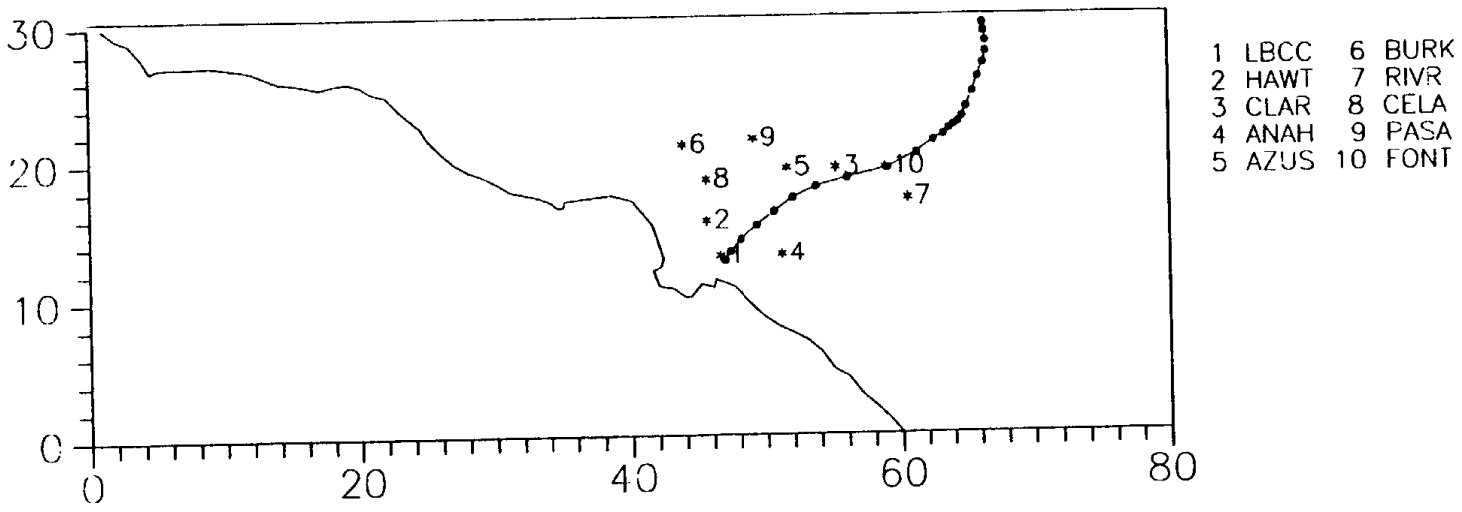

FIGURE 2.2.35. Trajectory starting at Long Beach on August 28, 1987, 1000 PST.

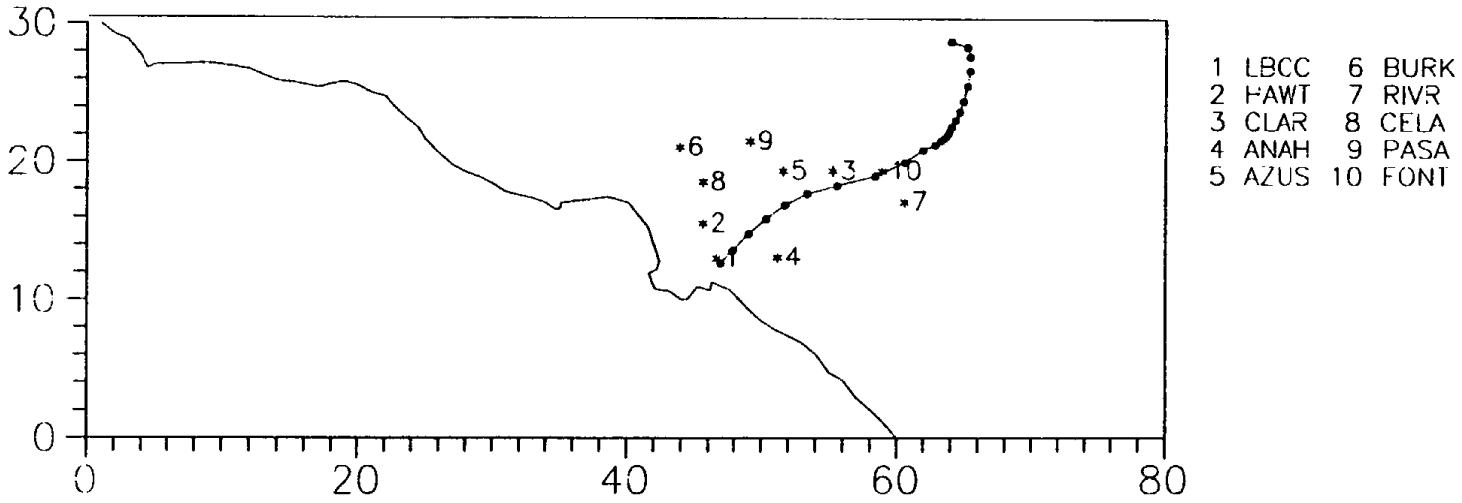

FIGURE 2.2.36. Trajectory starting at Long Beach on August 28, 1987, 1100 PST.

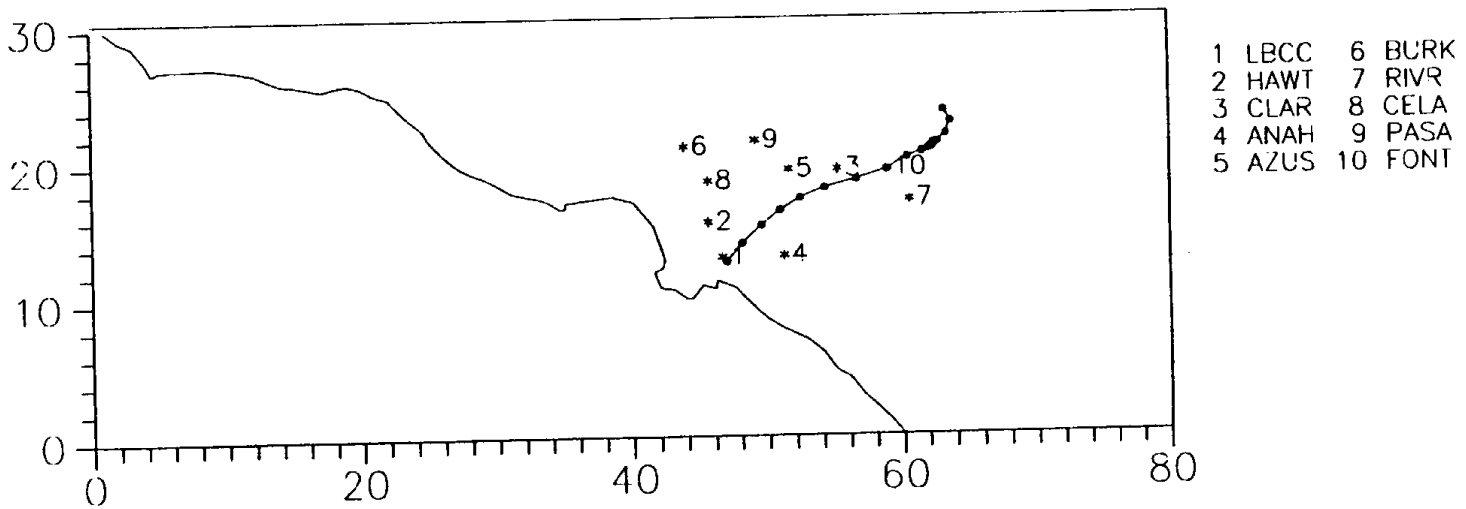

FIGURE 2.2.37. Trajectory starting at Long Beach on August 28, 1987, 1200 PST.

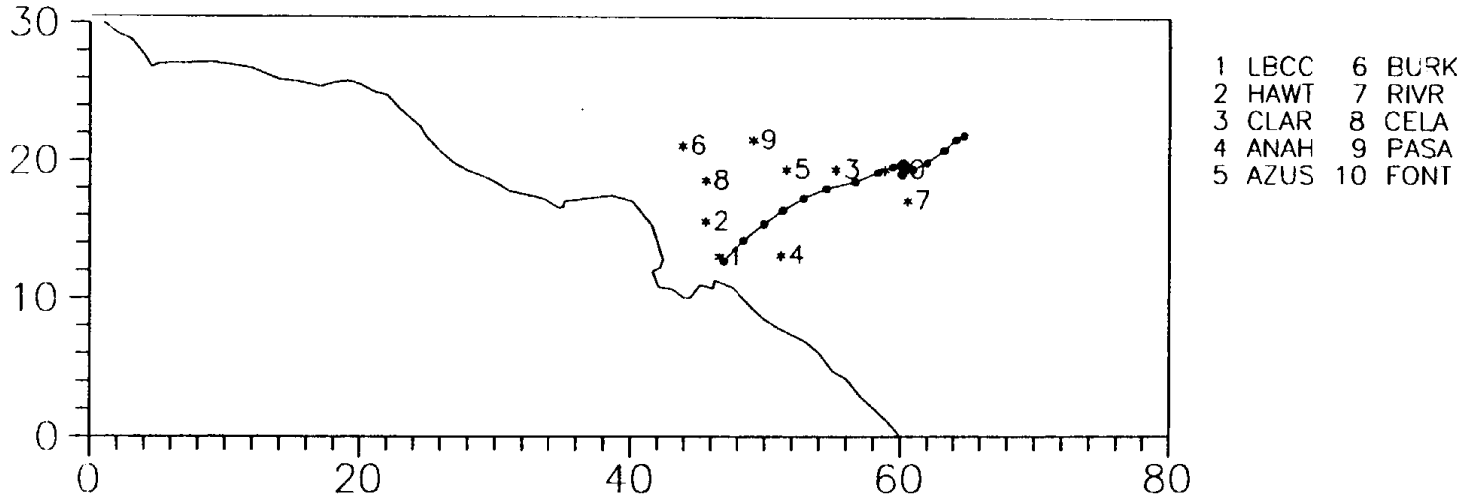

FIGURE 2.2.38. Trajectory starting at Long Beach on August 28, 1987, 1300 PST.

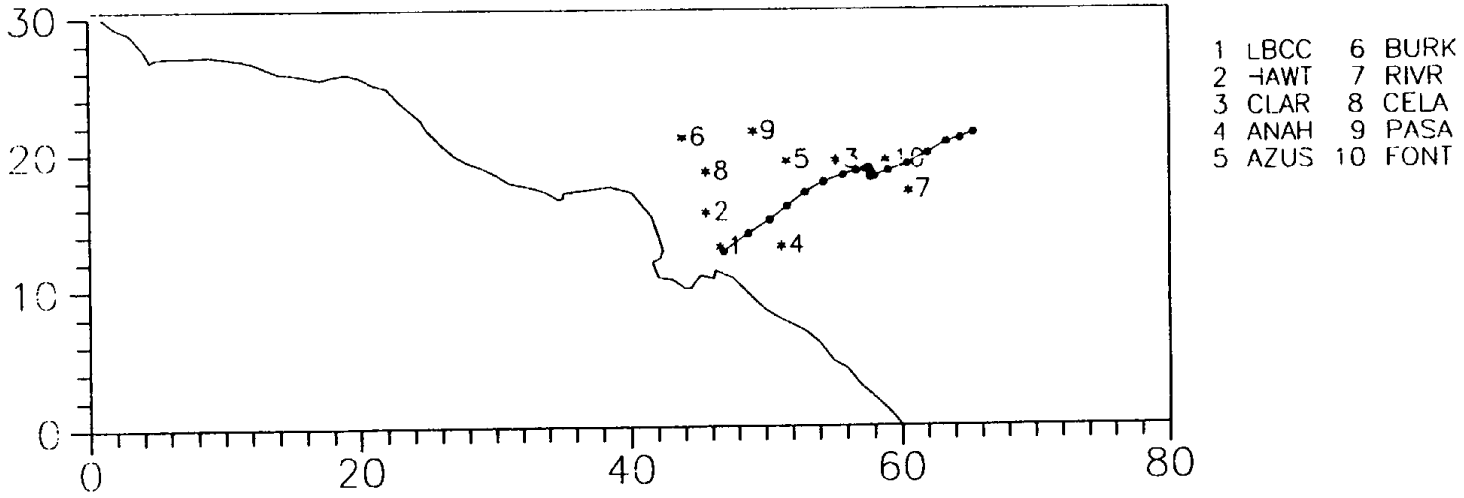

FIGURE 2.2.39. Trajectory starting at Long Beach on August 28, 1987, 1400 PST.

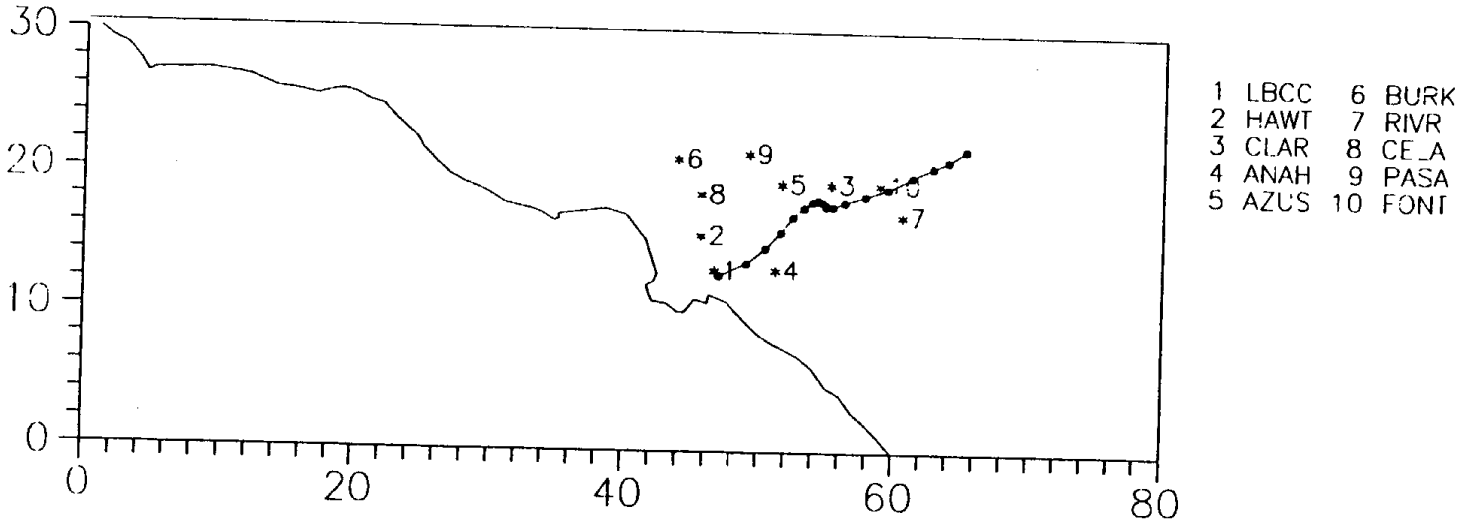

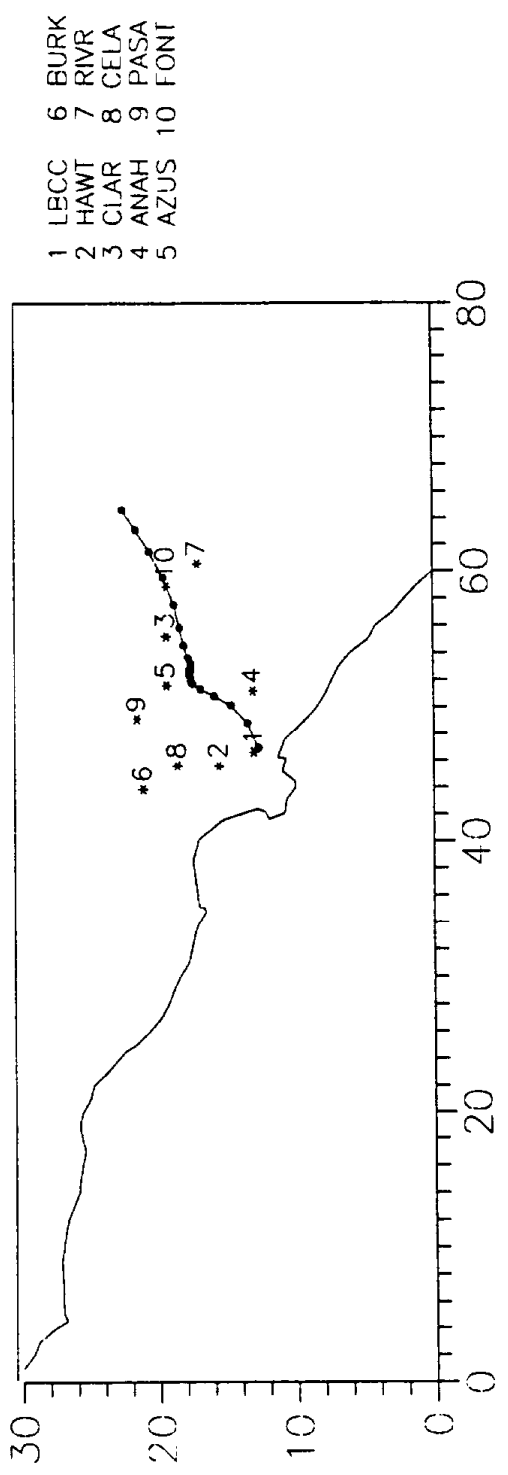

FIGURE 2.2.40. Trajectory starting at Long Beach on August 28, 1987, 1500 PST.

FIGURE 2.2.41. Trajectory starting at Long Beach on August 28, 1987, 1600 PST.

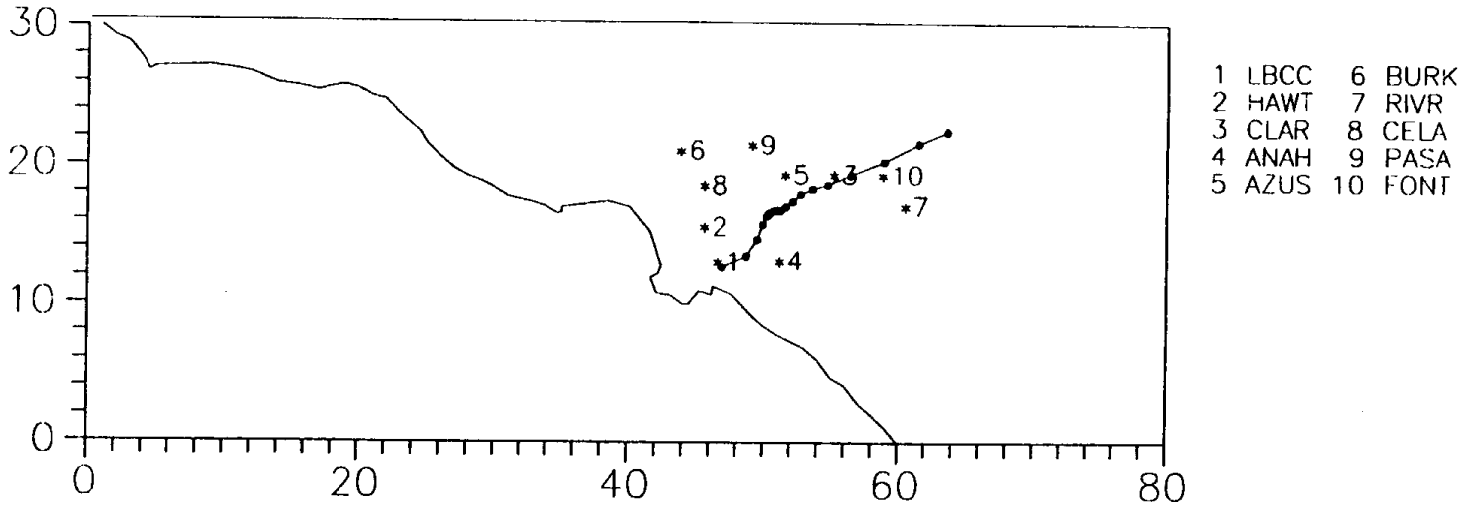

FIGURE 2.2.42. Trajectory starting at Long Beach on August 28, 1987, 1700 PST.

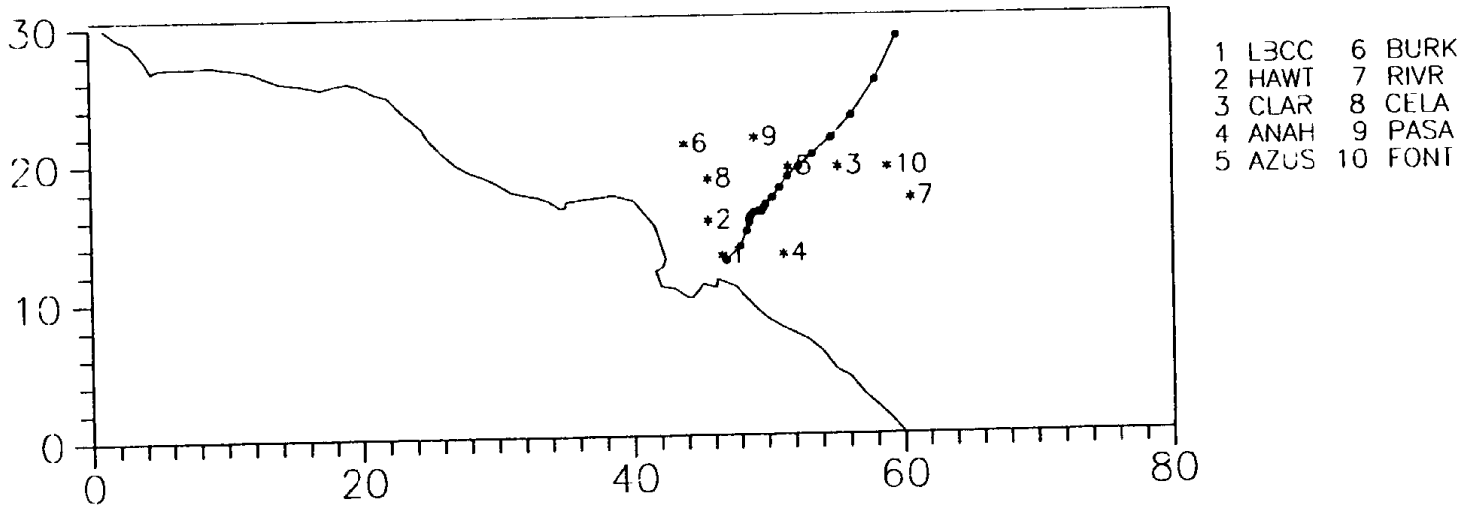

FIGURE 2.2.43. Trajectory starting at Long Beach on August 28, 1987, 1800 PST.

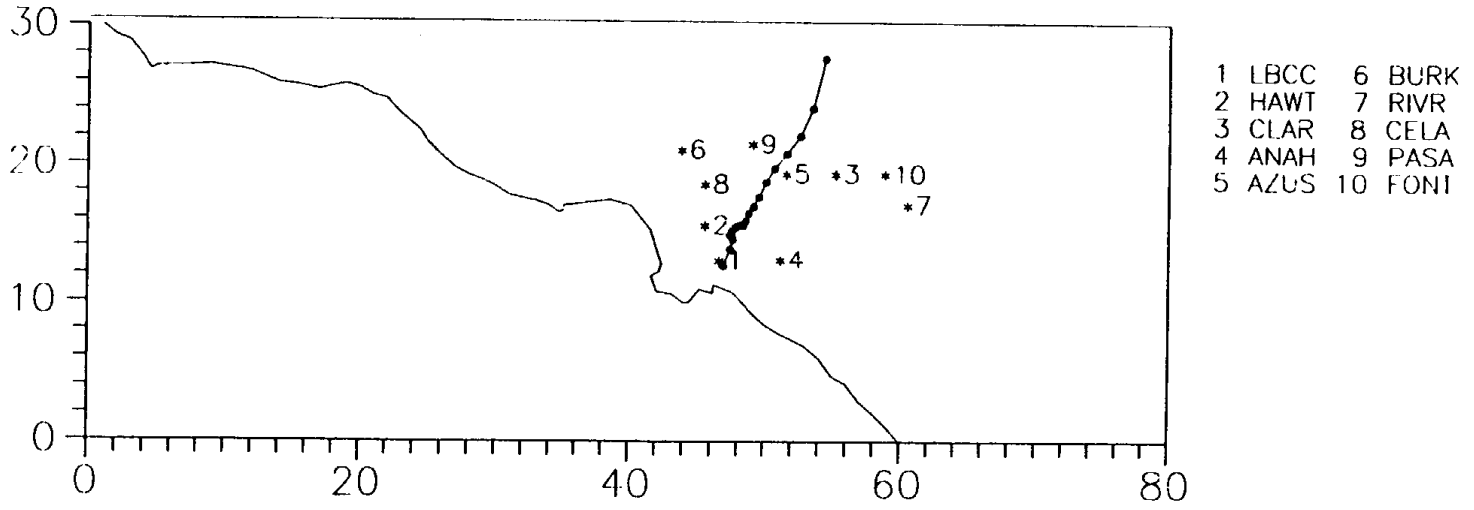

FIGURE 2.2.44. Trajectory starting at Long Beach on August 28, 1987, 1900 PST.

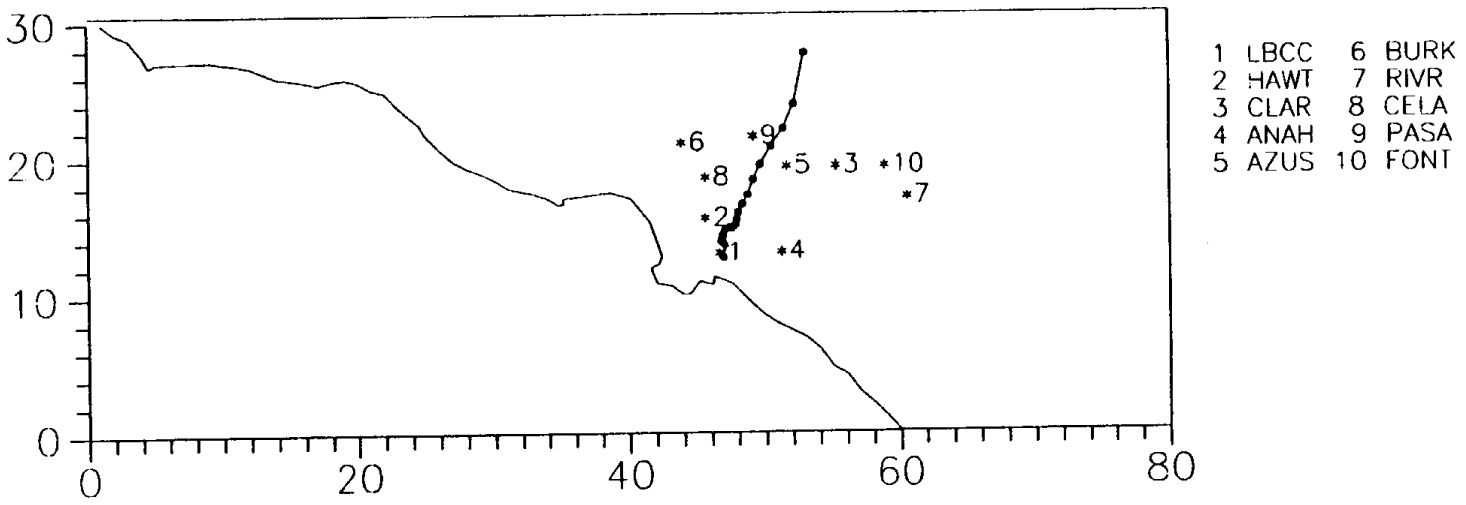

FIGURE 2.2.45. Trajectory starting at Long Beach on August 28, 1987, 2000 PST.

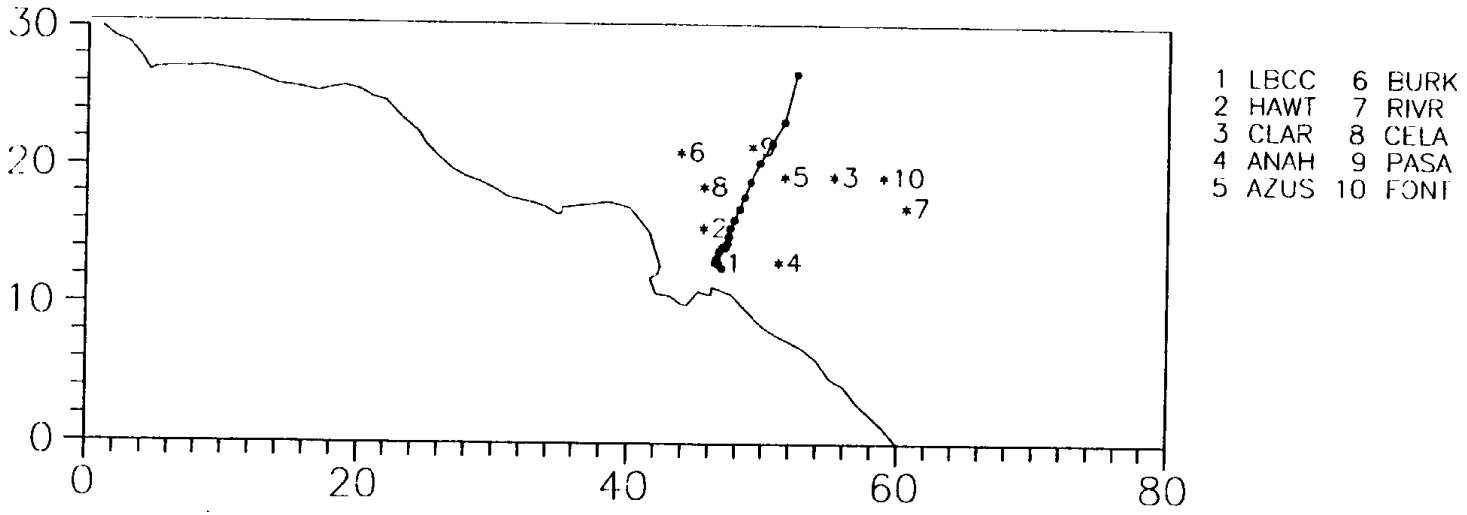

FIGURE 2.2.46. Trajectory starting at Long Beach on August 28, 1987, 2100 PST.

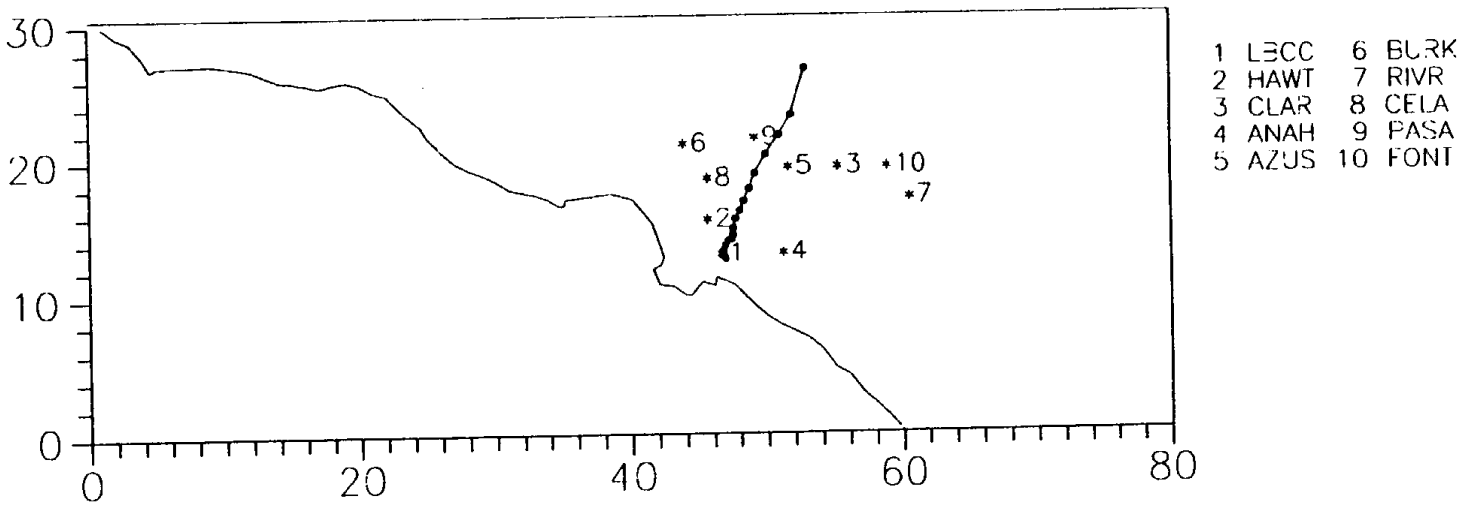

FIGURE 2.2.47. Trajectory starting at Long Beach on August 28, 1987, 2200 PST.

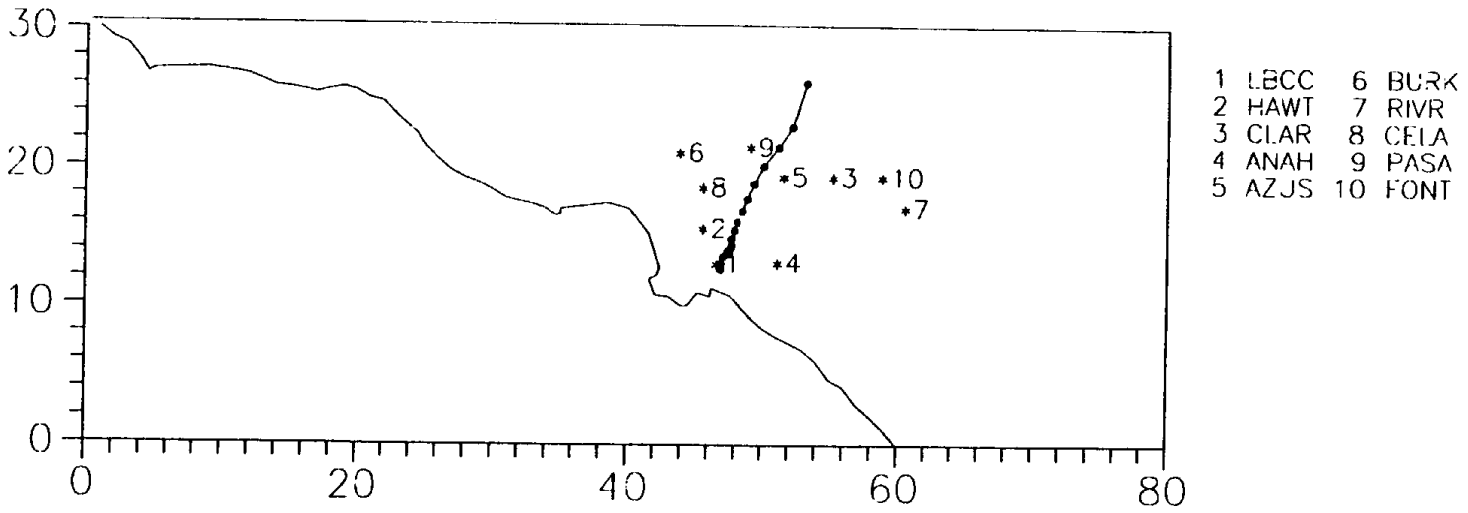

FIGURE 2.2.48. Trajectory starting at Long Beach on August 28, 1987, 2300 PST.

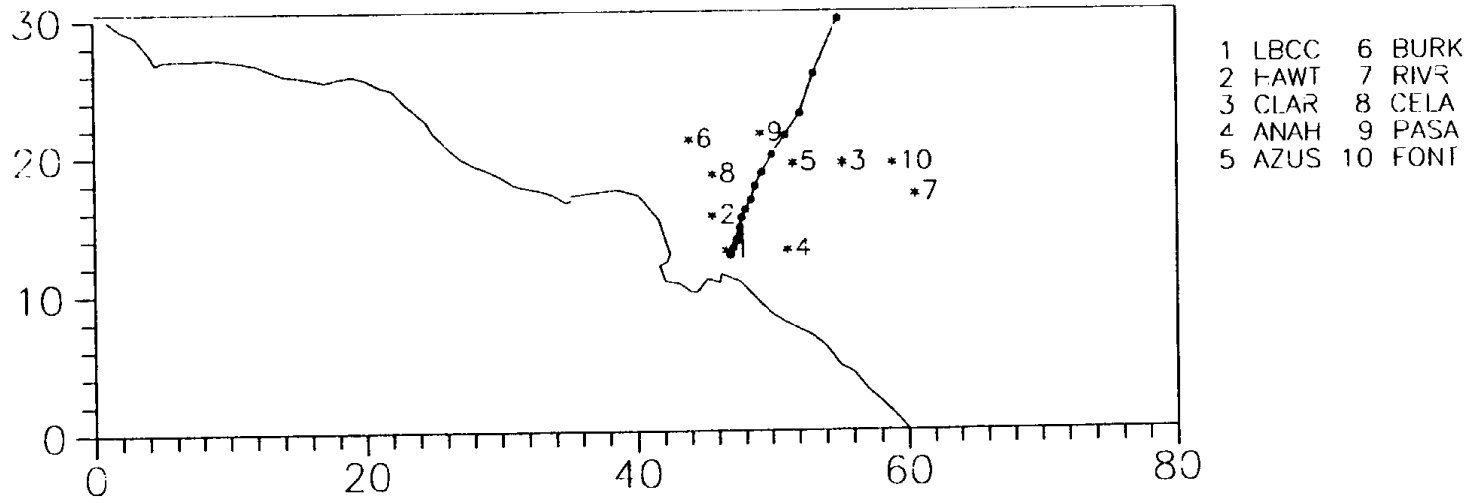

Appendix A.2

TRAJECTORIES STARTING AT LONG BEACH FROM DECEMBER 10, 1987, 0000 PST-DECEMBER 10, 1987, 2300 PST

FIGURE 2.2.49. Trajectory starting at Long Beach on December 10, 1987, 0000 PST.

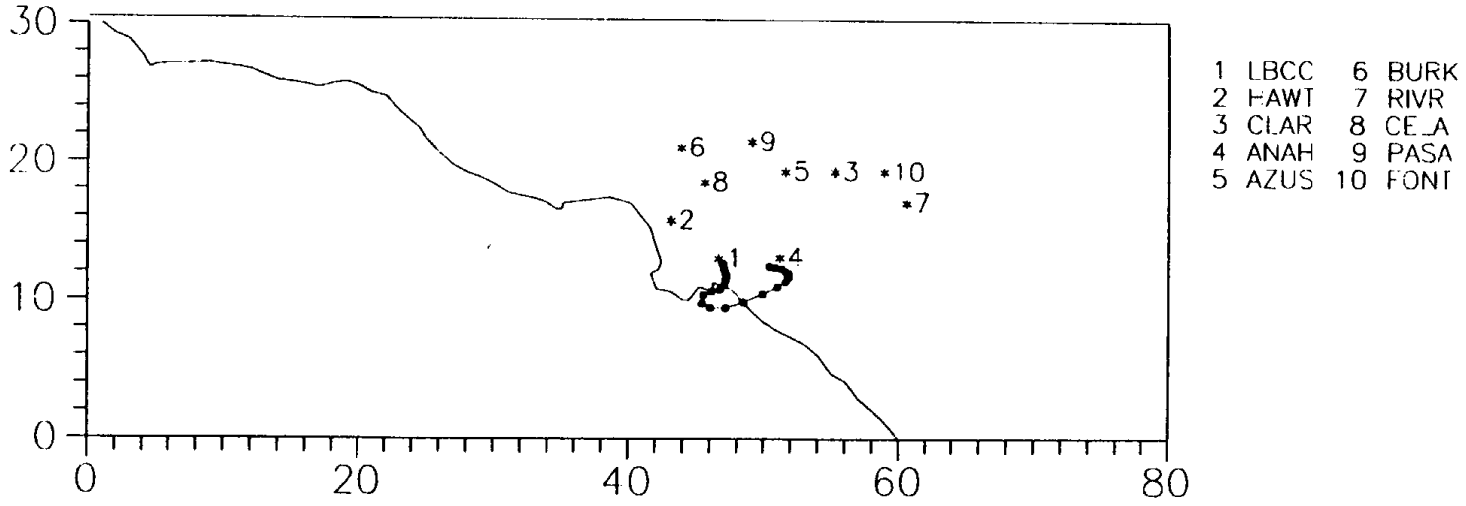

FIGURE 2.2.50. Trajectory starting at Long Beach on December 10, 1987, 0100 PST.

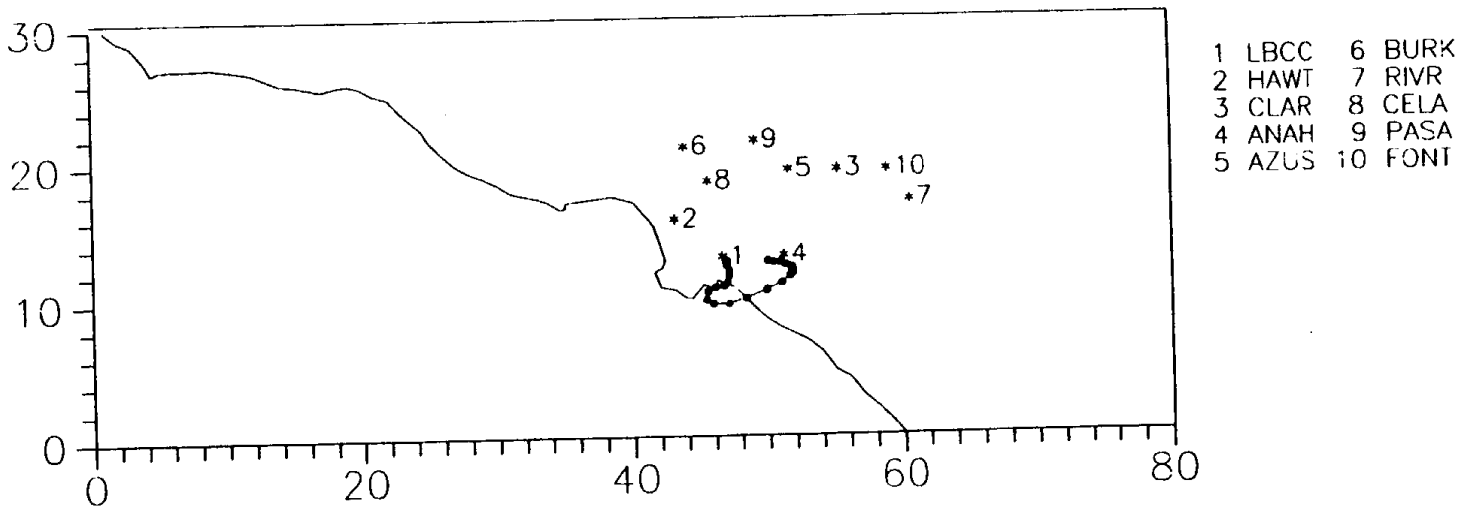

FIGURE 2.2.51. Trajectory starting at Long Beach on December 10, 1987, 0200 PST.

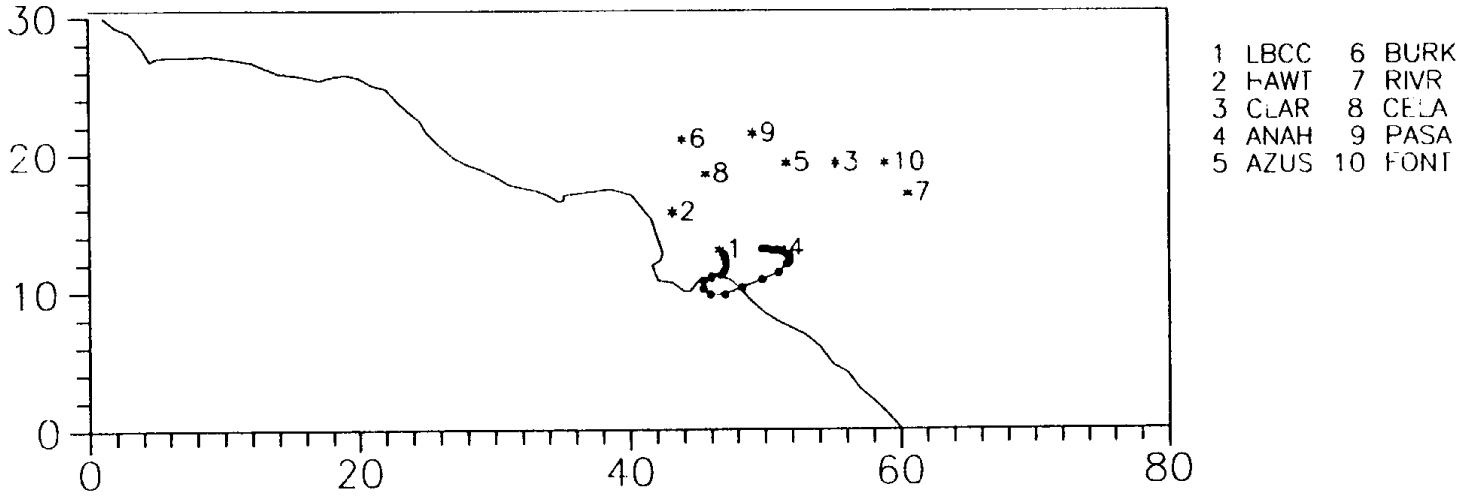

FIGURE 2.2.52. Trajectory starting at Long Beach on December 10, 1987, 0300 PST.

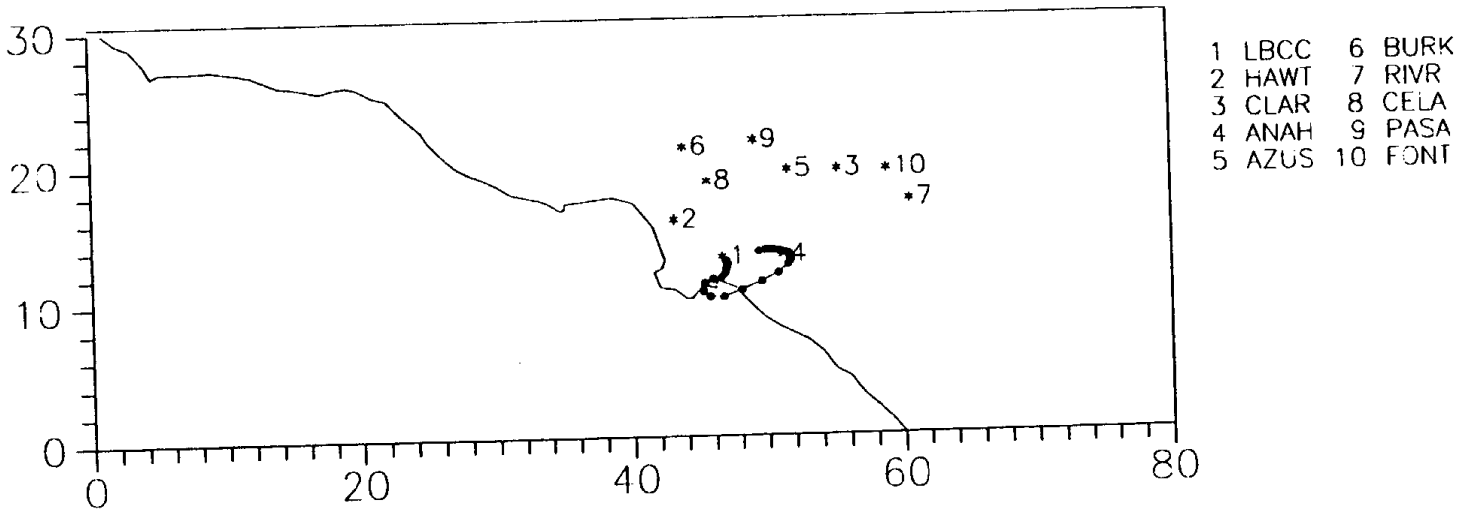

FIGURE 2.2.53. Trajectory starting at Long Beach on December 10, 1987, 0400 PST.

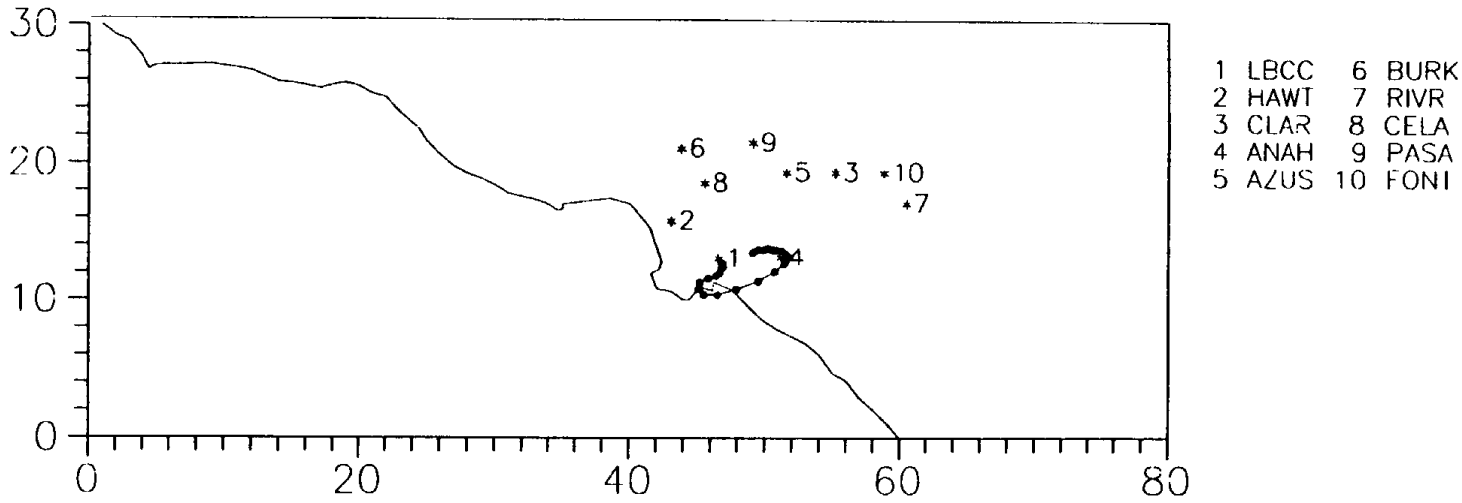

FIGURE 2.2.54. Trajectory starting at Long Beach on December 10, 1987, 0500 PST.

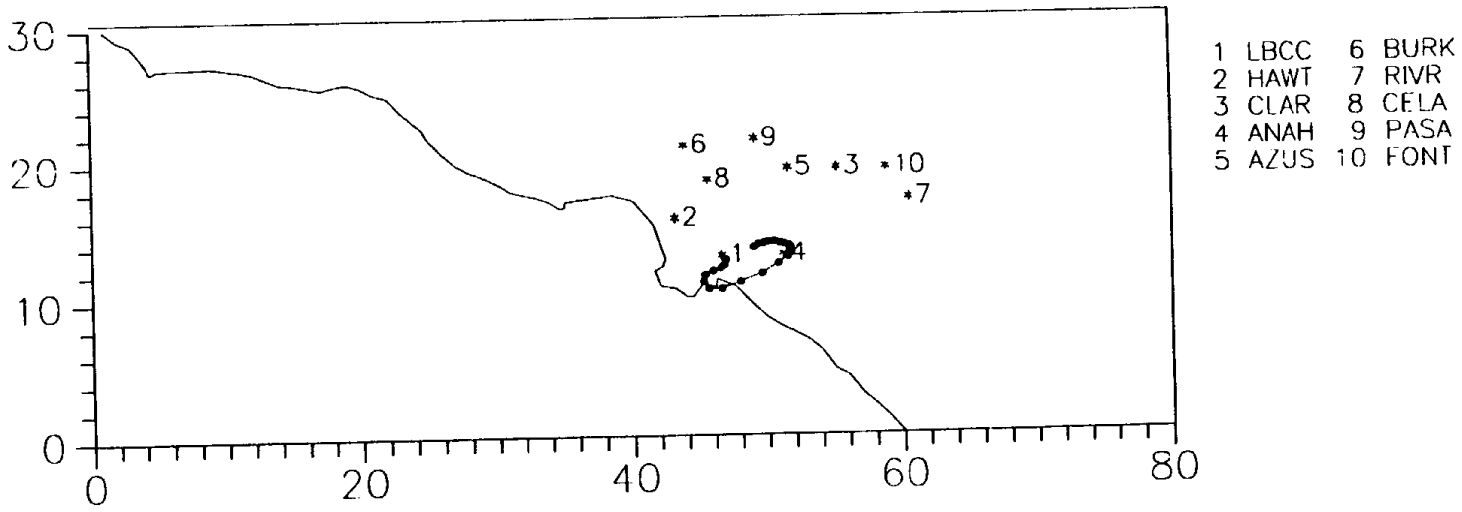

FIGURE 2.2.55. Trajectory starting at Long Beach on December 10, 1987, 0600 PST.

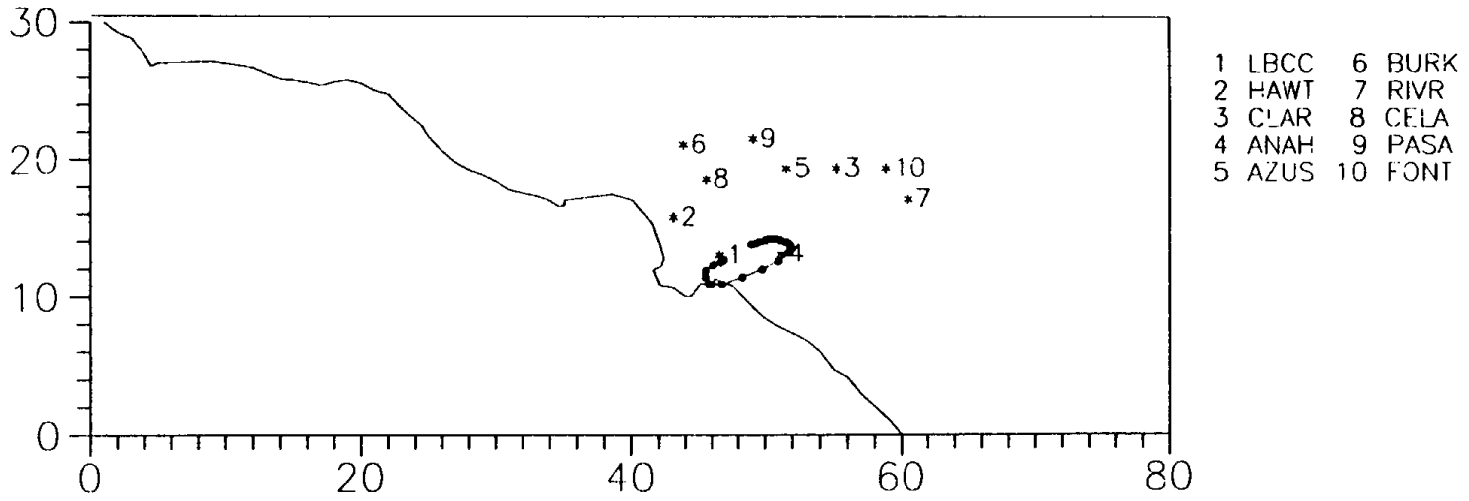

FIGURE 2.2.56. Trajectory starting at Long Beach on December 10, 1987, 0700 PST.

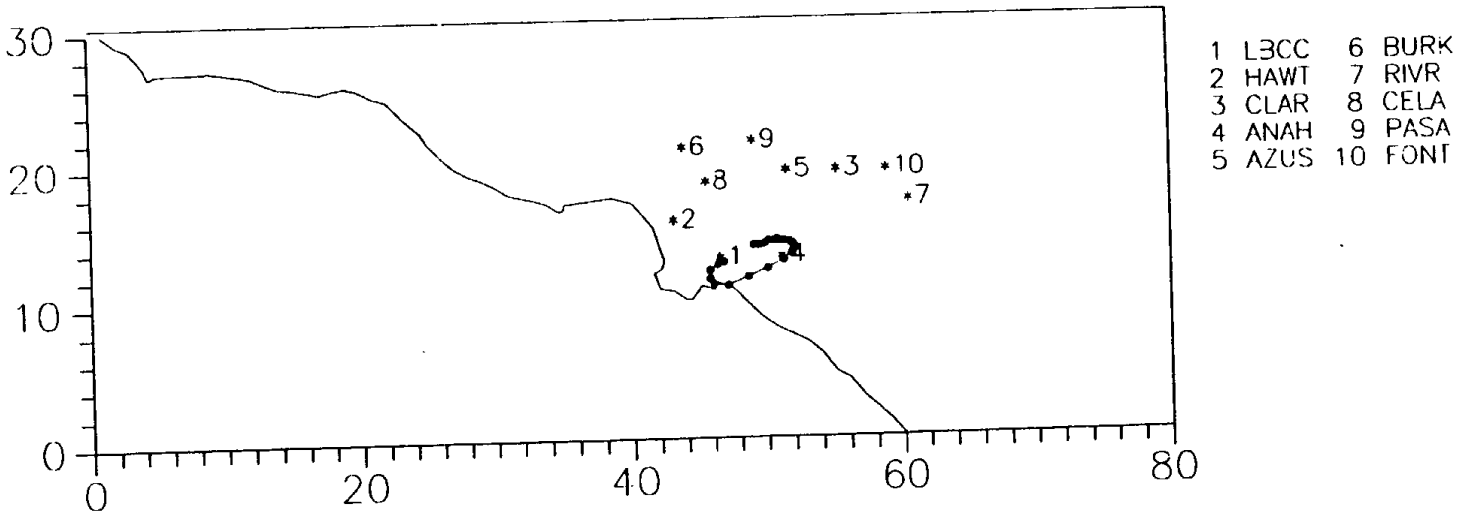

FIGURE 2.2.57. Trajectory starting at Long Beach on December 10, 1987, 0800 PST.

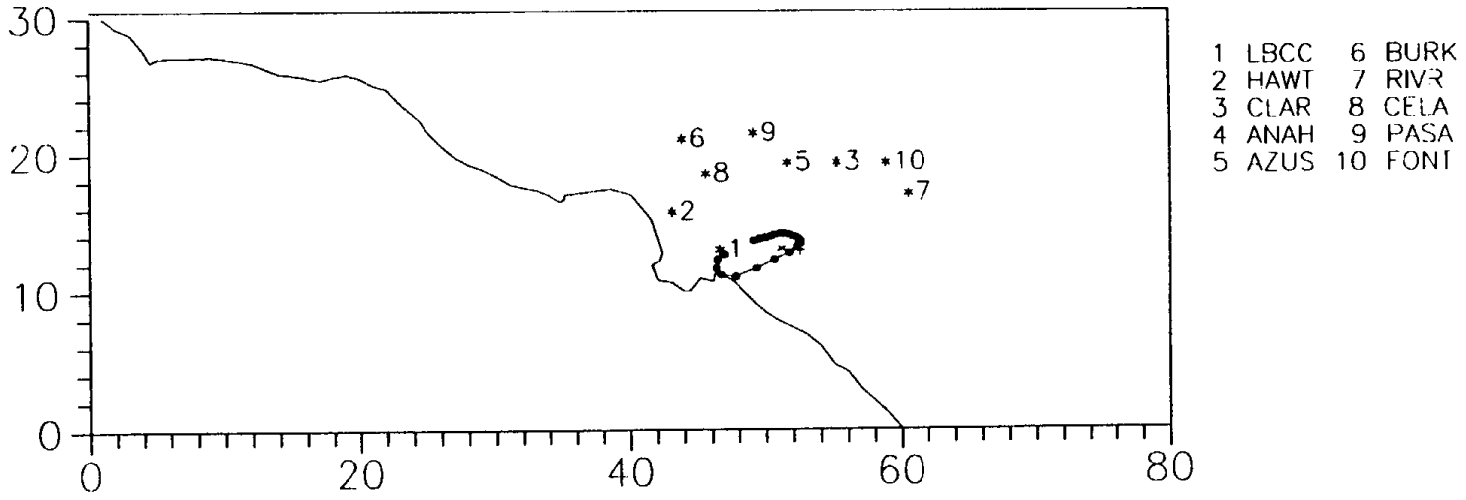

FIGURE 2.2.58. Trajectory starting at Long Beach on December 10, 1987, 0900 PST.

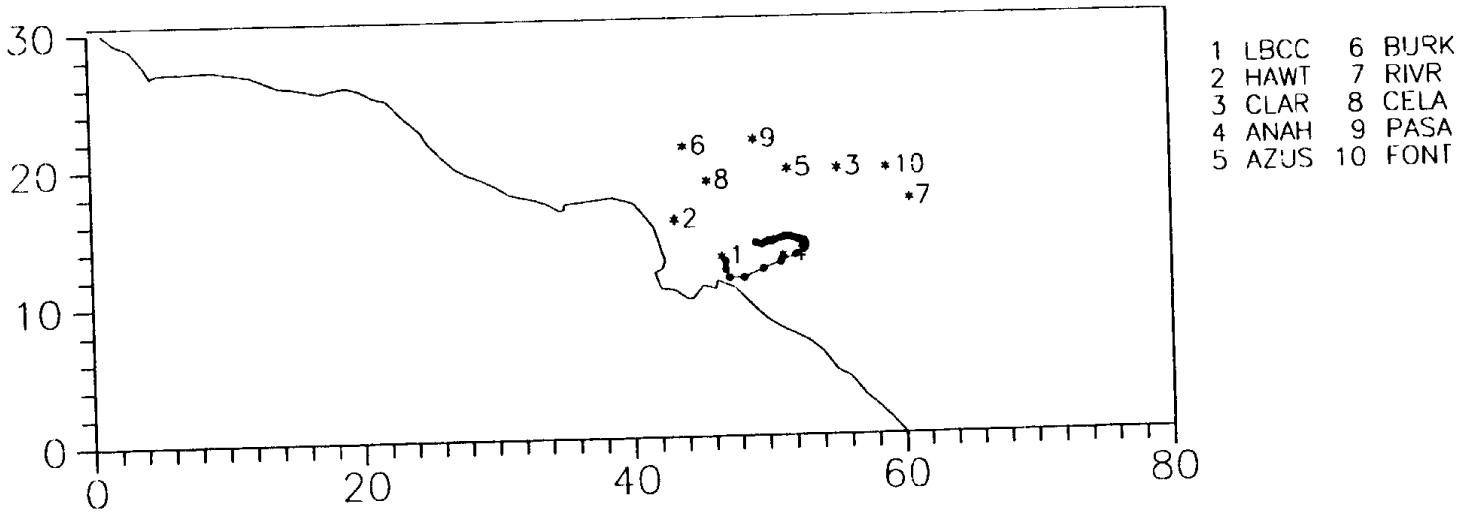

FIGURE 2.2.59. Trajectory starting at Long Beach on December 10, 1987, 1000 PST.

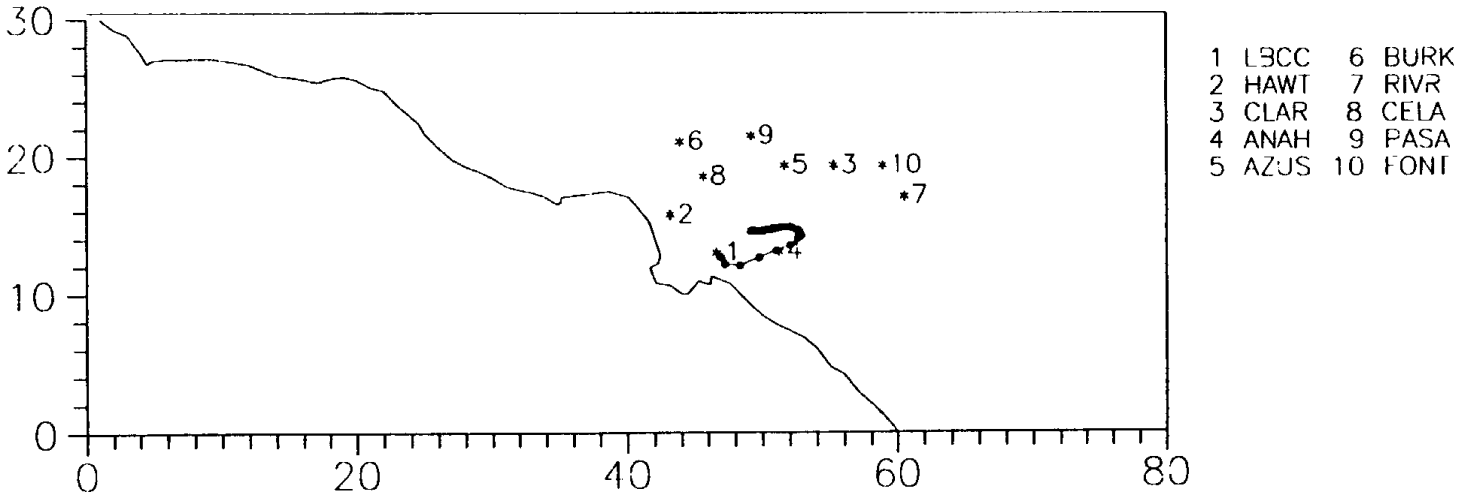

FIGURE 2.2.60. Trajectory starting at Long Beach on December 10, 1987, 1100 PST.

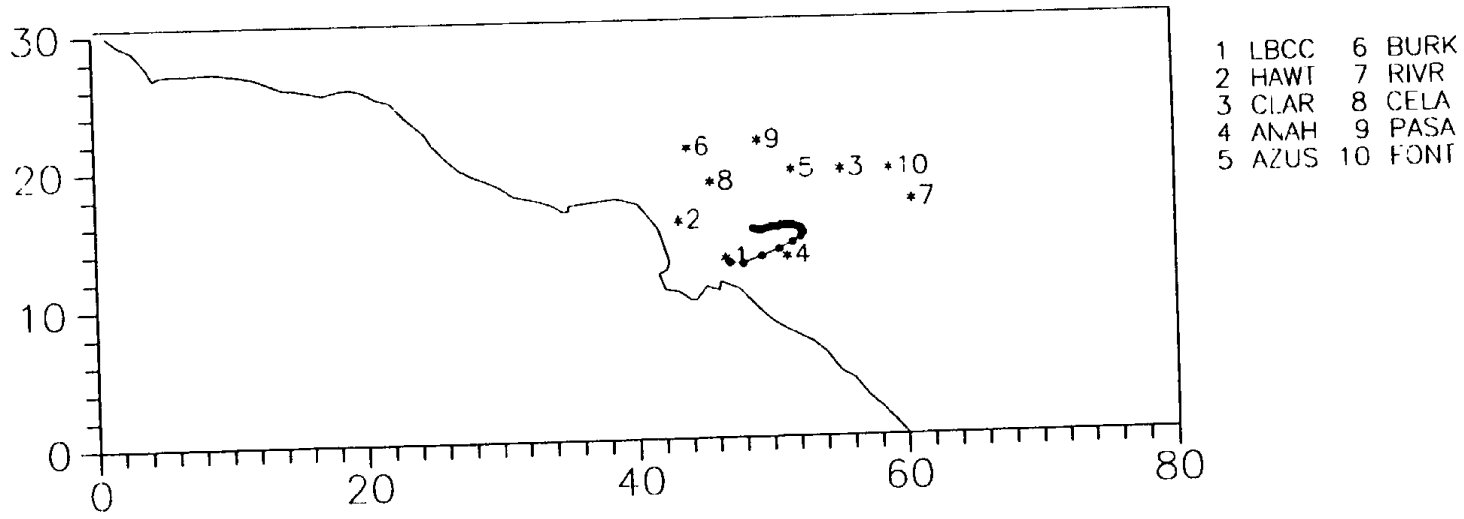

FIGURE 2.2.61. Trajectory starting at Long Beach on December 10, 1987, 1200 PST.

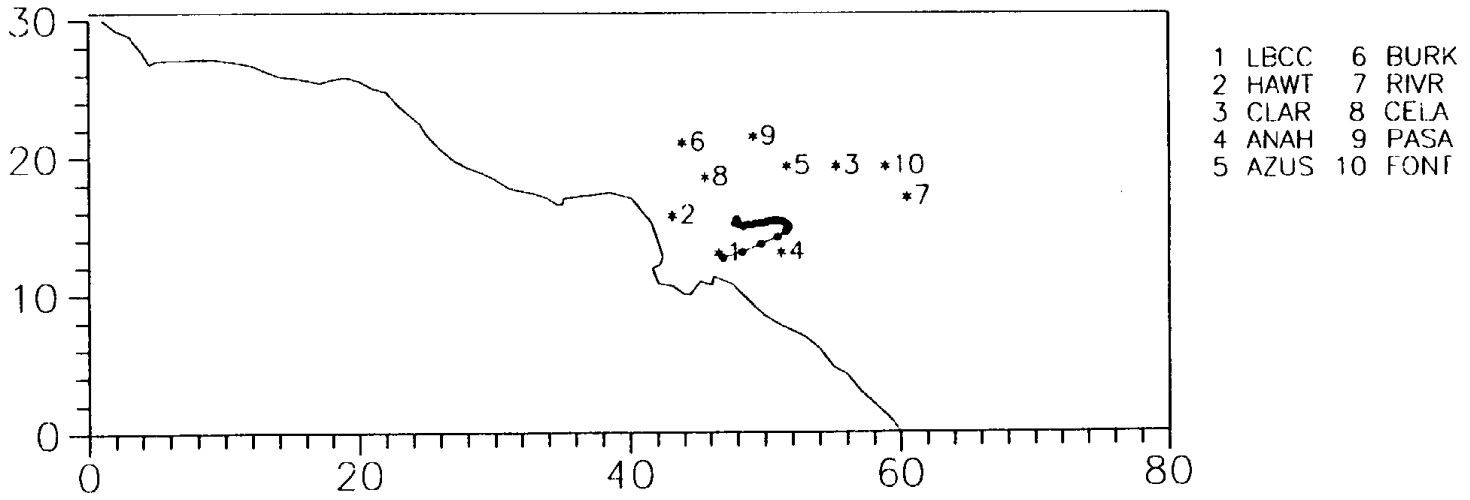

FIGURE 2.2.62. Trajectory starting at Long Beach on December 10, 1987, 1300 PST.

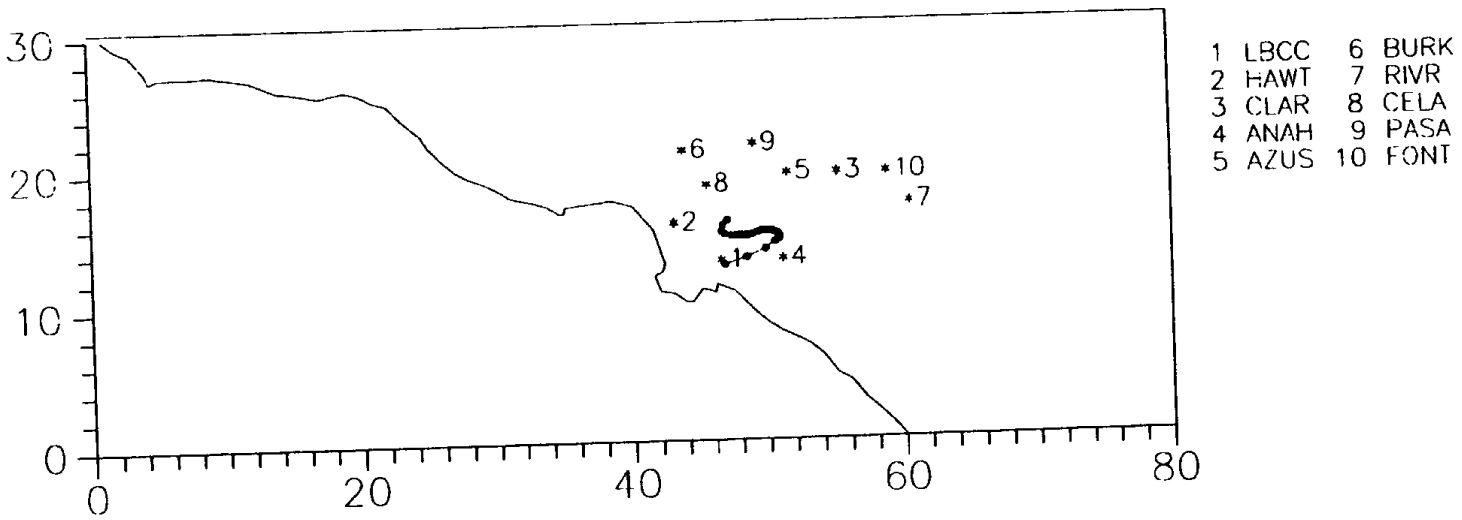

FIGURE 2.2.63. Trajectory starting at Long Beach on December 10, 1987, 1400 PST.

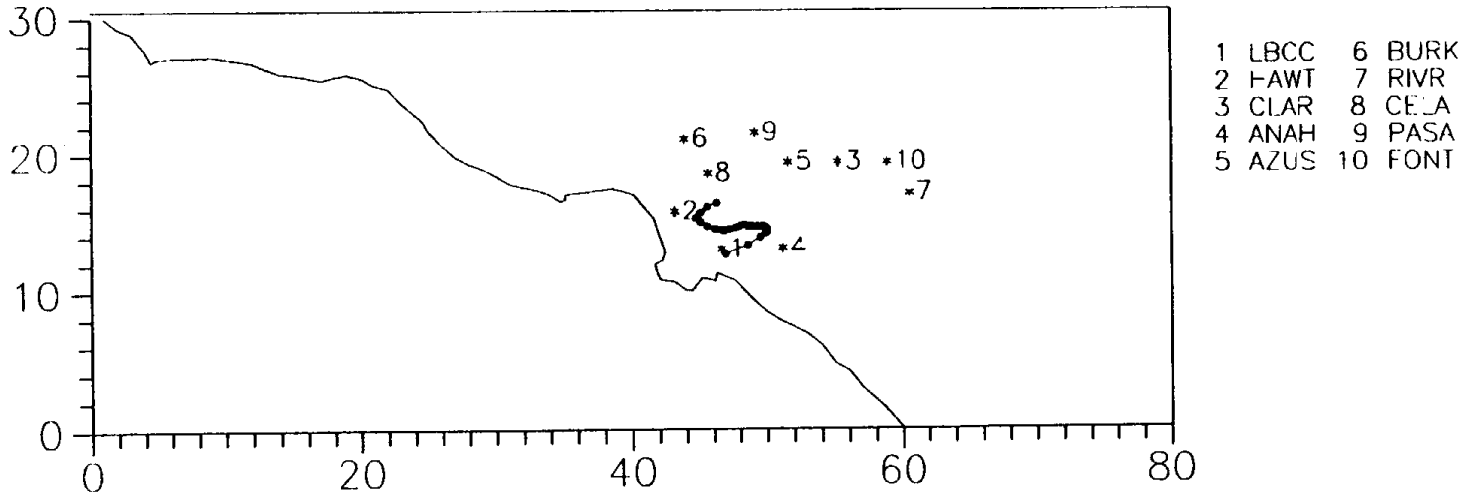

FIGURE 2.2.64. Trajectory starting at Long Beach on December 10, 1987, 1500 PST.

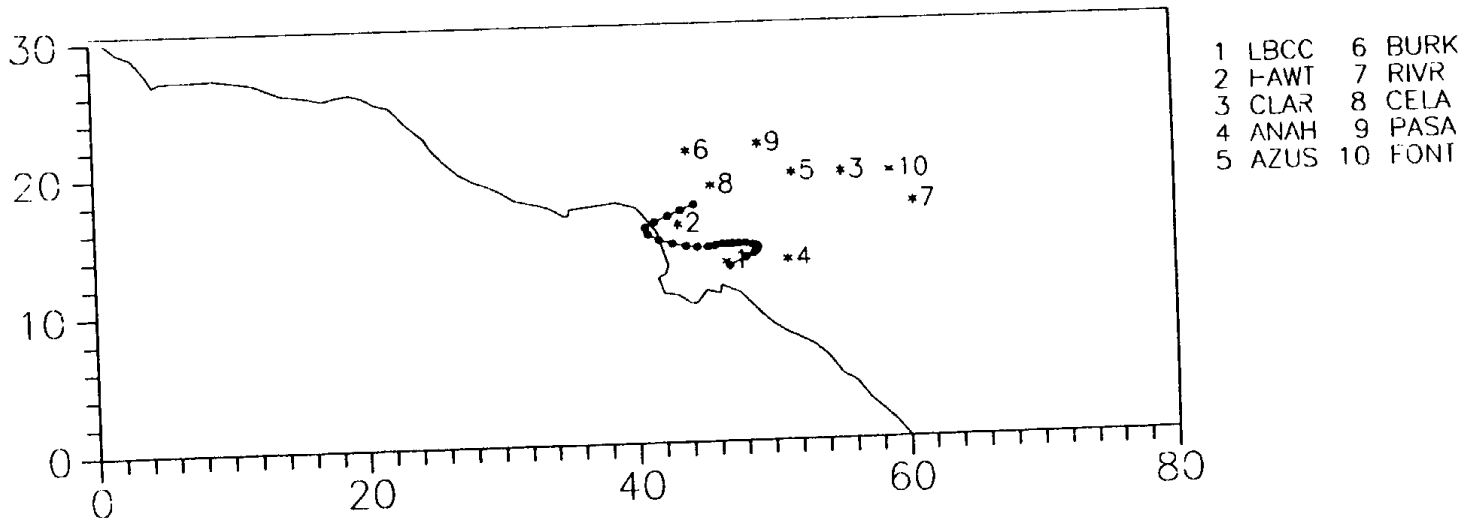

FIGURE 2.2.65. Trajectory starting at Long Beach on December 10, 1987, 1600 PST.

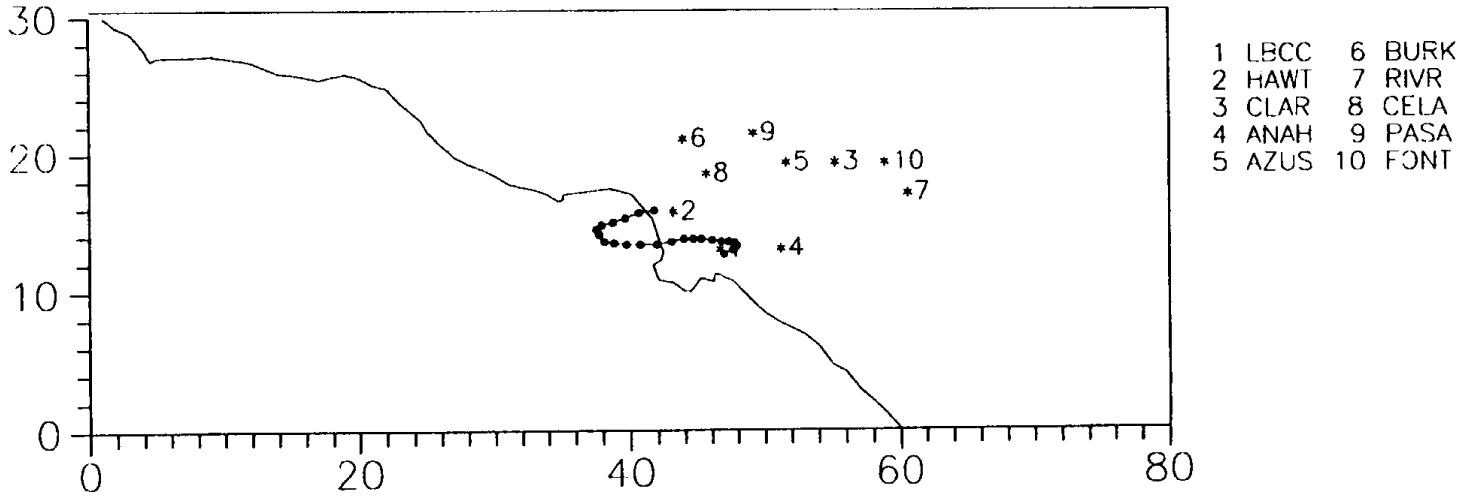

FIGURE 2.2.66. Trajectory starting at Long Beach on December 10, 1987, 1700 PST.

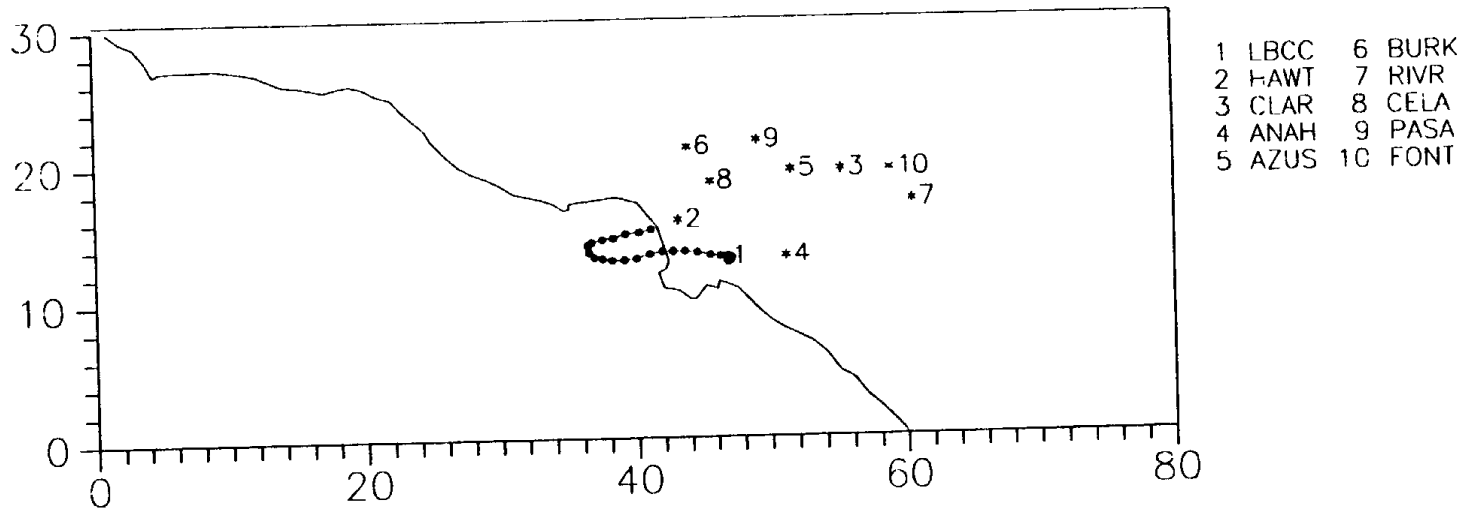

FIGURE 2.2.67. Trajectory starting at Long Beach on December 10, 1987, 1800 PST.

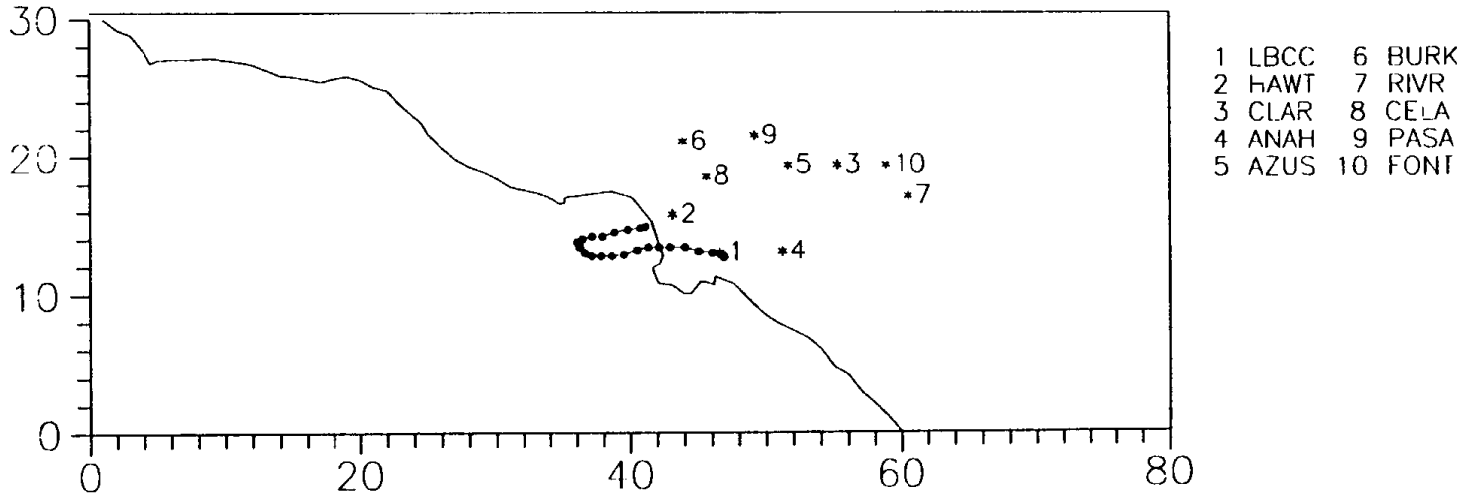

FIGURE 2.2.68. Trajectory starting at Long Beach on December 10, 1987, 1900 PST.

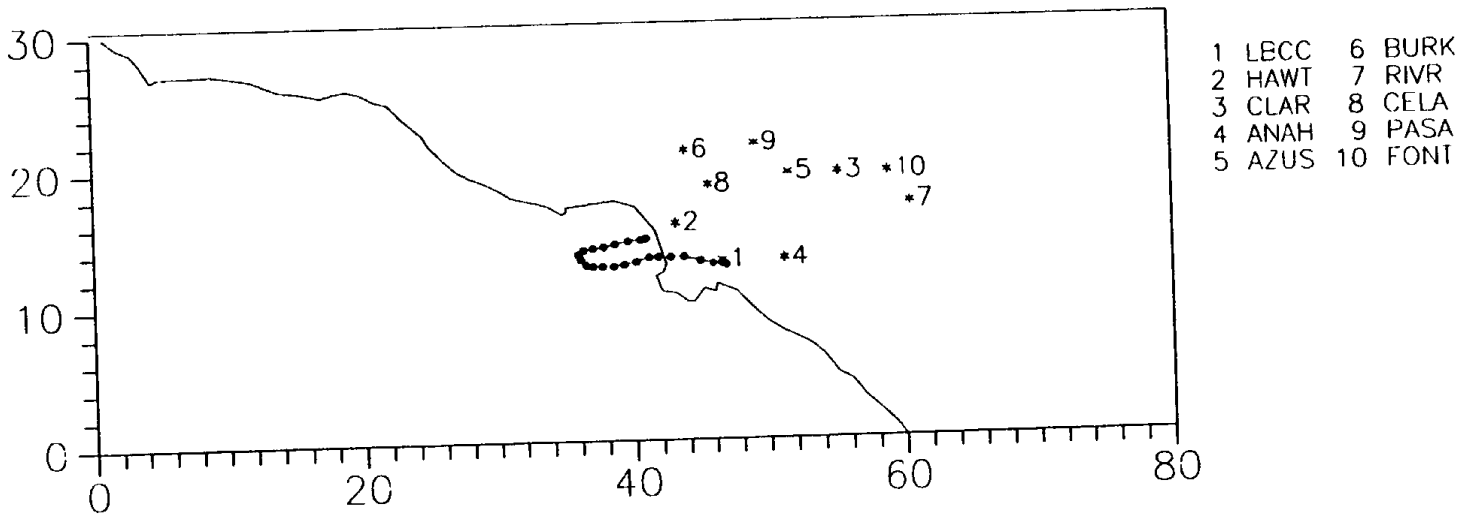

FIGURE 2.2.69. Trajectory starting at Long Beach on December 10, 1987, 2000 PST.

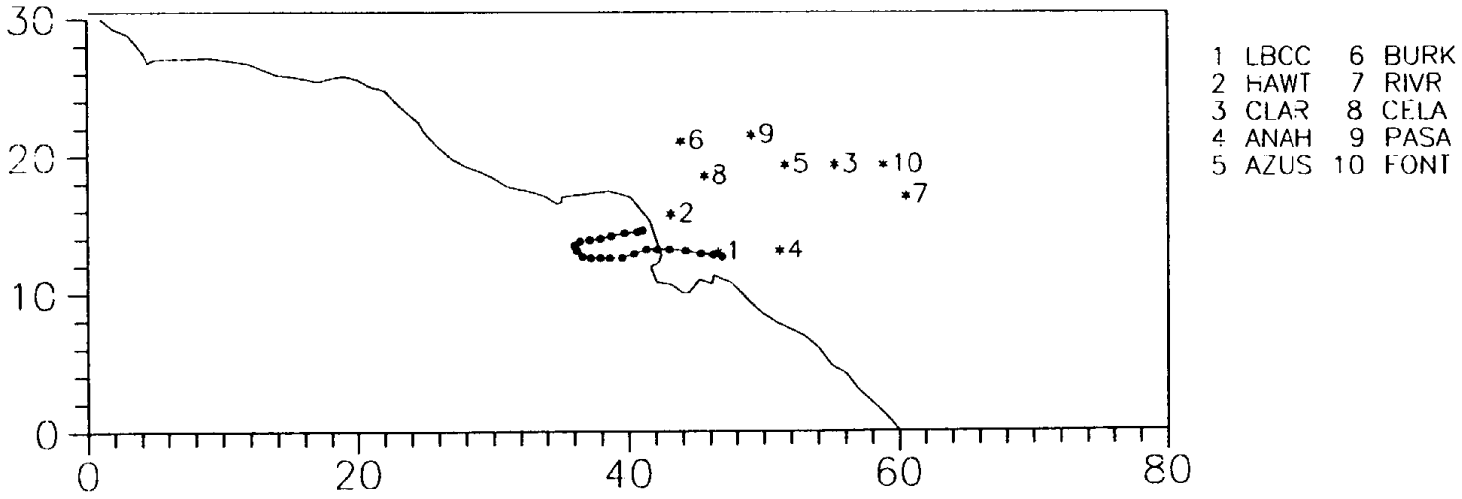

FIGURE 2.2.70. Trajectory starting at Long Beach on December 10, 1987, 2100 PST.

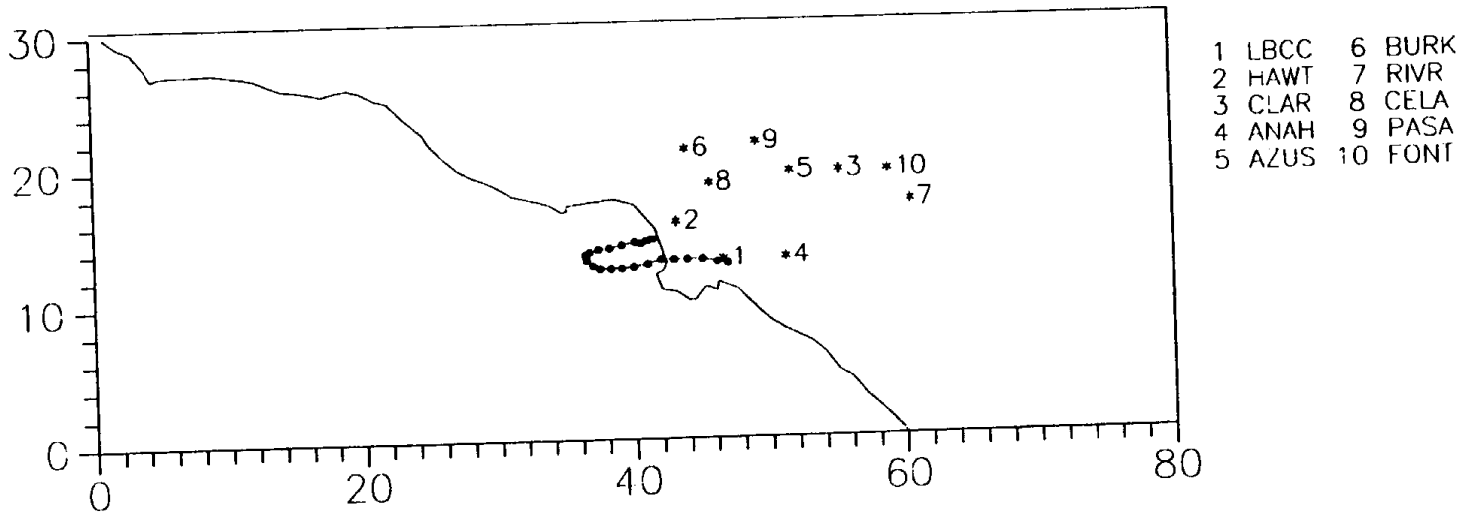

FIGURE 2.2.71. Trajectory starting at Long Beach on December 10, 1987, 2200 PST.

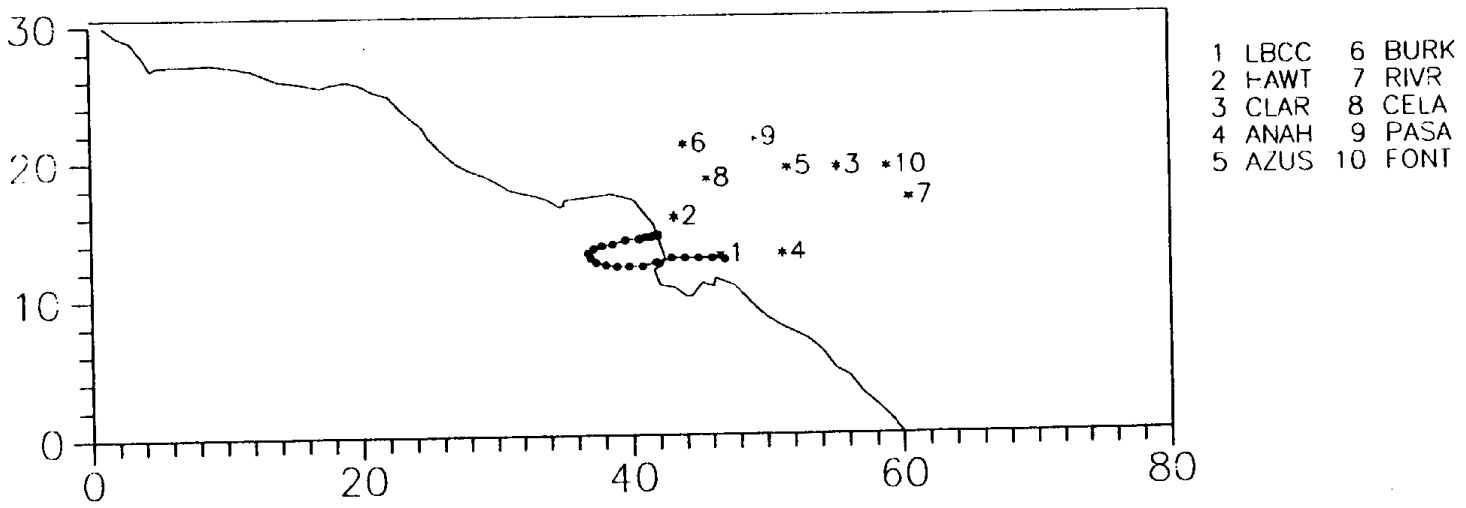

FIGURE 2.2.72. Trajectory starting at Long Beach on December 10, 1987, 2300 PST.

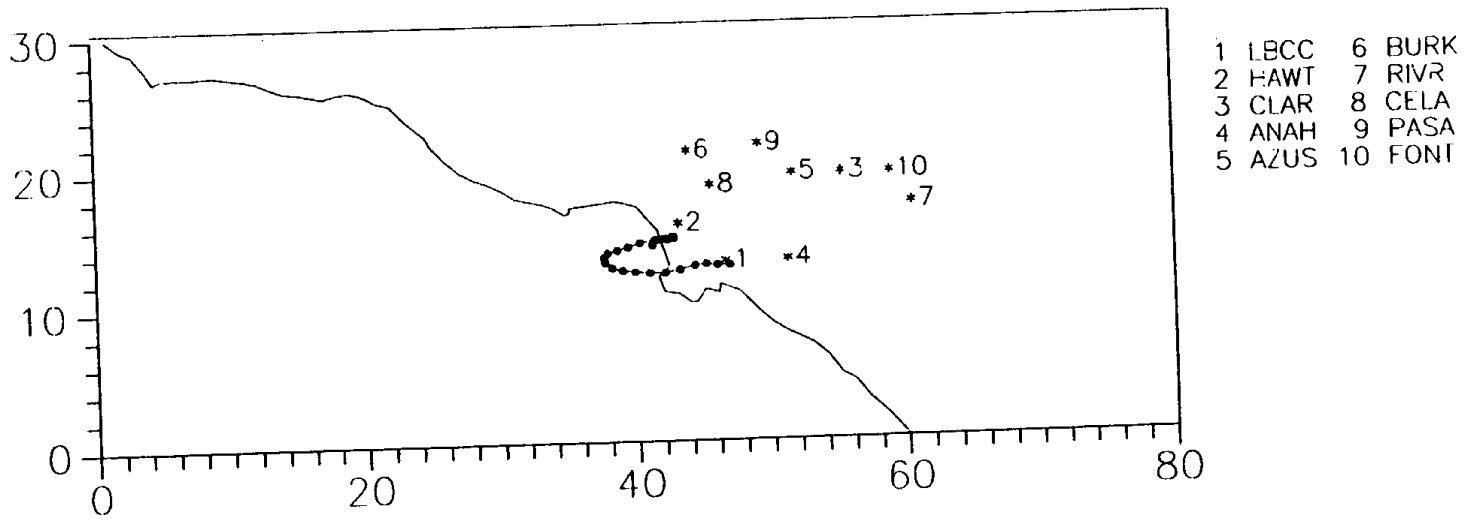

Appendix B

MAPS OF THE TRAJECTORIES TO EACH SITE FOR EACH SAMPLING DAY DURING THE SCAQS EXPERIMENTS

APPENDIX

Maps of the Trajectories to Each Site

for each Sampling Day during the SCAQS Experiments

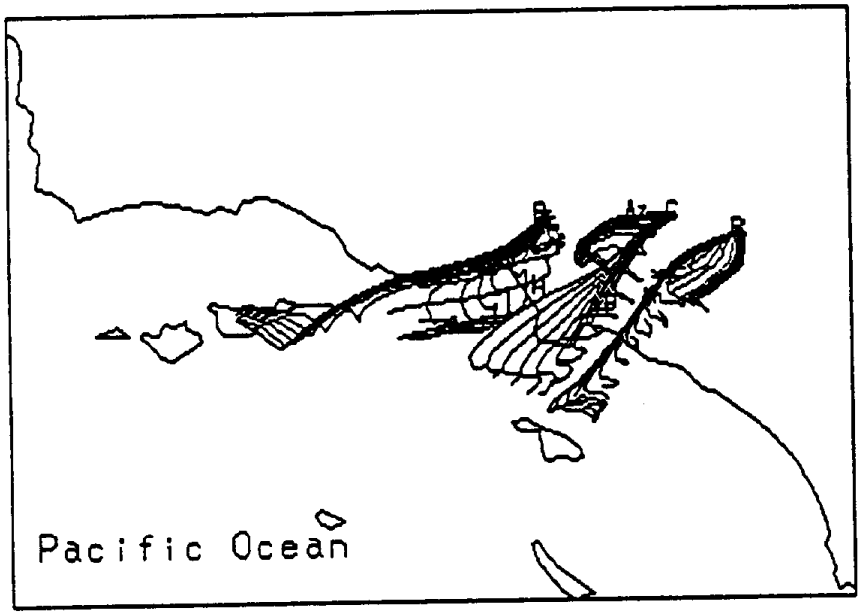

Figure 78. June 19, 1987.

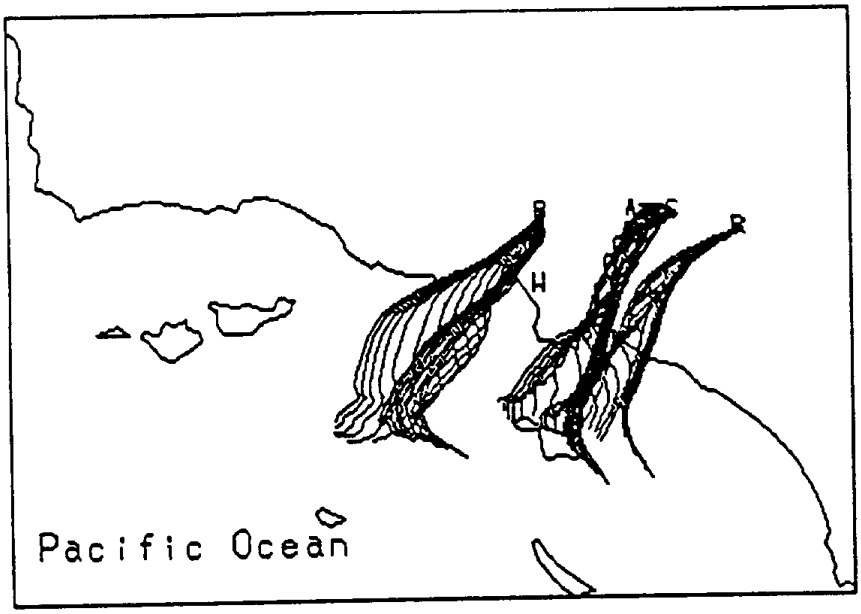

Figure 79. June 24, 1987

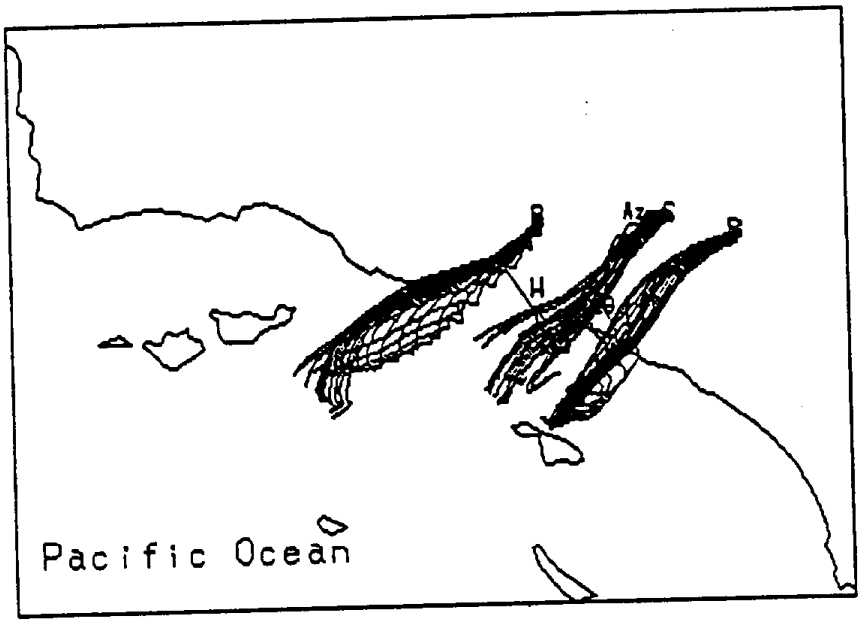

Figure 80. June 25, 1987.

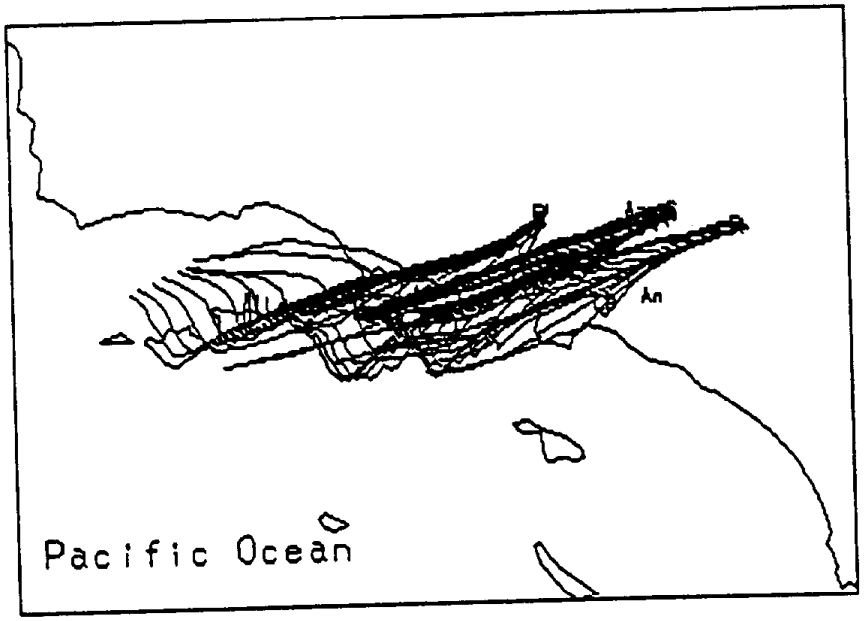

Figure 81. July 13, 1987.

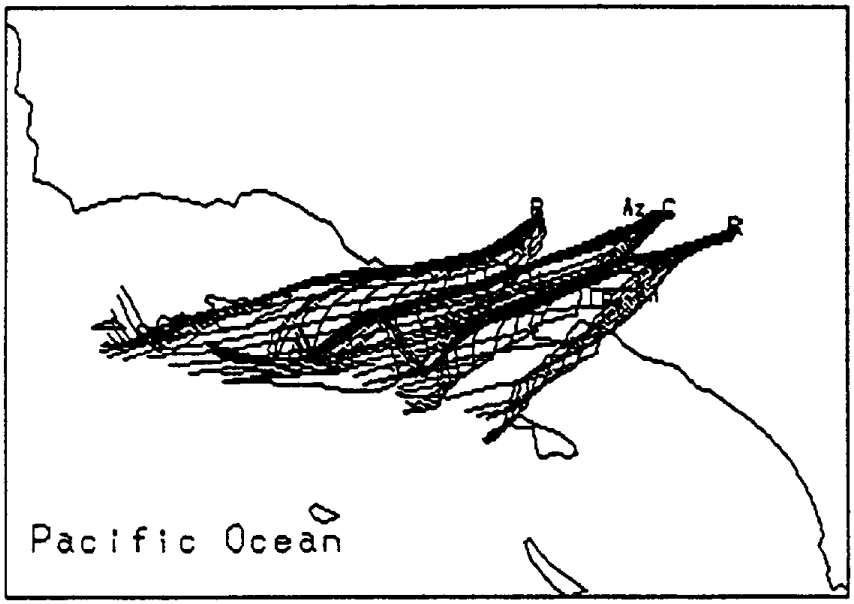

Figure 82. July 14, 1987.

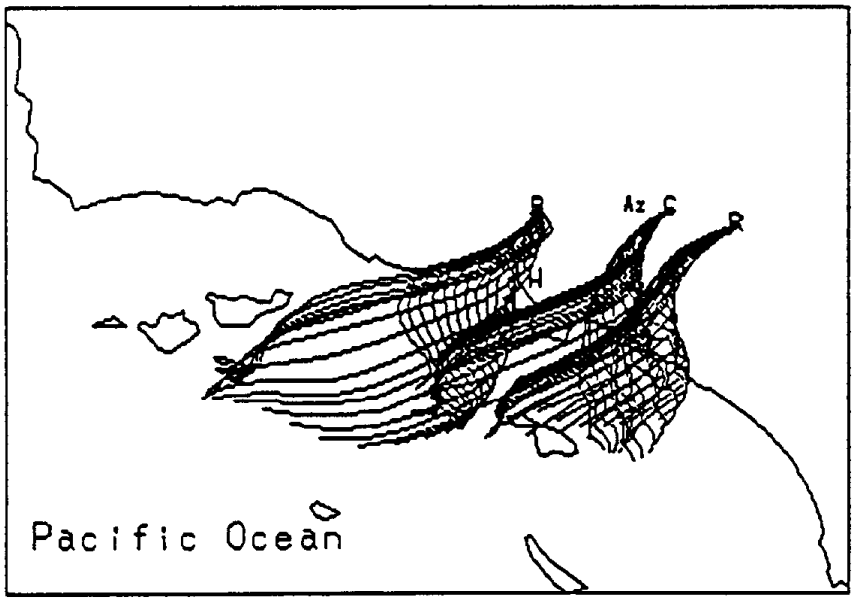

Figure 83. July 15, 1987.

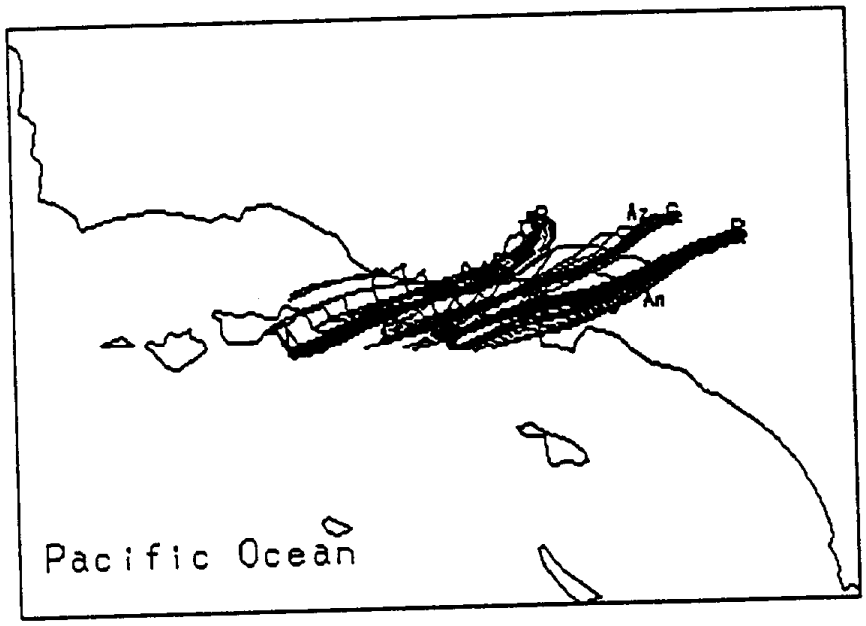

Figure 84. August 27, 1987.

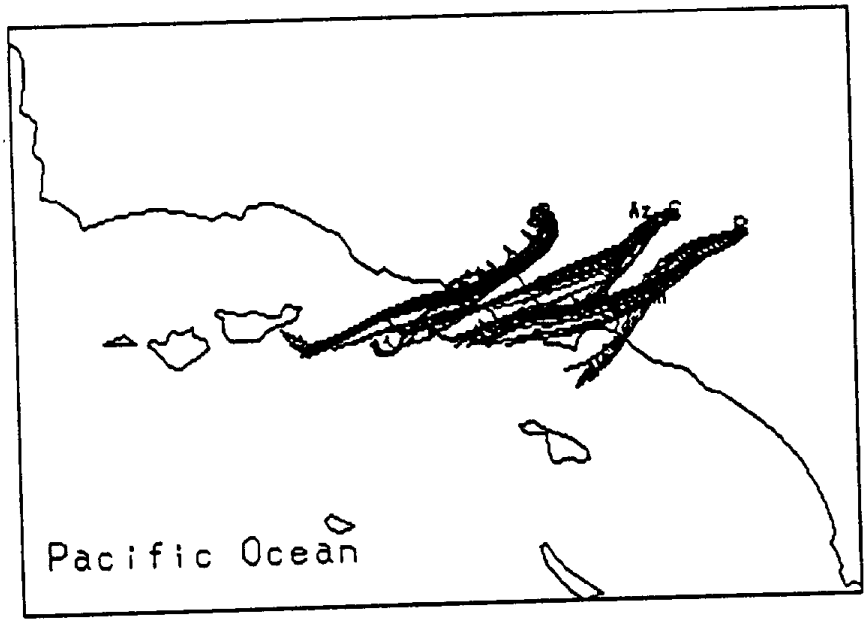

Figure 85. August 28, 1987.

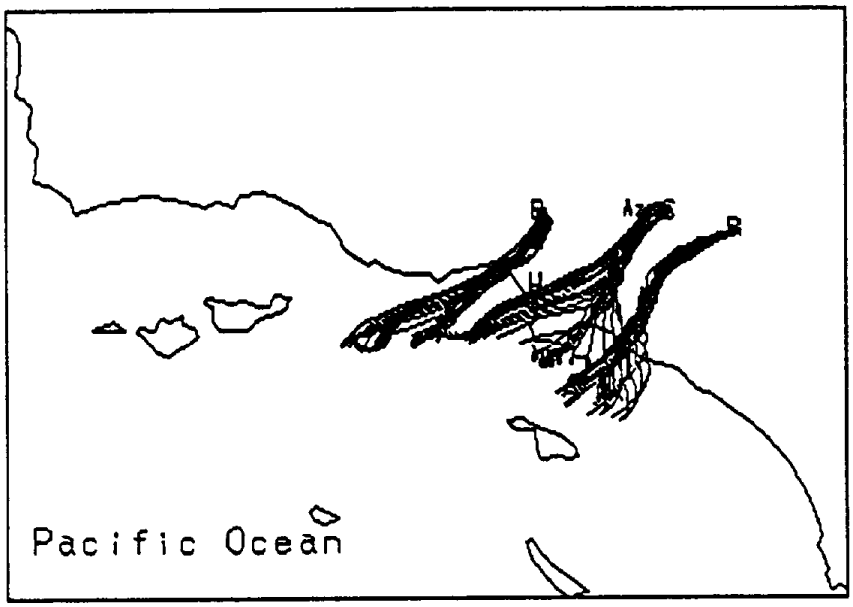

Figure 86. Aug 29, 1987.

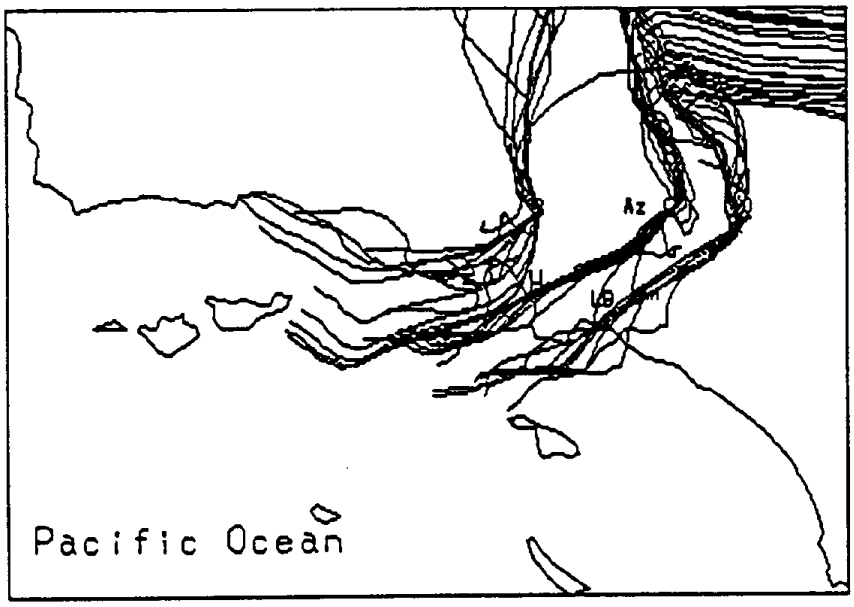

Figure 87. September 02, 1987.

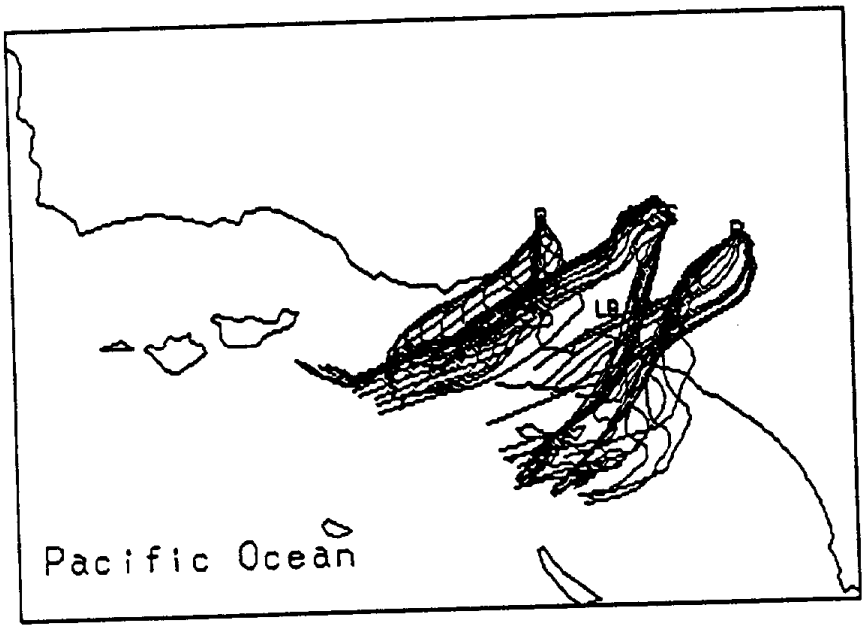

Figure 88. September 03, 1987.

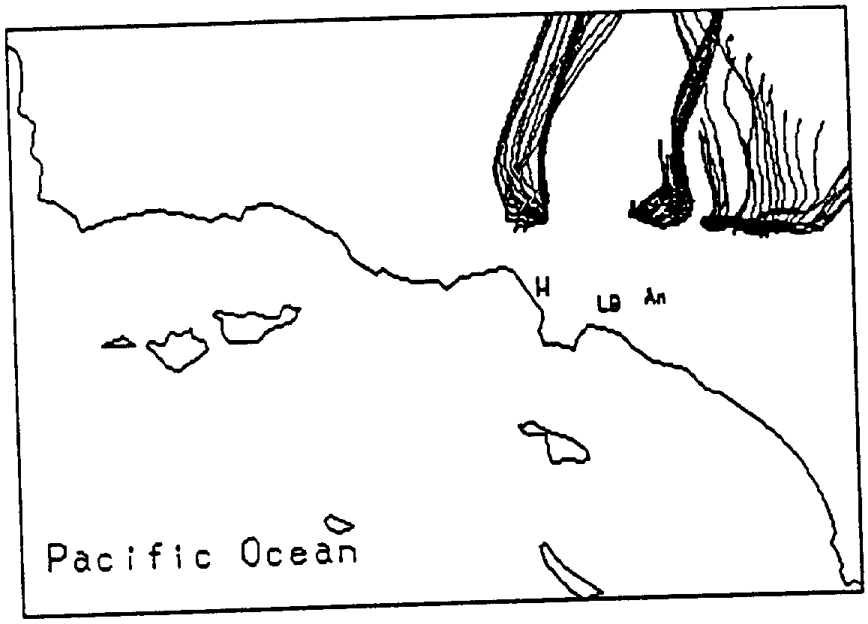

Figure 89. November 11, 1987.

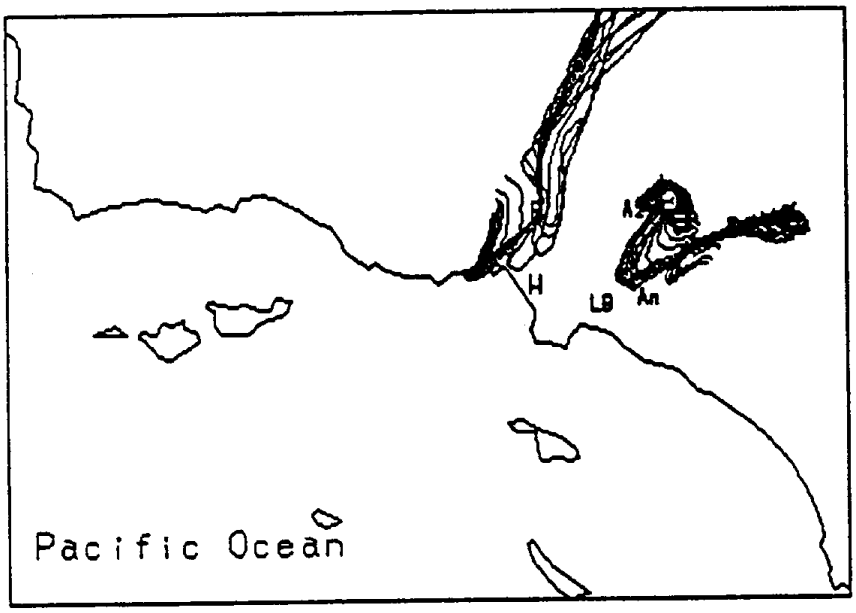

Figure 90. November 12, 1987.

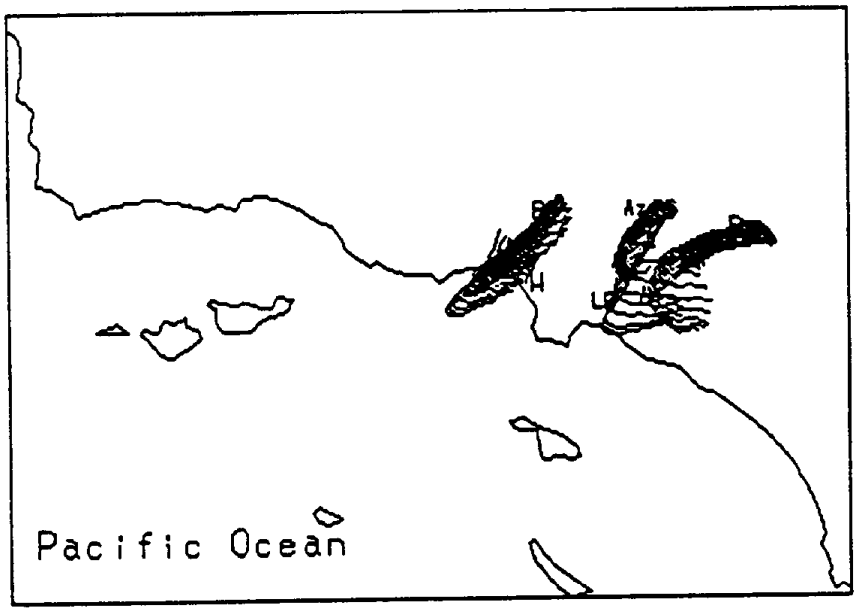

Figure 91. November 13, 1987.

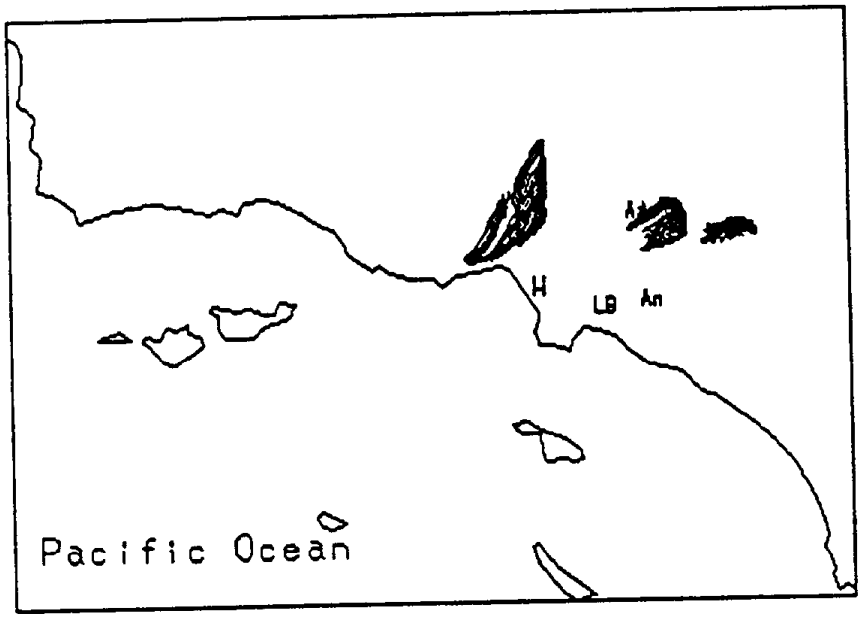

Figure 92. December 03, 1987.

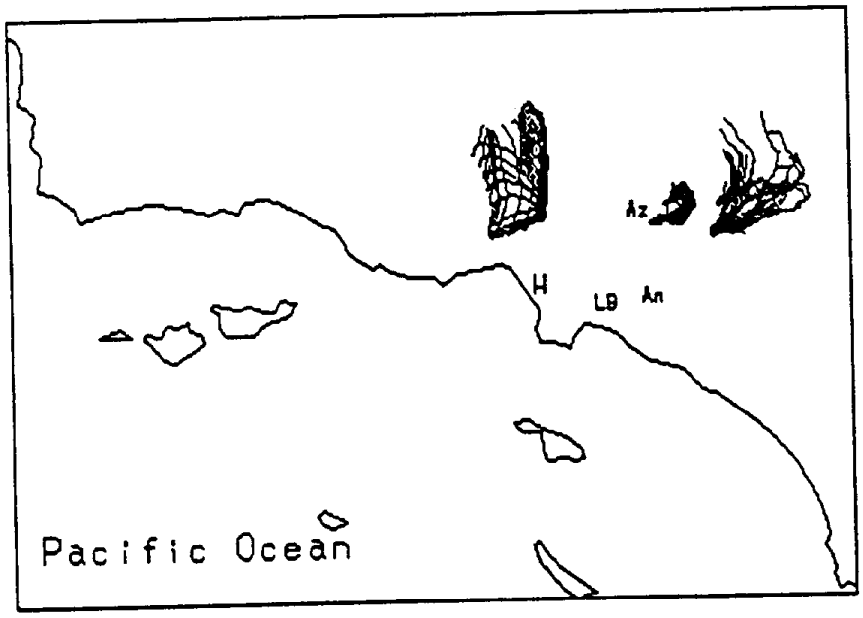

Figure 93. December 10, 1987.

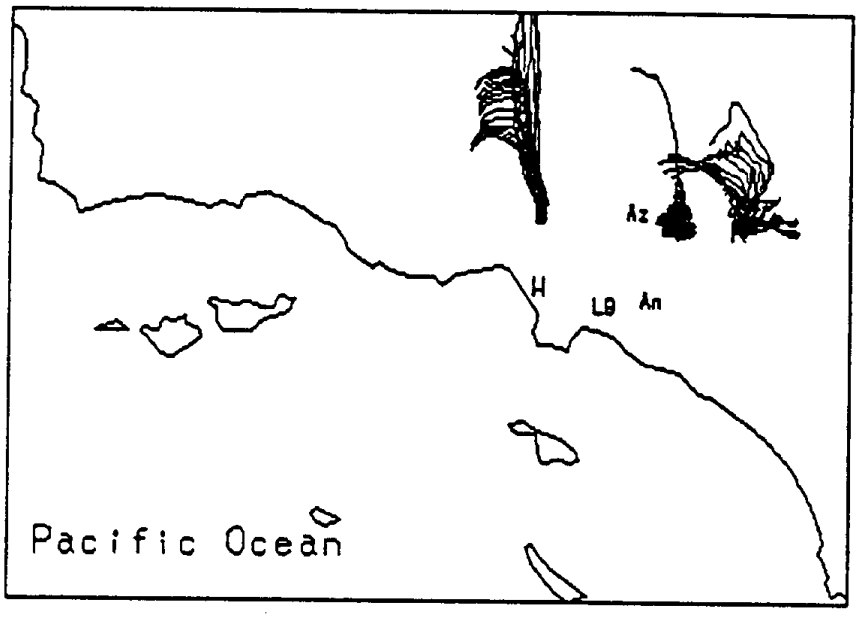

Figure 94. December 11, 1987.

Appendix C

A MULTICOMPONENT SIZE-CLASSIFYING AEROSOL AND GAS SAMPLER FOR AMBIENT AIR MONITORING

89-140.1

A MULTI-COMPONENT SIZE-CLASSIFYING AEROSOL AND GAS SAMPLER FOR AMBIENT AIR MONITORING

DENNIS FITZ AND MICHAEL CHAN

AEROVIRONMENT, INC.
MONROVIA, CALIFORNIA

GLEN CASS

CALIFORNIA INSTITUTE OF TECHNOLOGY
PASADENA, CALIFORNIA

DOUGLAS LAWSON
LOWELL ASHBAUGH

CALIFORNIA AIR RESOURCES BOARD
SACRAMENTO, CALIFORNIA

AIR & WASTE MANAGEMENT ASSOCIATION

SINCE 1907

For Presentation at the
82nd Annual Meeting & Exhibition
Anaheim, California
June 25-30, 1989

INTRODUCTION

The Southern California Air Quality Study (SCAQS) required a sampler that could collect gaseous and sized-resolved aerosol samples and that the sampling media could be changed quickly by an inexperienced technician. Since no commercial sampler met all the required criteria, a special sampler was built for this study based on the latest technology. In the process of producing an integrated sampler some changes from the originally reported techniques were unavoidable; for this reason, several of the measurement methods were tested for accuracy. In addition, all nine samplers constructed were tested for precision.

PARAMETERS MEASURED AND TECHNIQUES USED

Table I shows the measurement parameters required for SCAQS. Figure 1 shows a schematic diagram of the sampler. Twelve independent sample lines were necessary and each used forty-seven millimeter filters to collect samples. These twelve lines were grouped into four components based on the type of inlet:

Component 1 - Total aerosol, in which an open-face filter holder was placed under a rain shield

Component 2 - PM-2.5 aerosol (fine fraction), which used a Teflon-coated cyclone for size resolution

Component 3 - PM-2.5 aerosol (fine fraction), which used a stainless steel cyclone to remove larger particles

Component 4 - PM-10 aerosol with an impactor for obtaining the size cut.

Component 1 consisted of two sample lines. Line 1 is a filter pack with a Teflon (Gelman Teflo) front filter and a nylon (Gelman Nylasorb) back filter laid one-on-top-the-other. The Teflon filter prevents the nylon from plugging. This line measures total nitrate (both particulate and gas phase). Particulate nitrate is retained by the Teflon filter, while the nylon filter quantitatively collects nitric acid in the ambient air or that volatilized from the front filter[1]. Nylon filters were not subjected to further penetration evaluations. These filters are coextracted for analysis by ion chromatography. Line 2 was also a filter pack, having a Teflon (Gelman Zefluor) front filter to remove particles and a sodium-carbonate-impregnated cellulose filter (Whatman 41) to collect sulfur dioxide. These filters were separated using a two-stage holder. The latter filter is extracted and analyzed for sulfate by ion chromatography. An open-face filter holder to sample ambient air directly was necessary to avoid adsorption of SO_2 in an inlet or aluminum filter holder[2]. The flow rate and concentration of impregnating solution was determined by laboratory penetration studies.

After passing through a short, half-inch PFA tube inlet to a cyclone[3] at 22 lpm to remove particles larger than 2.5 μm, the flow of Component 2 divides into three sample lines using a manifold constructed of half-inch PFA tube fittings (Fluorocarbon). This type of manifold presents á surface relatively inert to nitric acid and results in short retention times; these features minimize wall losses[4]. Line 3 quantitatively collects particulate nitrate. It consists of a nitric acid denuder, followed by a filter pack with a Teflon (Gelman Teflo) front filter and nylon (Gelman Nylasorb) back filter; filters are laid one-on-top-the-other. As with Line 1, both filters are coextracted and analyzed for nitrate. The denuder is a tubular design consisting of ten tubes, 6mm OD, coated with magnesium oxide to remove nitric acid vapor[5] and was shown to have adequate efficiency and capacity[6]. Line 4 was similar to Line 3 except that a denuder is not used and the filter holder is made of Teflon (Savillex) instead of aluminum to minimize nitrate acid wall losses; filters are again in direct contact. Nitric acid concentrations are determined using the denuder difference technique[7] by subtracting the results from Line 3 (particulate nitrate) from those from Line 4 (particulate nitrate and nitric acid). Line 5 measures ammonia and fine ammonium. Ammonia is removed by a glass tube (6 mm OD, 30 cm long) coated with oxalic acid[8]; flow is limited to 4 lpm to ensure high collection efficiency. The tubes are extracted with water and analyzed for ammonium. We found it necessary to etch the tube with concentrated hydrofluoric acid for five minutes rather than the reported 30 seconds in order to quantitatively remove the gas. For sampler performance testing, these tubes were not reused. Below the ammonia denuder, an oxalic-acid-impregnated quartz filter (Pallflex QAO) quantitatively traps fine particulate ammonium for analysis after water extraction[9].

The inlet of Component 3 is a high capacity cyclone (110 lpm) necessary to obtain the required sensitivity for some of the parameters measured. Since reactive gases are not measured, a stainless steel cyclone (Sensidyne model 240) is adequate. The cyclone was greased lightly with Apiezon M to prevent large particle penetration. The cyclone is in a stilling chamber that consists of a four-liter metal cylinder with the bottom open. One meter of half-inch stainless steel tubing connected the cyclone to an aluminum sampling manifold (20 cm diameter pipe 10 cm long with end plates welded on). The manifold splits the flow into four lines. Line 6 samples at 5 lpm through a polycarbonate membrane filter (Nuclepore) to determine the absorption coefficient of the fine particulate matter[10]. Line 7 samples 35 lpm through a quartz filter which is analyzed by a thermal volatilization technique[11] for organic and elemental carbon. A single tared Teflon filter (Gelman Teflo) samples at 35 lpm from Line 8; this filter is analyzed for mass deposition and trace elements determined by X-ray fluorescence[12,13]. Line 9 consists of a Teflon front filter (Gelman Teflo), which is extracted and analyzed for nitrate, sulfate, chloride, and ammonium and a quartz back filter (in direct contact with the front filter) which was analyzed for organic carbon in order to estimate the collection artifact due to adsorption of organic gases by the filtration medium.

A medium volume PM-10 inlet (Andersen model GMW 254-I) is used for the three PM-10 sampling lines of component four. An aluminum manifold was used to adapt the 10 cm inside diameter of the inlet exhaust to three twelve mm stainless steel tubes suitable for the in-line filter holders used. The flow rates were evenly divided at 35 lpm each to meet the total flow required of the inlet. The manifold was tested for isokinetic splitting by comparing mass concentrations determined from the three in-line holders to that of one filter sampling from another identical PM-10 inlet; all concentrations agreed to within five percent. Sample Lines 10-12 were identical to Lines 7-9 respectively except that a quartz back filter was not used on line ten.

PHYSICAL LAYOUT

The components of the sampler are laid out in a 30 x 36 x 12 inch aluminum cabinet as shown schematically in Figure 2; Figure 3 is a photograph. A high-capacity fan, in combination with screened louver, circulates air to prevent heat buildup. The temperature rise was measured to be an acceptable 1°C when ambient temperatures were 33-35°C. Except for Line 4, all in-line filter holders are aluminum (Gelman part number 1235); the open face filters are constructed of Teflon (Savillex). The in-line filters are connected to their respective sample ports using o-ring fittings (Cajon Ultra-Torr), which allow quick and easy connection and unimpeded flow. The outlet of the holders attach to a vacuum manifold via PVC tubing and standard color-coded quick-connects keyed to prevent improper connection. The filter holders may therefore be easily and quickly removed for servicing. The ammonia denuder sample tubes are permanently encased in a three-quarter-inch PVC pipe. A small pump passes air warmed by a small light bulb through the pipe to prevent water from condensing in the denuder tube. Pipe and end caps attached before and after sampling prevent breakage of the fragile glass denuder tube. During construction, all sampler components upstream of the filters were washed thoroughly with methyl alcohol.

The pumping system consists of three vacuum manifolds; Components 1 and 2 share one while Components 3 and 4 have separate manifolds. The exhaust of the pumps is filtered through a high-capacity, high-efficiency filter to prevent carbon contamination. Separate three-quarter horsepower carbon vane vacuum pumps are used for each manifold. These are housed in a separate cabinet. Sample flow through each line is controlled by critical orifices. Flows are monitored at the inlet of all filter holders immediately before and after sampling with one of two rotameters, depending on the flow rate. This allows the detection of leaks and flow rate changes due to filter overloading. The rotameters were calibrated using a mass flowmeter traceable to NBS-standards prior to precision testing.

PRECISION TESTING

The precision testing consisted of two steps. First, a single sampler (the prototype) collected particulate mass on Teflon filters on all sample lines except Lines 5 and 6 (the

flow rates were too low to generate a mass loading that could be weighed accurately) to determine whether sampling lines of a given size range (total, PM-2.5 and PM-10) were equivalent. Next, all nine samplers were operated side by side, measuring all components as if they were being used for SCAQS.

In the first phase, 12 sets of samples were collected with one sampler for periods ranging from 4 to 24 hours. Table II summarizes the results, grouping the sample lines by inlet type. All concentrations were corrected for the median blank of that component. The greatest variation was between the open face filters; the variation within the other inlets was within the experimental error. Both of the cyclones gave the same mass concentrations within the experimental error. Particle losses through the nitric acid denuder were not significant. All PM-10 sample lines gave equivalent mass concentrations.

In the second phase, six sets of samples using all nine samplers were collected, with intervals varying from 3.5 to 12 hours; one complete set of field blanks were also collected in accordance with the SCAQS protocol. Using this protocol, field blanks were loaded into the sampler and allowed to sample ambient air long enough to obtain beginning rotameter values. The pumps were then shut off for four hours and turned back on just long enough to read all rotameter flows. The field blanks were sampling ambient air for about five minutes or about 2 percent of the shortest prescribed sampling interval. The samples were collected in early June during a period of relatively good air quality. This precision testing study also served as a final training exercise for site technicians.

In order to assess the statistical significance of side-by-side data, it is first necessary to determine the precision and sensitivity of the analytical method. The overall detection limit is defined as the analytical detection limit or three times the blank variability, whichever is the larger. Table III shows the detection limits calculated from the field blanks, assuming nominal flow rates and a collection period of 3.5 hours. Table IV gives the mean concentrations, the percent of the detection limit compared to the mean concentration and the coefficients of variation obtained during the side-by-side comparison; also included are typical concentrations for the South Coast Air Basin. Except for absorption measurements, the detection limits are all typically less than 20 percent of the typical concentrations. Except for fine chloride, the mean coefficients of variability are quite acceptable compared to the detection limit percent of the mean concentration; the chloride concentrations were extremely low. A more detailed analysis of the sampler variability of each parameter showed only ammonia obtained from Sampler 5 was differing significantly from the other samplers. This may have been due to improper attachment of the denuder tube to the sampling manifold; all technicians were further trained in this operation.

CONCLUSIONS

Compact, reliable, and easily serviced gas and aerosol samplers were constructed to meet the analytical requirements of SCAQS. Methods were based on state-of-the-art techniques and further validated as necessary, especially with regard to inlet losses and breakthrough losses of gases and isokinetic sampling of PM-10 particulate matter. The samplers were characterized for precision and found to be essentially equivalent, given the detection limits of the methods used. The SCAQS samplers provide an efficient approach to measuring many of the parameters needed to characterize ambient air quality.

ACKNOWLEDGMENTS

The design, construction, and testing of the SCAQS sampler was made possible by a large team of individuals whose contributions were greatly appreciated but all of whose names cannot be listed here due to space limitations. We wish to thank Drs. Bruce Appel, Richard Countess, Susanne Hering, Kenneth Knapp, and Paul Roberts for their helpful design comments. We are especially grateful to Dr. Richard Countess for coordinating the preparation and analysis of filters used during the testing procedure. Other analyses were conducted by Barbara Wright, Thomas Cahill and Bob Kellogg. Finally, we would like to thank Paul Pruss for his tremendous effort in leading the construction team.

REFERENCES

1. B. R. Appel, S. M. Wall, Y. Tokiwa, and M. Haik, "Simultaneous nitric acid, particulate nitrate and acidity measurements in ambient air," Atmos. Environ., 14:549 (1980).

2. R. L. Byer and S. W. Davis, "Sulfur dioxide adsorption and desorption on various filter media," JAPCA, 20:236 (1970).

3. W. John and G. Reischl, "A cyclone for size-selective sampling of ambient air," JAPCA, 30:872 (1980).

4. B. R. Appel, V. Povard and E. L. Kothny, "Loss of nitric acid within inlet devices intended to exclude coarse particles during atmospheric sampling," Atmos. Environ., 22:2535 (1988).

5. R. W. Shaw, Jr., R. K. Stevens, J. Bowermaster, J. W. Tesch and E. Tew, "Measurements of atmospheric nitrate and nitric acid: The denuder difference experiment," Atmos. Environ., 16:845 (1982).

6. P. A. Soloman, S. M. Larson, T. Fall and G. R. Cass, "Basinwide nitric acid and related species concentrations observed during the Claremont nitrogen species comparison study, Atmos. Environ., 22:1587 (1988).

7. *Ibid.*

8. M. Ferm, "Method for determination of atmospheric ammonia," Atmos. Environ., 13:1385 (1979).

9. S. J. Cadle, R. J. Contess and N. A. Kelly, "Nitric acid and ammonia in urban and rural locations," Atmos. Environ., 16:2105 (1982).

10. H. E. Gerber and E. E. Hinkman, Light Absorption by Aerosol Particles, Spectrum Press, Hampton, VA, 1982.

11. P. K. Mueller, K. Fung, S. Heisler, D. Grosjean, and G. M. Hidy, Particulate Carbon: Atmospheric Life Cycle, G. T. Wolff and R. L. Klimisch, eds., Plenunum Press, New York, 1982, p. 343.

12. R. L. Bennett, J. Wagman and K. T. Knapp, "Application of a multichannel fixed and sequential spectrometer system to the analysis of air pollution particulate samples from source emissions and ambient air," Adv. X-Ray Anal., 19:393 (1975).

13. K. T. Knapp, T. G. Ellestad and L. Stockburger, "Elemental mass determinations of PM 2.5 and PM 10 particles by X-ray fluorescence from the 1987 Southern California Air Quality Study, " to be published in Atmos. Environ.

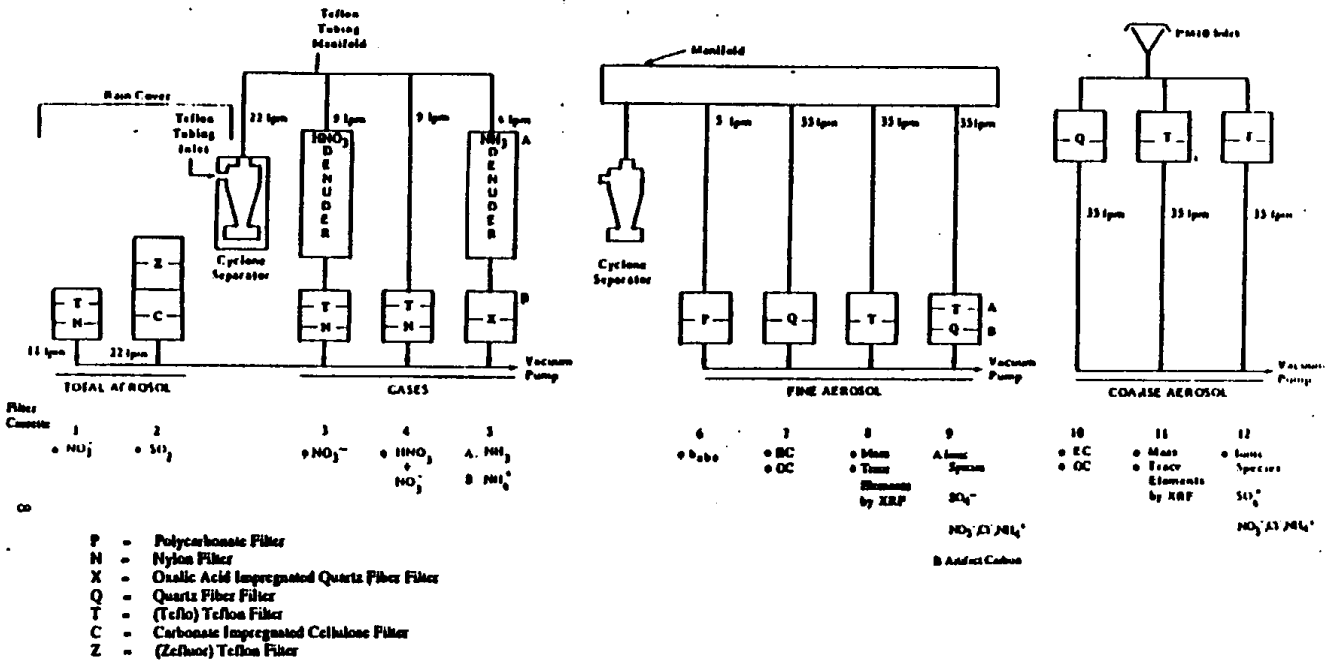

FIGURE 1. Schematic diagram of SCAQS sampler.

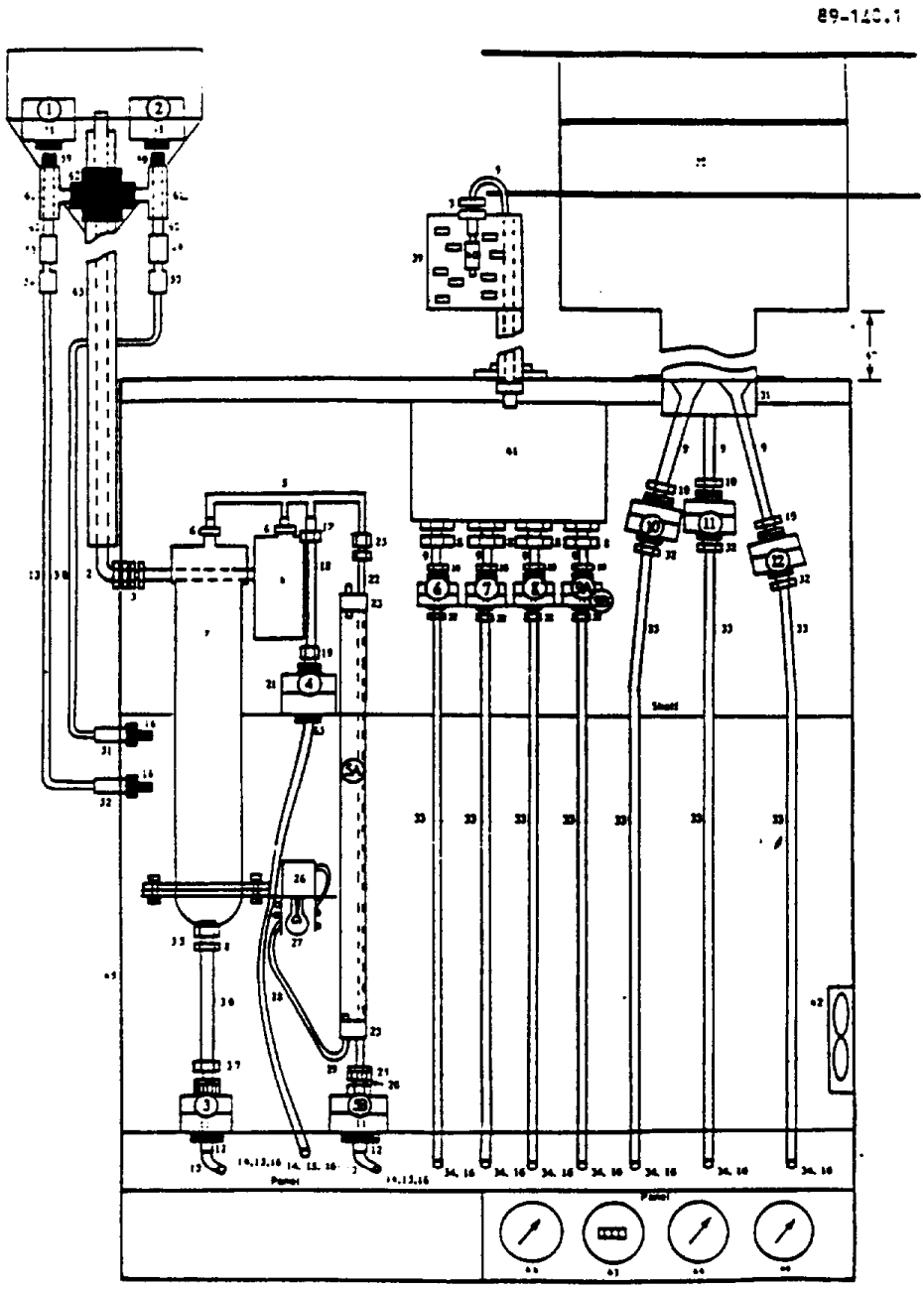

FIGURE 2. SCAQS sampler schematic layout.

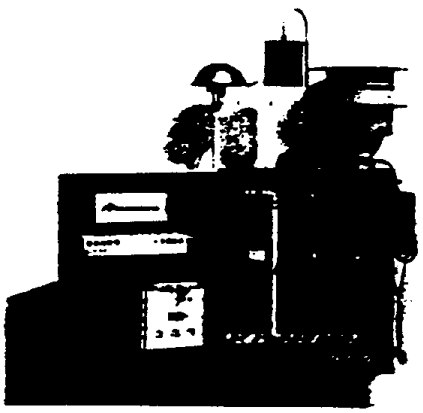

FIGURE 3. SCAQS sampler.

TABLE I. SCAQS sampler measurement parameters and methods.

Observable	Method
Gases	
SO_2	Impregnated Filter — IC
NH_3	Denuder Tube — Technicon
HNO_3	Denuder Difference — IC
Total Aerosol	Open-Face Filter
HNO_3, NO_3^-	Filter — IC analysis
10 μm Aerosol Fraction	Size selective inlet
Mass	Filter — Gravimetry
$SO_4^=$	Filter — IC
NO_3^-	Filter — IC
NH_4^+	Filter — Technicon
Cl^-	Filter — IC
Trace elements	Filter — XRF
Elemental carbon	Filter — Thermal Volatilization
Organic carbon	Filter — Thermal Volatilization
2.5 μm Aerosol Fraction	Cyclone
Mass	Filter — Gravimetry
$SO_4^=$	Filter — IC
NO_3^-	Denuder — Filter — IC
NH_4^+	Denuder — Filter — Technicon
Cl^-	Filter — IC
Trace elements	Filter — XRF
Elemental carbon	Filter — Thermal Volatilization
Organic carbon	Filter — Thermal Volatilization
b_{abs}	Filter — Spectrometry

TABLE II. Statistical summary of mass concentrations (blank corrected) for SCAQS prototype precision testing ($\mu g/m^3$).

Inlet	Filter Position	Nominal Flow (ALPM)	Mean
Total	1	20	42.0
Total	2A	35	55.7
Total	Mean		48.9
2.5 μm (LC)[a]	3	10	21.5
2.5 μm (LC)	4	10	23.6
2.5 μm (LC)	Mean		22.6
2.5 μm (HC)[b]	7	37	21.6
2.5 μm (HC)	8	37	23.0
2.5 μm (HC)	9	37	21.8
2.5 μm (HC)	Mean		22.1
10 μm	10	38	40.0
10 μm	11	38	37.8
10 μm	12	38	39.1
10 μm	Mean		39.0

[a] LC = Low capacity
[b] HC = High capacity

TABLE III. Detection limits for species collected by the SCAQS sampler during the side-by-side comparison.

TABLE III. Detection limits for species collected by the SCAQS sampler during the side-by-side comparison.

Line No.	Species	Collection Substrate	Flow Rate (lpm)	Sample Volume (m^3)	Extraction Volume (ml)	Analytical Detection Limit* (µg/ml)	Analytical Detection Limit* ($\mu g/m^3$)	Filter Blank Variability (3σ (µg/filter)	Overall** D.L. ($\mu g/m^3$)
1	Total Nitrate	Nylon	11	1.9	10 (IC eluent)	0.018	0.09	1.2	0.8
2	SO_2	$CO_3^=$-CE behind Teflon	20	4.2	10 (0.00% H_2O_2) 0 (H_2O)	0.015	0.14	0.69	0.16
3	PM-2.5 NO_3^-	Nylon behind MgO denuder	9	1.9	10 (IC eluent)	0.018	0.09	1.5	0.8
4	HNO_3 + PM-2.5 NO_3^-	Nylon	9	1.9	10 (IC eluent)	0.018	0.09	1.5	0.8
5a	NH_3	Oxalic acid denuder	4	0.84	10 (H_2O)	0.012	0.14	0.65	0.54
5b	PM-2.5 NH_4^+	Oxalic acid-CE	4	0.84	10 (H_2O)	0.012	0.14	0.9	1.1
6	B-absorption	Polycarbonate	5	1.2	--	--	32**	96**	96**
7	PM-2.5 Org C.	Quartz	37	7.8	--	--	0.13		0.39
7	PM-2.5 Elem C.	Quartz	37	7.8	--	--	0.13		0.39
9a	Organic Artifacts	Quartz	37	7.8	--	--	0.13		0.39
8	PM-2.5 Elements (S)	Teflon	37	7.8	--	--	0.06	0.93	0.12
8	PM-2.5 Mass	Teflon	37	7.8	--	15 µg	1.9	130	19
9	PM-2.5 $SO_4^=$	Teflon	37	7.8	15 (H_2O)	0.015	0.03	1.35	0.17
9	PM-2.5 Cl^-	Teflon	37	7.8	15 (H_2O)	0.015	0.03	0.21	0.03
10	PM-10 Org. C	Quartz	38	8.0	--	--	0.13		0.39
10	PM-10 Elem. C	Quartz	38	8.0	--	--	0.13		0.39
11	PM-10 Elements (Fe)	Teflon	38	8.0	--	--	0.06	0.30	0.06
11	PM-10 Mass	Teflon	38	8.0	--	15 µg	1.9	79	9.9
12	PM-10 $SO_4^=$	Teflon	38	8.0	15 (H_2O)	0.015	0.03	1.35	0.17
12	PM-10 Cl^-	Teflon	38	8.0	15 (H_2O)	0.015	0.03	0.21	0.03

* Assume 3.5 hour collection
** Overall detection limit = 3 x filter blank variability (µg/filter) divided by m^3
* Analytical detection limit µg/ml x ml divided by m^3
** Units - 10^{-6} m^{-3}

TABLE IV. Summary of SCAQS side-by-side evaluation.

Line	Species	Mean Concentration for the Evaluation µg/m3	Detection Limit[a] % of Mean Concentration	Mean Coefficient[b] of Variation %	Typical Concentration for the SCAB µg/m3
1	Total NO_3^-	5	16	9	10
2	SO_2 as $SO_4^=$	1	16	21	15
3	PM-2.5 NO_3^-	3	26	7	8
4	HNO_3 + PM-2.5 NO_3^-	4	20	11	21
5A	NH_3 as NH_4^+	1	54	42	3
5B	PM-2.5 NH_4^+	4	28	30	5
6	b_{abs}	200[c]	40	238	20[c]
7	PM-2.5 OC	1	4	9	15
	PM-2.5 EC	1	39	25	2
8	PM-2.5 Mass	40	48	8	40
	PM-2.5 S	2	6	6	0.5
9A	PM-2.5 Cl^-	0.1	18	43	3
	PM-2.5 $SO_4^=$	5	3	6	5
9B	Organic Artifacts	6	7	10	3
10	PM-10 OC	13	3	10	20
	PM-10 EC	2	20	20	4
11	PM-10 Mass	60	17	5	50
	PM-10 Fe	2	2	9	2
12	PM-10 Cl^-	0.7	4	11	5
	PM-10 $SO_4^=$	6	3	7	5

[a] Mean overall detection limit is the overall detection limit expressed as a percentage of the mean value for the study.

[b] Mean coefficient of variation is the mean of the coefficients of variation for each period.

[c] Units $10^{-4}m^{-1}$